UNIVERSITY OF CALIFORNIA
Los Angeles

Unraveling the origin of the L-H isotope effect at the DIII-D tokamak

A dissertation submitted in partial satisfaction
of the requirements for the degree
Doctor of Philosophy in Physics

by

Kyle Jerry Callahan

2024

ABSTRACT OF THE DISSERTATION

Unraveling the origin of the L-H isotope effect at the DIII-D tokamak

by

Kyle Jerry Callahan
Doctor of Philosophy in Physics
University of California, Los Angeles, 2024
Professor Troy A. Carter, Chair

Over the course of this PhD thesis, the dominant physics underlying the isotope dependence of the low- to high confinement (L to H-mode) transition in the DIII-D tokamak has been studied in detail. Historically, the pronounced isotope dependence of the L-H power threshold has been attributed to differences in thermal transport and in the radial electric field at the plasma edge. In this thesis, extensive gyrofluid and local gyrokinetic modeling via the TGLF and CGYRO codes attribute the observed increased thermal transport in hydrogen to three important effects: 1) a reduced critical gradient for Ion Temperature Gradient (ITG) modes, caused by reduced carbon sputtering and impurity dilution in hydrogen plasmas; (2) electron non-adiabaticity (leading to increased transport fluxes in hydrogen), and (3) the main ion mass dependence of $\vec{E} \times \vec{B}$ shear stabilization (leading to reduced edge turbulence suppression in hydrogen). Turbulence predictions from CGYRO gyrokinetic simulations are compared to experimental measurements including electron temperature, density and $\vec{E} \times \vec{B}$ velocity fluctuations, and are found to be in good agreement with available experimental turbulence data. In addition to validating edge transport predictions, this thesis has focused on the isotopic dependence of the edge radial electric field. A two times larger edge radial electric field in hydrogen plasmas, compared to deuterium, is believed to play a fundamental role in setting the requisite conditions which trigger the L-H transition. Two effects are found to contribute to these isotopic differences in E_r: A larger radial

gradient of the turbulent Reynolds stress in hydrogen, and an increased outer strike point electron temperature and space potential on open field lines. Dedicated experiments were also performed to actively reduce the L-H power threshold in hydrogen plasmas (a topic of great relevance for the initial non-nuclear ITER experiments). The goal of this work was to artificially increase Z_{eff} via carbon seeding to match the deuterium experiments, and possibly reduce the L-H power threshold based on gyrokinetic predictions of reduced ITG-driven thermal transport. While ITG turbulence was indeed observed to be reduced as expected with carbon seeding, no discernible change in L-H power threshold was found. A detailed investigation determined that the Reynolds stress and edge radial electric field were nearly unchanged in the presence of carbon seeding and ITG stabilization. Hence, taken together these experiments point to the differences in electric field (and associated $\vec{E} \times \vec{B}$ shear) as the most likely origin of the isotope dependence of the L-H power threshold in deuterium and hydrogen.

The dissertation of Kyle Jerry Callahan is approved.

Lothar W. Schmitz

William W. Heidbrink

Christoph Niemann

Eduardo Paulo Da Costa Alves

Troy A. Carter, Committee Chair

University of California, Los Angeles

2024

To my parents Steve and Maria Callahan, for supporting me for so many years on my educational journey.

TABLE OF CONTENTS

LIST OF FIGURES

LIST OF TABLES

ACKNOWLEDGMENTS

I would like to thank my advisors Professor Troy Carter and Dr. Lothar Schmitz for their years of support and guidance. To Troy, your devoted work ethic and commitment towards improving the fusion research community has inspired me to not be afraid of taking on new, exciting challenges, whether they be research related or otherwise. To Lothar, your patience, technical know-how, and dedication to my learning have pushed me to become the best fusion community member and scientist I can be. Your mentorship has shaped me into the student I am today. I am indebted as well to all the researchers at DIII-D who have helped me along my journey. To Dr. Colin Chrystal, Dr. Shaun Haskey, and Dr. Brian Grierson for continuing my mentorship long after my SULI days, the time spent operating CER and bugging you with questions would routinely be a highlight of my week. To Dr. George McKee and Dr. Zheng Yan, your tireless support during the many DIII-D reviews, presentations, and experiments helped me better understand the utter strangeness and sometimes contradictory nature of hydrogen plasmas. I am grateful to Dr. Alessandro Bortolon, Dr. Alex Nagy, and Dr. Florian Effenberg, your impurity powder dropper expertise and knowledge was essential to the success of my PhD experiments. I thank Dr. Kathreen Thome, Dr. Matthias Knolker, and Dr. Al Hyatt for your Physics Operator skills, which taught me how to navigate operational problems I didn't even know existed. To Dr. Gary Staebler, your patience and willingness to answer my dumb questions taught me greatly about TGLF. I thank all my CGYRO mentors, Dr. Emily Belli, Dr. Chris Holland, Dr. Tom Neiser, and Dr. Arash Ashourvan, your advice helped me learn how to intelligently plan for and submit gyrokinetic simulations. I thank Dr. Sterling Smith from granting the NERSC DIII-D resources used to perform the gyrokinetic simulations presented in this thesis. To Dr. Chris Holland, Dr. Terry Rhodes, Dr. Guiding Wang, and Dr. Shaun Haskey also for your advice and guidance on the synthetic BES and CECE diagnostic tools, without which all of thesis chapter 5 would not have been possible. Additionally, I am indebted to Dr. Robert Wilcox, Dr. Filippo Scotti, and Dr. Andreas Holm for their guidance and expertise in understanding the scrape off layer and langmuir probe observations, which helped unravel

the mystery of the edge radial electric field isotope effect. For all the UCLA and DIII-D graduate students and post-docs I had the opportunity to work alongside: Quinn Pratt, Ryan Chaban, Raul Gerru, Filipp Khabanov, Kenny Gage, Genevieve DeGrandchamp, Xuan Sun, Josh Larson, Phil Travis, Yhoshua Wug, Jesus Perez, Gurleen Bal and many, many more. Your support helped keep me sane when I couldn't tell up from down, and the weekly volleyball games and farmers market pupusa runs were things I will remember for years to come. To my outreach friends Venezia Ramirez, Ingrid Maradiaga, Ileana Callejas, Jesus Perez, Casey Barkan, Oak Nelson, and Kunal Sanwalka for their shared enthusiasm for science communication and giving to those in need, you helped me learn how personally impactful outreach could be towards my own happiness.

Also to my supportive and ever-encouraging familia, this thesis is only possible due to all your love and guidance through out the years. To my mom and dad, Maria and Steve Callahan, all your efforts from NICU to present day, are what have shaped me into who I am today. To my twin brother Chad, for keeping me alive with the copious free food and company on the long drives to visit family, thank you for pushing me to be balanced and relentlessly persistent in my pursuit of higher education. To my extended friends and family, thank you for providing a sense of refuge where I could be myself, these times always remind me why I work hard to help shape the world into one with a hopefully bright (fusion-lit) future(:

VITA

1996	Born, Northridge, California, USA
2015	High School Graduation Valencia, Santa Clarita, California, USA
2019	B.S. (Physics) UCI, Irvine, California, USA
2020	M.S. (Physics) UCLA, Los Angeles, California, USA
2020-2024	Graduate Student Researcher UCLA, Los Angeles, California, USA Department of Physics and Astronomy

PUBLICATIONS

Isotope dependence of the edge radial electric field at the DIII-D tokamak
K.J. Callahan, US-EU Transport Task Force,
Asheville, North Carolina, USA, April 10th, 2024

Understanding the L-H transition isotope effect at the DIII-D tokamak
K.J. Callahan, Invited Talk, American Physical Society, Division of Plasma Physics Meeting,
Denver, Colorado, USA, Nov. 1st, 2024

On the origin of the DIII-D LH power threshold isotope effect

K.J. Callahan, et al., Nuclear Fusion, 63, 126009 (2023)

Isotope dependence of the L-H power threshold at the DIII-D tokamak
K.J. Callahan, Plenary Talk, US Transport Task Force,
Madison, Wisconsin, USA, May 2nd, 2023

Reducing the LH transition power threshold in ITER-similar-shape DIII-D hydrogen plasmas
L. Schmitz, et al., Nuclear Fusion, 62, 126050 (2022)

CHAPTER 1

Introduction

Fusion reactions, which underpin the process which powers all stars (including our own sun) has long been sought as a clean, green, and reliable energy resource. These reactions are highly desirable because they yield far more energy compared to that required to overcome the start up energy cost (due to coulomb electrical repulsion) and are often produced from isotopes of hydrogen, the most abundant element in the universe. As a result of their importance, these isotopes of hydrogen are given special names: deuterium (1 neutron and 1 proton) and tritium (2 neutrons and 1 proton). These types of hydrogen can be found on earth with a chemical abundance of 0.0156% and 10^{-15} % respectively. Tritium, because of its extremely small radioactive half-life (12.33 years), is virtually absent from nature, but can be manufactured from isotopes of lithium. The most prominently studied fusion reactions (including those used to make tritium) are:

$$\begin{aligned}
{}^2D +{}^3T &\rightarrow {}^4He\ (3.52\,MeV) +{}^1n\ (14.06\,MeV) \\
{}^2D +{}^2D &\rightarrow {}^3T\ (1.01\,MeV) +{}^1H\ (3.02\,MeV) \quad (50\%) \\
{}^2D +{}^2D &\rightarrow {}^3He\ (0.82\,MeV) +{}^1n\ (2.45\,MeV) \quad (50\%) \\
{}^1n +{}^6Li &\rightarrow {}^3T\ +{}^4He\ +4.784\,MeV \\
{}^1n +{}^7Li &\rightarrow {}^3T\ +{}^4He\ +{}^1n - 2.467\,MeV
\end{aligned} \tag{1.1}$$

Similar to the very core of the sun, experiments must achieve extremely high temperatures for these reactions to occur frequently enough to be self sustaining. Such temperature requirements, often quoted in the range of 100 million °C (10 keV) demand an extremely

efficient energy confinement system, where the working fluid is in the plasma state. The plasma state is one where electrons have been stripped off their atoms due to the excessive heat, and can move as independent electrically charged objects. There are several methods which potentially can permit efficient enough plasma energy confinement to enable self sustaining fusion reactions, including devices known as stellarators, tokamaks, and Z-pinches. The focus of this research is on the most mature of these devices, involving a machine called a tokamak.

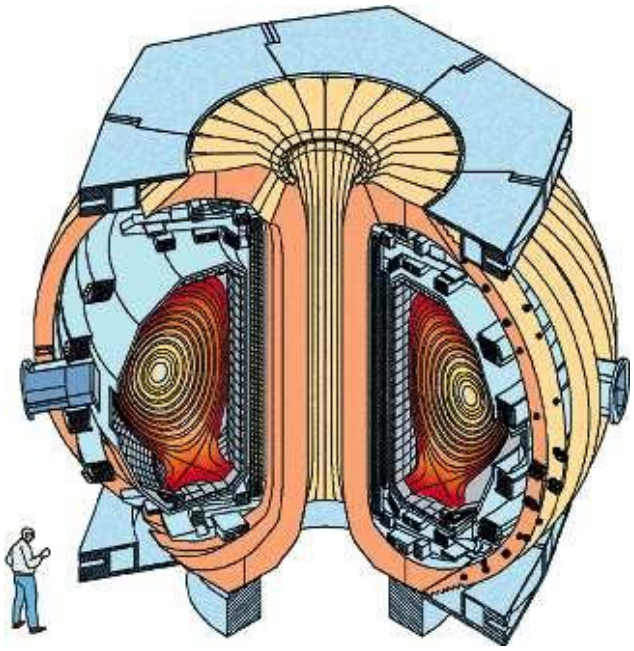

Figure 1.1: A diagram of the DIII-D Tokamak with a person shown for scale. Figure was generate by General Atomics, and can be found using the link: https://fusion.gat.com/global/diii-d/home.

A tokamak is a doughnut (torus) shaped device that uses a spiraled (helical) magnetic field line geometry to confine the plasma. The machine, which derives its name from a Russian acronym for "toroidal chamber with magnetic coils", has its primary toroidal (along the doughnut) magnetic field (B_{tor}) produced from strong poloidal coil currents, shown in Figure 1.1 as the yellow-orange structures in the DIII-D tokamak. This toroidal magnetic field goes as $B_{tor} \propto 1/R$ (the machine major radius). A secondary, poloidal, magnetic field (B_{pol}) is created by driving a large toroidal current through the plasma. The combination

of the toroidal and poloidal magnetic fields produces a twisted or "helical" field line, which connects back on itself to trace out surfaces. It is on these surfaces that both heat and particles are kept confined. Additional toroidal coils, shown as the structures in light blue, are often used to stretch and elongate the plasma surfaces to optimize performance. Such a setup often results in a plasma that is axisymmetric, or uniform along the toroidal direction. Coordinates traditionally used to describe a tokamak are plasma major radius (R), minor radius (r), poloidal angle (θ), and toroidal angle (ϕ). Under axisymmetric conditions, these coordinates are typically replaced by cylindrical coordinates (R, Z, ϕ), where Z=r sin(θ) is the distance above the tokamak midplane. The assumption of axisymmetry and equilibrium (force balance) imply that the plasma pressure (P= nT) must be constant along these magnetic surfaces. These flux surfaces, characterized by their normalized toroidal magnetic flux (ψ_N), with $\psi_N(R = R_0, Z = 0)$=0 at the magnetic axis and $\psi_N(R = R_0 + a, Z = 0)$=1 at the last closed flux surfaces (separatrix), are commonly used when showing experimental data. These experimental data, typically of the density and temperatures profiles, provide essential measurements of plasma transport and performance. More precisely, the shape of these profiles aid scientists in assessing the quality of the plasma relative to the amount of heating power applied. The goal of such analysis is to tailor the temperature and density profiles to exceed the Lawson criterion, a requirement which indicates more energy is being generated from fusion reactions than lost by the confinement system. The minimum Lawson criterion triple product (at 14 keV) is:

$$nT\tau_E \geq 3 \times 10^{21} keVs/m^3 \tag{1.2}$$

In the above expression, n is the plasma density, T is the temperature, and τ_E is the global energy confinement time. The energy confinement time is normally calculated as the ratio of the plasma stored energy (W) to the power losses (P_{loss}), such that $\tau_E = W/P_{loss}$. Losses of heat, particles, and momentum in tokamak plasmas is widely accepted to be the result of plasma turbulence. The properties of this turbulence can be measured experimentally using a suite of specialized plasma diagnostics, and has helped guide scientists to develop

accurate models which capture and quantify these phenomena. These codes, very recently, have become mature enough to quantitatively match experimental turbulence and profile observations. As part of this thesis, these codes were leveraged to develop a first principles understanding of turbulence induced transport in tokamak plasmas, specifically under the guise of isotope effects. These efforts have enabled quantitative verification of turbulence predictions from state of the art simulations based on experimental measurements, and significantly adds to research unraveling the decades long mystery of the L-H transition isotope effect.

1.1 Summary of dissertation

This thesis document investigates the L-H transition isotope effect using data and experiments conducted at the DIII-D tokamak. The data analyzed includes plasmas with both hydrogen and deuterium main ions, and leverages the excellent suite of diagnostic information available at the facility. These include, but are not limited to, profile diagnostics to determine quantities such as the electron density, ion temperature, and radial electric field, as well as turbulence diagnostics which allow for measurements of density, temperature, and radial velocity fluctuations. These comprehensive sets of experimental data, in coordination with state of the art turbulence modeling, have enabled the identification of several heat transport isotope effects between hydrogen and deuterium plasmas. Among these is turbulence stabilization by higher carbon dilution (higher Z_{eff}) due to increased physical sputtering of wall/tile material in deuterium plasmas, compared to hydrogen. Comparisons of experimental turbulence observations to these state of the art simulations has enabled a possible first of a kind validation of edge simulations using synthetic diagnostics. These synthetic diagnostics, in addition to confirming turbulence simulation predictions, demonstrate a clear radial electric field isotope effect between hydrogen and deuterium plasmas where $E_r(H) \approx 2E_r(D)$. Detailed analyses of these E_r differences between isotopes indicates two possible explanations for $E_r(H) \approx 2E_r(D)$: hotter outer strike points on open field lines and higher poloidal rotation in the closed field line region in hydrogen plasmas, compared

to deuterium. These observed heat transport and radial electric field differences between hydrogen and deuterium were tested by using DIII-D experimental run-time. Specialized hydrogen experiments with active carbon seeding using the impurity powder dropper system were undertaken to test whether heat transport and radial electric field isotope effects in hydrogen could be mitigated by turbulence stabilization. Experiment results, consistent with prior heat transport analysis, found increasing carbon content as stabilizing to plasma turbulence. These turbulence changes however, were found to have nearly no effect on the hydrogen L-H power threshold or edge radial electric field formation. These findings hint that systematic differences in the edge radial electric field between isotopes, and not heat transport effects per se, account for the nearly ubiquitously observed L-H transition isotope effect.

1.2 Outline

This dissertation is divided into 8 chapters and 4 appendices.

Chapter 1: Presented a summary and outline of this dissertation.

Chapter 2: Theory relating to the L-H transition and isotope effects.

Chapter 3: This chapter contains a brief introduction to the DIII-D tokamak, as well as the diagnostic systems necessary to understand the results presented in subsequent chapters.

Chapter 4: The observations used to infer the existence and origin of the heat transport isotope effects between hydrogen and deuterium plasmas in L-mode. Principle result is the naturally lower carbon content in hydrogen plasmas compared to deuterium resulted in more unstable Ion Temperature Gradient turbulence, and greater heat transport.

Chapter 5: Comparison of density and temperature fluctuations to results from heat transport isotope simulations discussed in chapter 4. Principle finding is that flux-matched CGYRO simulations are in strong coincidence with experimental turbulence measurements.

Chapter 6: Experimental observations of an edge radial electric field isotope effect between hydrogen and deuterium, and analysis on its potential physics origins. Principle conclusion

is $E_r(H) \approx 2E_r(D)$ in the plasma edge due to higher poloidal rotation and Reynolds stress spatial gradients in hydrogen plasmas.

Chapter 7: Experimental results from a special hydrogen L-H transition experiment involving seeding of more carbon than naturally sputtered. Key conclusion is that no change in the hydrogen L-H power threshold is observed with carbon seeding, concomitant with an unchanging edge E_r and Reynolds stress despite noticeable turbulence stabilization.

Chapter 8: The main experimental findings from the thesis, as well as a brief discussion of possible future directions.

Appendix A: Summary of a DIII-D L-H transition database formed from historical data. Includes all the TRANSP runIDs which comprise the hydrogen and deuterium transitions studied in detail.

Appendix B: Description of the constraints and considerations used to design the DIII-D PhD experiments.

Appendix C: Details regarding the gyrofluid and gyrokinetic simulations from the code TGLF and CGYRO.

Appendix D: Detailed descriptions of the analyses used to extract the radial electric field profiles for hydrogen and deuterium plasmas.

CHAPTER 2

Theory of the L-H transition and isotope effects

In this thesis chapter, the theoretical background necessary to understand the material presented in subsequent chapters is outlined for the reader's reference and review. These include discussions of pertinent tokamak nomenclature, electrostatic turbulent transport, the isotope effect, L-H transition theory, quasilinear transport modeling, and nonlinear gyrokinetic modeling respectively. The material presented is not meant to be comprehensive and exhaustive in nature, but provide the reader the theoretical foundation necessary for contextualizing and understanding the subsequent tokamak analyses that form the key discoveries documented in this doctoral thesis.

2.1 Tokamak nomenclature

As referenced previously in thesis Chapter 1, tokamaks are operated with helical magnetic field lines to enhance plasma confinement. The toroidal component of this field is generated from external poloidal coil currents, while the poloidal magnetic field is induced by driving a toroidal current through the plasma. The ratio of the strength of the toroidal magnetic field to the poloidal field is a very important quantity of merit in tokamak plasmas. More precisely, the degree of twisted-ness of the field lines on each flux surface is often described using a quantity called the magnetic safety factor (q). This quantity represents how many toroidal (ϕ) rotations the plasma undergoes in a single poloidal rotation ($\Delta\theta = 2\pi$). Under axisymmetric assumptions, q=$\frac{rB_{tor}}{RB_{pol}}$. Flux surfaces with rational numbered magnetic safety factors (q= 1, 2, 3, 3/2...) are important because they are often locations of wave-particle resonance. As the name implies, the magnetic safety factor also represents an important sta-

bility metric, where if $q \leq 1$ the plasma is kink unstable (the Kruskal–Shafranov limit). This instability boundary inherently limits the amount of plasma current and poloidal magnetic field that can safely be used in tokamak operation. In addition to this current based limit, limits to the achievable normalized plasma pressure $\beta = nT/(B_{tor}^2/2\mu_0)$ were uncovered early in tokamak research. Specifically, the Troyon limit with $\beta_{max} = \beta_N I_p/(aB_{tor})$ placed a hard ceiling on the achievable plasma performance [104]. In the previous expression, if I_p is the plasma current in MA, a is the minor radius in meters, B_{tor} is the external magnetic field in Tesla, and β_{max} is in %, the coefficient $\beta_N \approx 2.8$. The size of this numerical coefficient which controls this pressure limit, was discovered to increase with increasing non-circular cross-section plasma shaping [100]. It is with these macroscopic stability limits in mind that the DIII-D tokamak normally operates with edge magnetic safety factor $q_{95} > 3$ and with a "D" shaped plasma cross-section for enhanced performance.

It is these specially shaped magnetic surfaces that are commonly used to reconstructed experimental tokamak data into sensible information. These equilibrium reconstructions to zeroth order leverage the assumptions of equilibrium (force balance), where the plasma pressure is balanced against the magnetic pressure. Additionally because the cross-product of two vectors must be perpendicular to both original vectors, one finds that:

$$\begin{aligned} \vec{J} \times \vec{B} &= \nabla P \\ \vec{B} \cdot (\vec{J} \times \vec{B}) = 0 &= \vec{B} \cdot \nabla P \\ \vec{J} \cdot (\vec{J} \times \vec{B}) = 0 &= \vec{J} \cdot \nabla P \end{aligned} \tag{2.1}$$

As a result of this force balance, the plasma pressure along the magnetic surface (parallel to $\vec{B}$) must be a constant. This identification of pressure as a "flux function" is often used to vastly simplify tokamak diagnostic data, and will be referenced heavily in later chapters. It is noteworthy that this "flux function" relationship is not ubiquitous, but often assumed to be (reasonably) true to make the most of available diagnostic data.

Data interpretation often involves solving the Grad-Shafranov equation to determine the

plasma equilibrium:

$$\frac{\partial^2\psi}{\partial r^2} - \frac{1}{r}\frac{\partial\psi}{\partial r} + \frac{\partial^2\psi}{\partial z^2} = \mu_0 r^2 \frac{\partial P}{\partial\psi} - \frac{1}{2}\frac{\partial F^2}{\partial\psi} \tag{2.2}$$

Above F(ψ)=rB_{pol}, and P(ψ) is the plasma kinetic pressure. It is noteworthy that z in this instance is not the distance above the midplane, but instead a distance parallel to the toroidal angle ϕ. An equilibrium is largely determined by F(ψ) and P(ψ). An example Grad Shafranov equilibrium solution using the EFIT code is attached below for the readers reference in Fig. 2.1 [57]. The solutions shown are derived solely from magnetic data acquired along the machine wall [101], shown on the left panel as the black contour region. The pressure profile illustrated above, in more sophisticated modeling frameworks such as kinetic EFITS [56], can be determined explicitly from pressure profile measurements. These computations however are labor intensive. Equilibrium reconstructions such as that shown in Fig. 2.1 which treat pressure as a free parameter are very often sufficiently accurate for determining plasma flux surfaces and geometry. Subsequent analyses, shown in thesis chapters 4-7, use both the time dependent resistive-current diffusion equation and experimentally constrained pressure profile to solve the Grad-Shafranov equation using the plasma transport code TRANSP [43, 39].

The motion of the plasma electrons and ions, to zeroth order, can often be treated as individual particles on these surfaces. Under such a lens, these electrically charged particles are expected to execute helical motion with respect to the magnetic field lines. Perpendicular to the magnetic field, the particles have "Larmor" orbits, with the (cyclotron) frequency (f_c) and gyro-radius (r_L) of:

$$\begin{aligned} f_c &= \frac{q_s B}{2\pi m_s} \\ r_L &= \frac{m_s v_{s,\perp}}{q_s B} \end{aligned} \tag{2.3}$$

Above q_s, m_s, and $v_{s,\perp}$ are the species dependent electric charge, mass, and velocity perpendicular to the background magnetic field. Along the magnetic field lines, the particles are

free streaming. At higher order, the particles can execute more complicated motion. For example, in tokamaks the scaling of toroidal field as $B_{tor} \propto 1/R$ can result in a magnetic mirroring effect. This effect is due to the conservation of a quantity called the magnetic moment (μ):

$$\mu_s = \frac{m_s v_{s,\perp}^2}{2B} \tag{2.4}$$

As the magnetic field is increased, to conserve the magnetic moment, the perpendicular kinetic energy of a particle must also increase. Due to energy conservation, this increased perpendicular particle kinetic energy comes at the expense of slowing down the particle's parallel motion. If the magnetic field grows sufficiently large, all available particle energy may be converted into perpendicular motion, forcing a reflection to the area of lower magnetic field strength. This mirroring behavior is only possible if the particle converts all its parallel energy to perpendicular motion before reaching a sufficient maximum magnetic field, thus setting up two distinct particle classes. In modern tokamaks, these "classes" of particles are given special names due to their fundamental importance. The particles which have insufficient parallel energy and are forced to bounce are "trapped" particles, while those who can avoid reflection are called "passing" particles. The orbits these particles execute can be dramatically different, as illustrated in Fig. 2.1. The orbits of 45 keV neutral beam injected fast ion passing particles are shown in red, while trapped particle counterparts are illustrated in blue. The trapped orbits, on account of their shape in the poloidal plane, are often referred to as banana orbits.

The magnetic bottle formed by the flux surfaces within a tokamak are imperfect however, with collisions between particles allowing for substantial energy, particle, and momentum losses. This loss process, to the zeroth order, is a diffusive process, where over some unit of time and unit of space, particles will diffuse out from the hotter core to the cooler edge across magnetic field lines . The assumed step sizes in space and time in modern tokamak theory are the ion sound gyro-radius ρ_s and the plasma minor radius (a) normalized by the ion sound speed $c_s = \sqrt{T_e/m_i}$:

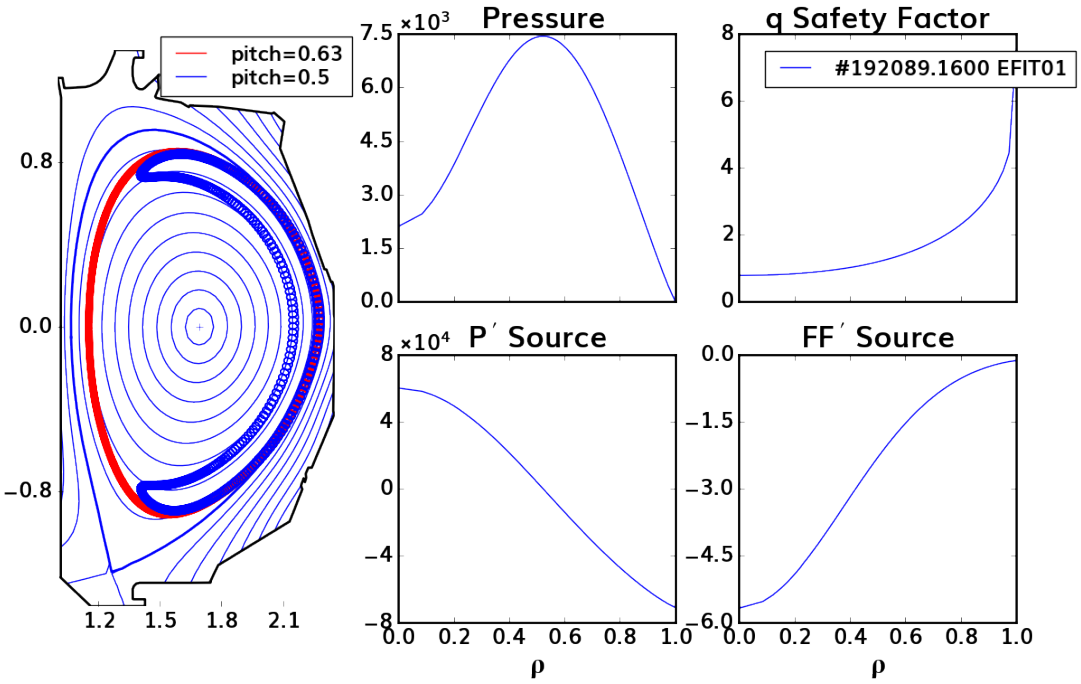

Figure 2.1: Equilibrium reconstruction of DIII-D discharge 192089 at 1600ms based solely on magnetic field data. The left-most panel indicates the resulting equilibrium reconstructed surfaces inferred by solving the Grad-Shafranov equation. The dark blue and red contours overlayed indicate the orbits of trapped and passing fast ion particles injected at full energy (45 keV). The right-hand panels show the associated pressure, magnetic safety factor, pressure gradient, and F=rB_{pol} gradient profiles versus $\rho = \sqrt{\Psi_N}$, the square root of the normalized toroidal flux. Fast ion orbit tracing generated with help from Dr. Kenny Gage.

$$\delta r = \rho_s = \frac{\sqrt{T_e m_i}}{ZeB} \tag{2.5}$$

$$\delta t = a/c_s = a\sqrt{m_i/T_e} \tag{2.6}$$

$$\chi = \frac{\delta r^2}{\delta t} = \frac{\rho_s^2}{a/c_s} = \frac{T_e m_i}{(ZeB)^2}\frac{\sqrt{T_e/m_i}}{a} \tag{2.7}$$

In the above expression T_e is the electron temperature, Ze is the ion electric charge, B is the background magnetic field, and m_i is the main ion mass. The heat diffusion coefficient χ, using the stated spatial and temporal step sizes, indicates gyro-Bohm like transport. This type of heat transport scaling is important because it suggests that a lower main ion mass plasma is expected to produce less heat transport. This theoretical expectation, as will be discussed in detail later, is opposite to experimental observations. A more precise figure of merit that will be used extensively in this thesis's gyrofluid and gyrokinetic analyses is the gyro-Bohm heat flux (Q_{GB}), which obeys the following expression:

$$Q_{GB} = n_e \frac{T_e}{a}\chi \tag{2.8}$$

2.2 Electrostatic Transport

Gyrofluid and gyrokinetic analyses, at their most basic level, attempt to model turbulent fluctuations and their associated heat, particle, and momentum transport which are driven by temperature and density gradients in the plasma. Under the circumstances of this thesis involving low collisionality and β L-mode plasmas, these turbulent fluctuations may be classified among 3 different types of drift-wave instabilities: Trapped Electron Modes (TEM), ion temperature gradient (ITG) modes, and electron temperature gradient (ETG) modes [48]. These instabilities transport particles, heat and momentum by producing coherent fluctuating fields. Under electrostatic assumptions, these fluctuating quantities include radial velocity fluctuations $\tilde{v}_r \approx \frac{\tilde{E}_{pol}}{B} = \frac{-\nabla_{pol}\tilde{\phi}}{B} = \frac{-k_\theta \tilde{\phi}}{B}$, electric potential fluctuations $\tilde{\phi}$, temperature

fluctuations $\tilde{T}$, and density fluctuations $\tilde{n}$. These quantities are directly related to turbulent particle (Γ_{turb}) and heat fluxes (Q_{turb}) given the following expressions:

$$\Gamma_{turb} = \langle \tilde{v}_r \tilde{n} \rangle_t \tag{2.9}$$

$$Q_{turb} = \frac{3}{2} \left(T_0 \langle \tilde{v}_r \tilde{n} \rangle_t + n_0 \langle \tilde{v}_r \tilde{T} \rangle_t \right) \tag{2.10}$$

Above the quantities n_0 and T_0 represent the non-fluctuating (equilibrium) density and temperatures respectively. The brackets shown as $\langle ... \rangle_t$ indicate ensemble averaging with respect to time. Noteworthy in the expressions above, both the fluctuation magnitudes and the cross phases of $\tilde{\phi} - \tilde{n}$ and $\tilde{\phi} - \tilde{T}$ are turbulence properties which may strongly influence the magnitude of turbulent transport. Experimentally, density and temperature fluctuations $\tilde{n}, \tilde{T}$ can be measured in tokamaks using specialized diagnostics, and will be discussed in detail in thesis chapter 3. Electric potential fluctuations $\tilde{\phi}$ however cannot be easily measured, preventing direct computation of turbulence induced heat and particle transport based purely on experiment. Due to these limitations, gyrofluid and gyrokinetic modeling seeks to accurately model and predict both turbulent fluctuations and their associated transport in tokamak plasmas. These model predictions, over the course of this thesis, will be compared to experimental turbulence measurements in an effort to validate these predictive tools. A brief summary of the assumptions and physics integrated into these models is as follows.

The gyrokinetic transport codes, such as the code CGYRO [20], calculate explicitly the turbulent fluctuations by solving the nonlinear gyrokinetic equations for some species (a) coupled to Maxwell's equations:

$$\frac{\partial \tilde{h}_a}{\partial \tau} - i(\Omega_\theta + \Omega_\xi + \Omega_d)\tilde{H}_a - i\tilde{\Psi}_a + \frac{2\pi a}{L}\frac{q\rho_s}{r}\tilde{h}_a * \tilde{\Psi}_a = \frac{a}{c_s}\sum_b C^L_{ab}\left(\tilde{H}_a\tilde{H}_b\right) \tag{2.11}$$

$$\tilde{H}_a = \tilde{h}_a + \frac{Z_a T_e}{T_a}\tilde{\Psi}_a \tag{2.12}$$

$$\tilde{\Psi}_a \approx J_0(\gamma_a)\left(\tilde{\phi} - \frac{v_\parallel}{c_s}\tilde{A}_\parallel\right) \tag{2.13}$$

$$(k_x^2 + k_y^2)\lambda_D^2\tilde{\phi} + \sum_a Z_a^2\frac{T_e}{T_a}\int d^3v\frac{f_{0,a}}{n_e}\tilde{\phi} = \sum_a Z_a\int d^3v\frac{f_0, a}{n_e}J_0(\gamma_a)\tilde{H}_a \tag{2.14}$$

$$\frac{2}{\beta_{e,unit}}(k_x^2 + k_y^2)\rho_s^2\tilde{A}_\parallel = \sum_a Z_a\int d^3v\frac{f_0, a}{n_e}\frac{v_\parallel}{c_s}J_0(\gamma_a)\tilde{H}_a \tag{2.15}$$

$$\tilde{f}_a = -\frac{Z_a e f_{0,a}}{T_a}\tilde{\phi} + e^{-ik\rho_a}\tilde{H}_a \tag{2.16}$$

In the expression above, $\tilde{H}_a$ is the non-adiabatic portion of the distribution function for plasma species a, $\tilde{\Psi}_a$ is the fluctuating field potential, $\tilde{\phi}$ are electrostatic fluctuations, and $\tilde{A}_\parallel$ are vector potential fluctuations parallel to the background magnetic field. Further variable and operator details may be found in reference [20] for additional documentation. In the limit of non-adiabatic electrons, $\tilde{H}_e = 0$. From this limit, equation 2.16 can be volume integrated, producing the following expression:

$$\int d^3v\tilde{f}_e = -\frac{Z_e e\int d^3 f_{0,e}}{T_e}\tilde{\phi} \tag{2.17}$$

$$\frac{\tilde{n}_e}{n_{0,e}} = \frac{e}{T_a}\tilde{\phi}$$

This relation between the perturbed density fluctuations and potential fluctuations is commonly known as the Boltzmann response, and mathematically results in temperature fluctuations where $\tilde{T}_e = 0$. Therefore, the non-adiabatic portion of the distribution function can be viewed as the part which permits finite temperature fluctuations. Gyrokinetic codes such as CGYRO, in words, are first principles codes which explicitly calculate the fluctuating distribution function (sometime referred to as delta-f codes) to infer heat, particle,

and momentum transport. These calculations, which must simultaneously solve both the gyrokinetic equation for multiple plasma species in addition to Maxwell's equations, are very computationally intensive. As such, they are traditionally solved using supercomputer cluster resources such as that found at the National Energy Research Scientific Computing Center (NERSC). Even then, these simulations may take hours to run, rendering these first principle's predictions intractable for routine use. It is with this computational cost in mind that substantial effort has been placed into creating reduced models which can capture the most important features of gyrokinetics, but with substantially lower resource requirements.

The gyrofluid transport model, namely based on solving the Trapped Gyro Landau Fluid system of equations [94, 55], commonly referred to as TGLF, is one such reduced model which predicts the turbulence based on quasi-linear physics. The quasi-linear approximation is one which assumes that the phase shift between fluctuating fields which produce transport (such as $\tilde{\phi} - \tilde{n}$ and $\tilde{\phi} - \tilde{T}$) are preserved going from the linear to nonlinear gyrokinetic solutions [112]. Based on this approximation, two quantities are necessary for approximating the full nonlinear gyrokinetic simulations: a linear calculation of the most unstable mode's electrostatic fluctuations and phase angles between electrostatic fluctuations and velocity moments of the perturbed distribution function. The latter quantity is colloquially referred to as the quasi-linear weights, and are normally expressed as the following, assuming the most unstable mode exists with radial wave-number $k_x = 0$ (very typically the case) [95, 92, 91]:

$$WQ_a^{QL} = \frac{3}{2} \frac{\langle \mathrm{Re}\left[ik_y \tilde{\phi}^* \tilde{p}_a\right]\rangle_t}{n_e e \langle \tilde{\phi}^2 \rangle_t} \tag{2.18}$$

$$W\Gamma_a^{QL} = \frac{\langle \mathrm{Re}\left[ik_y \tilde{\phi}^* \tilde{n}_a\right]\rangle_t}{n_e e/T_e \langle \tilde{\phi}^2 \rangle_t} \tag{2.19}$$

These quasilinear weights allow for dramatically reduced computational complexity and cost. The former quantity required for computing the quasilinear fluxes is the intensity of the most unstable mode's electrostatic fluctuations. These saturated intensity calculations are

modeled using a choice of three generations of saturation rules: sat 0, sat 1, and sat 2. The first generation, saturation rule 0, is a 1D model which calculates the electrostatic fluctuation intensity for each poloidal eigenmode independently (no coupling) [95], and which were calibrated based on nonlinear gyrokinetic predictions. The second generation, referred to as saturation rule 1, took the model into 2D (poloidal and radial directions) by coupling poloidal eigenmodes by zonal flow mixing [92] and using a spectral shift model for turbulence suppression by sheared flow [96]. The third generation, referred to as saturation rule 2, further improved the model to be 3D (poloidal angle + radial and poloidal wavenumbers) to include important geometrical effects. A fourth generation, saturation rule 3 [28], was released towards the end of this dissertation, and is referenced for completion despite it not being used in analysis due to its public release date. The saturated electrostatic potential fluctuation intensity in TGLF sat 2 is modeled using equation 2.20:

$$I_{k_y}^{model} = \langle G^2(\theta)\rangle^2 \left(\frac{\gamma_{k_y}^{model}}{k_x^{model} k_y} \right) \tag{2.20}$$

$$\gamma_{k_y}^{model} = b_2 \begin{cases} \gamma_{k_y} & k_y < k_{y,max} \\ \gamma_{max} & k_y \geq k_{y,max} \end{cases} \tag{2.21}$$

$$k_x^{model} = \frac{B_{unit}}{B_{norm}} \begin{cases} k_{y,cut}/|\nabla r|_0 & k_y < k_{y,cut} \\ k_{y,cut}/|\nabla r|_0 + b_1(k_y - k_{y,cut})G_q(0) & k_y \geq k_{y,cut} \end{cases} \tag{2.22}$$

In the expressions above, the quantity $\langle G^2(\theta)\rangle$ is the geometric shape factor and the linear growth rates γ_{k_y} are determined by solving the TGLF equations. Equation 2.21 is meant to emulate the saturation of turbulence by zonal flow mixing. The poloidal wavenumber where γ/k_y is maximized is indicated as $k_{y,max}$. Likewise γ_{max} represents this poloidal wavenumber's growth rate, with these two quantities together providing an estimate of the saturated amplitude of the root-mean-square zonal velocity such that $V_{ZF} = \gamma_{max}/k_{y,max}$. The coefficient b_2 is a free parameter calibrated on CGYRO nonlinear simulation results via least squares minimization. Equation 2.22 is a reduced model used to estimate the RMS radial wavenumber (k_x) width of the turbulence spectrum. Similar to b_2, the quantity b_1 is

explicitly calculated as a free parameter, whose best fitting coefficient to nonlinear CGYRO simulations is used. Additional model details may be found in reference [91]. Relevant to the discussion above, these simplifying assumptions (phase-shift preservation, estimation of nonlinear physics by the above zonal flow mixing and radial wavenumber width models, and solving the TGLF system of equations) allow for a dramatic reduction of turbulence simulation computational cost. These simulations, which would take hours of computation time on one of the world's largest supercomputing clusters, may now be completed in seconds on a single laptop. It is for this reason that the TGLF reduced model, and others like it, are often used as initial tests against tokamak experiment data prior to performing full nonlinear gyrokinetic calculations. Over the course of this thesis, gyrofluid predictions from the TGLF code will be validated against both select nonlinear CGYRO runs and experiment to infer the physics origin of the decades long conundrum referred to as the isotope effect.

2.3 The isotope effect

The isotope effect in plasma physics, is generally used to refer to a conflict between our most basic theory and experimental measurements. Experimentally heat and particle transport in magnetically confined plasmas has been found to depend on hydrogenic isotope mass, with a vast majority of experiments (fusion devices with both carbon and metallic wall materials) demonstrating larger transport in hydrogen, compared to deuterium and tritium plasmas [63, 84, 85, 62, 35, 105, 103]. From these many magnetic confinement experiments, which span several decades of research, a multi-machine scaling law for energy confinement time τ_E in both low and high confinement mode was developed with the goal of extrapolating observed heat transport trends to next step devices. Recall that the global energy confinement time τ_E contributes to the Lawson criteria calculations (equation 1.2), which controls how scientist's quantify closeness to "thermonuclear fusion conditions". Using data from both diverted and limited L-mode discharges, an engineering scaling for this regime's energy confinement time was calculated using standard power law regression analysis. The dataset used includes 1312 discharges from 12 different machines (Alcator C-mod, ASDEX, DIII-D, JET, JFT-

2M, JT-60, PBX-M, PDX, T-10, TEXTOR, TFTR, and Tore-Supra), with a large variety in both machine size and configuration. The scaling law inferred for L-mode thermal energy confinement time is:

$$\tau_{E,th}^{L} = 0.023 I^{0.96} B^{0.03} P^{-0.73} n^{0.4} M^{0.2} R^{1.83} \epsilon^{-0.06} \kappa^{0.64} \tag{2.23}$$

Above $\tau_{E,th}^{L}$ is the predicted L-mode thermal energy confinement time in seconds, I is the plasma current in MA, B is the toroidal magnetic field in Tesla, P is the loss power in MW, n is the line averaged density in $10^{19} m^{-3}$, M is atomic mass in AMU, R is the major radius in meters, ϵ is the inverse aspect ratio, and κ is the plasma elongation. The strongest dependencies within the scaling law are major radius R and plasma current I respectively. Of key note here, the energy confinement time increases with main ion mass M to the positive 0.2 power. This dependency is contradictory to "naive" gyro-Bohm transport theory, which predicts more heat transport (higher radial heat flux, Q) with increasing main ion mass:

$$Q_i = c_0 Q_{GBD} \sqrt{m_i / m_D} \tag{2.24}$$

$$Q_{GBD} = n_e T_e c_{s,D} \rho_{*,D}^2 \tag{2.25}$$

Above, c_0 is a mass-independent constant, m_i and m_D are the main ion and deuterium ion mass, Q_{GBD} is the normalized deuterium ion gyro-Bohm heat flux, n_e and T_e are the electron density and temperature, $c_{s,D} = \sqrt{T_e / m_D}$ is the deuterium ion sound speed, and $\rho_{*,D} = \sqrt{T_e m_D}/(a\, e\, B)$ is the normalized deuterium ion-sound gyro-radius (a, B, and e are the plasma minor radius, magnetic field, and elementary charge, respectively). The gyro-Bohm scaling above predicts ion thermal flux $Q_i \propto \sqrt{m_i}$. The thermal energy confinement time, defined as $\tau_E = W_{stored}/(P)$ where the loss power $P \propto Q_i$, implies $\tau_E \propto m_i^{-0.5}$ from gyro-Bohm theory. This heat flux scaling is opposite to experimental observations with $\tau_{E,th}^{L} \propto m_i^{0.2}$. It is this energy confinement *isotope effect*, a conflict between basic theory and

experimental observations, which has remained a mystery for several decades.

Gradient driven turbulent transport physics, which can break this gyro-Bohm scaling, is a leading framework for explaining this *isotope effect*. Within this sub-field, several mechanisms have been proposed in an attempt to explain these theory and observation differences. This effect is particularly important for efficiently achieving high-confinement (H-mode) plasmas, where fusion reactor relevant conditions are most easily met. This H-mode state, which can only be accessed by exceeding a minimum threshold input power P_{LH}, exhibits roughly double the energy confinement time compared to low confinement (L-mode) plasmas [106]. Modern tokamak experiments routinely observe a L-H threshold isotope effect, with reduced P_{LH} in plasmas with higher main ion mass [35, 79, 62, 45, 87, 81, 6, 105]. This mass dependent threshold power is important for projecting auxiliary heating power requirements on existing tokamaks, mostly in deuterium, to future reactors, which will operate with a 50:50 deuterium-tritium mixture. For example, the International Thermonuclear Experimental Reactor (ITER) [8] is designed to achieve a fusion gain of 10 using the H-mode operating scenario in a mixed deuterium-tritium plasma. ITER is especially vulnerable to the isotope effect during initial non-nuclear operation due to the use of hydrogen main ions, and may have insufficient heating (20-30 MW) for reliable H-mode access. The goal of this thesis is to study the potential physics origins of this isotope effect at the DIII-D tokamak, specifically with respect to the L-H transition.

2.4 The L-H transition

As mentioned previously, H-mode is a state which exhibits a nearly doubled energy and particle confinement time compared to L-mode plasmas. This novel plasma state was originally discovered by Wagner et al. at the ASDEX tokamak in 1982 [108], and was quickly reproduced at nearly all other existing tokamak devices. Access to this improved plasma state was found to be set by an input power threshold. That is, a critical amount of power must be added to the plasma in order to instigate the transition. Over the decades, this threshold power was found to have a very large number of dependencies. These include but are not

limited to plasma line averaged density ($\bar{n}$) [89], toroidal field strength (B_{tor}), machine size a [63], ion ∇B drift direction relative to the plasma X-point [107], divertor leg length [33], injected neutral beam torque [34], and main ion mass [35]. Substantial experimental and theoretical efforts have been undertaken to inform the physics which instigates this plasma state change. This bifurcation is commonly referred to as the L-H transition.

The first clues regarding the L-H transition phenomenology were initially uncovered as a result of an internal kink instability, commonly referred to as a sawtooth. This instability is the result of a portion of the plasma having magnetic safety factor $q \leq 1$, below the Kruskal–Shafranov limit. When kink unstable, the plasma profiles (mainly temperature and current density) flatten inside the $q \leq 1$ magnetic surface. This core energy is expelled as a heat pulse going from the core to the edge. On occasion it is found that the heat pulse resulting from a sawtooth instability, once in the edge, can provide the drive necessary for instigating the L-H transition [109]. Such findings suggested that the transition is spatially localized in nature, just inside the last closed flux surface in the closed field line region of the plasma. In this same region is where in H-mode an edge transport barrier is formed. Compared to L-mode, the kinetic profiles for both density and temperature are dramatically steepened. This steepening was believed to be the result of turbulence suppression, commonly seen as a sharp reduction in edge Balmer-α recycling light.

Based on these observations, many theories have been proposed to explain this transition phenomena. Following decades of experimental study and debate, both theory and experiment identified the edge radial electric field E_r as the parameter fundamental to triggering the L-H transition [51, 40, 17]. In particular, the radial electric field almost always exhibits a well structure in the edge near the L-H transition. This E_r well generates a strongly radially sheared $\vec{E} \times \vec{B}$ flow in the plasma edge which suppresses turbulence. The precise mechanism which causes this decorrelation of turbulence was uncovered by Biglari, Diamond and Terry [7], and confirmed experimentally shortly thereafter in the TEXT tokamak [76]. This theory posited that once the local $\vec{E} \times \vec{B}$ shear rate $\gamma_E = \frac{\partial V_{\vec{E}\times\vec{B}}}{\partial r}$ exceeds the turbulence decorrelation rate ω_D, the turbulent fluctuations are quenched. Therefore microscopically, the L-H

transition criteria is:

$$\gamma_E/\omega_D > 1 \tag{2.26}$$

To form a predictive theory for the L-H transition, details on how E_r shear is generated in the closed field line region is required. In the simplest form, the equilibrium radial electric field must satisfy the radial force balance equation:

$$E_r = \frac{1}{Z_i n_i e}\nabla P_i + v_{tor,i}B_{pol} - v_{pol,i}B_{tor} \tag{2.27}$$

In the above expression, the quantities ∇P_i, $v_{tor,i}$, and $v_{pol,i}$ are the ion pressure gradient, toroidal rotation velocity, and poloidal rotation velocity parallel to magnetic field lines respectively. The pressure gradient term ∇P_i is linked to edge power balance through turbulent transport physics. More precisely, the L-mode heat transport prior to transition sets the pressure gradient which contributes to E_r. Detailed investigation has suggested that while this contribution to the radial electric field is important in the H-mode state, it is very likely not the trigger phenomena [15]. Instead, it appears that the poloidal rotation velocity contribution to E_r is the L-H transition triggering term. This poloidal rotation term must obey a poloidal momentum balance equation of the form:

$$(1+2q^2)\frac{\partial v_{pol}}{\partial t} = -\mu\frac{q^2}{\epsilon^2}(v_{pol} - v_{pol}^{neo}) - \frac{\partial}{\partial r}\langle\tilde{v}_{pol}\tilde{v}_r\rangle \tag{2.28}$$

Further details on this poloidal momentum balance equation will be provided in thesis chapter 6. Modern L-H transition studies, particularly at the DIII-D tokamak, have found that zonal flows, or mean flows with $k_y = 0$ at some finite frequency originating from the spatial gradient of the turbulent Reynolds stress term $\frac{\partial}{\partial r}\langle\tilde{v}_{pol}\tilde{v}_r\rangle$, as the most important trigger phenomena [82, 118]. Simplified models with these physics considerations have been developed in attempt to translate the microscopic transition physics into a power threshold

prediction [116, 93]. These models however require experimental calibration and various assumptions, falling short of predictive capability. In light of such prediction limitations, a multi-machine scaling law for the L-H power threshold capturing the known L-H dependencies on line-averaged density, toroidal field, and plasma surface area is most commonly used for predictions on future devices such as ITER [63]:

$$P_{Martin} = 2.15\ n_{e,20}^{0.782}\ B_{tor}[T]^{0.772}\ a[m]^{0.975}\ R[m]^{0.999} \tag{2.29}$$

In the expression above $n_{e,20}$ is the line-averaged electron density in units of $10^{20}m^{-3}$, B_{tor} is the toroidal magnetic field in Tesla, a in the plasma minor radius in meters, and R is the plasma major radius in meters. This scaling law however, by neglecting many of the known physics dependencies of P_{LH}, provides very limited extrapolation capability for reliable L-H threshold predictions on machines such as ITER. As a result of these shortcoming in the L-H transition understanding, this thesis seeks to leverage the excellent diagnostic capabilities at the DIII-D tokamak to identify what isotope physics, both related to turbulent transport and E_r generation, may be influencing the L-H transition isotope effect.

2.5 Summary

This thesis chapter has reviewed the basic theoretical background necessary for understanding material discussed in subsequent sections. These discussions, related to important tokamak nonmenclature, electrostatic heat transport, the isotope effect, and L-H transition theory, outline key physics aspects related to understanding results shown in chapters 4-7. With these introductions, it is hoped that the reader may be able to review the discoveries made over the course of this PhD, and understand how they contribute to the decades long effort at unraveling the L-H transition isotope effect phenomena.

CHAPTER 3

The DIII-D tokamak

3.1 Overview of DIII-D

The DIII-D tokamak is a conventional medium sized (major radius R=1.67 m, minor radius a=60 cm), graphite armored tokamak located in La Jolla, CA, USA [61]. The device, which has been in operation since Fall 1986, has both flexible plasma shaping capabilities and an extraordinarily comprehensive suite of plasma diagnostics. The following sections will describe the heating and diagnostic systems at the DIII-D device which are relevant to work involving this thesis. The auxilary heating systems available at the DIII-D tokamak, in particular neutral beam injection, will be reviewed briefly.

The Neutral Beam Injection (NBI) system at the DIII-D tokamak is compromised of 4 beam boxes, each containing 2 individual ion sources (LT and RT). Three of the neutral beam boxes inject particles in the co-current direction (30°, 330°, 150°), while one can inject in either the co or counter-current direction (210°) depending on the configuration. For the experiments analyzed in this thesis, the 210° neutral beams were kept in the counter-current direction to enable torque cancellation. Each ion source can be accelerated through a range of voltage drops (40-80 kV) and use a variety of perveances ($\Pi_{ext} = I_{ext}/V_{acc}^{3/2}$; within 10% of optimal), enabling fine control over both the injected beam torque and power deposited into the plasma. The ion sources after acceleration are collimated, neutralized, and injected into the main plasma chamber. A diagram of the neutral beam injection system in the top down viewing configuration may be found in the upper panel of Fig. 3.1, while a cartoon of the neutral beam injection components is shown on the lower panel. The neutral beams, in addition to being geometrically configurable, are designed to be duty cycled at up to a

rate of 200 Hz (5 ms). Duty cycled operation is regularly used as it enables much finer scale control of the injected power, so long as the duty cycle changes occur on a time-scale faster than the global energy confinement time τ_E (100-200 ms). Coupled to each of the neutral beams are a multitude of plasma diagnostics which rely on the injected neutral particles and their plasma perturbations for measurements. In particular, the 30° and 330° neutral beam sources are necessary for performing main ion or impurity charge exchange spectroscopy, while the 150° sources are needed for the Beam Emission Spectroscopy diagnostic.

The ion sources, which are fed either a source of deuterium or hydrogen gas, do not exclusively produce D/H^+ ions. Both diatomic and triatomic molecular ions (H_2^+ or H_3^+), and even ionic water H_2O^+, are produced by the ion sources in non-negligible amounts. As a result of their differing masses, these ions are accelerated to different velocities by the neutral beam's voltage drop. At neutralization, these molecular ions are typically dissociated, breaking up into their constituent elemental components. The neutral beam particles injected in the plasma, which are the products of these dissociated ions, have several different hydrogen/deuterium injection energy components: full, half, third, and water from H^+, H_2^+, H_3^+, and H_2O^+ ion accelerations respectively. These differing components are mentioned as they are important contributors to the Charge Exchange Recombination diagnostic signals.

3.2 The Charge Exchange Recombination (CER) diagnostic

The Charge Exchange Recombination Spectroscopy (CER) diagnostic is a system which measures both main ion and impurity densities, temperatures, toroidal rotation, and poloidal rotation. These quantities are extracted from the total intensity, Doppler broadening, and Doppler shift of an observed spectroscopic line. For the impurity system, the spectroscopic line commonly viewed is C-VI emission at 529 nm. In the main ion system, hydrogen/deuterium Balmer-α emission at roughly 656.1 nm is observed. The desired spectroscopic signal is produced by neutral beam particles charge exchanging with plasma impurities or main ions. After the charge exchange reaction occurs, the plasma ion will have acquired an electron in an excited state. By spontaneous emission, this electron will decay into a lower

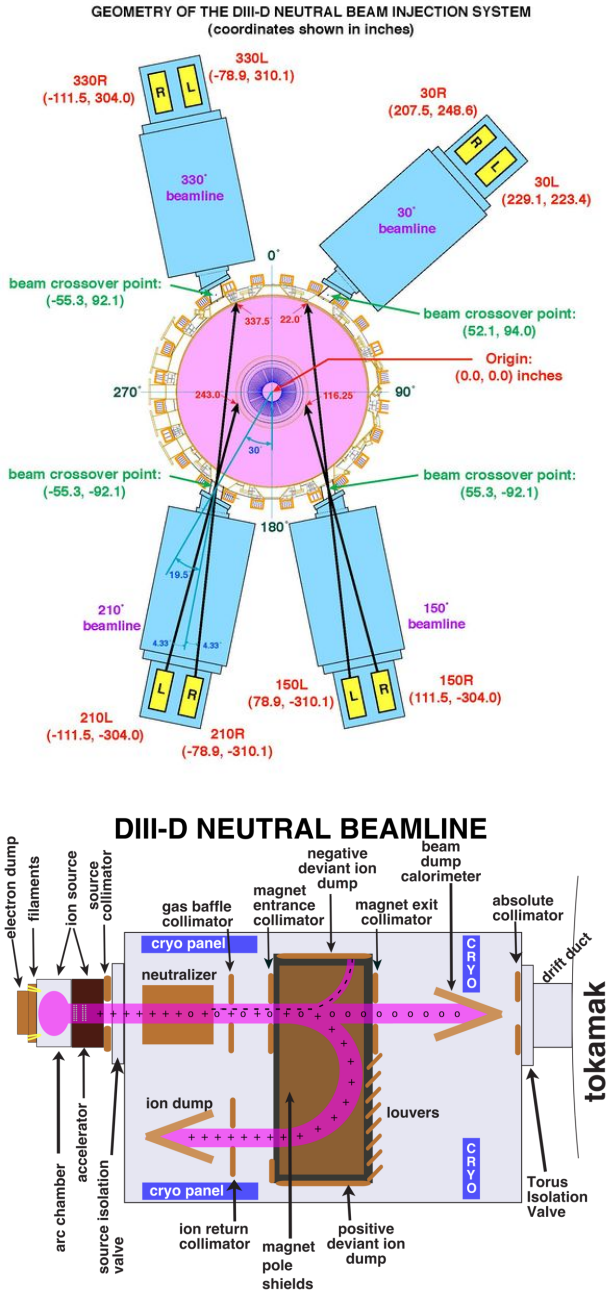

Figure 3.1: Upper panel: DIII-D Neutral Beam Injection system from the top-down tokamak view. Picture may be found at https://diii-d.gat.com/diii-d/Beams_generation. Lower panel: Cartoon of the internal components of the DIII-D neutral beam injection system. Figure may be found at https://diii-d.gat.com/diii-d/Beams_anatomy.

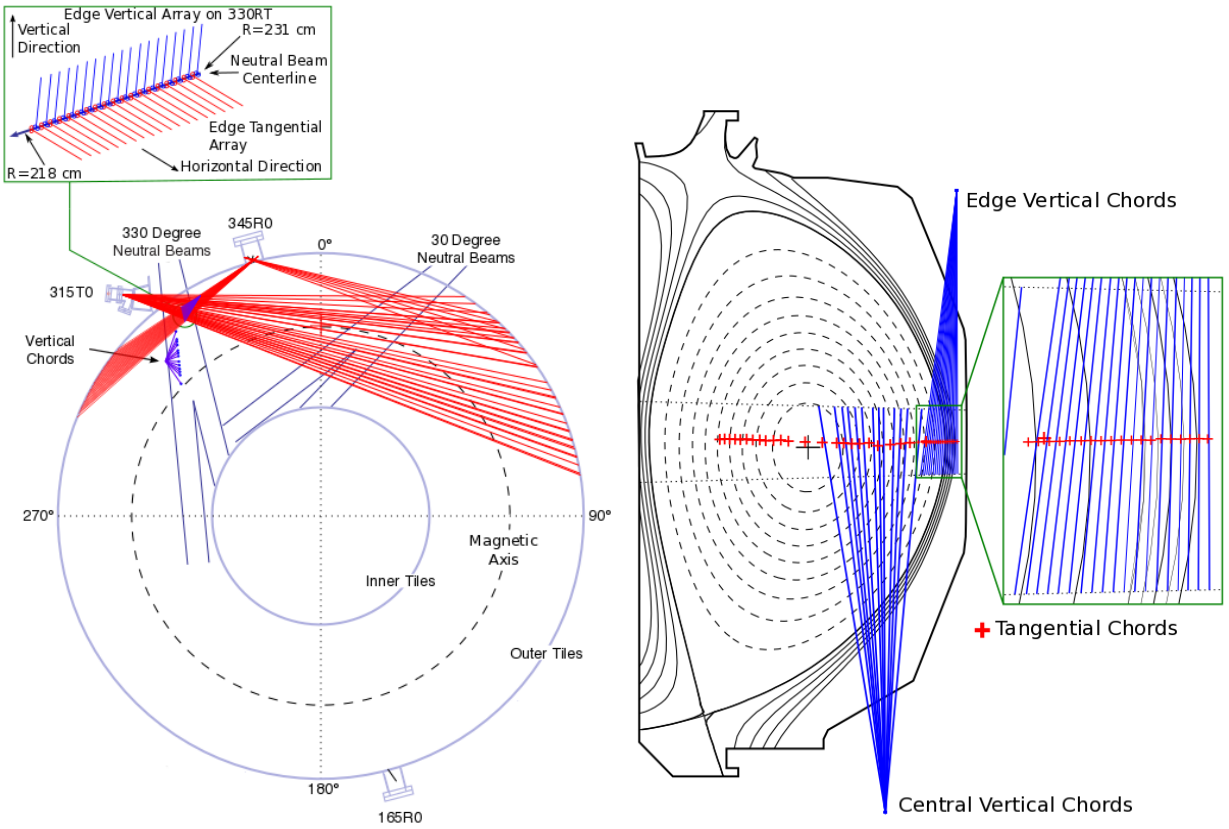

Figure 3.2: DIII-D Charge Exchange Spectroscopy diagnostic overview from the top-down (left) and poloidal cross-section (right) tokamak views. Solid red lines indicate tangential spectroscopic lines-of-sight, while dark blue indicate vertical viewchords. Light blue lines indicate the paths of the neutral beams through the plasma. At the intersection of the neutral beam and each spectroscopic viewchord is the measurement location.

energy level, emitting a photon in the process. This photon, due to the very short lifetime of the excited state, is localized to the spatial region near where the original charge exchange reaction occurred. In the tokamak, this translates to the CER measurements being localized to the intersection point between a viewchord and neutral beam. Fig. 3.2 illustrates the approximately 80 available viewchords as seen from the top-down and poloidal cross-section tokamak views at DIII-D on the left and right respectively. The red solid lines indicate tangential lines-of-sight, while dark blue illustrates vertical chords. The light blue lines illustrate the neutral beam trajectories in the plasma main chamber. The CER diagnostic, for publication level analysis, is analyzed normally using active spectroscopy. This measurement method leverages the neutral beam duty cycling for spectroscopic emissions while neutral

beams are on and off (passive). The latter measurement is due to charge exchange reactions and impact excitation emission from naturally occurring edge neutrals and plasma ions (passive emission), while the former measurement is a combination of the desired (active) emission from charge exchange reactions between neutral beam particles and plasma ions and passive components. Using (beam on)-(beam off) image subtraction allows for removal of passive emission contributions, enabling more accurate determination of temperatures, densities, and rotation velocities. Example measurements of carbon impurity (left) and main ion (right) spectra during beam on and beam off phases of a discharge are shown in upper panels of Fig. 3.3 in blue and black respectively. The lower panels illustrate the active signal component (beam on-beam off). The solid black vertical line on the leftward carbon spectral plots indicate the carbon rest wavelength. Likewise the solid red vertical line in the rightward main ion spectral plot shows the deuterium Balmer-α rest emission wavelength. The additional aqua vertical lines are from Doppler shifted neutral beam emission from the full, half, third, and water acceleration energies in solid, dashed, dashed-dotted, and dotted respectively. The remaining black vertical lines indicates carbon spectroscopic lines at their rest wavelengths. The Doppler shifted neutral beam emission further contains Zeeman splitting π and σ components from the strong background magnetic field. Learning how to run such impurity CER time slice subtraction analyses was undertaken as a educational aspect of this thesis, under the mentorship of Dr. Colin Chrystal and Dr. Shaun Haskey.

The impurity Charge Exchange Recombination Spectroscopy diagnostic, by measuring the carbon impurity density, temperature, and rotation velocities, enables direct inference of the radial electric field E_r using the ion radial force balance equation:

$$E_r = \frac{1}{Z_C n_C e}\nabla p_C + v_{tor,C} B_{pol} - v_{pol,C} B_{tor} \tag{3.1}$$

In the above equation, $\nabla P_C = \nabla(T_i n_c)$ is the impurity pressure gradient, $v_{tor,C} = R\Omega_C$ is the toroidal rotation velocity, $v_{pol,C}$ is the poloidal rotation velocity, B_{pol} is the poloidal magnetic field, and B_{tor} is the toroidal magnetic field. The radial electric field, in addition to the impCER diagnostic, can be independently determined by several of DIII-D's turbulence

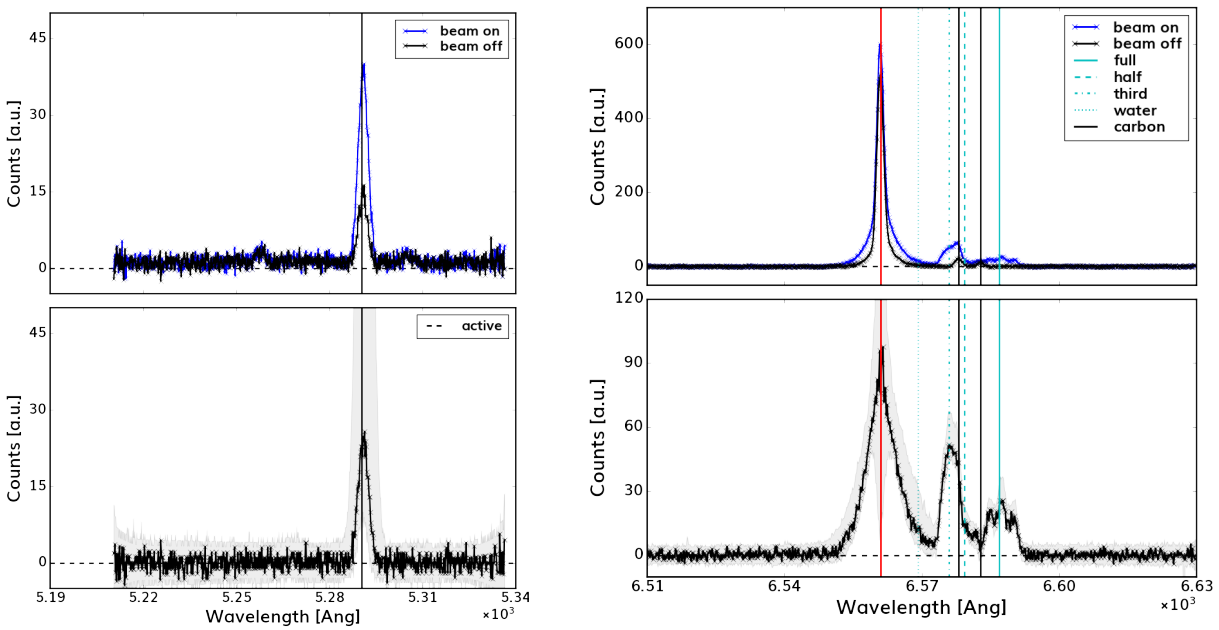

Figure 3.3: DIII-D Charge Exchange Spectroscopy example data for deuterium DIII-D shot # 192089. Left panels indicate measurements from the impurity CER sub-system, focused on carbon emission at 529 nm. The upper panel shows data acquired while a beam intersecting the spectroscopic line of sight in question is on (blue) and off (black). Immediately below is the (beam on-beam off) image produced by subtracting the two spectra to extract the active charge exchange emission component. Vertical black lines indicate the rest wavelength of carbon emission without Doppler shift. Right panels show equivalent spectra captured by the main ion CER sub-system. The vertical red and blue lines indicate rest and beam Doppler shifted deuterium Balmer-α emission (full, half, third, and water are shown as solid, dashed, dot-dashed, and dotted blue vertical lines respectively). Black vertical lines show carbon impurity emission line locations.

diagnostics. These diagnostics will be discussed briefly due to their relevancy to future chapters.

3.3 Turbulence Diagnostics

The DIII-D tokamak has a suite of excellent turbulence diagnostics. A select few of these systems have been used in Chapter 6 to determine the radial electric field E_r, such as the Doppler BackScattering (DBS) or Beam Emission Spectroscopy (BES) diagnostics, to identify a novel E_r isotope effect. In addition, quantitative comparison between two turbulence diagnostics (BES and CECE) and synthetic turbulence signals are used to validate nonlinear gyrokinetic simulation predictions in Chapter 5. Because of their relevancy to understanding results discussed later, the DBS, BES, and CECE diagnostics will be reviewed briefly.

3.3.1 Doppler BackScattering (DBS)

The Doppler BackScattering diagnostic at DIII-D is a millimeter-wave system used to measure plasma flows and electron density fluctuations by turbulent scattering. These measurements are conducted by injecting either an O or X-mode polarized beam into the main plasma from the outboard midplane at some oblique angle. In the DIII-D tokamak configuration, this roughly approximates to injected horizontally or vertically polarized beams respectively. Under O-mode polarization, the beam propagates in the plasma until its injection frequency approaches the electron plasma frequency $\omega_{p,e} = \sqrt{n_e e^2/m_e\epsilon_0}$. In the above expression, n_e is the local electron density, e is the elementary charge unit, m_e is the electron mass, and ϵ_0 is the vacuum permittivity. In X-mode, the probing beam can propogate slightly further, until it approaches the right-hand cutoff frequency $\omega_{RH} = \Omega_{c,e}/2 + \sqrt{\omega_{p,e}^2 + \Omega_{c,e}^2/4}$. $\Omega_{c,e}$ is the electron cyclotron frequency $\Omega_{c,e} = eB/m_e$. As the beam nears the cutoff frequency, it is refracted such that it is nearly tangent to the cutoff surface. This corresponds to either a flux surface in O-mode polarization, or a surface of constant right-hand cutoff magnitude in X-mode, which is dependent on the magnetic field strength (not constant on a flux surface).

As a result, the injected beam with wavenumber $\mathbf{k_{in}}$ and frequency ω_{in} may be scattered if the following Bragg matching conditions are satisfied:

$$\mathbf{k_{sc}} = \mathbf{k_{in}} + \mathbf{k_{\tilde{n}}} \tag{3.2}$$

$$\omega_{sc} = \omega_{in} + \omega_{\tilde{n}} \tag{3.3}$$

In the above expression the wavenumber $\mathbf{k_{\tilde{n}}}$ and frequency $\omega_{\tilde{n}}$ result from the electron density fluctuations within the plasma. The back-scattering condition therefore requires $\mathbf{k_{\tilde{n}}} = -2\mathbf{k_{in}}$ for momentum conservation, with the Doppler shift of the scattered wave relative to the injected frequency given as $\omega_{\tilde{n}} = \omega_{Doppler} = \omega_{sc} - \omega_{in}$. The Doppler shift $\omega_{Doppler}$ is a measurable DBS quantity which can be extracted from the fast Fourier transform (FFT) of the back-scattered signal received by the DBS antenna. The FFT signal is normally fit using a Gaussian-like function, with the peak location used to infer $\omega_{Doppler}$. The quantity k_{in} can additionally be calculated using beam tracing numerical modeling, such as with the code GENRAY [88]. With these two quantities, it is possible to determine the radial electric field from the following equality:

$$v_{Doppler} = \frac{\omega_{Doppler}}{-2k_{in}} = v_{\vec{E}\times\vec{B}} + \tilde{v}_{ph} \tag{3.4}$$

In the above expression $v_{\vec{E}\times\vec{B}} = E_r/B$ and $\tilde{v}_{ph}$ is the turbulent phase velocity, usually a constant offset.

The DBS diagnostic at DIII-D is comprised of 2 main subsystems located toroidally at the 60° and 240° port locations respectively. Either system can be tuned to X-mode or O-mode polarization, and consists of eight channels each with beam injection frequencies ranging from 55-75 GHz. Both subsystems can be poloidally steered by approximately ±10° away from tangential injection, enabling tuning to low and high wavenumber modes based on the injection angle. Example ray trajectories based on shot # 183521 at 1800 ms are shown in Fig. 3.4 to illustrate k_{in} sensitivity with poloidal injection angle β. The left-most panel shows the ray trajectories as colored contours vs. the DIII-D poloidal cross-section.

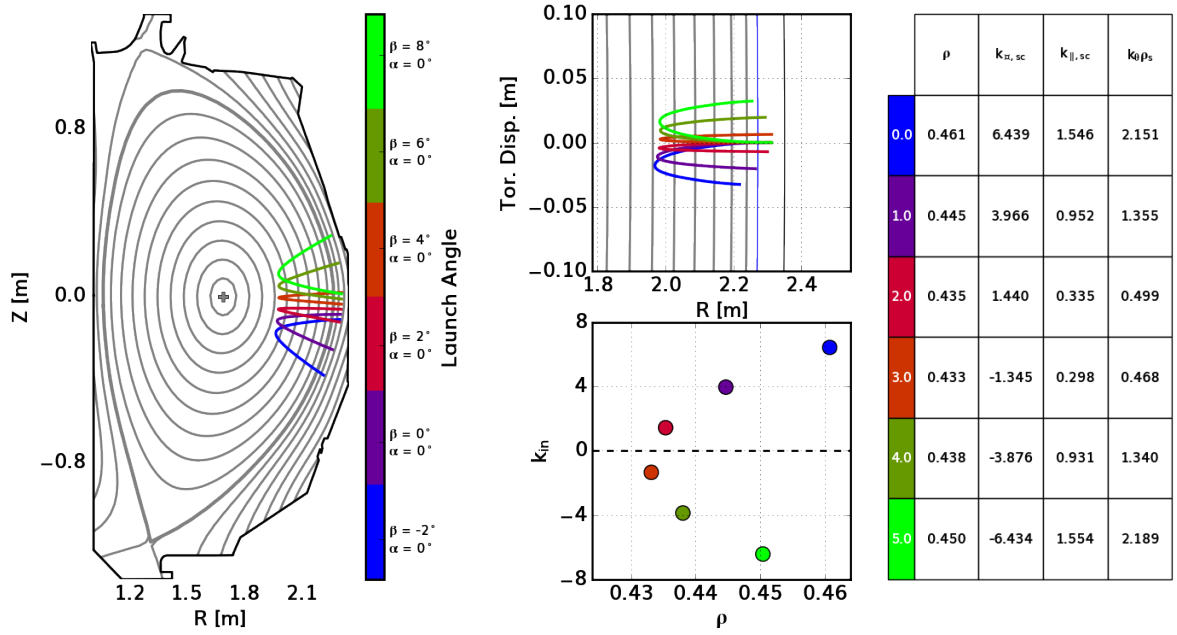

Figure 3.4: Overview of the DIII-D Doppler BackScattering diagnostic. The left-most panel shows DBS beam trajectories predicted from GENRAY simulations for differing poloidal injection angle β vs. the tokamak poloidal cross-section. The upper-middle column likewise displays the same color coded rays from the top-down tokamak view. The lower middle column shows the injected wavenumbers (k_{in}) for each ray. The right-most table dictates for each ray the cut-off location and scattering wavenumbers in the perpendicular, parallel, and poloidal directions.

The upper middle panel shows the ray trajectories from the top-down tokamak view. The lower middle panel shows the injected k_{in} for different poloidal launch angles. The right-most panel shows for each GENRAY simulation the cut-off location ($\rho = \sqrt{\psi_N}$), perpendicular wavenumber, parallel wavenumber, and normalized poloidal wavenumber respectively.

In this thesis, the DBS60 sub-system specifically was used to extract E_r profiles. In-depth details on these calculations are included in Appendix C. In addition to flow measurements, DBS can measure wavenumber resolved density fluctuation amplitudes. These measurements however, require absolute calibration of the back-scattered DBS power received by each channel. Such absolutely calibrated measurements were not pursued for the analyses described in this thesis, as they are the focus of concurrent UCLA graduate student Quinn

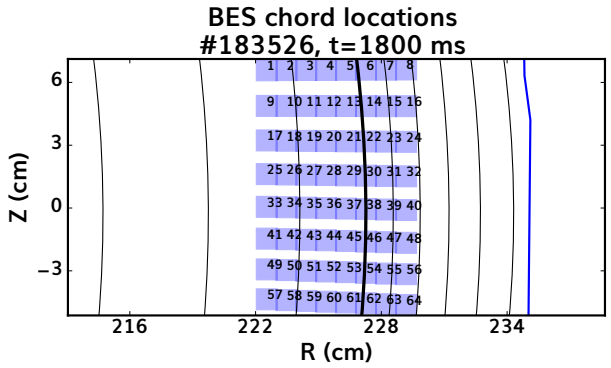

Figure 3.5: Beam Emission Spectroscopy channel layout for hydrogen shot #183526 in the R vs. Z plane. Blue squares indicate BES channels, and black contours show EFIT01 flux surfaces. The bold contour indicates the last closed flux surface.

Pratt's PhD thesis and require detailed interpretation. Density fluctuation measurements were instead extracted using the Beam Emission Spectroscopy diagnostic.

3.3.2 Beam Emission Spectroscopy (BES)

The Beam Emission Spectroscopy diagnostic is a visible spectroscopy system which measures collision induced, Doppler shifted Balmer-α (n= 3 $\rightarrow$ 2) emission from the 150° neutral beam particles at the DIII-D tokamak. The diagnostic, akin to the previously described miCER system, observes Doppler shifted full, half, third, and water emission. Slightly different from miCER, BES views blue-shifted instead of red-shifted spectra due to different viewing geometries. The BES system is comprised of 64 individual channels, using a custom-designed transmission filter with a band-pass of $\lambda = 652 - 655.5$ nm to observe only the blue Doppler shifted contributors of Balmer-α emission. An example experimental layout of the 64 available channels which enables 2D turbulence imaging capabilities is illustrated in Fig. 3.5. The channel separation is approximately 1 cm radially, and 1.5 cm vertically.

The light from each channel is transmitted using high-throughput fiber optics and optical components, converted to a current using a photodiode, and processed for digitization using specialized LabView instrumentation. More in-depth diagnostic details may be found in reference [65]. The system setup enables a data acquisition rate of 1 MHz. This sampling rate

is an order of magnitude slower than the Einstein spontaneous emission rate $A_{3\rightarrow 2} = 44$ MHz, and therefore slow enough to model the atomic emission process as an instantaneous response. The emission seen is from impact excitation of neutral beam particles by plasma electrons, main ions, and impurities into the n=3 atomic state. Consequently, the fluctuations to lowest order are linearly proportional to local plasma density fluctuations. Detailed calculations involving the dependence between beam emission and density fluctuations may be found in [31], and will be discussed in greater detail in thesis Chapter 5. The BES turbulence diagnostic system, unlike DBS, cannot resolve wavenumber specific turbulence behavior. Instead it observes a mixture of modes, and is most sensitive to turbulence with normalized perpendicular wavenumber $k_{\perp}\rho_s < 1$ (large scale structures).

The high sampling rate, and 2D turbulence imaging capabilities of BES enables a wide suite of potential analyses. Some of these analysis techniques include time-delay correlation and velocimetry analyses to extract turbulence correlation times and Reynolds stress [65, 66], which will be discussed in detail in Chapter 6. The analysis techniques which will be used for comparing BES measurements with predictions from nonlinear gyrokinetic simulations in Chapter 5 will be summarized briefly. Starting from the time series of BES data from channel A and B as x(t) and y(t) respectively, we take the fast Fourier transform of each signal. The Fourier transforms, X(f) and Y(f), are then used to calculate a cross power:

$$P_{xy}(f) = |\langle X(f)Y^*(f)\rangle| \tag{3.5}$$

$Y^*(f)$ is the complex conjugate of the initial Fourier transform of y(t). The operator $\langle ...\rangle$ indicates an ensemble average of the FFT products, and $|...|$ is the absolute value operation for the resulting complex numbers. This cross power represents the first comparison quantity which will be shown in Chapter 5. The second, related comparison quantity, is the cross-phase:

$$\Phi_{xy}(f) = Arg(\langle X(f)Y^*(f)\rangle) \tag{3.6}$$

The operation $Arg(...)$ in this context refers to finding the phase angle of the resulting complex numbers, in radians. The BES extracted cross phase is of particular importance because it may be used to additionally infer the radial electric field E_r. Specifically, taking the derivative of the cross-phase vs. frequency $\partial\Phi_{xy}/\partial f = 2\pi\tau_c$ between two vertically adjacent channels displaced by ΔZ, the vertical velocity may be estimated using the following expression:

$$v_z = \Delta Z/\tau_c = v_{\vec{E}\times\vec{B}} + \tilde{v}_{ph} \tag{3.7}$$

Above, the turbulent phase velocity $\tilde{v}_{ph}$ is not the same phase velocity which is measured by DBS. More precisely, this turbulence quantity is known to depend on the poloidal wavenumber k_θ, which is different between either diagnostic as a result of their disparate mode sensitivities. Historically, BES measurements have found that $\tilde{v}_{ph} \approx 0$, as seen in Fig. 7 of [65] when comparing impCER and BES E_r measurements. These same correlation analyses are applied to the Correlation Electron Cyclotron Emission diagnostic to extract temperature fluctuations.

3.3.3 Correlated Electron Cyclotron Emission (CECE)

The Correlation Electron Cyclotron Emission (CECE) diagnostic is a radiometry system which measurements both the mean and fluctuating electron temperatures in DIII-D plasmas [114]. The system observes harmonics of the electron cyclotron frequency ($\Omega_{c,e} = eB/m_e$) in either the O-mode (horizontal) or X-mode (vertical) polarization, which are emitted as black body radiation. The emission frequency is spatially localized due to the plasma's toroidal magnetic field decreasing as 1/R. Normalizing to the on-axis magnetic field B_0 and major radius R_0, the spatially dependent nth harmonic of the electron cyclotron frequency may be expressed as follows:

$$n\Omega_{c,e} = \frac{eB_0R_0}{Rm_e} \tag{3.8}$$

The blackbody intensity of such emission is given by the following expression, in the Rayleigh-Jeans low frequency limit:

$$I_{BB}(\Omega_{c,e}) = \frac{\Omega_{c,e}^2 T}{8\pi^3 c^2} \tag{3.9}$$

c above is the speed of light, 3×10^8 m/s, and T is the temperature of the radiating body. When the plasma's emission is optically thick, or sufficiently absorbed to be modeled as a blackbody radiator, the radiation temperature is equal to the local electron temperature $T = T_e$. Consequently, the radiometer's intensity measurements are directly proportional to the local electron temperature in the emitting layer. In the cooler plasma edge however, insufficient absorption of the emitted cyclotron radiation can make the emitting layer an imperfect blackbody. Consequently, more sophisticated modeling is necessary to interpret such CECE data. Under such circumstances, the emission intensity is optically gray, obeying the following relation [75]:

$$I(\Omega_{c,e}) = I_{BB}(\Omega_{c,e}) \frac{1 - e^{-\tau}}{1 - \chi e^{-\tau}} \tag{3.10}$$

Above the quantity χ represents the effective wall reflectivity and τ is the optical depth, which is the integral of the absorption coefficient α from the emission layer along the exit trajectory of the radiation [10]. Note how in the limit of $\tau \to \infty$, the emission intensity is exactly equal to the blackbody intensity formula. In the vicinity of $\tau \approx 1$ however, the emission intensity deviates from pure blackbody emission. It is under these two lenses that comparisons of experimental CECE measurements in Chapter 5 will be conducted.

The CECE diagnostic at the DIII-D tokamak consists of an 8 channel correlation system (2 channels per correlation pair) designed to measure emission between 72-108 GHz [102, 114] at slightly above the outboard midplane. In the cases acquired for this thesis, the CECE system was tuned to 2nd harmonic X-mode polarized electron cyclotron emission. A diagram of the 1st, 2nd, and 3rd harmonic electron cyclotron frequencies, alongside the CECE channel frequencies is shown in upper right panel of Fig. 3.6 in green and black respectively for shot

#183521. The location where the CECE channels overlap the 2nd harmonic emission contour indicates the spatial localization of the emission region. This spatial localization is further shown in the lower right panel, with each channel's flux mapped spatial position ρ plotted vs. time in ms. The left-most panel illustrates the magnetic equilibrium reconstruction used for each flux mapping calculation, with color-coding showing individual time slices. The solid black arrow shows the location of the CECE radiometry system's optical path.

Similar to the BES diagnostic, the very high data sampling rate of approximately 5 MHz of the CECE diagnostic enables detailed turbulence measurements. The diagnostic is likewise sensitive to long-wavelength fluctuations with $k_\theta < 2$ cm^{-1}, $k_r < 4$ cm^{-1}. The time series of the CECE data can be broken into 3 distinct parts:

$$V(t) = V_{\bar{T}} + V_{\tilde{T}}(t) + V_{\tilde{N}}(t) \tag{3.11}$$

The 1st contribution to equation 3.11 is the mean component, proportional to the mean electron temperature in the blackbody limit. The 2nd is proportional to the temperature fluctuations due to microturbulent instabilities. The 3rd term is from thermal EC blackbody fluctuations, which are independent of the desired turbulence fluctuations. It is noteworthy that EC thermal fluctuations almost always drown out the microturbulent fluctuations. As a result, single channel analysis cannot extract turbulent temperature fluctuation measurements due to thermal blackbody noise dominance. These blackbody thermal fluctuations instead are proportional to the mean signal according to the following expression [111]:

$$\frac{V^2_{\tilde{N},RMS}}{V^2_{\bar{T}}} = 2\frac{B_{vid}}{B_{IF}} \tag{3.12}$$

The root mean square of the thermal fluctuations $V_{\tilde{N},RMS}$ are proportional to the ratio of video bandwidth low-pass filter B_{vid} and the IF bandpass filter B_{IF} frequencies used in the CECE diagnostic signal processing circuit. Fig. 3.7 illustrates the thermal fluctuation behavior predicted in equation 3.12 compared to CECE tokamak data for the reader's reference. The upper panel shows in blue electron temperature measurements from the regular DIII-D

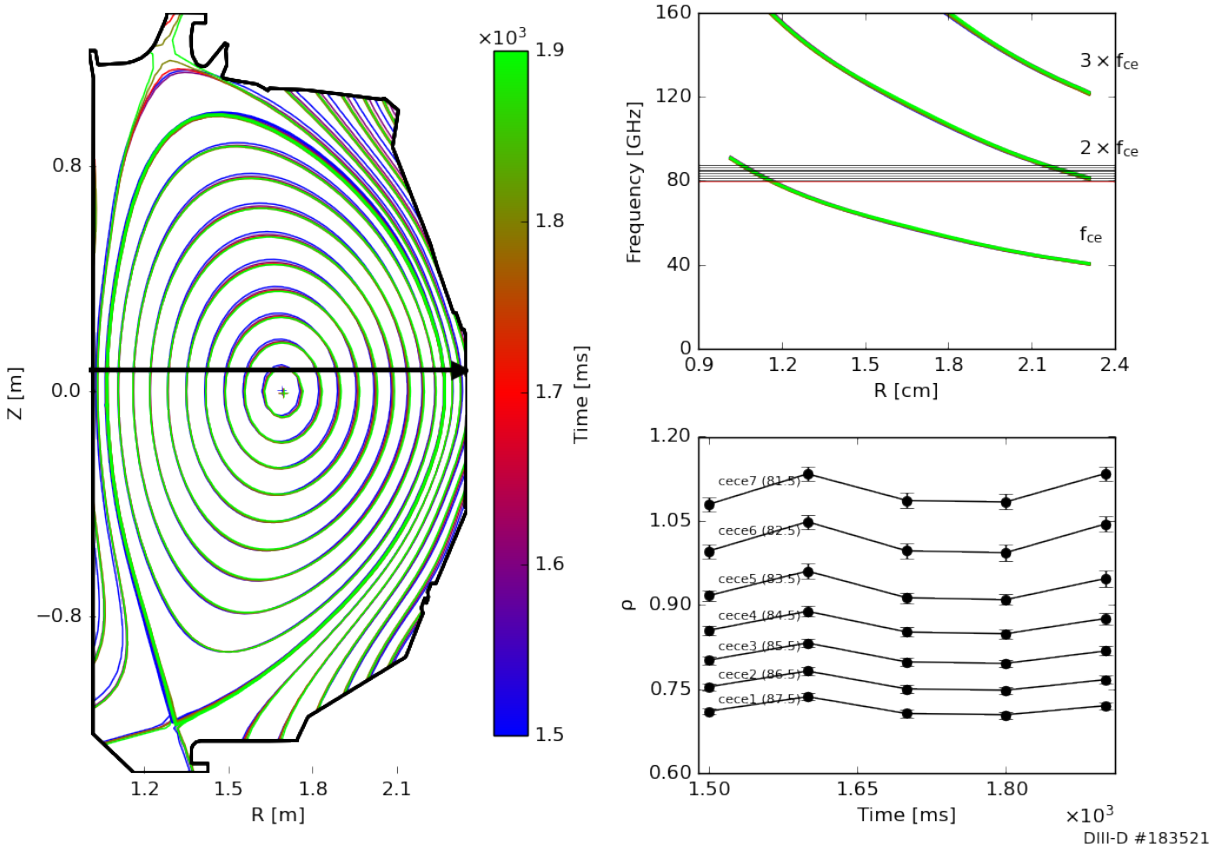

Figure 3.6: DIII-D Correlation Electron Cyclotron Emission Diagnostic for shot #183521 in the X-mode 2nd harmonic viewing settings. The left panel indicates the EFIT equilibrium reconstructions used for flux mapping, which are colored by time-slice. The upper right panel illustrates the electron cyclotron harmonics in green, and the CECE diagnostic channel frequencies in black vs. major radius R. The lower right panel shows the flux mapped channel locations inferred from the intersection of the black and green 2nd harmonic curves in the panel above, in addition with the equilibrium reconstructions to the left.

electron cyclotron emission (ECE) radiometry system [3], compared to CECE measurements at the same flux surface in red (cece1a). Note how the data acquisition rate of the CECE system is much higher than standard ECE. The lower panel calculates the RMS T_e fluctuations seen by the CECE system, normalized by the mean temperature, in solid red circles. In the blue dashed horizontal line are fluctuation predictions based on B_{vid}=1900 kHz, B_{IF} = 150 MHz respectively. Note how the red circles appear to align well with the dashed blue line predictions. As a result, the EC thermal fluctuations observed in experiment appear to indeed be well approximated by equation 3.12. This proportionality is important as it allows for the extraction of relative temperature fluctuations without the need for absolute radiometry calibrations. Specifically, using the nonmenclature of equation 3.5, the normalized electron temperature fluctuation power spectrum $P_{\tilde{T}}$ can be calculated from the following formula:

$$\gamma^2(f) = \frac{|P_{V_a V_b(f)}|^2}{P_{V_a V_a}(f) P_{V_b V_b}(f)} \tag{3.13}$$

$$P_{\tilde{T}}(f) = \frac{1}{B_{IF}} \frac{\gamma_c(f)}{1-\gamma_c(f)} \tag{3.14}$$

In the above expressions, the quantity $\gamma_c(f) = \sqrt{\gamma^2 - \gamma_b^2}$ is the bias corrected CECE coherency, $\gamma_b^2 = (1-\gamma^2)^2/M$ is the coherency bias error, and M is the number of realizations in the ensemble averaging. Note how the raw CECE coherency γ^2 between channels A and B is a ratio of the cross-power between A-B, and the auto-powers from A and B respectively. Experimentally, the channel pairs A and B are radially separated from one another by approximately 0.3 cm (150 MHz in frequency space at B_0= 2 T). This analytic method does not require an absolutely calibrated CECE signal to give accurate results due to the auto-powers being proportional to the mean temperature signals within a constant factor of $2B_{vid}/B_{IF}$. It is with these analytic techniques that experimental CECE measurements were used to calculate the normalized electron temperature fluctuation power spectrum $P_{\tilde{T}}$. This power spectrum will be compared to synthetic turbulence signals in Chapter 5, including in both optical thick and optical gray conditions.

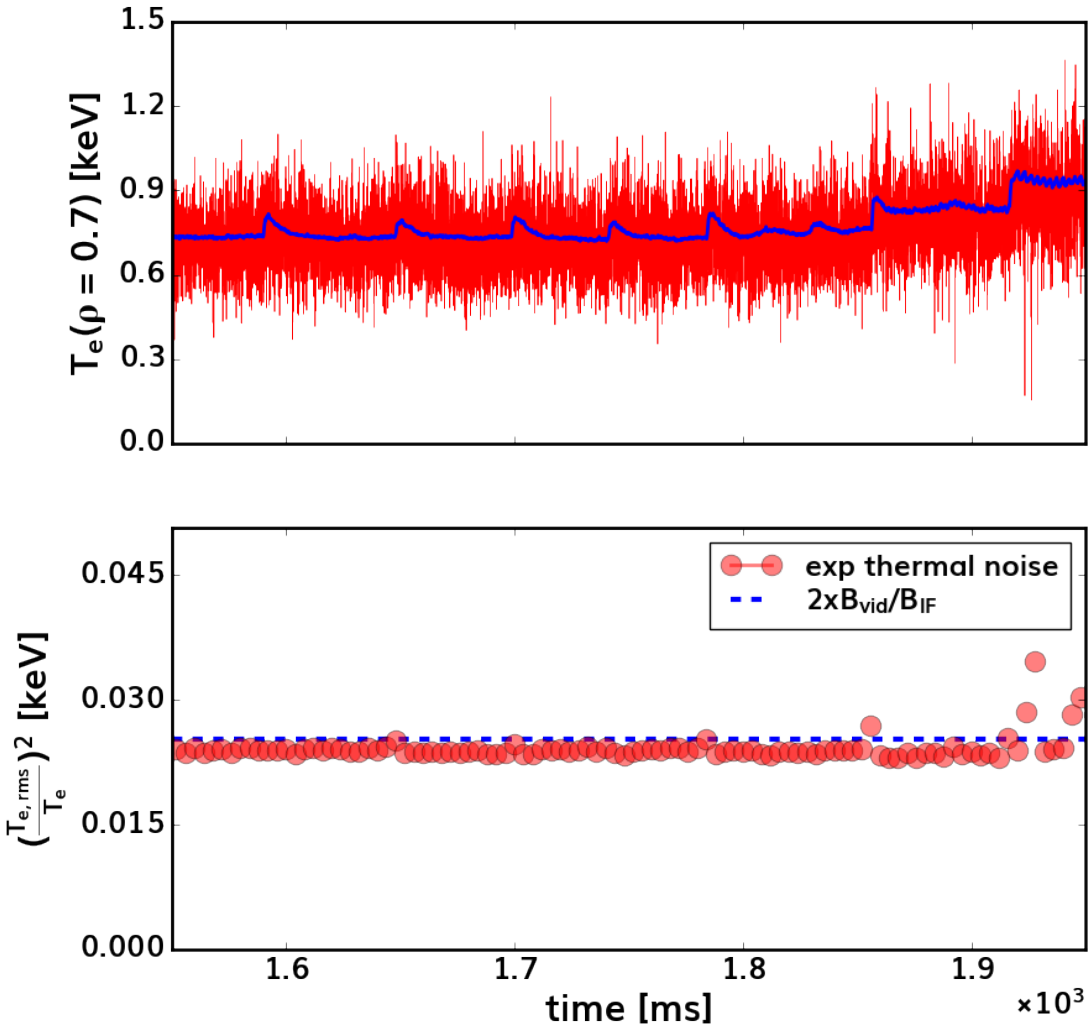

Figure 3.7: DIII-D Correlation Electron Cyclotron Emission data for shot #183521 in the X-mode 2nd harmonic viewing configuration. The upper panel indicates electron temperature measurements from the CECE and standard ECE systems in red and blue respectively. The lower panel calculates the RMS fluctuations inferred from the CECE experimental data as red closed circles, compared to predictions using equation 3.12 in the blue dashed line.

3.4 Impurity Powder Dropper (IPD)

In addition to the above turbulence diagnostics, a specialized impurity seeding system, called the Impurity Powder Dropper, was used as a key part of this thesis work. As a result, its key components and capabilities will be described briefly.

The Impurity Powder Dropper (IPD) system [70], as the name may imply, is designed to drop a variety of impurities (in powder form) into the tokamak main plasma chamber at a controllable mass flow rate. The injection system is comprised of a single vertical drop tube which can be fed by 4 distinct powder feeder units, each containing approximately 80 ml of materials. In each of the powder feeder units are two piezo-electric blades which are driven sinusoidally to vibrate the feeder unit. These vibrations are used to slowly push forward a horizontal layer of powder to fall into a drop tube and plasma main chamber. A schematic of the IPD system at the DIII-D tokamak is provided in Fig. 3.8 to illustrate the feeder system in detail. On the far-left is a bench-test image of the IPD feeder system vibrated to continuously drop powder down the horizontal channel. Note that powder can be seen continuously falling off the edge of the channel, successfully demonstrating its "dropping" capability. It is at this same vertical location in the completed system that the vertical drop tube is housed to allow for injection into the DIII-D main chamber. In the middle, a cartoon rendition of the feeder system, with the dashed black arrow indicating the trajectory of the fed powder may be found for the reader's reference. The right-most figure illustrates a CAD drawing of the IPD system. In this diagram, note how there are two diagonally oriented piezo-electric razors supporting the channel and hopper above the mounting base. It is these razors which enable the system to vibrate, and controllably push powder down the horizontal channel. The piezo-electric razors may be driven with some amplitude Δx and frequency f to control the dropping rate. The rate at which the powder falls into the drop tube is dictated by the velocity of the horizontal layer of powder. Specifically, the drop rate R_{drop} follows the following empirical expression [70]:

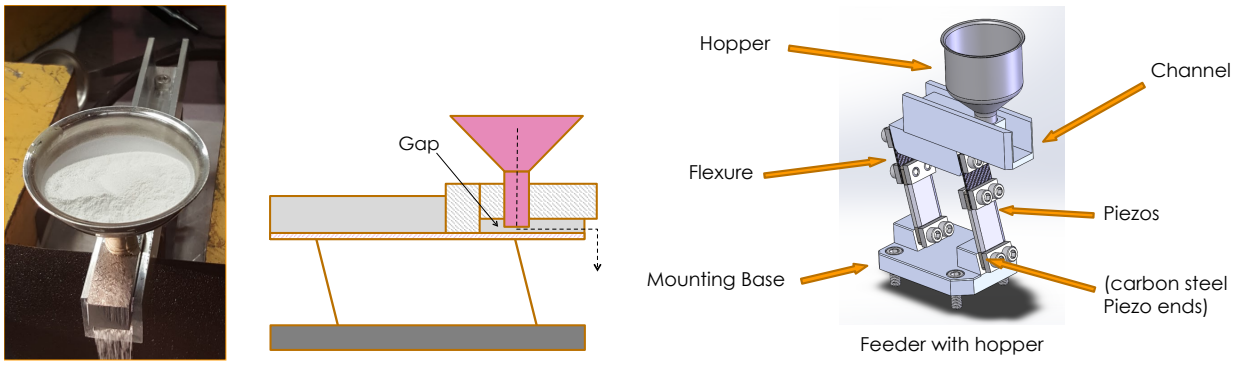

Figure 3.8: Left panel: Bench-test picture of the Impurity Powder Dropper feeder unit actively vibrated to demonstrate powder dropping. Middle panel: cartoon of the IPD feeder sub-system illustrating the trajectory of the injected powder in the dashed black line. Right panel: CAD drawing of the IPD system's feeder unit showing the structural mounting and piezo-electric razors used for vibration. Diagram provided in great thanks to Dr. Alex Nagy.

$$R_{drop} = \rho_{mass} P_f w_p h_p v_p \tag{3.15}$$

Above ρ_{mass} is the mass density, P_f is the packing factor, w_p is the width, h_p is the height, and v_p is the velocity of the horizontal powder layer. The piezo-electric blades, by applying more voltage, can create larger amplitude (Δx) oscillations. These oscillations generate the powder velocity $v_p = f\Delta s$ which continuously drops impurities into the drop tube. The step size Δs is linearly proportional to the piezo-electric oscillation amplitude Δx, however varies with different impurity powders and therefore must be determined experimentally. For the experiments conducted over the course of this PhD thesis, the injected material was graphite (carbon) powder with an intended injection rate between 1-10 mg/s. To achieve such injection rates, the system's piezo-electric razors were driven sinusoidally at 186 Hz with an approximately 1 volt amplitude.

3.5 Summary

The DIII-D systems described in the prior sections of this chapter are essential to understanding results presented in subsequent chapters. Material involving the neutral beam heating systems, charge exchange recombination spectroscopy diagnostic, DBS, and BES are important for understanding results presented in Chapter 6, pertaining to the radial electric field calculations, and the main ion poloidal/radial momentum balance subsections. The materials shown with respect to the BES and CECE turbulence diagnostics are essential to understanding the comparisons to synthetic diagnostics in Chapter 5. As a result, it is the hope that this thesis section has provided the reader sufficient background to understand the key results presented in subsequent material.

CHAPTER 4

Observation of isotope L-mode heat transport effects

In this thesis chapter, several heat transport isotope effects between DIII-D hydrogen and deuterium plasmas are investigated. The material presented has been published in the Nuclear Fusion scientific journal in [19]. The sections below outline the paper's key findings in greater detail than the originally published manuscript. The key investigations discussed include using a large DIII-D L-H transition database to elucidate L-H power threshold trends with respect to collisionality and effective ion charge Z_{eff}, and using gyro-fluid and gyrokinetic modeling to infer the origin of isotopic heat flux differences seen in dimensionally matched H and D experiments. The principle findings are that the heat flux differences in DIII-D low collisionality hydrogen plasmas (compared to deuterium) result from impurity (carbon) content changes. These changes in carbon content between hydrogen and deuterium are themselves an isotope effect, due to reduced (mass-dependent) physical and chemical sputtering of graphite in hydrogen compared to deuterium. These natural impurity content changes are found, using both Trapped Gyro-Landau Fluid (TGLF) quasilinear simulations and local non-linear gyrokinetic CGYRO simulations, to modify Ion Temperature Gradient (ITG) driven turbulence by main ion dilution. Additional secondary isotope effects in the plasma edge at $\rho = 0.9$ due to electron non-adiabaticity and mass dependent $\vec{E} \times \vec{B}$ shear stabilization in the shear layer at $\rho = 0.95$ are uncovered from non-linear CGYRO simulations. The shear layer isotope effect in particular was found to be consistent with the previously documented Garcia effect [32]: more effective $\vec{E} \times \vec{B}$ stabilization with heavier main ions due to the mass dependent shear stabilization criteria: $\gamma_{\vec{E}\times\vec{B}}/\gamma_{linear} \propto c_{s,i}/a \propto 1/\sqrt{m_i}$. Inspection of the raw turbulent fluctuations from flux-matched CGYRO simulations indicates changes in $\tilde{v}_r$, and not $\tilde{n}$ or $\tilde{T}$ as being responsible for the observed heat flux differences.

Such flux-matched simulations lay the foundation for results discussed in Chapter 5, which compare turbulence predictions to experimental measurements from the BES and CECE diagnostics. While these studies attribute the isotopic dependence of the thermal ion flux to differences in Z_{eff}, this effect has been ruled out as controlling the isotope dependence of the L-H power threshold, as discussed in detail in thesis chapter 7.

4.1 Historical DIII-D data

From DIII-D's suite of diagnostics, key parameters relevant to the L-H transition were documented for approximately 500 recent (>2010) hydrogen and deuterium discharges. Details of the database may be found in Appendix A for the reader's reference. Parameters at transition, such as plasma current (I_p), impurity content (Z_{eff}), and ion temperature (T_i), were recorded in addition to other quantities relevant to the L-H power threshold (power sources and sinks). The threshold power is calculated as:

$$\begin{gathered} P_{LH} = P_{sep}(t = t_{LH}) = \\ P_{NB} + P_{ECH} + P_{OH} - \frac{\partial W_{dia}}{dt} - P_{rad,core} \end{gathered} \tag{4.1}$$

The injected neutral beam, electron cyclotron, and ohmic powers are P_{NB}, P_{ECH}, and P_{OH} respectively. The power consumed by changing the diamagnetic stored energy and lost by core plasma radiation are $\frac{\partial W_{dia}}{dt}$ and $P_{rad,core}$ respectively. All quantities were time-averaged over the 30 ms window preceding the L-H transition. Identification of the transition time was performed manually by inspecting discharges for a simultaneous drop in Balmer α recycling light emission and rise in line-averaged density. An example of such a transition can be found in Fig. 4.1, illustrating the 1st L-H transition of deuterium DIII-D shot # 192089. On the upper panel are the time averaged neutral beam injected power P_{NB}, ohmic power P_{OH}, electron cyclotron power P_{ECH}, core radiation loss power $P_{rad,core}$, power losses from changes in the plasma stored energy dW_{dia}/dt, and total separatrix power P_{sep} given by equation 4.1 in blue, violet, orange, green, red, and black respectively. Note how the time averaged neutral

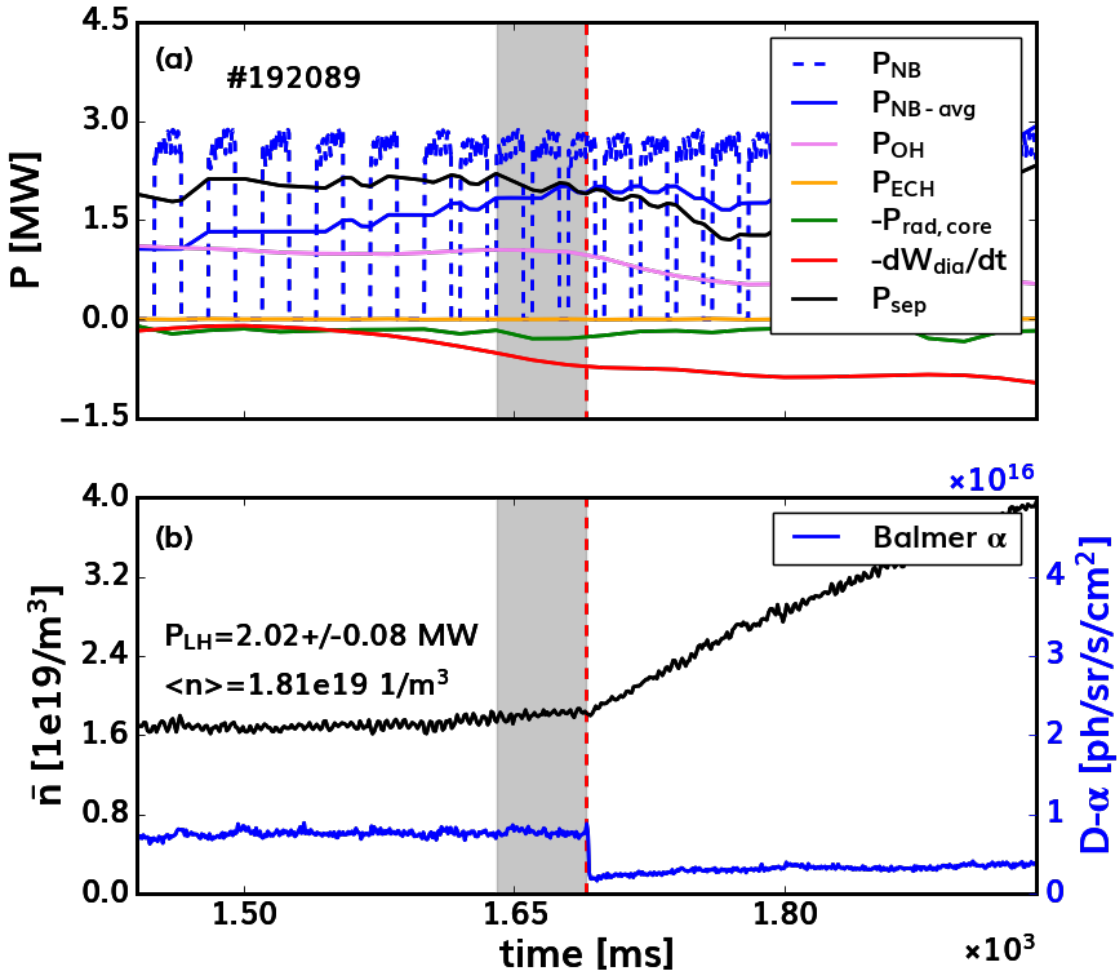

Figure 4.1: (a) Contributions to the L-H threshold power vs. time, with P_{sep} in black. The red vertical line and gray shaded region indicate the exact time of L-H transition and time averaging window for calculated quantities. (b) Line-averaged density ($\bar{n}$) and Balmer α recycling light emission during a typical L-H transition.

beam injected power is steadily increased by changing the instantaneous beam duty cycle. The red dashed vertical line indicates the L-H transition time for this discharge, with the gray shaded region before the transition time illustrating the time-averaging window used by the experimental database algorithm. The lower panel illustrates the line average density $\bar{n}$ and edge Balmer-α recycling light vs. time in black and blue respectively. Note how at times after the L-H transition time, the line-averaged density continuously rises while the Balmer-α light appears consistently lower than that prior to transition.

Historically, P_{LH} is often observed to have a minimum vs. line-averaged density at

transition $\langle n \rangle$ in most tokamaks [89]. This trend is observable in the referenced DIII-D L-H transition database in both hydrogen and deuterium discharges, most easily seen on the left-most panel of Fig. 4.2. This panel illustrates in red $\triangle$ and blue $\bigcirc$ hydrogen and deuterium data respectively in ITER similar shape (ISS) with edge magnetic safety factor $q_{95} \approx 5$ and injected torque $|T_{inj}| < 1Nm$. The ITER similar shape is that shown in Fig. 2.1, with the last closed flux surface intersecting the machine walls at the lower divertor. Injected torque is kept low by balancing co and counter neutral beam sources, described in section 3.1. The y-axis is the measured P_{LH} in MW, and the x-axis is the L-mode line-average density at transition $\langle n_e \rangle$ in $10^{19}m^{-3}$. Note how both the hydrogen and deuterium data appear to contain a P_{LH} minimum at $\langle n_{min} \rangle \approx 3 - 4 \times 10^{19}m^{-3}$. The area below this minimum density is normally called the low-density branch, while the region above is coined the high density branch. This minimum however is not always observed in the tokamak data. An example of this is shown in the right-hand panel of Fig. 4.2, which similarly illustrates hydrogen and deuterium transitions with P_{LH} in MW vs. $\langle n_e \rangle$ in $10^{19}m^{-3}$. These data however were acquired under different tokamak operational conditions. Specifically here, the data illustrated have lower edge magnetic safety factors $q_{95} = 5 \rightarrow 3.6$ (higher plasma current I_p) compared to the left-hand discharges. Note how both hydrogen and deuterium data appear to be relatively flat with respect to line-averaged density. These comparisons highlight the complex dependencies observed within tokamak P_{LH} threshold data. Theoretical work performed by Bourdelle suggests the origin of this low and high density branch behavior is due to a transition from Trapped Electron Mode/Ion Temperature Gradient Mode (TEM/ITG) to Resistive Ballooning Mode (RBM) dominated turbulence [12]. The absence of a density minimum in the low $q_{95} \approx 3.6$ discharges is suspected to be from changes in plasma collisionality $\nu^*_{95} \propto n_{95}q_{95}$ permitting only TEM/ITG dominant turbulence. Collisionality, in words, refers to the ratio of the electron-ion or ion-ion Coulomb collision rate normalized by the banana transit frequency. A high collisionality, where $\nu^* > \epsilon^{-3/2} \approx 5$, is called the Pfirsch-Schluter limit with trapped particles undergoing collisions quicker than they take to complete one banana orbit, causing detrapping into passing orbits. Medium collisionality instead is characterized by $1 < \nu^* < \epsilon^{-3/2}$, coined the plateau regime, where particles can execute

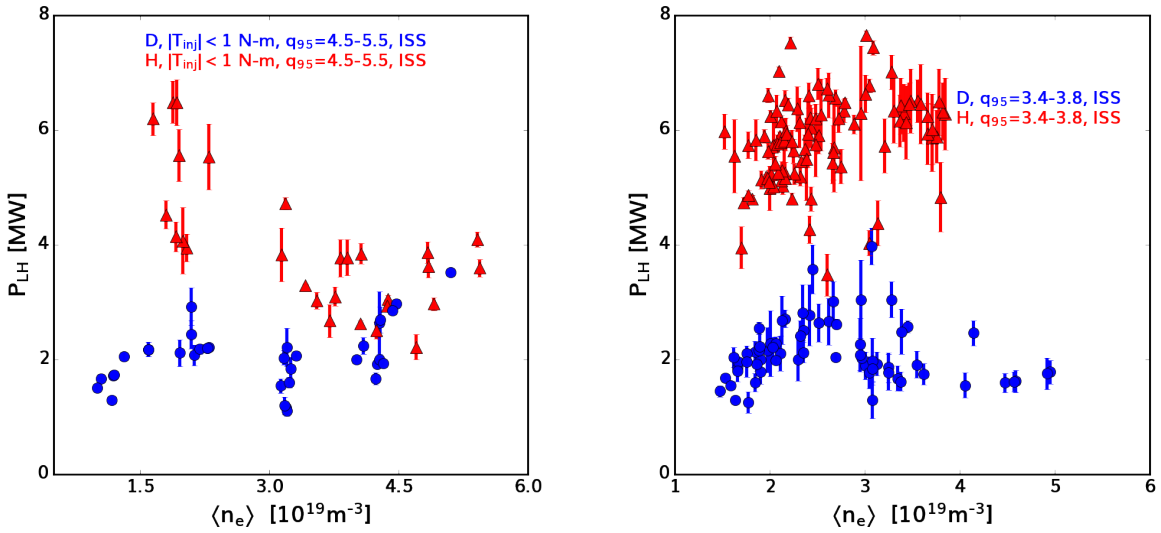

Figure 4.2: DIII-D L-H transition database results for hydrogen and deuterium discharges in red △'s and blue ◯'s respectively. The left panel shows P_{LH} in MW vs. L-mode line-averaged density at transition in $10^{19}m^{-3}$ for ISS plasmas with $q_{95} \approx 5$ and $|T_{inj}| < 1$ N-m. The right-panel shows similar data, however with lower magnetic safety factor $q_{95} \approx 3.6$.

nearly full banana orbits before undergoing Coulomb collisions. Low collisionality is the limit where $\nu^* < 1$, referred to as the banana regime where trapped particles can execute many banana orbits prior to undergoing Coulomb collisions and detrapping. These regimes constitute dramatically different trapped particle behavior, and as a result are often used as lenses to distinguish between different types of tokamak plasmas. In an attempt to discern key differences between hydrogen and deuterium discharges, a distinction between low and high density (collisionality) branch data is used to simplify comparisons. Such data separation techniques were used to discern key behavioral differences between plasmas.

From the DIII-D database, in ITER similar shape with $\langle n \rangle$=1-2.5$\times 10^{19}/m^3$, below the density where P_{LH} exhibits a minimum at DIII-D $\langle n_{min} \rangle$=3-4e19/m^3, the L-H power threshold was found to decrease strongly with increasing effective ion charge $Z_{eff} = \sum_i Z_i^2 n_i/n_e$. Z_{eff} is measured by Charge Exchange Recombination Spectroscopy (CER) [27] and Thomson Scattering [72] using the fully ionized carbon and electron densities $n_{C^{6+}}$ and n_e at a normalized minor radius $\rho = \sqrt{\psi_N} = 0.7$, assuming a single light impurity species. This

Z_{eff} dependence is shown in Fig. 4.5(a) with P_{LH} plotted with respect to impurity content on the x-axis. Noteworthy is that DIII-D hydrogen plasmas almost never reach the impurity levels of their deuterium counterparts. This difference is attributed to the well known graphite sputtering isotope effect between hydrogen and deuterium. Specifically the larger (mass dependent) physical and chemical sputtering yield of the graphite (carbon) divertor and main chamber tiles by deuterium, compared to hydrogen tends to create a larger carbon source in deuterium plasmas, leading to greater carbon impurity content [41].

To determine how changes in Z_{eff} may be altering the threshold power, profile fitting analysis of an ensemble of nearly 80 L-H transitions, with a range of line-averaged densities $\langle n_e \rangle$ = 1-5.5$\times 10^{19}/m^3$, edge safety factors q_{95} = 3.0-7.0, and neutral beam injected torques T_{inj} =0-5 N-m was undertaken. Such analyses allow for accurate determination of normalized plasma physics variables such as collisionality ν^*, temperature ratios T_e/T_i, and normalized ion gyro-radii $\rho^* = \rho_s/a$ for more plasma physics informed data organization. During profile fitting analysis, correction of impurity ion temperature (T_i) measurements for Zeeman and Fine Structure Doppler broadening effects [9], and checking Z_{eff} measurements against visible bremsstrahlung continuum emission [115, 18] was performed to ensure high data quality. TRANSP power balance analysis was performed using these profiles, taking care to match transport metrics (neutron rate, plasma stored energy, loop voltage, inductance, $\bar{n}$) to minimize errors in power accounting [39]. An example of such transport metric matching for a reference deuterium plasma is shown in Fig. 4.3 for the reader's reference. The upper-left panel shows a comparison of the measured neutron rate in dark blue to the total TRANSP prediction using the experimental data in red for shot #192089. The green and violet contours show contributions from beam-beam and beam-target neutron rates predicted by TRANSP respectively. The upper-right panel shows a comparison of the magnetics only EFIT01 stored plasma energy in dark blue, compared to the total TRANSP predictions in red. The lower-left panel shows the time-averaged surface voltage in dark blue compared to TRANSP predictions in red. The lower-right panel illustrates a comparison between the magnetics only equilibrium reconstruction and TRANSP predicted internal inductance in

dark blue and green respectively. Note that for this discharge, the neutron rate, stored energy, and surface voltage are reasonably well matched between TRANSP simulations and experiment. The internal inductance is less well matched, but still within a factor of 10% of the EFIT equilibrium reconstruction measurements. Transport metric comparisons for a hydrogen counterpart experiment #183521 from TRANSP simulation 183521K55 are shown in Fig. 4.4. The plots shown are identical to those from the deuterium comparisons in Fig. 4.3. Note how in this hydrogen comparison, the neutron rates are nearly 2 orders of magnitude lower than the deuterium counterpart due to the neutrons being produced from the hydrogen experiment's residual deuterium thermonuclear fusion. In this discharge the plasma surface voltage and internal inductance are well matched between simulation and EFIT01 equilibrium reconstructions. The plasma stored energy is mismatched by approximately 20%, possibly as a result of the inclusion of TRANSP fast ion energy contributions to total energy. These TRANSP simulations, which are generated using experimental profile data, are in good but not perfect agreement with observed transport metrics. These disagreements are expected, as the TRANSP solutions shown solve the more rigorous time-dependent resistive current diffusion Grad-Shafranov equations when performing kinetic equilibrium reconstructions. These simulations and data quality checks form the basis of the ensemble of 80 discharges analyzed.

Detailed power balance analysis of 10 of these hydrogen and deuterium L-H transitions, shown in Fig. 4.5(b), indicates that both electron and ion heat fluxes (Q_e, Q_i) in L-mode just before transition contribute to P_{LH}. Fig. 4.5(b) illustrates this by showing the pre-transition separatrix ($\rho = 1$) ion and electron loss power, overlayed with P_{LH}. On average, $Q_e + Q_i \leq P_{LH}$ due to TRANSP accounting for additional loss channels, such as charge exchange for ions and neutral ionization work for electrons. Both ion and electron loss powers are observed to decrease with increasing Z_{eff}. Discharges in this limit were found to have low collisionality ($\nu_i^*, \nu_e^* \leq 1$ at $\rho = 0.95$), where trapped particles can complete many banana orbits prior to Coulomb scattering and detrapping.

At higher collisionality (above the P_{LH} density minimum on the high density branch),

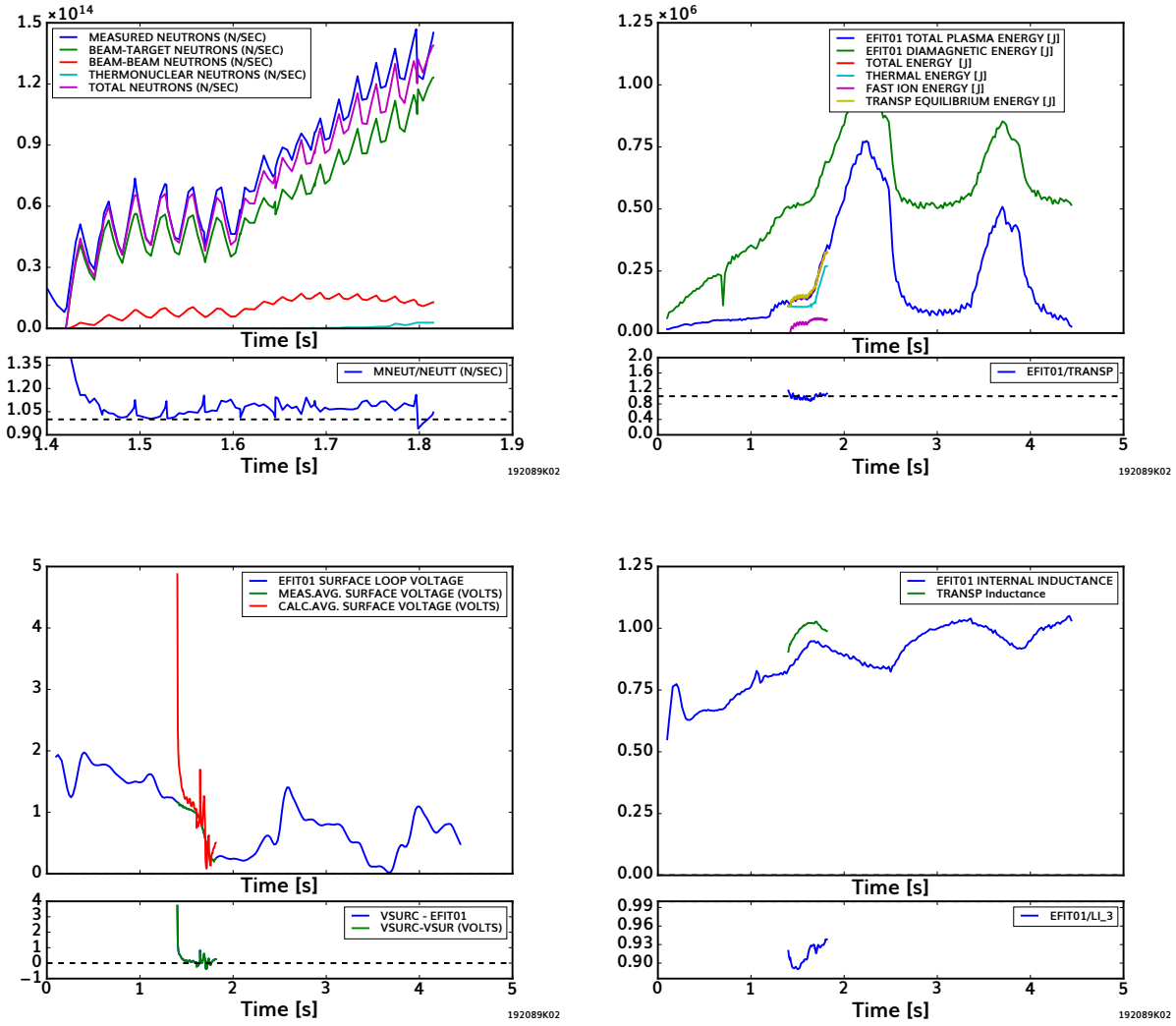

Figure 4.3: Deuterium TRANSP simulation 192089K02 comparison to experiment. Upper-left panel shows the neutron rate in particles/second vs. time. Upper-right panel shows a comparison to the plasma stored energy in Joules. Lower-left panel illustrates the TRANSP calculated surface voltage vs. experiment in volts. Lower-right panel shows internal inductance, a unitless parameter, for the magnetic only EFIT01 reconstruction and TRANSP solution which solves the time-dependent resistive current diffusion Grad-Shafranov equation.

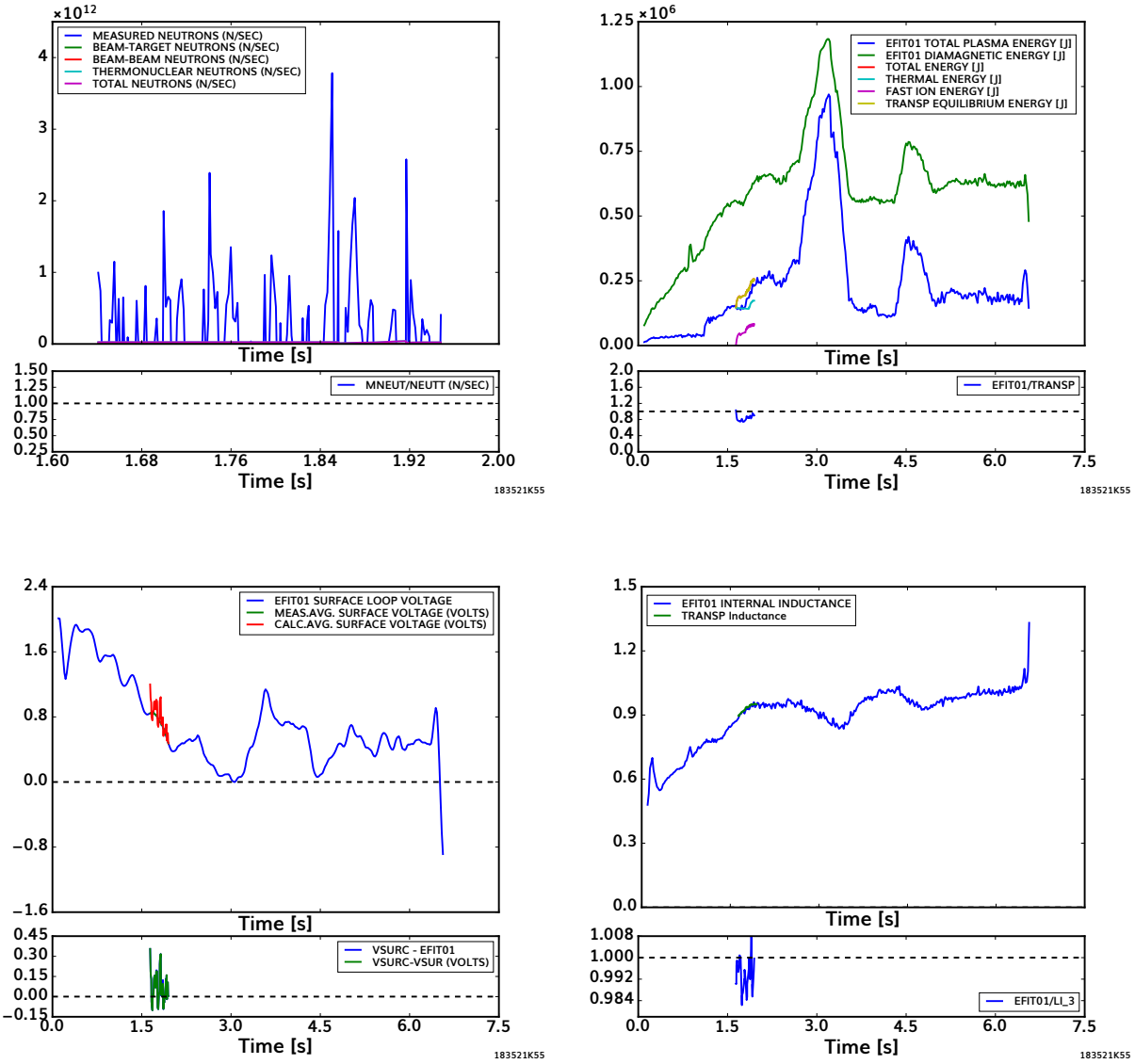

Figure 4.4: Hydrogen TRANSP simulation 183521K55 comparison to experiment. Upper-left panel shows the neutron rate in particles/second vs. time. Upper-right panel shows a comparison to the plasma stored energy in Joules. Lower-left panel illustrates the TRANSP calculated surface voltage vs. experiment in volts. Lower-right panel shows internal inductance, a unitless parameter, for the magnetic only EFIT01 reconstruction and TRANSP solution which solves the time-dependent resistive current diffusion Grad-Shafranov equation.

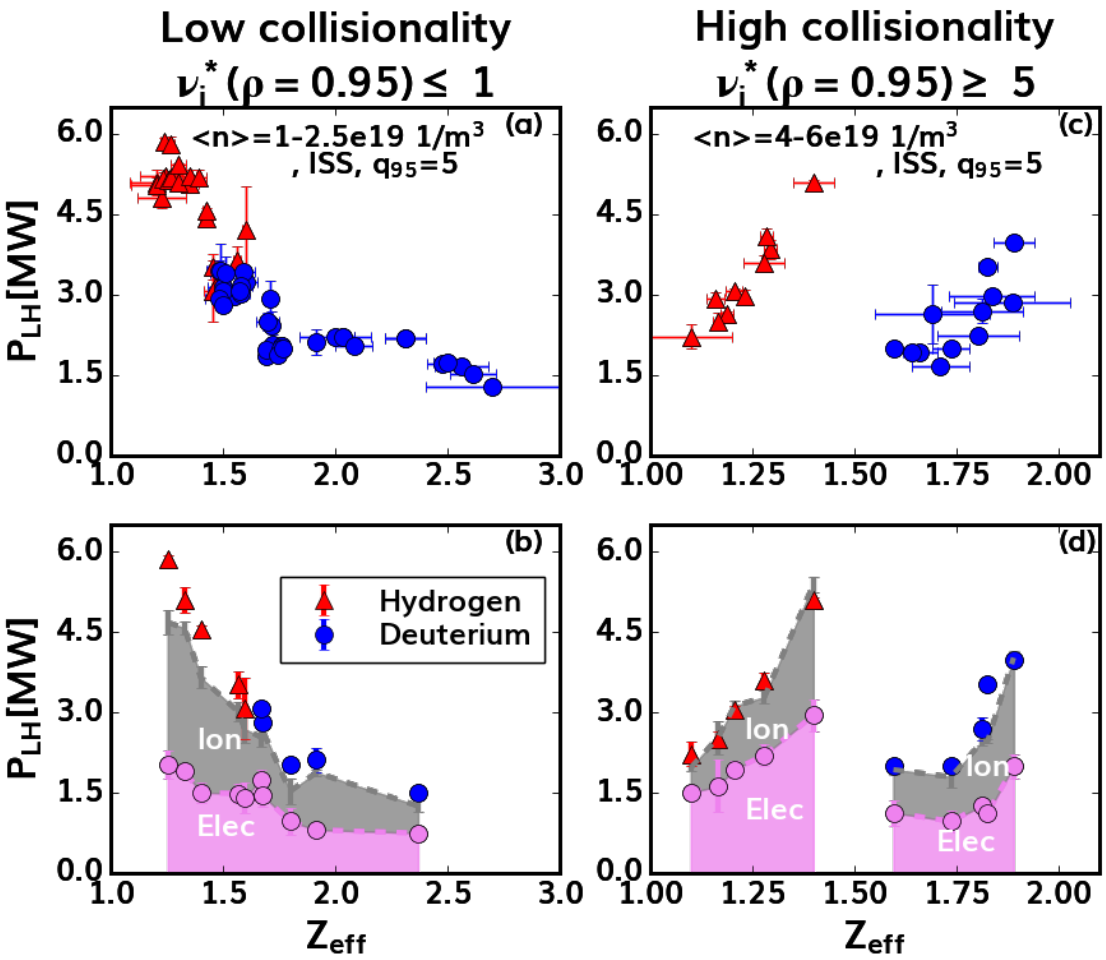

Figure 4.5: Panels (a) and (c) illustrate the observed P_{LH} trend with Z_{eff} at low and high collisionality in hydrogen and deuterium plasmas. Panels (b) and (d) show results of power balance analysis using the TRANSP code. The L-mode separatrix heat fluxes carried by ions (gray) and electrons (violet) for a sample of transitions are shown in panels (b) and (d).

the hydrogen and deuterium power thresholds increase with increasing Z_{eff} [Fig. 4.5(c)], consistent with past JET findings at high L-mode density [12]. Experimentally, $T_e \approx T_i$ for almost all transitions in Fig. 4.5(c). Assuming $T_e = T_i$, power balance analysis indicates $Q_i \leq Q_e$, with both heat channels contributing to increasing P_{LH}. Collisionally, these transitions are in the Pfirsch-Schluter (PS) regime, and converging to similar P_{LH} independent of isotope and Z_{eff}, as previously observed by Yan [117]. This convergence is not observed on several other tokamaks however (such as ASDEX Upgrade [79]) and is currently not well understood. These initial comparisons however suggest two very useful normalized plasma physics parameters which can be used to organize the existing DIII-D L-H power threshold database data: edge ion collisionality ν_i^* and effective ion charge Z_{eff}. It is under these lens that the nearly 80 hydrogen and deuterium TRANSP simulation results were organized.

Distinguishing all 80 analyzed transitions by neoclassical transport regime using edge ion collisionality (banana, plateau, and Pfirsch-Schluter regimes), one finds that the isotope effect is strongest at low collisionality, and suppressed approaching the Pfirsch-Schluter limit [Fig. 4.6]. Ion collisionality is approximated as [46]:

$$\nu_i^* \simeq \frac{4}{3}\sqrt{\pi}\frac{qR}{T_i^2} n_e e^4 Z_{eff}^2 \frac{log(\Lambda_i)}{\epsilon^{3/2}} \tag{4.2}$$

R, $\log(\Lambda_i)$, and ϵ represent the major radius, Coulomb logarithm, and inverse aspect ratio respectively. The observed P_{LH} vs. Z_{eff} trend reversal from low to high collisionality is consistent with a transition from Trapped Electron Mode/Ion Temperature Gradient (TEM/ITG) turbulence to Resistive Ballooning Mode (RBM) dominated turbulence previously observed in simulations [11]. Analogous to simulations scanning density which included ITG/TEM and RBM modes by Bourdelle, the collisionality/density of minimum P_{LH} is observed to increase with lower Z_{eff} [Fig. 4.6]. L-H transitions at similar Z_{eff} and collisionality are found to have nearly identical power thresholds, independent of m_i (hydrogen in $\triangle$ and deuterium in $\bigcirc$) in different collisionality regimes. The solid lines within Fig. 4.6 represent parabolic fits to the experimental data using a narrow range of Z_{eff} values, shown via color-coded text on the left-hand side of the figure. All data included in the figure represent hydrogen

and deuterium plasmas without extrinsic impurity injection. Instead, Z_{eff} is from carbon sputtered from plasma-wall interactions, which depends strongly on plasma conditions. As a result, no conclusions about the causality between Z_{eff} and heat transport or P_{LH} can yet be made due to possible correlation with other variables. It is noteworthy that using ν_i^* and Z_{eff} to organize the L-H power threshold data explicitly ignores other known dependencies such as injected torque, X-point height, and divertor closure. Some of these actuators are indeed co-linear with the chosen variables Z_{eff} and ν_i^*. For example, within the L-H transition database, an inter-dependence between injected torque T_{inj} and effective ion charge Z_{eff} is observed, with higher torque plasmas being routinely more clean. As a result, caution should be used when interpreting existing data-base results to inform actual plasma physics processes which may change P_{LH}. To this end, much more sophisticated modeling is undertaken for a select pair of low collisionality hydrogen and deuterium discharges to decipher the origins of the apparent heat transport and P_{LH} relations between experiments.

4.2 Quasilinear transport analysis using TGLF

The discharge pairs chosen were as ITER relevant as possible, with banana regime edge ion collisionality $\nu_i^*(\rho = 0.95) < 1$, low line-averaged density $\langle n_e \rangle = 1.6 \times 10^{19}/m^3$, safety factor $q_{95} = 3.6$, ITER similar shaping, and low neutral beam torque [83]. Additionally, the discharges had L-mode radial kinetic profiles just before L-H transition (n_e, T_e, T_i) that were very closely dimensionally matched, enabling a more controlled comparison between the two isotopic experiments. Fig. 4.7 illustrates each plasma's L-mode profiles approximately 10 ms before the L-H transition in red and blue for hydrogen and deuterium respectively. The deuterium plasma normalized carbon density gradient was used to infer the core electron density due to the lack of reliable inner core Thomson scattering and reflectometry data. The hydrogen plasma inner core toroidal rotation measurements (Ω_C) were not available. The most substantial difference between these two plasmas, aside from main ion species, was carbon impurity content (Z_{eff}). Despite such similar profiles, heat fluxes calculated from TRANSP power balance analysis were nearly two times larger in H compared to D.

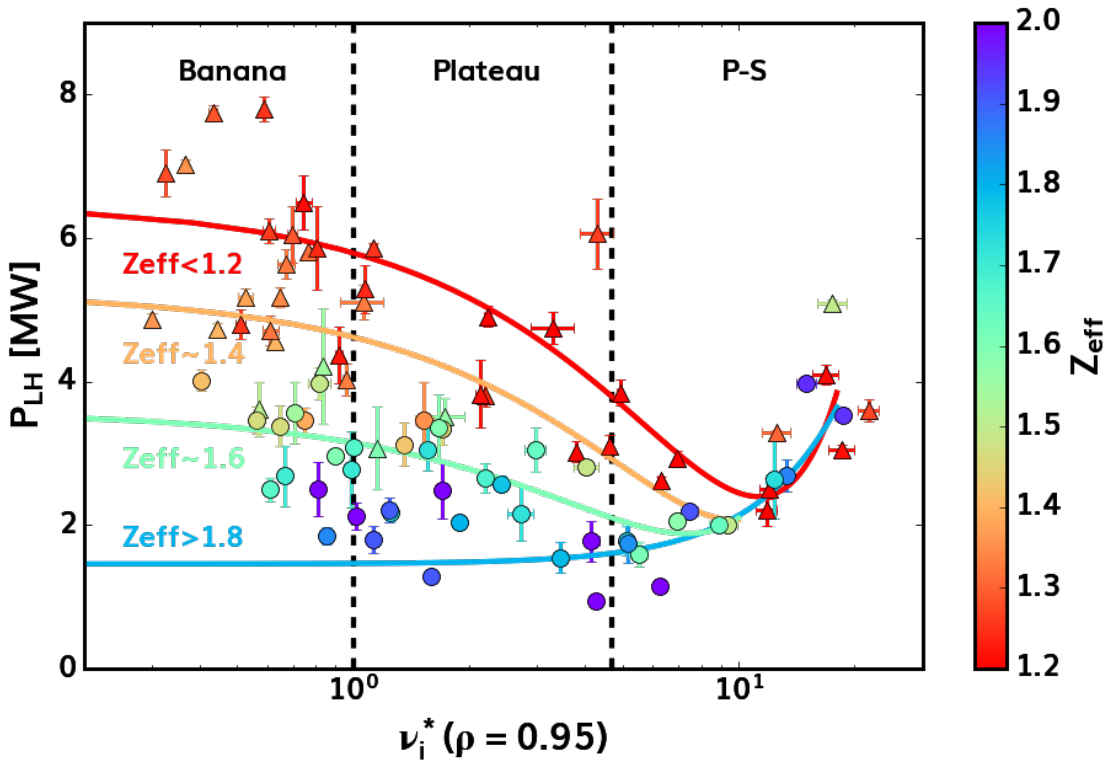

Figure 4.6: P_{LH} vs. edge ion collisionality ($\rho = 0.95$). Heat map shows low (red) and higher (purple) Z_{eff}, and symbol shapes indicate plasma species ($\triangle$ for H and $\bigcirc$ for D). Solid lines are parabolic fits to shown data for a narrow range of Z_{eff}. Vertical dashed lines divide collisionality into neoclassical transport regimes (banana, plateau, and Pfirsch-Schluter).

Heat flux uncertainty bands represent the time averaged variation in the 50 ms time interval preceding the L-H transition. Main ion charge exchange analysis indicated $T_{C^{6+}} = T_{H/D}$ after correcting impurity measurements for Zeeman and fine-structure effects [42]. Review of many L-mode pre-transition profiles similar to Fig. 4.7 suggested that nearly identical kinetic profiles (n_e, T_e, T_i) are a potential commonality among L-H transitions in deuterium and hydrogen, as observed in previous experiments [23, 34, 62, 45, 78, 105]. This is believed to be due to the required edge ion pressure profile providing sufficient $\vec{E} \times \vec{B}$ shear to trigger a positive feedback turbulence suppression loop [82]. As a result, it is hypothesized that the heat flux needed to sustain the pre-transition L-mode radial gradients sets P_{LH}, and causes the isotope effect.

Stability analysis using quasilinear thermal fluxes from the gyro-fluid stability code TGLF [110] was undertaken to identify the origin of the large isotopic difference in thermal fluxes. TGYRO simulations, which adjust radial temperature and density gradients to match power balance and TGLF-predicted heat fluxes, were run until convergence to match the experimentally observed heat fluxes by adjusting the T_e and T_i profiles, holding the n_e profile fixed. A more complete description of the TGLF and TGYRO codes used may be found in Appendix C for the reader's reference. Converged solutions were obtained after 20 iterations, using an extended perpendicular wavenumber ($k_\theta \rho_s$) grid model to capture long wavelength modes. All three TGLF quasilinear saturation rules [95, 92, 91] with and without electromagnetic effects were tested, with saturation rule 2 most closely matching both experimental temperature gradients and profiles. Appendix C includes for the reader's reference the results from all applied saturation rules. The sat 2 simulation results may be seen in Fig. 4.7 in orange (H) and light blue (D) as the closed star symbols. Saturation rule 2 builds on previous models by including realistic geometry effects and species dependent Landau averaging. Electromagnetic (EM) corrections, although included in the analysis, were found to contribute negligibly to the TGLF predicted thermal fluxes, consistent with electrostatic ITG/TEM turbulence. TGLF results predicted nearly identical H and D kinetic profiles, consistent with experimental observations. These comparisons may be viewed in Fig. 4.8

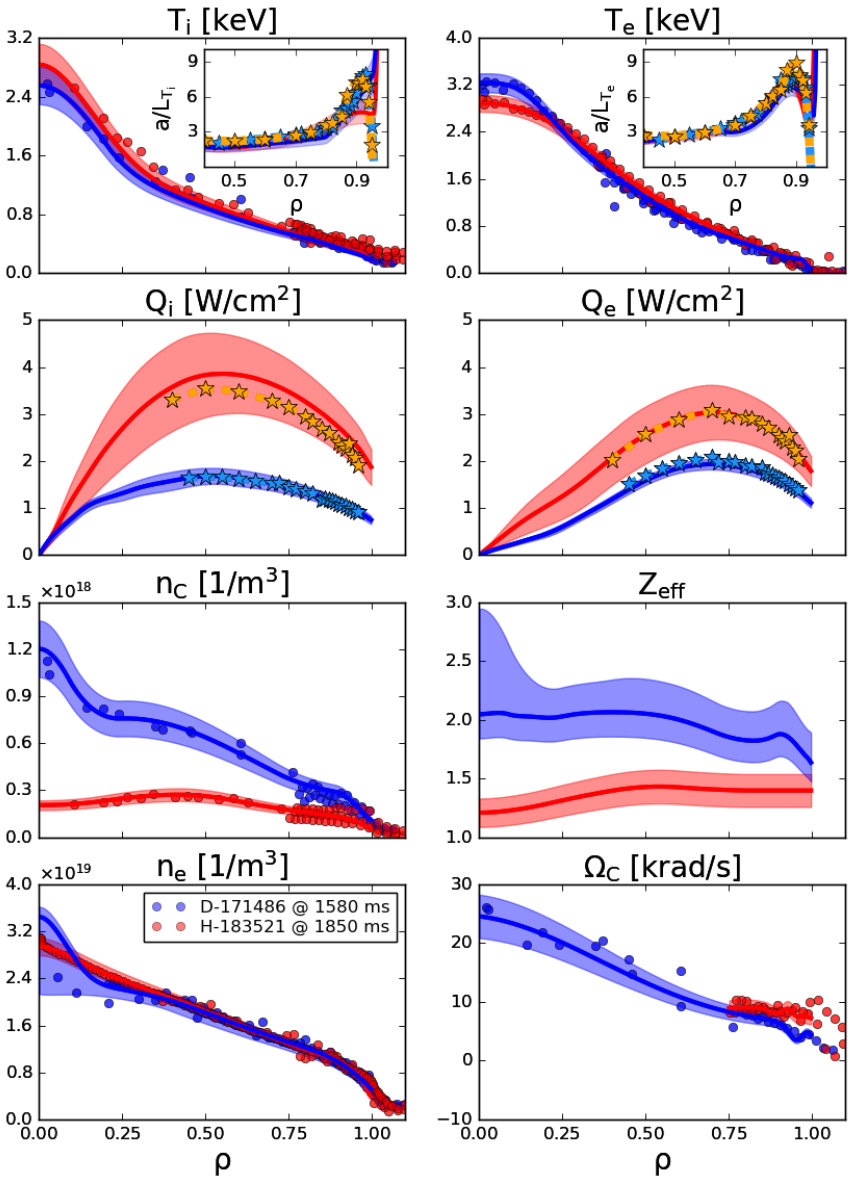

Figure 4.7: L-mode profiles and gradients approximately 10 ms before L-H transition for hydrogen (red) and deuterium (blue) plasmas at DIII-D vs normalized radius ρ. Dots are raw experimental data. Heat flux profiles are from TRANSP power balance analysis, with the time-averaged variation in heat flux as error bands. Orange and light blue (H,D) stars indicate TGLF flux matching solutions to T_i and T_e using sat. rule 2.

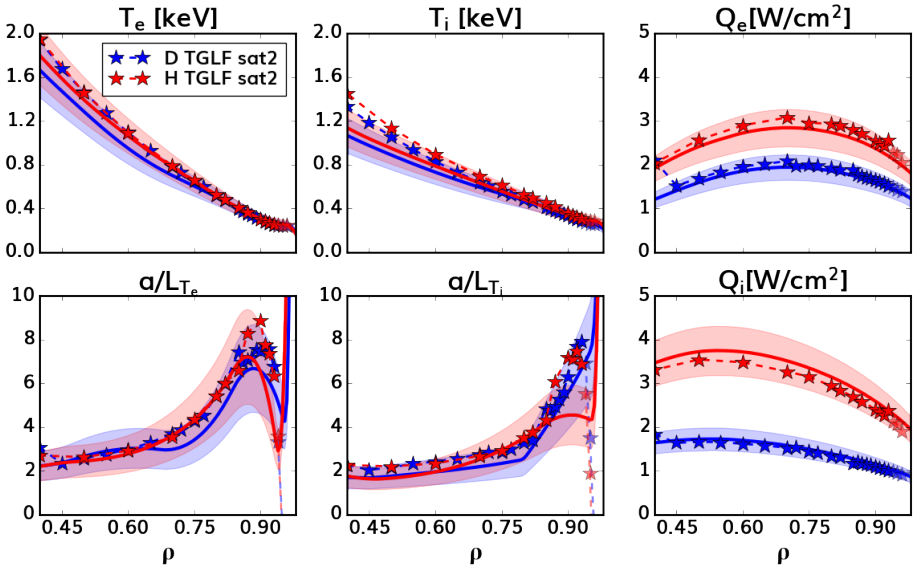

Figure 4.8: L-mode temperature profiles and normalized gradients approximately 10 ms before L-H transition for hydrogen (red) and deuterium (blue) plasmas at DIII-D vs normalized radius ρ in solid lines. Heat flux profiles are from TRANSP power balance analysis, with the time-averaged variation in heat flux as error bands, also shown as solid lines. Red and blue (H,D) dashed lines and closed star symbols indicate TGLF flux matching solutions to T_i and T_e using sat. rule 2.

for hydrogen and deuterium in red and blue respectively in greater detail. The solid lines indicate the experimentally measured temperature profiles, normalized gradients, and heat fluxes from TRANSP power balance. The dashed lines with closed star symbols illustrate the converged TGYRO flux-matching solutions. It can be observed that the TGLF simulations seem to capture the observed heat flux isotope effect between the two experiments. To discern the physics at play, the flux-matched TGYRO solutions were analyzed using 1D normalized gradient scans. Such analyses are useful for determining what type of turbulent modes are most unstable, and responsible for the observed heat and particle losses seen in experiment.

Gradient scans in the outer core plasma (ρ=0.7) were performed to identify the origin of the heat flux difference required to maintain the same profiles in H and D, as shown in Fig. 4.9. Scans identified characteristics of ion temperature gradient (ITG) turbulence

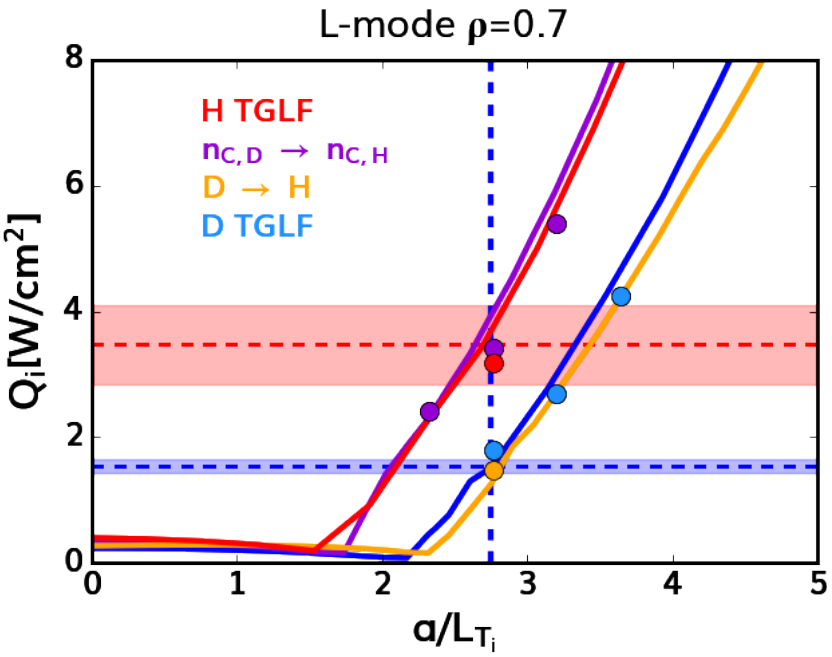

Figure 4.9: Scan of normalized T_i gradient at $\rho = 0.7$ vs. ion heat flux. Solid lines (closed circles) indicate the TGLF (CGYRO) calculated thermal fluxes. The vertical dashed line indicates the flux matching gradient for both D and H experimental heat fluxes (blue and red horizontal lines). Simulations in blue and red are from deuterium and hydrogen conditions shown in Fig. 4.8. Yellow and purple data are based on deuterium, but with reduced m_i and main ion dilution respectively.

(low $k_\theta \rho_s$ dominant spectra, mode propagation in the ion diamagnetic direction, a critical T_i gradient), with a shift in the T_i critical gradient observed as the dominant unstable mode feature driving the thermal flux differences. TGLF calculations demonstrate that the difference in carbon content is responsible for the shift in critical ITG gradient, in agreement with database results and predictions of ITG turbulence behavior with impurities [69]. Such results are consistent with observations of turbulence suppression with impurity seeding, dubbed the RI-mode, documented extensively at TEXTOR, DIII-D, and ISX-B [64, 52, 68, 58]. Changing species from D to H with fixed main ion dilution fraction had no effect on the heat flux levels (yellow line in Fig. 4.9), however reduced main ion dilution of the D plasma led to a critical gradient that matches the H-plasma critical gradient (purple vs. red), indicating main ion dilution as the precise origin of this effect.

4.3 Nonlinear gyrokinetic transport analysis using CGYRO

First principles local flux-tube nonlinear ($k_\theta \rho_s < 1.1$) CGYRO [20] simulations around the TGLF optimized gradients confirmed reduced model predictions. These nonlinear CGYRO simulations may be seen as the closed circles nearly overlapping with the TGLF predictions illustrated as solid lines shown in Fig. 4.9. In addition to confirming TGLF predictions, these simulations were used to benchmark TGLF saturation rules 1 and 2 to discern which reduced model was more consistent with the first principle calculations. 1D ion temperature gradient scans similar to Fig 4.9 were performed using non-linear CGYRO as part of the benchmarking test. Both the heat flux spectra at identical input conditions, as well as 1D scans of a/L_{T_i} vs. integrated heat flux were compared for TGLF sat 1, sat 2, and nonlinear CGYRO shown in Fig. 4.10 in orange, red, and dark blue respectively. Note how in the left-hand panel, the ion and electron heat fluxes are peaked around normalized poloidal wavenumber $k_\theta \rho_s \approx 0.3$ for all simulations. In the right-hand corner, the total (integrated) heat fluxes scanned vs. ion temperature gradient illustrate stiffness consistent with saturation rule 2. Saturation rule 1 stiffness, or the slope of the heat flux vs. gradient relationship, is lower compared to the CGYRO predictions. These comparisons therefore provide confirmation that saturation rule 2 better matches the first principle gyrokinetic simulation results it is meant to model compared to the less sophisticated saturation rule 1.

Based on these initial nonlinear CGYRO validated TGLF simulations, nonlinear gyrokinetic simulations using the code CGYRO [20] in both the plasma near edge (ρ=0.9) and shear layer (ρ=0.95) were undertaken to identify and quantify the isotope effects at play within these lowest density L-mode plasmas just before L-H transition. Identical to the ρ=0.7 simulations, these nonlinear runs were local flux-tube simulations with electromagnetic fields (ϕ and $A_\parallel$), limited to ion scales ($k_\theta \rho_s$ <1.1, where ρ_s is the deuterium ion sound gyro-radius) and tested for numerical convergence by increasing simulation box size and radial resolution to identify if any substantive changes in turbulent fluxes were found. All results presented are those which passed such tests and were run until long after nonlinear saturation (usually for 700-1000 c_s/a, where $c_s = \sqrt{T_e/m_D}$ is the deuterium ion sound speed). Simulations

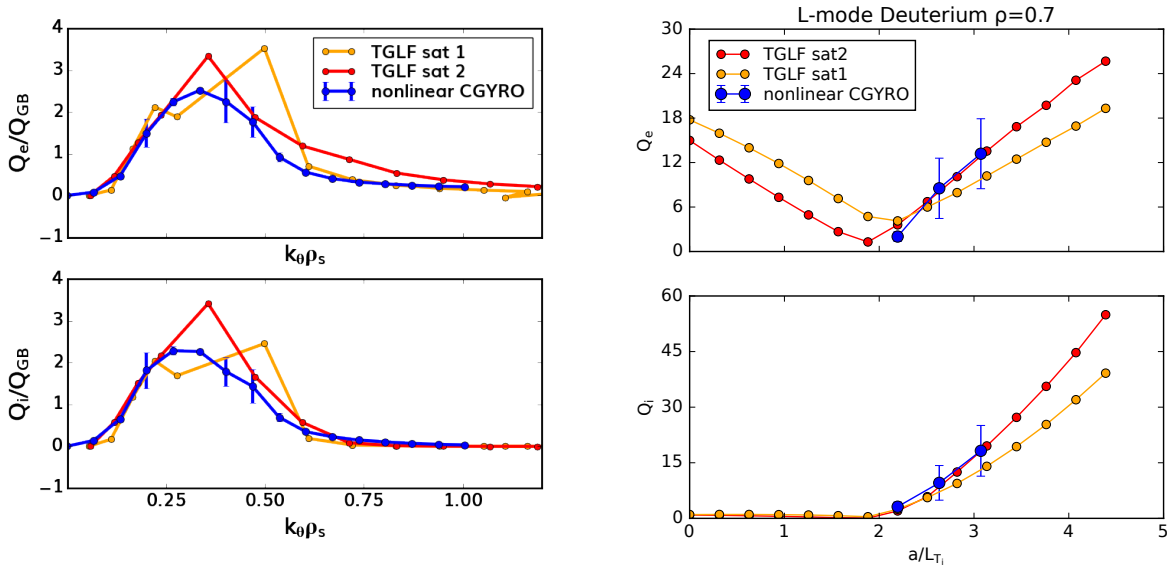

Figure 4.10: A benchmark test of nonlinear CGYRO predictions (blue) in comparison to the TGLF saturation rule 1 and 2 models (orange and red). The left panel shows the heat flux spectra from all three simulations versus normalized poloidal wavenumber $k_\theta \rho_s$. The right panel shows the integrated heat flux predictions while scanning the normalized ion temperature gradient a/L_{T_i}. Results demonstrate CGYRO predictions consistent more with TGLF saturation rule 2.

included 3 plasma species: electrons, hydrogenic ions (deuterium or hydrogen), and carbon impurities. All simulations were generated from the deuterium experimental case 171486.

CGYRO scans at ρ=0.9 in the plasma edge reproduced both D electron and ion heat fluxes as shown in blue circles on Fig. 4.11 at the (deuterium) experimental conditions. Single changes to CGYRO of m_i and $n_{C^{6+}}$ (yellow and purple respectively) indicated the presence of two isotope effects: one from main ion dilution (similar to the findings at ρ=0.7 shown in Fig. 4.9) and another from intrinsic m_i changes. Changing both m_i and $n_{C^{6+}}$ (shown in red) allowed matching the observed electron thermal flux in hydrogen, and a near match of the ion thermal flux. Electron non-adiabaticity was determined as the likely origin of the m_i mass effect by modifying the parallel electron response time [4, 5]. In simulations imposing hydrogen main ion mass (red and yellow dots), re-scaling the parallel electron response time to its deuterium value ($\sqrt{2}$) nearly accounted for the difference in heat fluxes with changing m_i in gyro-Bohm heat flux units (Q/Q_{GBi}). This can be seen in Fig. 4.11 with the $\star$ simulations (yellow $\rightarrow m_H$, red $\rightarrow m_H + n_{C^{6+}}$), which are converted from gyro-Bohm to exp heat flux units using Q_{GBD} (not Q_{GBH}) for direct comparison to deuterium counterparts (purple and blue).

These same simulations were then scanned with respect to effective ion charge Z_{eff} to determine if a heat flux trend similar to that observed in Fig. 4.5 is predicted by nonlinear gyrokinetics. Z_{eff} is varied in these simulations taking care to maintain both density and density gradient quasi-neutral. The solid red symbols illustrate simulations where the main ion mass was changed from deuterium to hydrogen. Note that this results in a 15% increase in heat flux in experimental units [W/cm^2] and 50% increase in gyro-Bohm normalized units at nearly all Z_{eff} values. For both deuterium and hydrogen simulations, increasing Z_{eff} is found to lower both the turbulent ion and electron heat fluxes. The same star simulations shown previously with parallel electron response time rescaled by $\sqrt{2}$ are found to observe deuterium levels of heat transport in gyro-Bohm normalized units.

These edge ρ=0.9 nonlinear gyrokinetic simulations imply that the origin of the heat transport isotope effect between our discharges is approximately 85% due to natural changes

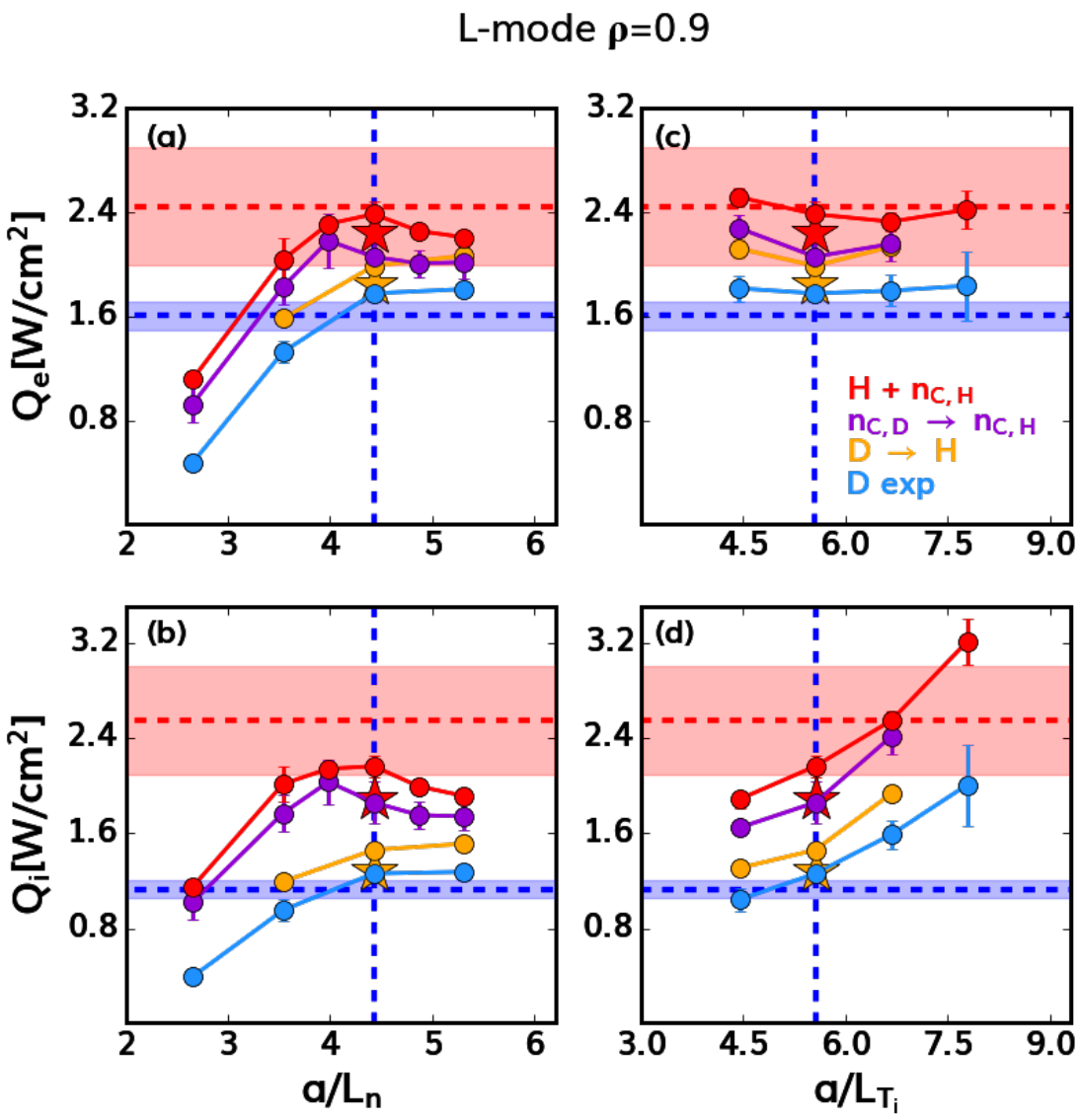

Figure 4.11: Nonlinear CGYRO simulations at ρ=0.9 around deuterium experimental gradients (blue vertical lines). Panels (a,c) show electron heat flux, and (b,d) ion heat flux. Panels (a,b) illustrate a density length scale scan, and (c,d) a T_i gradient scan. Horizontal lines with shaded region indicate the power balance heat fluxes and uncertainty (blue → D, red →H). Yellow and red ⋆ symbols illustrate simulations with hydrogen main ion mass and parallel electron response time rescaled to deuterium values.

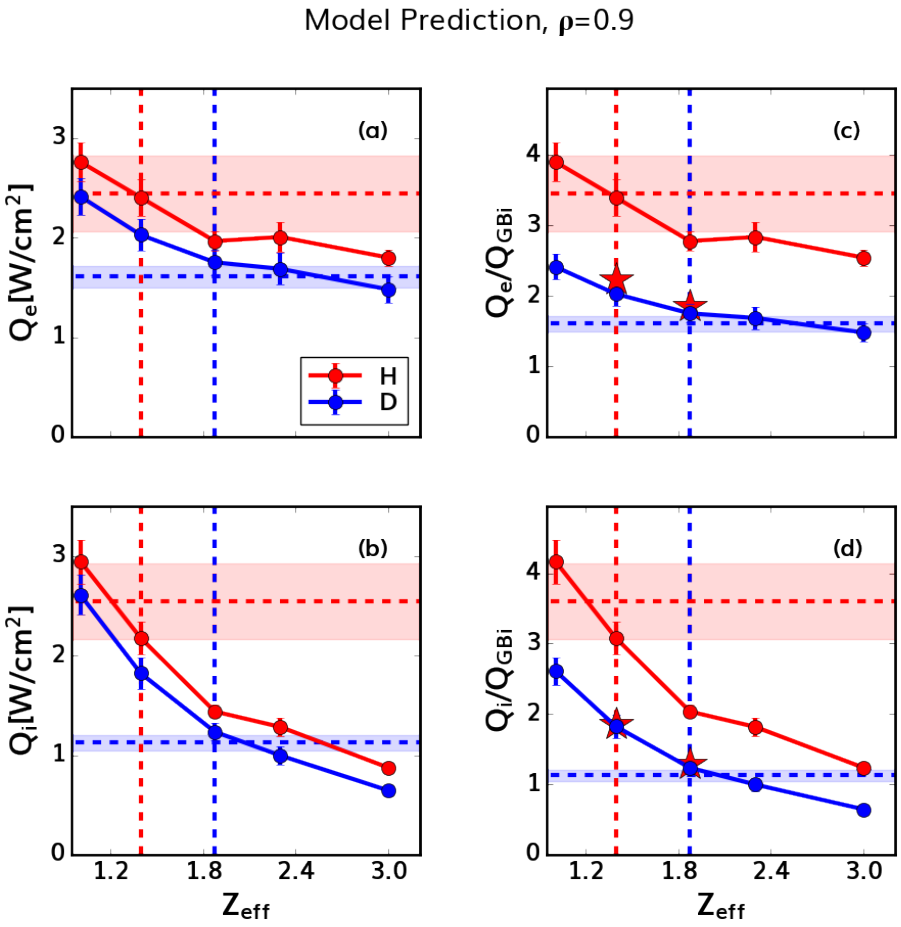

Figure 4.12: Nonlinear CGYRO simulations at ρ=0.9 with deuterium (blue) and hydrogen (red) main ions. Left/right columns indicate electron (top) and ion (bot) heat flux in W/cm^2 (gyro-Bohm heat flux units) vs Z_{eff}. Vertical (horizontal) lines indicate deuterium and hydrogen experimental Z_{eff} (heat fluxes).

in Z_{eff}, and 15% due to intrinsic main mass effects, here from electron non-adiabaticity analogous to previous simulations by Belli [4, 5]. The successful flux-matching of these simulations at the experimental plasma gradients gave confidence to push even further into the plasma edge, in the relatively untested shear layer region at ρ=0.95.

Shear layer simulations, at ρ=0.95, were found to be consistent with TRANSP power balance ion and electron heat fluxes when the normalized ion and electron temperature gradients (a/L_{T_i} and a/L_{T_e}) were increased by 2.66 and 1.66 above their experimental values respectively. Such large deviations away from experimental gradients are consistent however with profile measurements at the neighboring minor radius location, ρ=0.96. Therefore, such gradient discrepancies could be explained by small inaccuracies in flux mapping or profile fitting errors in the sensitive steep gradient edge region of the plasma. The flux matching condition was found while setting $a/L_{T_e} = a/L_{T_i}$ when changing the temperature gradients, holding all else fixed. This temperature gradient equality assumption was used to minimize the number of nonlinear CGYRO simulations necessary for finding a near flux matching condition, and is based on the experimental observation of nearly equal partition of electron and ion heat fluxes from TRANSP simulations. The left-hand panels of Fig. 4.13 show the effective temperature gradient scan produced when attempting to flux match CGYRO simulations to experimental power balance results. In the figure, the solid closed circles show nonlinear CGYRO simulations with deuterium and hydrogen main ions in blue and red respectively. The shown hydrogen simulations, in addition to having a changed main ion mass, have the deuterium carbon density profile replaced with the hydrogen experimental profiles ($n_{C,D} \rightarrow n_{C,H}$) and the hydrogen $\vec{E} \times \vec{B}$ shearing rate as simulation inputs. The dashed horizontal lines indicate the power balance heat fluxes. The black arrow indicates the simulations using the experimental temperature gradients, without enforcing $a/L_{T_e} = a/L_{T_i}$. Both the hydrogen and deuterium simulations are nearly flux matched with $a/L_T \approx 12$. The corresponding linear CGYRO eigenvalue spectra of these hydrogen and deuterium simulations are shown on the right-hand side of Fig. 4.13 for the reader's reference. Note in particular how the hydrogen simulation's peak growth rate is slightly higher compared to

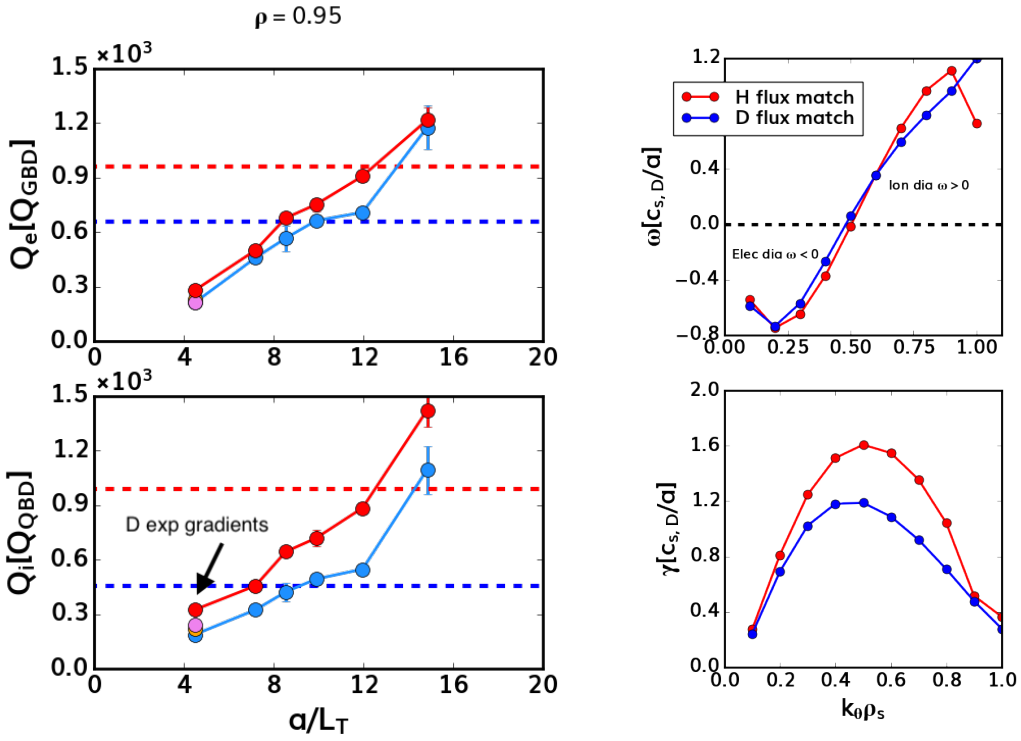

Figure 4.13: Nonlinear CGYRO simulations at ρ=0.95 vs the normalized temperature gradient a/L_T. The upper and lower panels show the electron and ion heat fluxes in deuterium gyroBohm normalized heat flux units. Deuterium simulations are shown as closed blue circles, while red show hydrogen counterparts with $n_{C,D} \rightarrow n_{C,H}$ and hydrogen $\vec{E} \times \vec{B}$ shearing rates. The horizontal dashed lines show the TRANSP power balance inferred heat fluxes.

deuterium, with the poloidal wavenumber $k_\theta \rho_s$ of maximum growth rate additionally being up-shifted.

These flux matched solutions, by scanning the $\vec{E} \times \vec{B}$ shear around experimental values, were found to have noticeable $\vec{E} \times \vec{B}$ shear stabilization of turbulence, shown in Fig. 4.14 by the solid lines. Altering the simulations by changing the main ion mass from deuterium to hydrogen, shown in yellow, is found to noticeably increase the ion and electron heat fluxes particularly at high shearing rates. Changing only the plasma Z_{eff}, using the experimental hydrogen n_C profile (in purple), instead was found to only affect the ion heat flux channel, particularly at low shearing rates. Changing both the simulation Z_{eff} and hydrogen isotope (in red) was found to be additive, increasing both ion and electron heat fluxes at both low

and high shearing rates. These scans indicated 2 distinct isotope effects at play within the shear layer: one due to main ion mass and one due to main ion dilution. The intrinsic main ion mass effect, contrary to results found at ρ=0.9, was determined to not originate from electron non-adiabaticity. Normalizing the $\vec{E} \times \vec{B}$ shearing rate by the maximum linear growth rate from linear CGYRO, was found to bring simulations with differing main ions but identical Z_{eff} into coincidence (blue with yellow, and purple with red). Such a scaling is consistent with the previously documented Garcia effect [32]: more effective $\vec{E} \times \vec{B}$ stabilization with heavier main ions due to the mass dependent shear stabilization criteria: $\gamma_{\vec{E}\times\vec{B}}/\gamma_{linear} \propto c_{s,i}/a \propto 1/\sqrt{m_i}$.

These shear layer ρ=0.95 nonlinear CGYRO simulations imply, similar to both ρ=0.7 & 0.9 results, that there is a noticeable heat transport isotope effect from the natural differences in carbon dilution between isotopes. This effect however is nearly equal to an intrinsic main ion effect, here from mass dependent $\vec{E} \times \vec{B}$ shear stabilization. The two combined comprise the total shear layer isotope heat transport effect. These simulations therefore appear to suggest that the main ion dilution heat transport isotope effect is dominant in the core, and diminishing in strength as one on goes closer to the plasma edge and separatrix regions. Therefore, it is an open question if the main ion dilution heat transport effect is directly linked to the L-H transition isotope effect. DIII-D hydrogen experiments intentionally seeding more carbon than sputtered intrinsically, discussed in chapter 7, attempts to test this research question in detail. In short, it is found that while the carbon content changes control the heat transport isotope effects observed, they are not casually linked to the isotopic L-H power threshold effects seen.

The successful flux matching of L-mode core, edge, and shear layer CGYRO simulations have enabled novel isotopic comparisons of experimental turbulence measurements to simulations, which will be discussed in further detail in Chapter 5. Detailed inspection of the raw fluctuation contributions to ion and electron heat flux in flux-matched simulations indicated similar density and temperature spectra vs. $k_\theta \rho_s$ between isotopes, but higher ($\approx$2) velocity fluctuations in hydrogen simulations compared to deuterium. The ρ=0.7, 0.9, & 0.95 flux

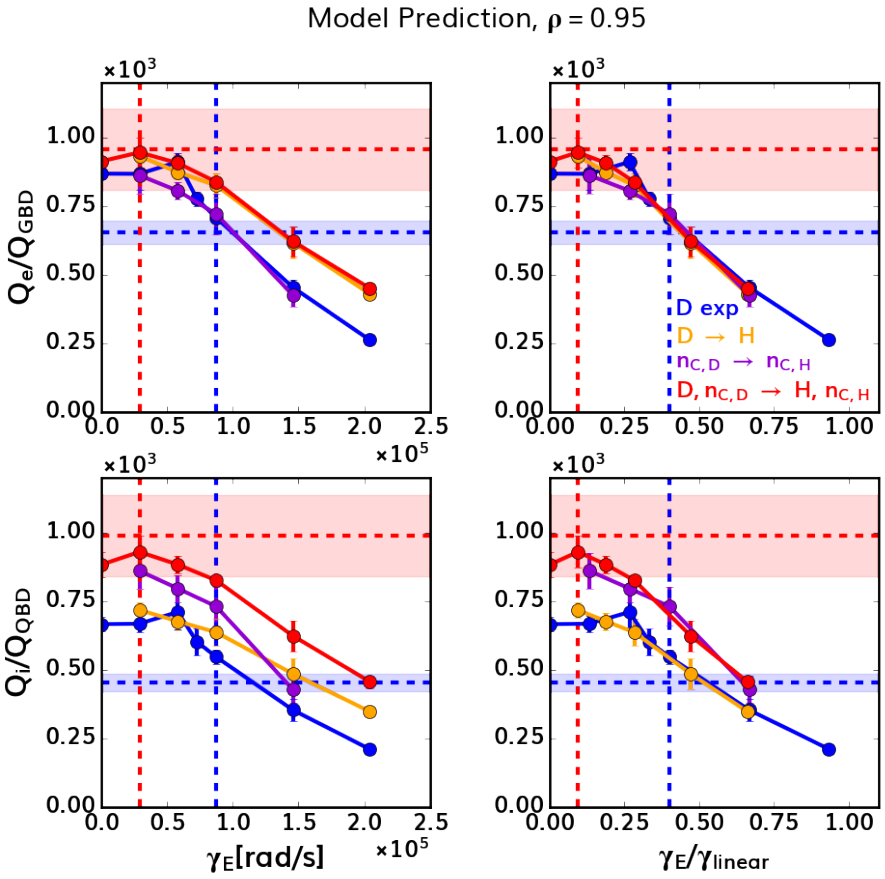

Figure 4.14: Nonlinear CGYRO simulations at ρ=0.95 vs $\vec{E} \times \vec{B}$ shearing rate. Left/right column indicates electron (top) and ion (bot) heat flux vs $\vec{E} \times \vec{B}$ shearing rate in [rad/s] and normalized by the maximum CGYRO linear growth rate γ_{linear} vs. $k_\theta \rho_s$ respectively. Vertical (horizontal) lines indicate deuterium and hydrogen experimental shearing rates (heat fluxes).

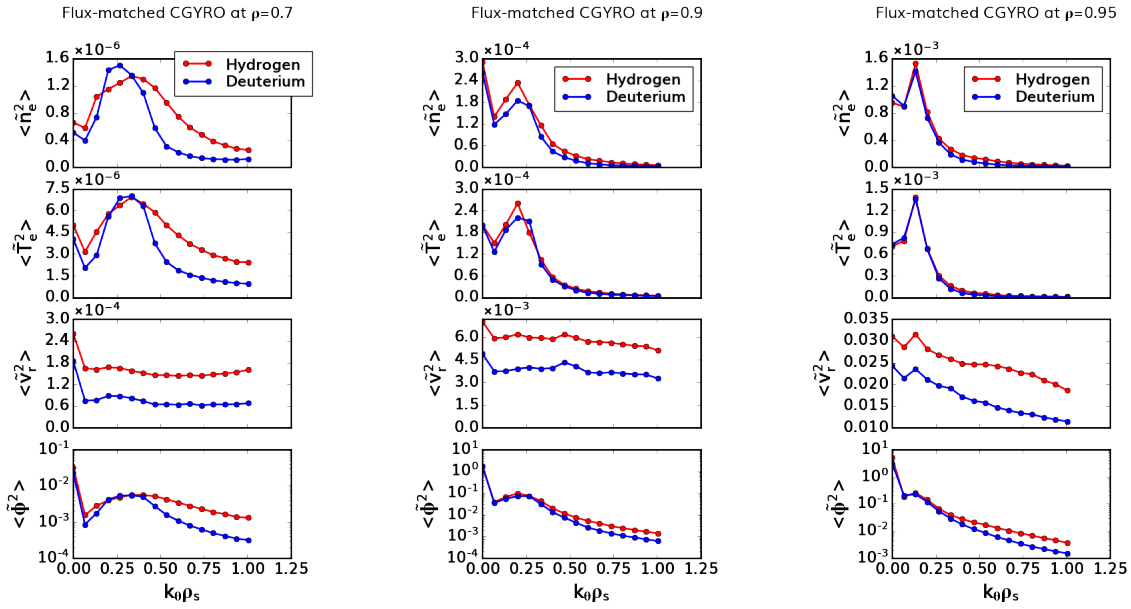

Figure 4.15: Turbulence fluctuation results from flux-matched nonlinear CGYRO simulations at ρ=0.7, 0.9, & 0.95 in the left, center, and right columns respectively. In all columns, flux matched hydrogen (deuterium) simulations are shown in red (blue) vs. normalized poloidal wavenumber $k_\theta \rho_s$.

matched hydrogen and deuterium cases are shown in Figure 4.15 in the left, center, and right respectively to illustrate these differences. Recall the electrostatic turbulent heat flux equation:

$$Q_j = \frac{3}{2} P_j \left\langle \frac{\tilde{T}_j}{T_j} \tilde{v}_r + \frac{\tilde{n}_j}{n_j} \tilde{v}_r \right\rangle \tag{4.3}$$

Such results suggest that the difference in observed heat fluxes between isotopes is primarily due to different velocity fluctuations ($\tilde{v}_r \approx \tilde{E}_\theta / B_\phi = -k_\theta \tilde{\phi} / B_\phi$) and not temperature or density fluctuations. Therefore, careful interpretation of DIII-D turbulence diagnostic signals, which measure $\tilde{n}$ (BES) and $\tilde{T}_e$ (CECE) is necessary. It is noteworthy that the $\tilde{v}_r$ difference between isotopes predicted by nonlinear CGYRO matches velocimetry results shown in Fig. 6.11(a) in Chapter 6.

4.4 Summary

In this thesis chapter, experimental analyses were detailed which have helped uncover the potential origins of the isotopic L-mode heat transport effects routinely seen in tokamak experiments. Using a large L-H transition database, trends in the power threshold P_{LH} with respect to the unit-less plasma physics parameters of ion collisionality ν_i^* and effective ion charge Z_{eff} were identified. In the low collisionality limit, the power threshold was found to decrease with increasing Z_{eff}. In the opposing high collisionality limit, the isotope effect appears to be negligible with increasing Z_{eff} correlating with increased P_{LH}. Detailed study of 2 dimensionally matched hydrogen and deuterium discharges just before L-H transition in the low collisionality limit uncovered similar profiles at L-H transition despite substantially larger input power in hydrogen compared to deuterium. Using both gyrofluid and gyrokinetic simulations, the origin of these heat flux differences between experiments was uncovered. In the plasma core at ρ=0.7, it is entirely attributable to natural differences in carbon content between isotopes changing the ion temperature critical gradient. In the plasma edge at ρ=0.9, heat flux differences are still mostly attributable to differences in Z_{eff} between species, with minor contributions from electron non-adiabaticity intrinsic main ion mass effects. In the plasma shear layer at ρ=0.95, heat transport differences originate equally from natural changes in carbon content between species, and an intrinsic main ion mass effect resulting from mass dependently $\vec{E} \times \vec{B}$ shear stabilization of turbulence. Inspection of raw turbulent fluctuations from these gyrokinetic simulations uncovered radial velocity fluctuation $\tilde{v}_r$ differences between isotopes, not temperature $\tilde{T}$ or density $\tilde{n}$ fluctuation changes, being the primary driver of heat and particle transport differences. These heat transport isotope effects controlled by Z_{eff} are found in Chapter 7 to be merely correlated with the L-H power threshold, and not the controlling isotope behavior responsible for the L-H power threshold differences between isotopes. These flux-matched CGYRO simulations additionally layed the groundwork for results discussed in Chapter 5, comparing turbulent fluctuation measurements to nonlinear simulations.

CHAPTER 5

Comparison of measured turbulent fluctuations with CGYRO simulations

In this thesis chapter, turbulent density and electron temperature fluctuations from the Beam Emission Spectroscopy (BES) and Correlation Electron Cyclotron Emission (CECE) systems will be compared to predictions from nonlinear gyrokinetic simulations using the code CGYRO. The research presented here has been submitted to the Nuclear Fusion scientific journal. The salient investigations discussed include descriptions of the experimental isotopic measurements, synthetic diagnostic procedures used, and comparisons between experiment and simulation. Key conclusions include verification of synthetic diagnostic predictions as consistent with experimental measurements for both hydrogen and deuterium, and identification of differences in $\vec{E} \times \vec{B}$ rotation between H and D experiments in the plasma edge.

5.1 BES measurements

The Beam Emission Spectroscopy diagnostic, as previously described in thesis Chapter 3, measures Doppler shifted Balmer-α light intensity fluctuations resulting from impact excitation emission of injected neutral beam particles. These light intensity fluctuations, to lowest order, are proportional to local plasma density fluctuations. The measured signals, using the formalism of equation 3.5, can be cross-correlated to compute a cross-power spectrum such as those shown on the upper panels of Fig. 5.1. The left and right panels illustrate the experimental BES cross-power spectra for the reference hydrogen and deuterium discharges studied

in Chapter 4. The frequency integrated cross-powers of these measurements, shown in red and blue in the lower panel of Fig. 5.1 versus normalized minor radius coordinate ρ, illustrate that either discharge observes similar normalized light intensity fluctuations in L-mode just prior to L-H transition. It is these fluctuation measurements which will be compared to nonlinear gyrokinetic simulation results. The following section will discuss in detail the synthetic diagnostic techniques used to convert the CGYRO gyrokinetic predictions shown in Fig. 4.15 to quantities suitable for comparison to experimental BES measurements.

5.2 Synthetic BES from CGYRO

The conversion of gyrokinetic simulation density fluctuations into synthetic BES signals suitable for comparison to experimental measurements is based on the atomic and collisional processes which generate neutral beam Balmer-α emission. The light intensity of Balmer-α emission, and its associated fluctuations, are caused by m=3 atomic state hydrogen or deuterium spontaneously decaying into the m=2 lower energy state, emitting a photon in the process. The quantity m (not n) is used for atomic state principle quantum number to avoid confusion with densities represented with the symbol n. As a result, the emission intensity fluctuations can be shown to obey equation (6) in [31]:

$$\frac{\tilde{I}}{I} = \frac{\tilde{n}_{m=3}}{n_{m=3}} \frac{1}{1 + \frac{R_{depop}^{m \to x}}{n_{m=3} A_{m=3}}} \tag{5.1}$$

Above, $\tilde{I}/I$ are the normalized Balmer-α light intensity fluctuations, $\tilde{n}_{m=3}/n_{m=3}$ are the normalized m=3 atomic density fluctuations, $R_{depop}^{m \to x}$=$n_m(\sum_x(n_e\langle\sigma v\rangle_{e,exc}^{m \to x} + n_i\langle\sigma v\rangle_{i,exc}^{m \to x} + n_c\langle\sigma v\rangle_{c,exc}^{m \to x})$ is the total depopulating rate of the m=3 atomic state in units of $cm^{-3}s^{-1}$, and $A_{m=3} = \sum A_{m \to x}$ is the total spontaneous emission Einstein coefficient from the m=3 atomic state in units of s^{-1}. The quantities $n_e\langle\sigma v\rangle_{e,exc}^{m \to x}$, $n_i\langle\sigma v\rangle_{i,exc}^{m \to x}$, and $n_c\langle\sigma v\rangle_{c,exc}^{m \to x}$ represent the electron, main ion, and carbon impurity impact excitation rates which depopulate the m=3 state to some new state x. The rates are constructed from the respec-

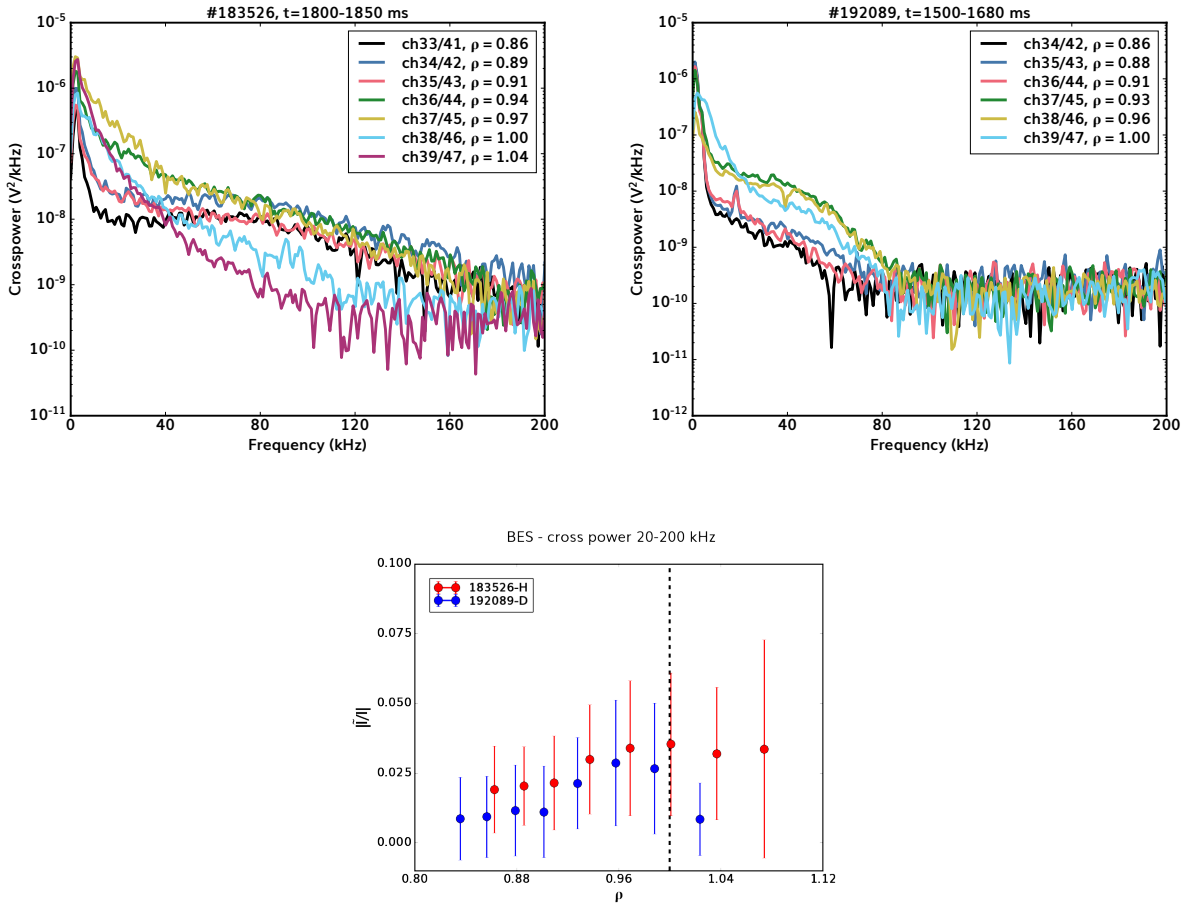

Figure 5.1: Hydrogen and deuterium reference plasma BES measured cross-power spectra vs. frequency on the left and right respectively. Color mapping indicates the vertical channel pairs and associated normalized minor radius locations for each turbulence measurement with respect to flux coordindate $\rho = \sqrt{\psi_N}$. Lower panel: Normalized and frequency integrated BES cross-power spectra for hydrogen (red) and deuterium (blue) from 20-200 kHz vs. normalized minor radius coordinate ρ.

tive local plasma species densities n_{sp} and Maxwell distribution averaged rate coefficients $\langle\sigma v\rangle_{sp,exc} = \int dv f_{sp}(|v_{sp} - v_{NB}|)\sigma(|v_{sp} - v_{NB}|)|v_{sp} - v_{NB}|$. $\sigma(v)$ represent the atomic cross sections, and $f_{sp}(v) = (\frac{m_{sp}}{2\pi T_{sp}})^{3/2} 4\pi v^2 \ exp(-\frac{m_{sp}v^2}{2T_{sp}})$ is the species specific Maxwellian distribution function with temperature T_{sp}. Based on equation 5.1, it is desired to find an expression which relates the atomic density $n_{m=3}$ to measurable plasma quantities n_e, n_i, and n_c. To find such an expression, we consider the collisional radiative modeling formalism. In this theoretical framework, the population rate of change of the atomic state $n_{m=3}$ obeys the following expressions:

$$\frac{dn_m}{dt} = R_{tot,m} = R^{x\to m}_{exc} + R^{x\to m}_{dexc} + R^{x\to m}_{spon} - R^{m\to\infty}_{ion} - R^{m}_{cx} - R^{m\to x}_{depop} - A_m n_m \tag{5.2}$$

$$R^{x\to m}_{exc} = \sum_{x<m} n_i n_x \langle\sigma v\rangle^{x\to m}_{i,exc} + n_e n_x \langle\sigma v\rangle^{x\to m}_{e,exc} + n_c n_x \langle\sigma v\rangle^{x\to m}_{c,exc} + n_i n_x \langle\sigma v\rangle^{x\to m}_{i,cx} \tag{5.3}$$

$$R^{x\to m}_{dexc} = \sum_{x>m} n_i n_x \langle\sigma v\rangle^{x\to m}_{i,dexc} + n_e n_x \langle\sigma v\rangle^{x\to m}_{e,dexc} + n_c n_x \langle\sigma v\rangle^{x\to m}_{c,dexc} + n_i n_x \langle\sigma v\rangle^{x\to m}_{i,cx} \tag{5.4}$$

$$R^{x\to m}_{spon} = \sum_{x>m} n_x A_{x\to m} \tag{5.5}$$

$$R^{m\to\infty}_{ion} = n_m (n_i \langle\sigma v\rangle^{m\to\infty}_{i,ion} + n_e \langle\sigma v\rangle^{m\to\infty}_{e,ion} + n_c \langle\sigma v\rangle^{m\to\infty}_{c,ion}) \tag{5.6}$$

$$R^{m}_{cx} = n_m n_c \langle\sigma v\rangle^{m}_{c,cx} \tag{5.7}$$

$$\frac{\tilde{n}_m}{\tau_m} = \frac{\tilde{n}_m}{n_m} R_{tot,m} = \tilde{R}^{x\to m}_{exc} = R^{x\to m}_{e,ex}\frac{\tilde{n}_e}{n_e} + R^{x\to m}_{i,ex}\frac{\tilde{n}_i}{n_e}\frac{n_e}{n_i} + R^{x\to m}_{c,ex}\frac{\tilde{n}_c}{n_e}\frac{n_e}{n_c} \tag{5.8}$$

Equation 5.2 is the rate balancing equation traditionally solved in collisional radiative modeling. Each term in the equation represents an atomic interaction which may either populate or depopulate the m=3 atomic state. Note that the finite lifetime of the excited state causes the neutral to radiate at a different spatial location than where it is excited, potentially an issue for the accuracy of modeling in the steep gradient pedestal region, since quantities in the above equations are functions of spatial position. Explicitly this model neglects such spatial position issues, however more advanced FIDASIM [44] simulations can be performed to account for such distortions. Equation 5.3 represents reactions by background plasma ions or electrons which can impact-excite beam atoms from some lower state x into the

desired m=3 state. Similarly, equation 5.4 represents reactions which can impact-de-excite neutral beam atoms from a higher state x into m=3. Equation 5.5 represents populating the m=3 state due to spontaneous emission from some higher state x. Equation 5.6 captures reactions between background neutral beam atoms and plasma ions or electrons which are sufficiently energetic to ionize the beam atom from the m=3 state. The reaction captured by 5.7 is a depopulating reaction which occurs when the incident neutral beam atom in the m=3 state and a fully stripped carbon atom undergo charge exchange. To find a relation between the perturbed atomic m=3 density and plasma densities, we evaluate the perturbed version of 5.2 to the lowest order including only impact excitation reactions, resulting in equation 5.8. With some slight rearranging, equations 5.8 and 5.1 can be combined to relate Balmer-α light intensity fluctuations directly to plasma density perturbations:

$$\frac{\tilde{I}}{I} = \frac{1}{1 + \frac{R^{m\to x}_{depop}}{n_{m=3}A_{m=3}}} \left(\frac{R^{x\to m}_{e,ex}}{R_{tot,m}} \frac{\tilde{n}_e}{n_e} + \frac{R^{x\to m}_{i,ex}}{R_{tot,m}} \frac{\tilde{n}_i}{n_e} \frac{n_e}{n_i} + \frac{R^{x\to m}_{c,ex}}{R_{tot,m}} \frac{\tilde{n}_c}{n_e} \frac{n_e}{n_c} \right) \tag{5.9}$$

This expression, although complex and requiring detailed information involving atomic rate coefficients, is calculable by leveraging the code FIDASIM [44]. FIDASIM is a comprehensive collisional radiative modeling code commonly used for tokamak fast ion physics. These FIDASIM simulations were used to extract the weights for translating gyrokinetic density fluctuation predictions such as those shown in Fig. 4.15 into signals suitable for comparison to experimental BES measurements. The weights calculated for the reference deuterium and hydrogen plasmas analyzed in Chapter 4 were: $w_{e,H} = 0.77, w_{i,H} = 1.15, w_{c,H} = 3.79$ and $w_{e,D} = 1.48, w_{i,D} = 1.85, w_{c,D} = 1.109$.

With these weights, the density fluctuation predictions from the code CGYRO were translated to light intensity changes. The framework used for converting the simulation density fluctuation results, enumerated by the bi-normal and radial wavenumbers k_y and k_x, to real space was that established by White and Holland [113, 47]. The steps in the conversion process were as follows:

1. Convert from the plasma to lab frame: $\tilde{n}^{PF}_{sp}(k_y, k_x, t) = \tilde{n}^{LF}_{sp}(k_y, k_x, t)e^{-in_{tor}(\omega_0 t + \Delta\phi)}$

2. Convert from spectral to real space using a 2D spatial FFT: $\tilde{n}_{sp}^{LF}(k_y, k_x, t) \rightarrow \tilde{n}_{sp}^{LF}(R, Z, t)$

3. Calculate the synthetic diagnostic signal using the experimental point spread function: $\tilde{n}_{sp}^{LF,syn}(t) = \int\int dRdZ\ \tilde{n}_{sp}^{LF}(R, Z, t) \times PSF(R - R_0, Z - Z - Z_0)$

4. Compute the temporal FFT of the synthetic signal: $\tilde{n}_{sp}^{LF,syn}(t) \rightarrow \tilde{n}_{sp}^{LF,syn}(f)$

A more detailed description of the synthetic diagnostic protocols used may be found in reference [47]. Above, the quantity $n_{tor} = \frac{k_y r}{q\rho^*}$ is the toroidal mode spacing, $\omega_0 = -qcE_r/rB$ is the equilibrium Doppler shift due to $\vec{E} \times \vec{B}$ rotation, t is the simulation time, k_y is the binormal wavenumber, and k_x is the radial wavenumber respectively. The point spread functions $PSF(R, Z)$ used in the hydrogen and deuterium synthetic diagnostics for the $\rho = 0.9$ simulations may be found in Fig. 5.2 as black contours for the reader's reference. Note how the point spread function for hydrogen is slightly larger than deuterium counterparts, as a result of hydrogen plasma's naturally greater beam smearing [31]. The electron density fluctuations from the Doppler shifted and real space mapped CGYRO simulations are shown additionally on Fig. 5.2. The color mapping indicates over-densities (red) and under-densities (blue) resultant from turbulence predictions. The convolution of these two quantities, the point spread functions and CGYRO fluctuation predictions, were used to generate an array of vertically separated synthetic diagnostic signals $\tilde{n}_{sp}^{LF,syn}(t)$. The FFT of these signals, identical to cross-power and cross-phase analysis described in equations 3.5 and 3.6, were used to compute synthetic cross-correlation spectra vs. frequency.

It is these synthetic diagnostic based cross-power and cross-phase spectra, weighted according to equation 5.9, that are suitable for comparison to experimental BES measurements. Such a comparison of synthetic turbulence measurements with experimental data, shown in Fig. 5.3, are found to be in good agreement. The light blue lines (orange) represent the experimental deuterium (hydrogen) BES data, and the dark blue (red) data represent the synthetic BES generated from flux matched CGYRO simulations. The frequency was converted from the plasma frame (CGYRO) to the laboratory frame using $v_{\vec{E}\times\vec{B}}$ rotation derived from E_r measurements, discussed in detail in Chapter 6. The deuterium experimental BES

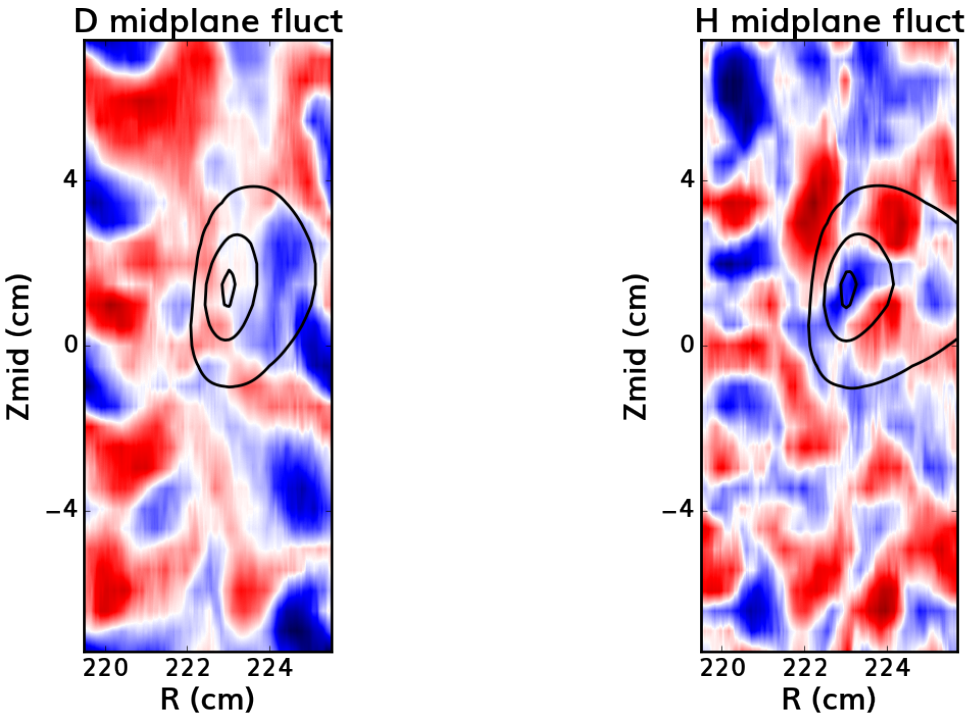

Figure 5.2: Left (right) column: deuterium (hydrogen) synthetic BES point spread function and CGYRO turbulence results over-plotted. Black contours indicate the 10%, 50%, and 90% contours of the experimental point spread function. Color mapping indicates CGYRO results mapped to real-space, with over-densities illustrated in red, and under-densities in blue.

data illustrated in light blue in Fig. 5.3, was observed with a malfunctioning, partially closed shutter. Potentially as a result, ρ=0.9 synthetic and experimental deuterium comparisons illustrate matching cross-power and cross-phase shapes, but an unknown factor of 3 deviation in cross-power magnitude. BES channels closer to the core observed similarly low cross-power signals compared to hydrogen counterparts, viewable in Fig 5.1. Channels closer to the edge, such as the shear layer channels at ρ=0.96 did not appear to be affected. Specifically, no appreciable cross-power magnitude difference between synthetic signals and experiment was observed. Deviations between the experimental measurements and synthetic diagnostics at low frequencies are believed to be due to beam emission noise, illustrated in Fig. 5.3 as the gray shaded region below 20 kHz. Such comparisons between turbulence measurements and predictions from flux-matched simulations highlight the accuracy of flux-tube CGYRO simulations in describing turbulence, particularly in the relatively untested plasma edge. Furthermore, recall how the raw simulation predictions from CGYRO, shown in Fig. 4.15, indicate nearly identical $\tilde{n}/n$ between hydrogen and deuterium simulations. These observations, in conjunction with noticeable differences in the experimental frequency resolved spectra, highlight the importance of synthetic modeling which accurately accounts for indirect isotope effects originating from differences in atomic rate coefficients, beam smearing, and Doppler shift between experiments. For both edge and shear layer simulations, very noticeable differences in E_r profiles and $\vec{E} \times \vec{B}$ rotation were found to specifically be responsible for the differing cross-phase and cross-power spectra shapes between isotopes. The success of these comparisons motivated additional benchmarking of gyrokinetic simulation results, now against temperature fluctuations from the Correlation Electron Cyclotron Emission diagnostic.

5.3 CECE measurements

The Correlation Electron Cyclotron Emission (CECE) diagnostic, as mentioned in thesis Chapter 3, measures fluctuations in electron cyclotron harmonic radiation emitted by the plasma. The emission is typically, but not always, radiated as a perfect blackbody, making

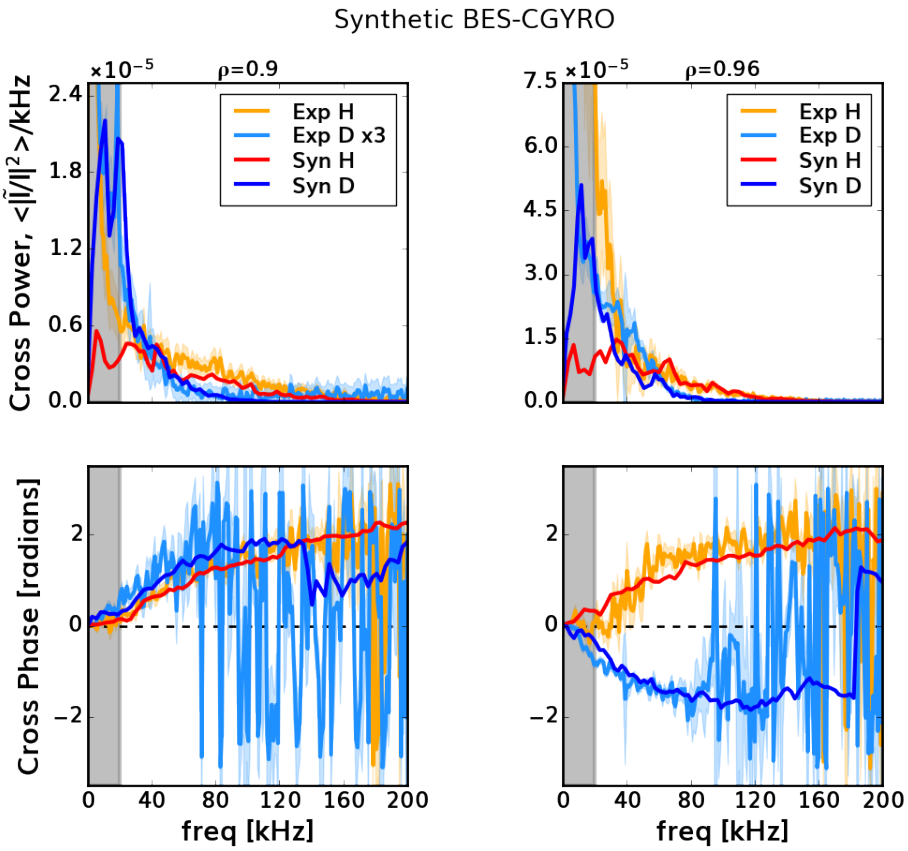

Figure 5.3: BES cross power + cross phase spectra in kHz for 4 experimental cases. The left (right) column illustrates data from the plasma edge (shear layer). Light blue (orange) lines illustrate exp. deuterium (hydrogen) data, and dark blue (red) indicates the synthetic BES derived from flux matched CGYRO simulations. Gray area indicates potential beam noise contamination region.

the emission intensity proportional to the local electron temperature at the location monitored. For the hydrogen and deuterium discharges studied in detail in Chapter 4, the CECE diagnostic was tuned to observe 2nd harmonic X-mode radiation. Using the formalism of equation 3.14, the CECE power spectra were calculated for these reference discharges. Results of such calculations are shown in Fig. 5.4. Note how, similar to both BES density fluctuation and raw CGYRO turbulent fluctuation predictions in Fig. 5.1 and Fig. 4.15 respectively, the frequency integrated turbulent amplitudes are remarkably similar between hydrogen (red) and deuterium (blue) discharges prior to L-H transition. Important to note on this figure is the dashed gray vertical line, which indicates where the 2nd harmonic X-mode optical depth parameter τ_{X2} drops below 4. The optical depth (the integral of the photon absorption coefficient α over the path length exiting the plasma ds), $\tau = \int \alpha \, ds$, is a quantity normally used to qualify whether a plasma is optically thick (black body) or optically gray, with τ_{crit}=4. Below this critical opacity value, the electron cyclotron emission radiation fluctuation measurements are no longer due purely to electron temperature changes, but also electron density changes. As a result, more complex modeling of electron cyclotron emission spectra is necessary in the edge regions with $\rho > 0.72$ prior to comparing to experimental CECE measurements. The vertical dashed black line in Fig. 5.4 illustrates the last closed flux surface.

5.4 Synthetic CECE from CGYRO

Similar to the Beam Emission Spectroscopy synthetic turbulence diagnostic described previously, the Correlation Electron Cyclotron Emission synthetic diagnostic converts raw turbulent fluctuation predictions to signals suitable for comparison to experiment based on the diagnostics's innate EC measurement properties. Namely, the details of electron cyclotron emission discussed in detail in thesis Chapter 3 were used by Rempel to derive the following CECE fluctuation formula, accounting for contributions from both temperature and density fluctuations in the emission process [75]:

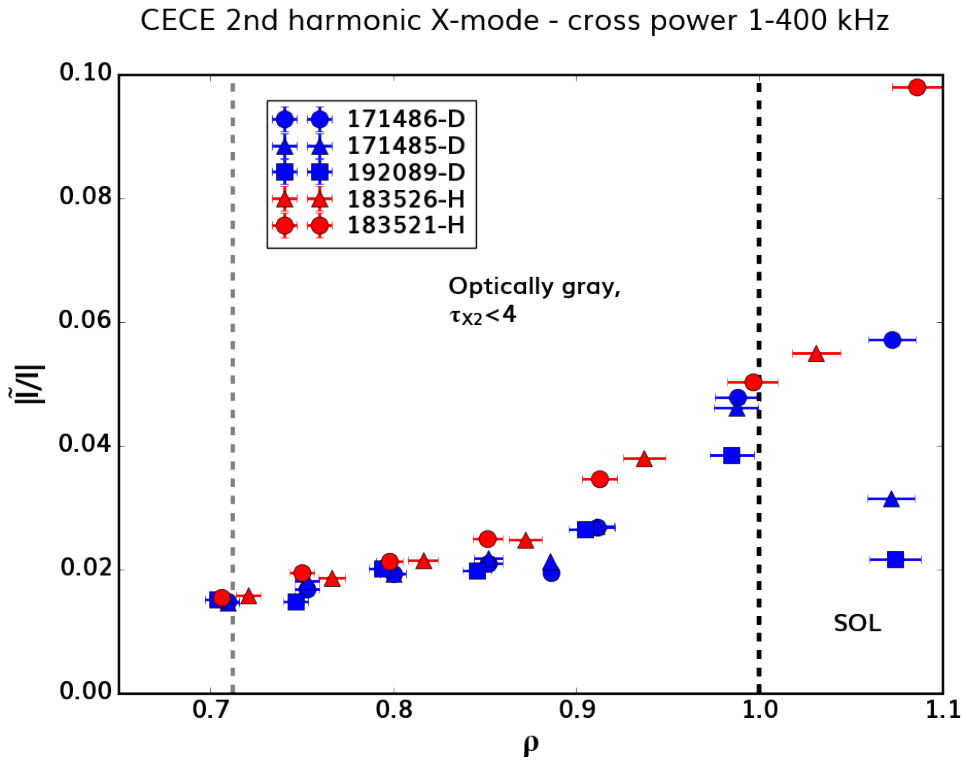

Figure 5.4: Hydrogen and deuterium reference plasma frequency integrated and normalized cross-power CECE spectra (1-400 kHz) in red and blue respectively vs. normalized minor radius coordinate $\rho = \sqrt{\psi_N}$. The vertical gray dashed line indicates the region where $\tau_{X2} < 4$, indicating optically gray emission. The vertical black dashed line shows the last closed flux surface, beyond which is the open field line plasma region.

$$\frac{<\tilde{I}_1\tilde{I}_2^*>}{I^2} = (1-e^{-\tau})^2\left((1+A_2)^2(\frac{\tilde{T}_e}{T_e})^2 + (A_2\frac{\tilde{n}_e}{n_e})^2 + 2(1+A_2)A_2\frac{Re[\langle\tilde{T}_e\tilde{n}_e\rangle]}{T_e n_e}\right) \tag{5.10}$$

$$A_2(\tau,\chi) = \frac{\tau\, e^{-\tau}}{1-e^{-\tau}}\left(1-\chi\frac{1-e^{-\tau}}{1-\chi e^{-\tau}}\right) \tag{5.11}$$

The quantity χ represents the effective wall reflectivity, measured previously in DIII-D as χ=0.76 [2]. The latter two additive terms of equation 5.10 are negligibly small when optically thick. Under optically gray conditions however, these additional $\tilde{n}_e$ terms can be significant contributors to the total CECE signal. With this analytic formula, electron temperature and density fluctuations from the CGYRO simulations shown in Chapter 4 were translated into electron cyclotron radiation fluctuation predictions. The framework used for converting the CGYRO simulation results into actual synthetic signals was nearly identical to that employed for synthetic BES modeling mentioned previously, pioneered by White and Holland [113, 47]:

1. Convert from the plasma to lab frame: $\tilde{T}_{sp}^{PF}(k_y,k_x,t) = \tilde{T}_{sp}^{LF}(k_y,k_x,t)e^{-in_{tor}(\omega_0 t+\Delta\phi)}$
2. Convert from spectral to real space using a 2D spatial FFT: $\tilde{T}_{sp}^{LF}(k_y,k_x,t) \rightarrow \tilde{T}_{sp}^{LF}(R,Z,t)$
3. Calculate the synthetic diagnostic signal using the experimental point spread function: $\tilde{T}_{sp}^{LF,syn}(t) = \int\int dRdZ\ \tilde{T}_{sp}^{LF}(R,Z,t)\times PSF(R-R_0,Z-Z-Z_0)$
4. Compute the temporal FFT of the synthetic signal: $\tilde{T}_{sp}^{LF,syn}(t) \rightarrow \tilde{T}_{sp}^{LF,syn}(f)$

Dissimilar to BES synthetic diagnostics, the point spread functions are isotope independent and controlled by CECE optical geometry and emission layer physics. Identical to calculations performed by White, the CECE point spread function was modeled as a bi-directional Gaussian in the Z and R directions with the following expression:

$$PSF(R-R_0,Z-Z_0) = \frac{exp(-8\left(\frac{(R-R_0)^2}{L_r^2}+\frac{(Z-Z_0)^2}{L_z^2}\right))}{\int\int dRdZ\ exp(-8\left(\frac{(R-R_0)^2}{L_r^2}+\frac{(Z-Z_0)^2}{L_z^2}\right))} \tag{5.12}$$

The vertical and radial spot sizes L_z and L_r for these point spread function calculations represent the $1/e^2$ CECE point spread diameters, extracted from vacuum beam propagation and emission layer thickness modeling respectively.

The vertical spot size was determined from the $1/e^2$ beam power diameter of CECE optical geometry modeling, illustrated in Fig. 5.5. The shown optical modeling simulations were completed in great thanks to graduate student Quinn Pratt and Dr. Guiding Wang. The upper panel shows the beam-waist radius calculated going from the detector to the measurement locations, calculated using Gaussian beam optics. The solid black vertical lines represent the lenses and mirrors the radiation must pass through prior to detection. The dashed light and dark blue lines illustrate the location of the CECE channels needed for synthetic diagnostic modeling. At the intersection of these dashed lines and solid green contour is the beam-waist radii w_r for CECE1 and CECE5, measured as 2.6 cm and 3.1 cm respectively. These modeling results were used to infer the vertical spot sizes via $L_z = 2w_r$. The vertical black dashed line illustrates the tokamak R=0 axis. The lower panel indicates the beam's radius of curvature as it propagates from the measurement locations towards the detector.

The radial spot sizes L_r were determined, in part, from the natural line-width of the CECE emission layers. The natural line-widths were calculated from the experimentally inferred emissivity profiles, identical to procedures used by White for past DIII-D CECE modeling [113]. Recall that the optical depth $\tau = \int \alpha \; ds$ is the integral of the absorption coefficient α over the optical path exiting the plasma ds. From these same quantities, the plasma emissivity can be calculated from the following expression, using the nomenclature of Bornatici [10]:

$$j(s) = I_{BB}(s)\alpha(s)e^{-\tau(s)} \tag{5.13}$$

Above the emission intensity is given by equation 3.9 from Chapter 3. The natural emission

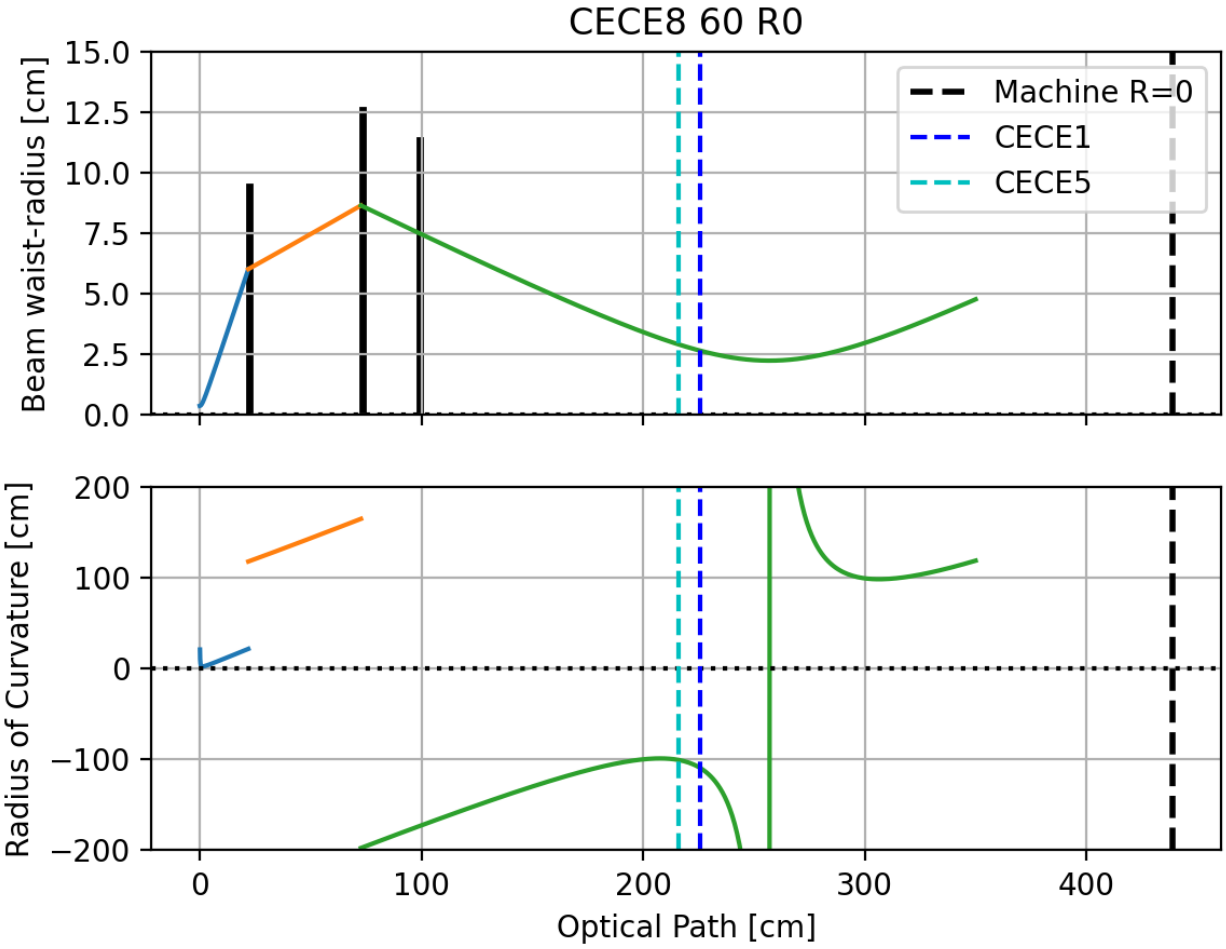

Figure 5.5: Gaussian beam optical modeling of the Correlation Electron Cyclotron Emission system. The upper panel illustrates the calculated beam-waist, and the lower panel indicates the beam radius of curvature vs. optical path from the detector. The solid black lines indicate optical components along the beam trajectory, and the dashed blue lines show the spatial positions of the modeled CECE channels. The dashed black line indicates the tokamak machine axis.

linewidths are extracted from the integral of emissivity along the optical path $\int j(s)ds$, as the radial distance between where 95% and 5% of the emitted radiation escapes towards the detector. These natural linewidths however, only capture the plasma emission at a fixed frequency. The CECE diagnostic however uses an IF bandpass filter of approximately 150 MHz, introducing a small but non-negligible radial extent in measurement volume in addition to natural linewidth effects. Taking the superposition of 2 emissivity profiles displaced by this bandpass frequency range, we infer the radial spot size L_r. Fig. 5.6 illustrates the results of such natural linewidth and IF bandpass superposition calculations for CECE channels CECE1 and CECE5 for the reader's review. The blue curves illustrate the integral of plasma emissivity inferred using equation 5.13 vs. plasma major radius R for channels CECE1 and CECE5. The yellow curves show a similar calculation, frequency displaced by 150 MHz to illustrate the bandpass frequency effects. The dashed lines show the 95% and 5% power levels of the superposition of the two emissivity profiles, with the distance between the two regions enumerated by the horizontal red line. The radial spot sizes L_r extracted from the plasma emissivity analyses described were 2.11 cm and 1.39 cm for channels CECE1 and CECE5 respectively. The bandpass contributions to this spot size for either channel was on the order of 0.3 cm.

Using these calculated vertical and radial spot sizes in conjunction with equation 5.12, nonlinear CGYRO turbulence predictions were used to produce synthetic signals for a radially separated pair of channels suitable for comparison to experimental CECE measurements. These channel pairs were then cross-correlated according to equation 5.10 to generate synthetic CECE signals. Comparisons between synthetic predictions and turbulence measurements are illustrated in Fig. 5.7 with experimental deuterium (hydrogen) CECE in light blue (orange), and synthetic CECE signals extracted from flux matching deuterium (hydrogen) CGYRO simulations in dark blue (red). Similar to the synthetic BES analysis, the CGYRO simulations were transformed from the plasma to laboratory frame using the $v_{E\times B}$ rotation from measurements. For the shown simulations, there is an unknown factor of 2 discrepancy in synthetic and experimental cross power, previously observed in flux matched CGYRO

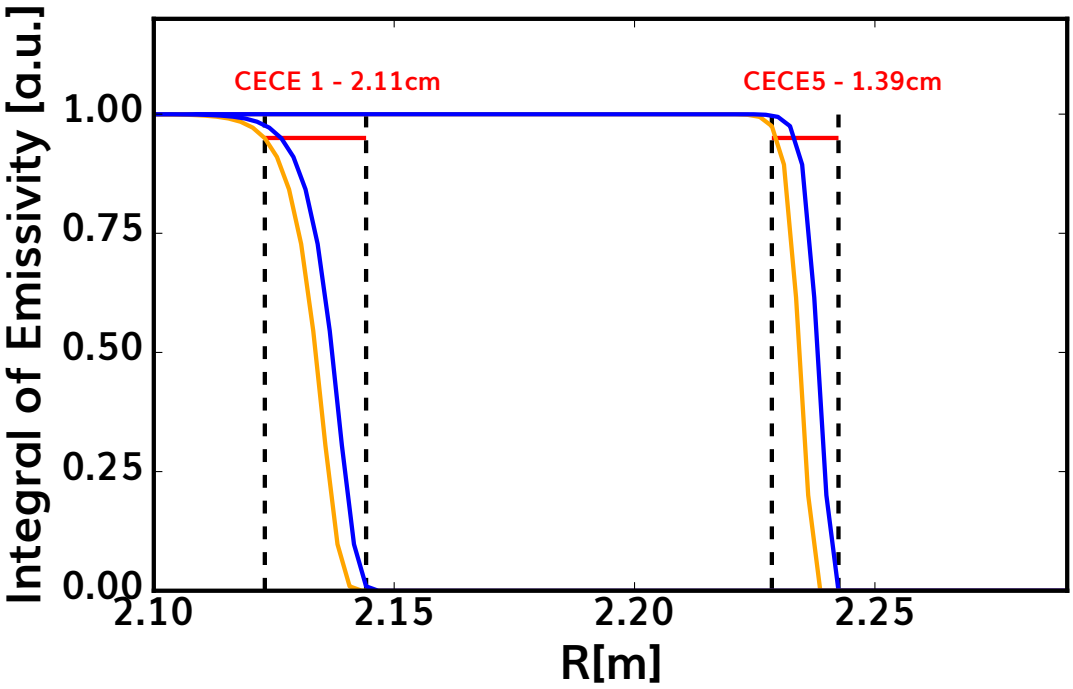

Figure 5.6: The experimental linewidth calculations determined from $\int j(s)ds$ for CECE channels CECE1 and CECE5. The y-axis illustrates the normalized plasma emissivity vs. major radius R. The blue contours show the natural linewidth calculations at a single frequency, and yellow contours show similar calculations shifted by the bandpass filter frequency difference 150 MHz. The dashed vertical lines indicate the superposition of these two profiles at the 95% and 5% escaping power levels. The red horizontal lines show the inferred radial spot sizes L_r.

DIII-D H-mode simulations by Howard [50]. For the optically thick outer core ($\rho = 0.7$), the principal contributor to the CECE signals is electron temperature fluctuations. The edge ρ=0.9 simulations however are optically gray, with contributions from both the $\tilde{T}_e$ term (gray shaded region, 83%) and $\tilde{T}_e\tilde{n}_e$ cross term (purple shaded region, 17%). The $\tilde{n}_e$ terms contributed negligibly to the total edge CECE signals. Such comparisons uphold the standard notion that under optically gray conditions, care must be taken when interpreting CECE signals. Similar to synthetic BES signals, synthetic CECE measurements observe distinct frequency spectra between hydrogen and deuterium despite remarkably similar raw $\tilde{T}_e$ and $\tilde{n}_e$ spectra from nonlinear CGYRO. These differing spectral shapes are likewise found to be due to substantially different $\vec{E}\times\vec{B}$ rotation measurements between isotopes. These comparisons illustrate possibly the first multi-channel transport verification of nonlinear CGYRO predictions against experiment in the plasma edge, and help support the nonlinear gyrokinetic simulation results documented in Chapter 4.

5.5 Summary

Over the course of this thesis chapter, turbulent density and temperature fluctuation measurements from the Beam Emission Spectroscopy (BES) and Correlation Electron Cyclotron Emission (CECE) diagnostics were quantitatively compared to predictions from flux-matched nonlinear CGYRO simulations. These comparisons involved translating raw density and temperature fluctuation spectra shown in Fig. 4.15 into synthetic turbulence signals, and indicate good agreement between experiment and synthetic predictions. Beam Emission Spectroscopy predictions were modeled to include isotopic effects related to collisional excitation rates, beam smearing, and $\vec{E}\times\vec{B}$ rotation differences between hydrogen and deuterium. CECE measurements were modeled and extended to account for $\vec{E}\times\vec{B}$ rotation differences between isotopes similar to BES, and density fluctuations under optically gray emission conditions. These turbulence measurement comparisons demonstrated quantitative verification of CGYRO simulations, which predict that differences in radial velocity fluctuations $\tilde{v}_r$, and not $\tilde{n}$ or $\tilde{T}$, are responsible for observed heat flux differences between hydrogen and deuterium

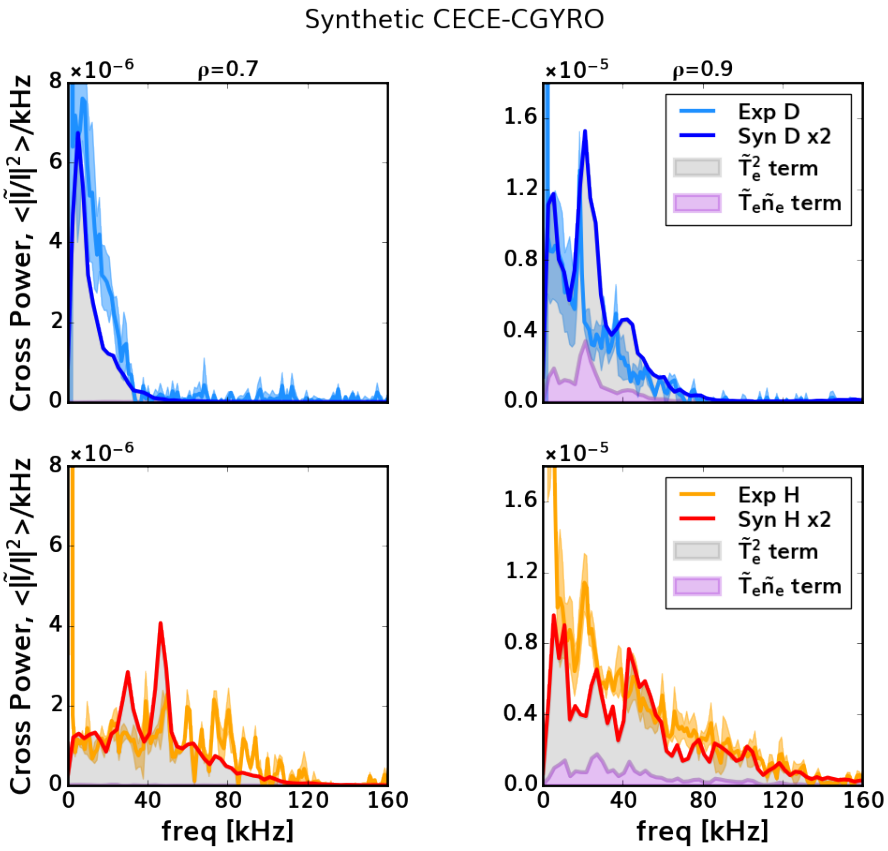

Figure 5.7: CECE cross power spectrum in kHz of 4 experimental cases. The left (right) column illustrates data from the outer core (edge). Light blue (orange) data illustrates exp. deuterium (hydrogen) data, and dark blue (red) indicates the synthetic CECE derived from flux match CGYRO. Gray and purple regions illustrate distinct contributions to the CECE signal.

experiments. Additionally such turbulence predictions, which show substantial differences in $\vec{E} \times \vec{B}$ rotation between hydrogen and deuterium, motivated a much deeper investigation into the edge radial electric field profiles just prior to L-H transition, undertaken in thesis Chapter 6.

CHAPTER 6

Observation of isotope L-mode radial electric field effects

In this thesis chapter, a radial electric field isotope effect between DIII-D hydrogen and deuterium plasmas is uncovered and investigated. The material presented has been submitted to the Nuclear Fusion scientific journal. The sections below outline the paper's key findings. The investigations include using 4 independent radial electric field measurements to confirm profile differences between hydrogen and deuterium, detailed extensively in thesis Appendix D for brevity. Based on these observations, the origin of the isotopic radial electric field differences are investigated from two perspectives: open field line effects and closed field line effects. The open field line effects are studied using Langmuir probe measurements and modeling using the tokamak multi-fluid edge plasma transport code UEDGE. Key findings are that higher outer strike point T_e in hydrogen are potentially responsible for radial electric field changes. These temperature differences between isotopes, from UEDGE modeling, are found to be correlated with a shift in the density profile just inside the separatrix ($\rho \approx 0.97 - 1.0$). Divertor-specific changes between species appear insufficient for explaining the observed temperature and electric field differences. In the closed field line region, radial force balance of both main ions and carbon impurities points to poloidal rotation differences being correlated to electric field changes between isotopes. Using poloidal momentum balance analysis, these poloidal rotation differences are identified as due to Reynolds stress changes. Reynolds stress differences between hydrogen and deuterium in turn are found to be consistent with $\vec{E} \times \vec{B}$ eddy tilting calculations, pointing to the potentially self-generated nature of the poloidal rotation and radial electric field inside the closed field line region.

6.1 Radial Electric Field Measurements

Differences in the edge radial electric fields between hydrogen and deuterium were discovered using a combination of 4 independent DIII-D diagnostics: impurity charge exchange recombination spectroscopy (impCER), Doppler BackScattering (DBS), Beam Emission Spectroscopy (BES), and Langmuir probe (LP) analysis. A shortened description of each method is included below, with further details included in Appendix D. The radial electric field is determined from the impCER diagnostic by solving the radial impurity ion force balance equality:

$$E_r = \frac{1}{Z_i n_i e}\nabla p_i + v_{tor,i}B_{pol} - v_{pol,i}B_{tor} \tag{6.1}$$

Above v_{pol} is the poloidal rotation, v_{tor} is the toroidal rotation ($v_{tor,i} = R\Omega_i$), and ∇p_i is the impurity ion pressure gradient. Results from impurity force balance analysis are shown in Fig. 6.1(h) as the solid lines. Doppler Back-Scattering determines the radial electric field instead by measuring the Doppler shift of microwaves refracted and back-scattered off density fluctuations in the plasma. The observed Doppler shift, in the lab frame, is a convolution of the bulk plasma rotation ($v_{E\times B}$) and the turbulent phase velocity:

$$v_{doppler} = v_{E\times B} + \tilde{v}_{ph} \tag{6.2}$$

The turbulence phase velocity is often found to be small or a nearly constant offset. The DBS measurements are illustrated in Fig. 6.1(h) as closed circles. Fixed Langmuir probe measurements are additionally used to determine the scrape off layer radial electric field by mapping outer strike point (OSP) Langmuir probe measurements to the outboard midplane (OMP). The outboard midplane space potential was calculated using the following expressions, which were derived from parallel momentum balance considerations in the open magnetic field line region [97, 26, 99, 71]:

$$\phi_{s,omp} = \phi_{fl} + \phi_{sheath,fl} + \phi_{\Delta T_e} \tag{6.3}$$

$$\phi_{sheath,fl} = \log_e \left(\frac{2m_i}{m_e \pi} \right) T_{e,osp}/2 \tag{6.4}$$

$$\phi_{\Delta T_e} = 0.71 + \frac{\log_e(2)}{\log_e(T_{e,omp}/T_{e,osp})} (T_{e,omp} - T_{e,osp}) \tag{6.5}$$

Above ϕ_{fl} and $T_{e,osp}$ represent the floating potential and electron temperature at the outer strike point measured by Langmuir probes, shown in Fig. 6.2(f,h). High field side counterparts may be viewed in Fig. 6.2(e,g) respectively. $T_{e,omp}$ represents the outboard mid-plane electron temperature, determined by power balance along the field lines [59, 98]. $\phi_{\Delta T_e}$ and $\phi_{sheath,fl}$ represent the thermal force and sheath contributions to the outboard midplane electric potential. A more complete explanation of the origin of these electric potential equations may be found in Appendix D for brevity. All Langmuir probe measurements, including both strike point electron densities (n_e), parallel heat fluxes (Q_e), and mid-plane mapped space potentials ($\phi_{s,omp}$) can be found in Fig. 6.2. Note that the higher outboard mid-plane space potential in hydrogen is due to a two times higher $T_{e,osp}$. In Fig. 6.2(j), exponential fits to the space potential data, shown as a solid lines, are used to extract LP E_r profiles. These Langmuir probe inferred scrape off layer E_r profiles are illustrated in Fig. 6.1(h) as the dashed lines, with the value at the separatrix represented as a closed star, and found to be in good consistency with DBS and CER force balance measurements. BES can similarly determine edge E_r by measuring the turbulent eddy time delay between two vertically separated channels. The time delay (τ_d), calculated from the linear slope of the channels' cross-phase vs. frequency relationship, along with vertical channel separation (Δz), can be used to estimate velocity: $v_z = \Delta z/\tau_d = v_{E\times B} + \tilde{v}_{ph}$. Fig. 6.1(h) illustrates BES E_r measurements as solid triangles. Note how all four E_r measurements observe a higher radial electric field in hydrogen compared to deuterium. The origin of this E_r difference between isotopes will be first investigated in the open field line region.

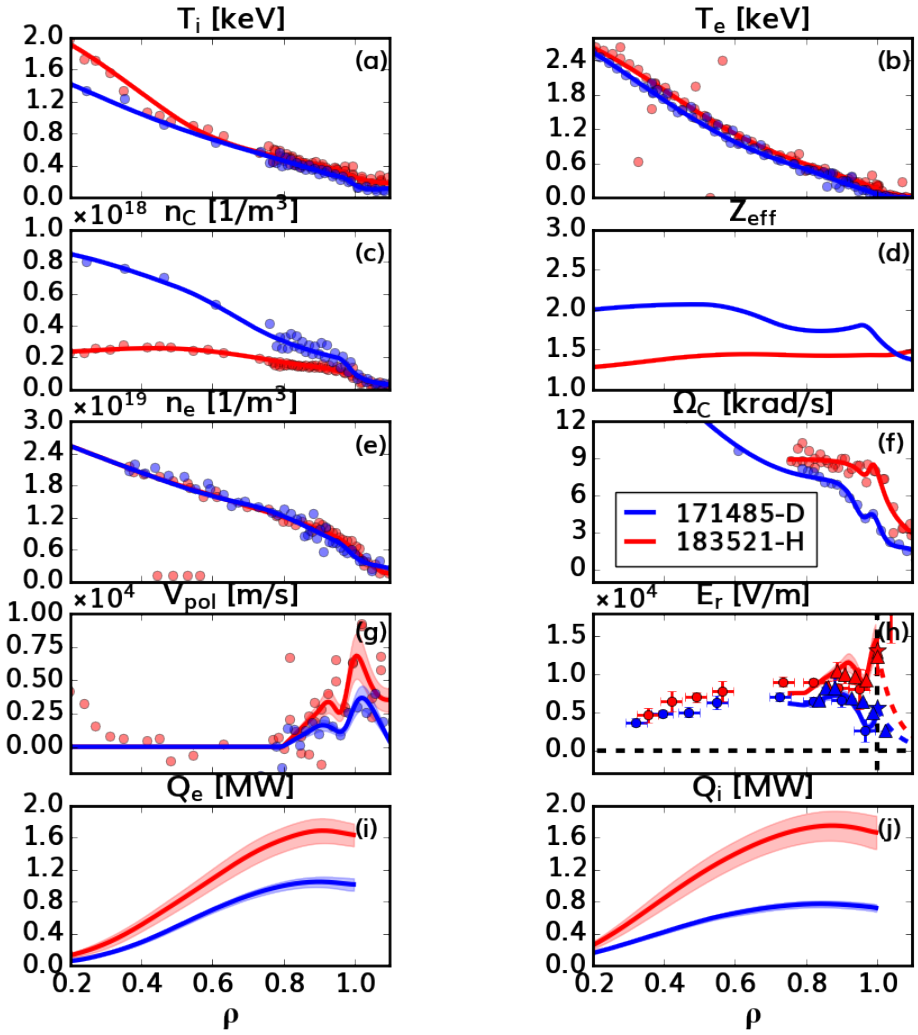

Figure 6.1: Kinetic profile measurements for a deuterium (blue) and hydrogen (red) DIII-D plasma in L-mode before L-H transition vs. ρ, the square root of the normalized toroidal flux $\sqrt{\psi_N}$. Solid lines indicate fits to exp. data, and closed circles indicate raw data. Panels (a), (b), (c), (d), (e), (f), (g), (h), (i), and (j) represent the measured ion temperature, electron temperature, carbon density, Z_{eff}, electron density, carbon toroidal rotation, carbon poloidal rotation, radial electric field, electron heat flux, and ion heat flux profiles respectively.

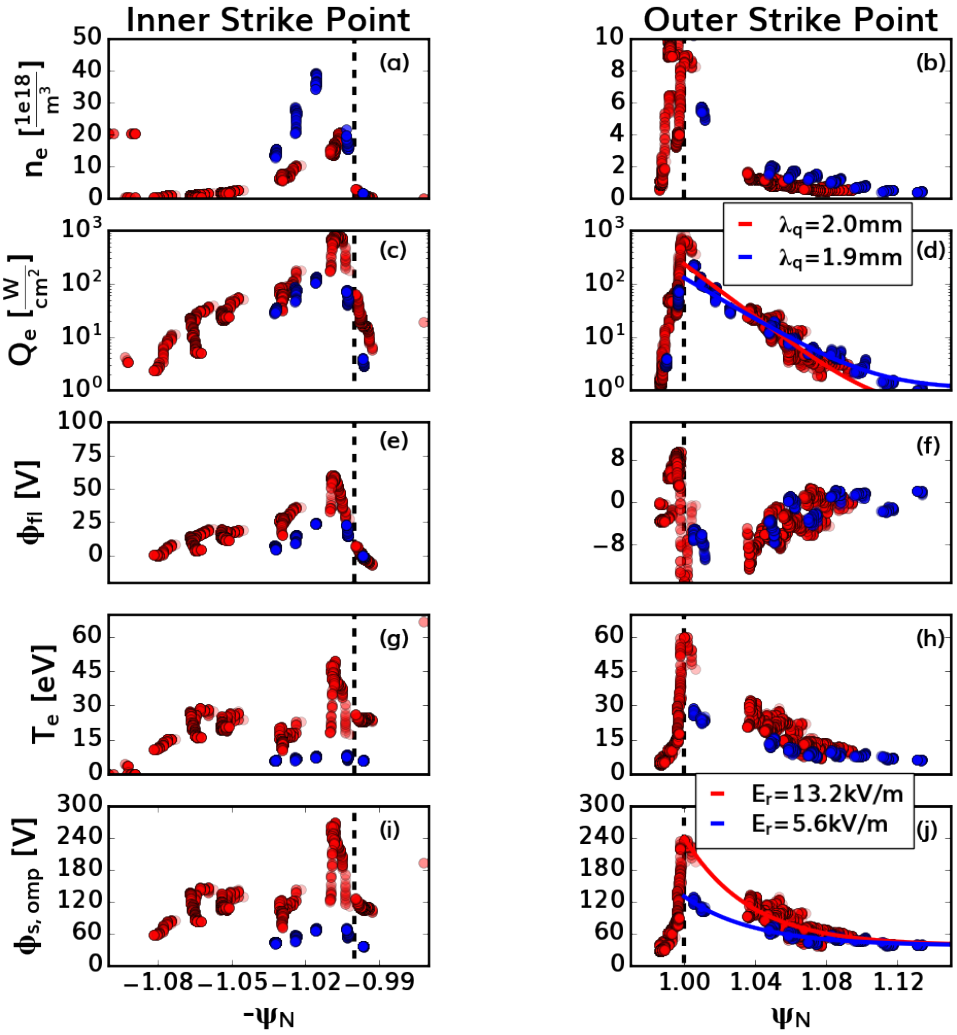

Figure 6.2: Fixed Langmuir probe measurements for D (blue) and H (red) L-mode plasmas before L-H transition. Left/right columns indicate inner/outer strike point data. Solid lines indicate fits used to extract E_r and λ_q values shown in the legends. Panels (a-b), (c-d), (e-f), (g-h), and (i-j) show the strike point electron density, parallel electron heat flux, floating potential, electron temperature, and outboard midplane space potential respectively.

6.2 Explanation 1: open field line region

Focusing on the explanation of the different L-mode radial electric fields between isotopes in the scrape off layer, it is important to consider the roles of neutral particles in dictating plasma conditions. In particular, it has long been suspected, and recently observed by Dr. Ryan Chaban [24] at DIII-D, that changing main ion mass alters the neutral penetration depth. In particular, as one changes from hydrogen $\rightarrow$ deuterium $\rightarrow$ tritium, it is expected that neutral particles incoming from the divertor and main chamber walls will penetrate less deeply before ionizing at a given temperature T_i due to their increasing main ion mass. Observationally, this would result in slight differences in radial profiles between isotopes. More acutely, hydrogen plasmas would be expected to have neutrals which penetrate the furthest in prior to ionization, shifting the electron density profile inwardly. These general theoretical expectations are tested using experimental neutral profile measurements from the DIII-D LLAMA diagnostic.

6.2.1 Neutral density measurements

The Lyman-α measurement apparatus (LLAMA) at the DIII-D tokamak is an ultraviolet spectrometer system which views both the low and high field side approximately 75 cm below the DIII-D tokamak mid-plane. As a result, it measures radial neutral density profiles nearly half-way between the outboard mid-plane and the strike points in ITER similar shape (ISS) configuration. The line-integrated data acquired from the system's cameras of Lyman-α emission at 121 nm are tomographically inverted to infer a local plasma emissivity. Using the measured temperature and density profiles shown in Fig. 6.1, EFIT magnetic equilibrium reconstructions, and known ADAS atomic rate coefficients, the plasma emission profiles are converted into atomic hydrogen/deuterium ionization rate and neutral density profiles. These quantities are extracted from the measured Lyman alpha brightness profile $Br_{L-\alpha}(\rho)$ using the following expressions:

$$n_0 = \frac{4\pi Br_{L-\alpha}}{n_e \ PEC^{exc}_{1\to 2}(T_e, n_e)} \tag{6.6}$$

$$S_{ion} = n_0 \ SDC(T_e, n_e) \tag{6.7}$$

In the above expression, the neutral densities n_0 are related to the Lyman-α brightness by the ADAS Photon Emissivity Coefficient for electron impact excitation from ground to m=2, $PEC^{exc}_{1\to 2}$ [1], which is dependent on the local electron density and temperature of the background plasma. The ionization rate S_{ion} is likewise related to the calculated neutral density n_0, local electron density n_e, and ADAS Effective Ionization Coefficient SDC [1]. The results of these calculations, performed by Dr. Raul Gerru, are illustrated in Fig. 6.3 for hydrogen and deuterium just before L-H transition in red and blue respectively. The upper row shows the inferred neutral particle densities on the high and low fields side on the left and right respectively as solid lines. Over-plotted are the inner and outer Langmuir probe electron density measurements at the strike points shown as closed circles. On the lower row are the LLAMA inferred ionization rates for hydrogen (red) and deuterium (blue). Note-worthily, both Langmuir probe electron density and LLAMA neutral density profiles appear remarkably similar in profile shape.

The neutral density profiles illustrate an in-out density asymmetry, commonly seen in favorable ion ∇B drift directed DIII-D plasmas [77], which is slightly stronger in deuterium compared to hydrogen. Further, an inward shift in the low field side neutral density profile going from deuterium to hydrogen consistent with naive neutral penetration theoretical expectations is observed. The ionization rate, similar to the densities, appear in both hydrogen and deuterium to be stronger on the high field side by almost an order of magnitude. The low field side shift observed from neutral density profile measurements is not seen with the ionization rate measurements, with both deuterium and hydrogen showing a peak ionization rate just inside the closed flux region near $\rho \approx 0.99$. These experimental measurements, together with observations from the fixed Langmuir probe array have allowed for more conclusive statements about differences between isotopes in the L-mode edge and scrape off

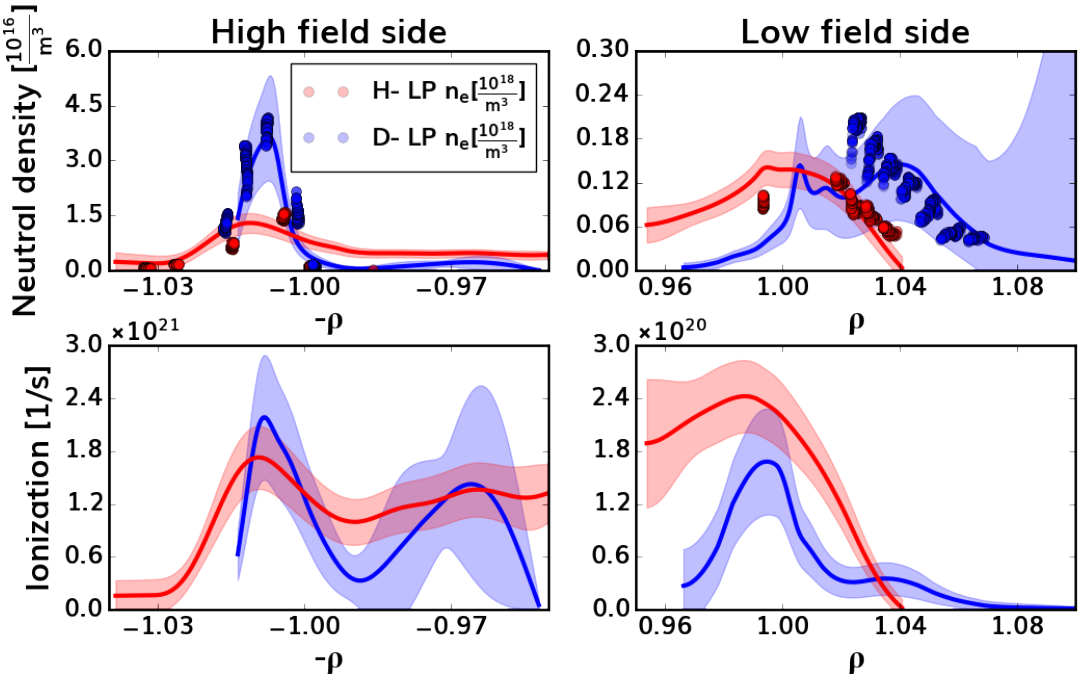

Figure 6.3: Upper row: Lyman Alpha spectroscopy inferred deuterium (blue) and hydrogen (red) neutral density profiles in L-mode before L-H transition vs. ρ on the high (left) and low (right) field side of the tokamak. Solid lines indicate exp. neutral profile data obtained from spectroscopic data, and closed circles indicate scaled Langmuir probe n_e measurements at the inner and outer strike points, illustrating strong coincidence between neutral density and strike point n_e measurements. Lower row: deuterium and hydrogen ionization rate profiles in L-mode on the high (left) and low (right) field sides of the DIII-D tokamak.

layer related the neutral fueling. These observations motivated divertor/open field line fluid simulations using the code UEDGE in an attempt to capture the physics aspects potentially responsible for the observed differences in scrape off layer radial electric field between isotopes.

6.2.2 UEDGE simulations

The goal of this exercise is to determine the origin of the sheath potential differences between hydrogen and deuterium. This was attempted by using the UEDGE code, a fluid based plasma boundary and scrape off layer code commonly used in experimental tokamak research to simulate divertor and mid-plane scrape off layer conditions. The code solves the Braams transport equations in both the parallel and perpendicular direction with respect to the magnetic field [13]. Parallel transport is taken to be classical, while perpendicular transport is assumed to be anomalous and radially varying. In addition to these transport equations, the core plasma density just inside the separatrix at $\psi_N = 0.95$ ($\rho = 0.97$), as well as the ion and electron heat fluxes crossing the seperatrix according to TRANSP are taken as simulation inputs. Following the findings outlined in the neutral density and Langmuir probe sections above, UEDGE simulations were performed for these hydrogen and deuterium experiments to identify the physics origin of the experimental observed sheath potential changes. All UEDGE simulation results shown were performed by, and in great thanks to, Dr. Andreas Holm. Converged UEDGE runs were found for both the hydrogen and deuterium reference cases which matched upstream experimental temperature and density profiles. Recall that UEDGE is a flux-driven simulation code, with adjustable perpendicular particle and heat transport coefficients. By adjusting these degrees of freedom, a match to experimental conditions was found. The transport coefficients needed to match the edge experimental density and temperature profiles are shown in the first row of Fig. 6.4. These transport coefficients were determined using a gradient driven method similar to that documented in reference [22]. On the second row, the UEDGE-predicted ion density and electron temperature profiles for hydrogen (red) and deuterium (blue) are shown as solid lines. In red and blue cross-hairs,

divertor Thomson Scattering data from the respective hydrogen and deuterium reference discharges are illustrated. The Thomson data shown are taken during a long time window prior to L-H transition to improve the signal-to-noise ratio of the data and resolve small differences in edge profiles. Note how Thomson scattering density data illustrate an inward shift in electron density between hydrogen and deuterium plasmas, consistent with Langmuir probe and LLAMA measurements. This shift in the upstream radial profile appears limited to $\psi_N \approx 0.95$ or $\rho \approx 0.97$, and is captured by the UEDGE simulations. No such shift is observed in the Thomson electron temperature data. The hydrogen and deuterium UEDGE particle diffusivities needed to match the experimental profiles are larger in deuterium compared to hydrogen, implying stronger particle losses in deuterium are needed to maintain particle balance. This observation is inconsistent with ionization rate measurements by the LLAMA diagnostic, which show ionization is dominant on the high field side and nearly equal between isotopes. Conversely, the hydrogen UEDGE simulations require a higher electron heat diffusivity compared to deuterium for profile matching, consistent with TRANSP power balance expectations. The UEDGE electron temperature profiles are only moderately able to capture the upstream experimental data for hydrogen and deuterium, which shows a steep gradient region just inside the separatrix. The temperatures at the separatrix for hydrogen and deuterium (T_e = 105, 80 eV) match power balance expectations however, discussed in detail in Appendix D.

These upstream profile matched hydrogen and deuterium UEDGE simulations, by solving the perpendicular and parallel transport equations, also provided predictions of the outer strike point conditions. As a result, comparison of Langmuir probe observations to UEDGE predictions can be made. Recall how the hydrogen plasmas observed a larger peak outer strike point T_e compared to deuterium. This change in strike point temperature increased the sheath potential in hydrogen compared to deuterium, resulting in a higher space potential and radial electric field E_r. The UEDGE simulations previously described captured this experimental trend between isotopes. Results are shown in Fig. 6.5. The left-hand figure illustrates the raw UEDGE predictions as orange and light blue lines for hydrogen and

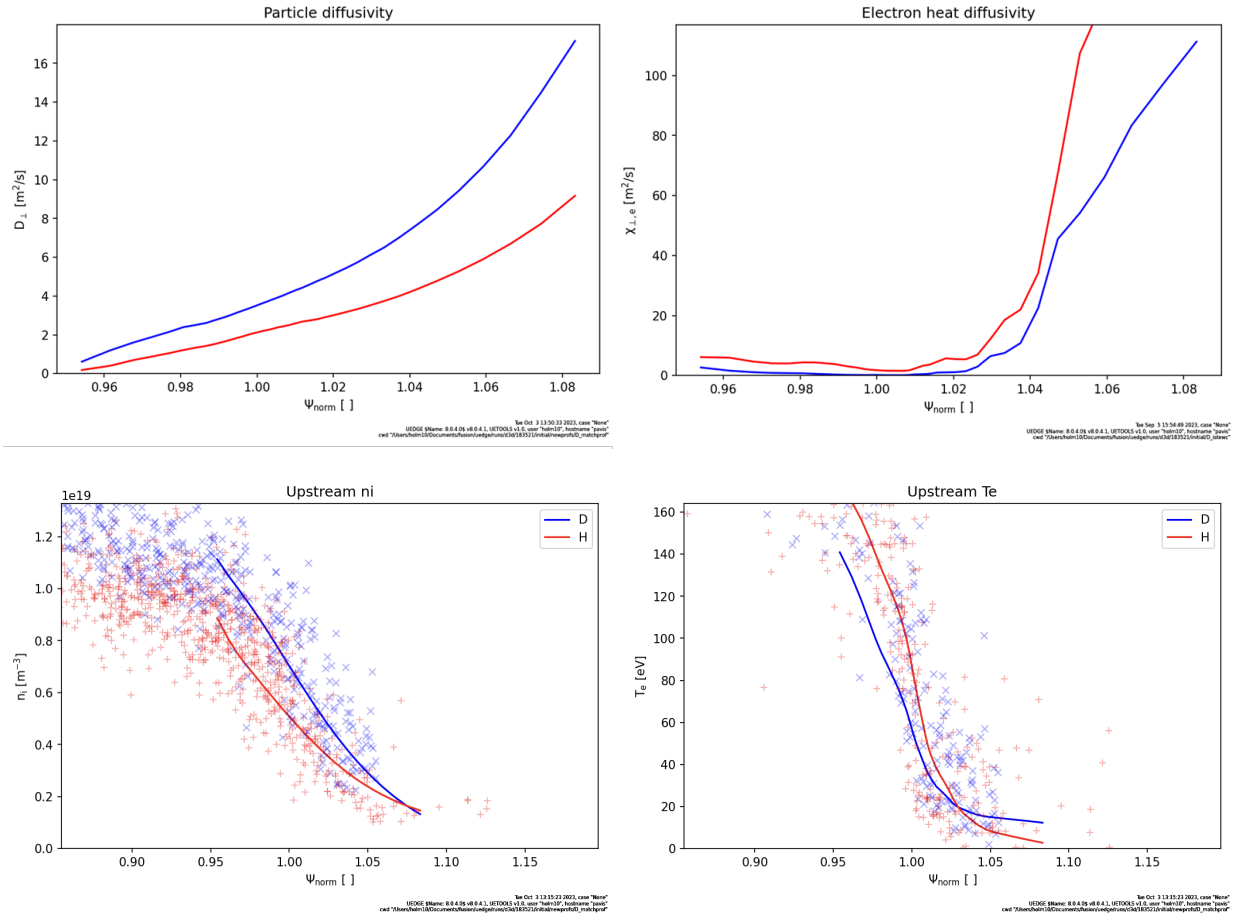

Figure 6.4: UEDGE input perpendicular particle (upper left) and heat (upper right) flux transport coefficients for the converged hydrogen (red) and deuterium (blue) analyses of shots 183521 and 192089 respectively. Lower panels show the resulting UEDGE predicted upstream main ion density (left) and electron temperature (right) profiles compared to TS data. Note that the radial coordinates used for plotting are ψ_N and not $\rho = \sqrt{\psi_N}$.

deuterium respectively. Closed circles and solid lines indicate Langmuir probe and LLAMA measurements (red-H, blue-D). Note that the outer strike point density n_e is potentially over-predicted by UEDGE compared to Langmuir probe measurements. This discrepancy may be either a LP diagnostic or simulation effect. The LP density measurements, derived from ion saturation current measurements, must assume an effective probe collection area to infer n_e. As a result, errors in effective probe area calibrations may account for this difference. If the measurements are to be trusted, a potential simulation based explanation of this discrepancy is possibly the neutral pumping strength used, an input parameter which controls how many outer strike point particles are pumped away from the simulation grid. The strike point temperature T_e appears reasonably well matched to experiment, apart from a temperature drop near $\psi_N \approx 1.02$ likely due to a geometry effect of the shelf and pump duct on the simulation grid not captured by experimental strike point sweeps. These differences between experiment and simulation result in a rough factor of 2 lower T_e at the strike point. Despite these discrepancies, UEDGE in relative terms predicts T_e, ϕ_s, and E_r in good agreement with experiment. The right-hand figure in 6.5 illustrates the re-scaled UEDGE results which account for the discrepancies between experiment and prediction (factors of 1/4, 2, & 2 for n_e, ϕ_s, and & E_r) which potentially come from these probe area or neutral pumping, pump duct geometry, and sheath potential errors respectively. These simulation results hint that the difference in scrape off layer E_r observed between experiments are correlated with strike point changes resulting from upstream density differences between isotopes. To assess this possibility in greater detail, additional UEDGE simulations were performed.

These dedicated UEDGE simulations were performed using the deuterium solutions above, freezing the perpendicular particle and heat transport coefficients inside the last closed flux surface. The plasma transport equations were solved for the open field lines, attaining steady state solutions. This simulation setup was used in order to distinguish if the divertor region isotope effects captured by UEDGE are responsible for the changes in temperature, potential, and E_r observed in the previously discussed simulations. Fig. 6.6 illustrates the UEDGE simulation grid used for these dedicated runs in the left-hand panel,

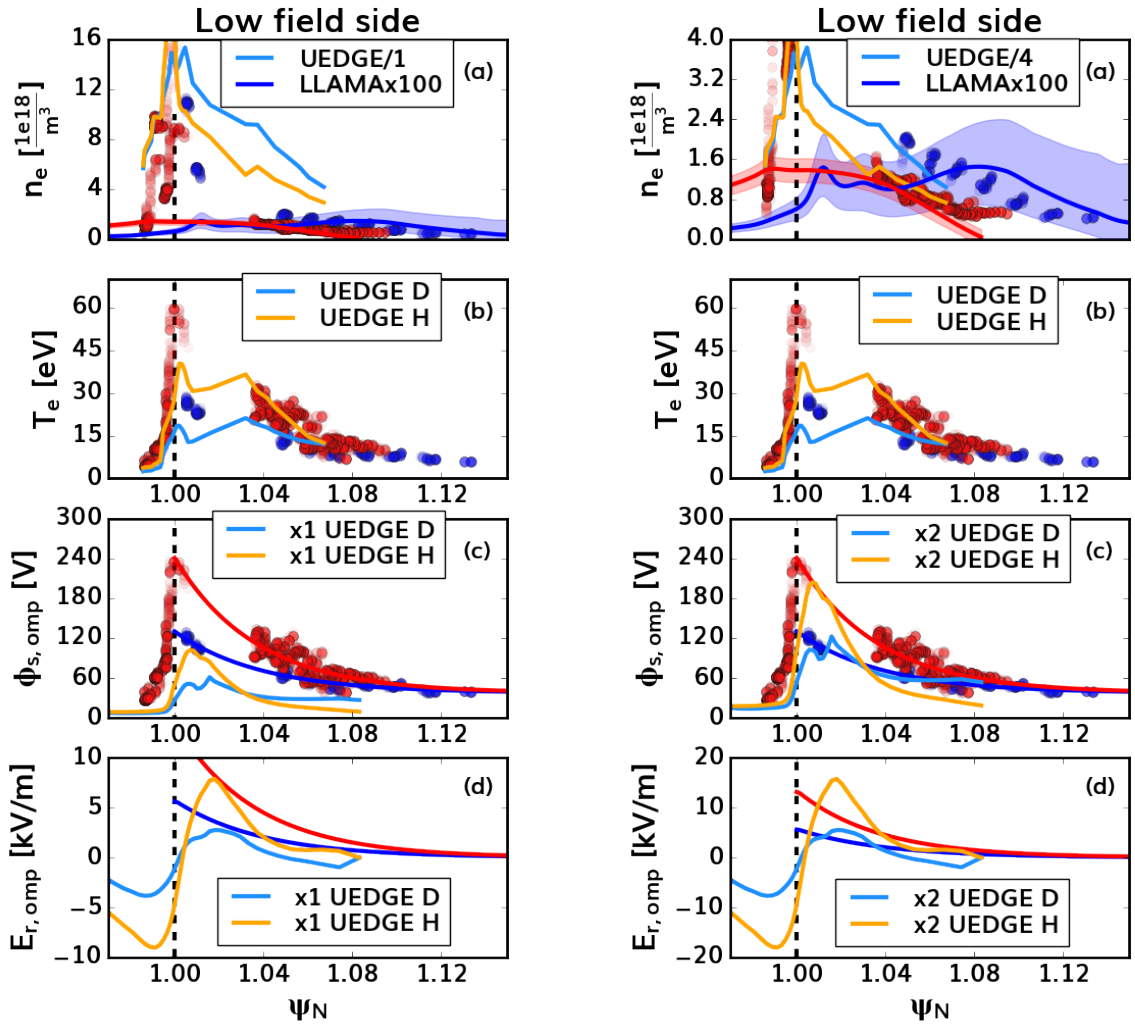

Figure 6.5: Left column: Raw UEDGE predictions of the outer target density, temperature, space potential, and outboard midplane E_r profiles for hydrogen (red) and deuterium (blue) on panels (a), (b), (c), and (d) respectively. Orange and light blue lines indicate hydrogen and deuterium UEDGE predictions, and closed circles show Langmuir probe experimental data. Right column: Rescaled UEDGE predictions for comparison to experimental LP data.

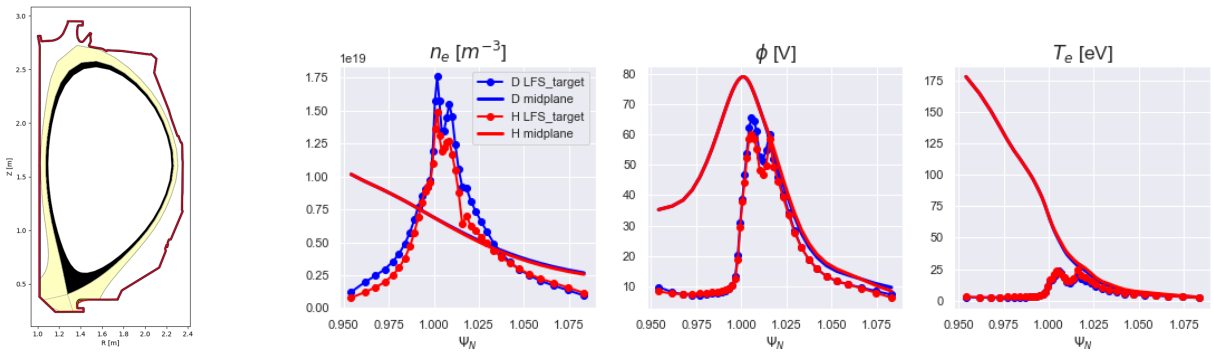

Figure 6.6: UEDGE predictions using frozen closed field line transport. Left-hand panel shows the UEDGE grid, with the black shaded region showing the region with frozen transport and yellow the grid region still permitted to vary. Right-hand panels show the outer target electron density, space potential, and electron temperature predictions from UEDGE. Solid contours indicate midplane profiles, and lines with closed circles show outer target profiles. Color coding indicates simulations with hydrogen and deuterium main ions in red and blue respectively.

with the region of frozen transport and profile equations shown in black. In light yellow is the remaining grid covering the open field line region, which is free to evolve based on the Braams transport equations. The regions in white are plasma regions not included in the simulation grid and the red contours illustrate the limiter (machine wall) boundary. The figures in the right-hand side of Fig. 6.6 show the input upstream electron density, electric potential, and temperature profiles going from left and right respectively as solid lines. The red and blue contours indicate runs with hydrogen and deuterium main ions respectively. Note how the temperatures and densities inside the separatrix ($\psi_N < 1.0$) are overlapping between simulations. In the open field line region however, the temperature and density profiles no longer overlap with one another. In particular, the hydrogen main ion simulations have a slightly higher temperature and lower density. These isotopic trends are similar to those observed experimentally between hydrogen and deuterium, but much weaker in magnitude.

These simulations enabled prediction of strike point and open field line conditions for either isotope. Due to the identical profile and transport solutions in the closed field line region, these simulations effectively isolate the impact of divertor isotope effects on the radial electric field E_r. Comparing these dedicated deuterium and hydrogen simulations, one finds

a slightly higher hydrogen strike point T_e and lower n_e compared to deuterium, with changes of a similar magnitude to the upstream profiles. These outer target density and temperature predictions may be found on the right-hand panels of Fig. 6.6 as the lines containing closed circles, with deuterium and hydrogen runs in blue and red respectively. Note how the changes are much smaller than the nearly factor of 2 changes seen in prior UEDGE comparisons. The resulting space potential differences between hydrogen and deuterium simulations are now opposite to experiment, with the hydrogen simulations having a nearly 10% lower electric potential than deuterium counterparts. These simulations, by freezing the close field line simulation region, have therefore shown that including only UEDGE divertor isotope effects are insufficient for reproducing the profile changes seen in Fig. 6.5. Changes to profiles inside the closed flux surface region appear to be important contributors for explaining the radial electric field isotope differences between experiments. In particular, changes to the upstream density profile, possibly from changes in neutral penetration between isotopes, appear from UEDGE modeling to be essential to reproducing the experimental temperatures, densities, space potentials, and E_r in the scrape off layer region. Divertor isotope effects, at least in the cases studied here, appear to be subdominant to closed field line effects. As a result, the tentative conclusion from both UEDGE modeling and experimental data is that the origin of the scrape off layer E_r differences between hydrogen and deuterium are likely due to closed field line density changes.

6.3 Explanation 2: closed field line region

Building on these open field line studies, detailed analysis of the closed field line region was undertaken. From impurity force balance analysis of the 80 discharges analyzed via TRANSP in thesis chapter 4, a consistently higher edge radial electric field is observed in hydrogen plasmas compared to deuterium. These observations are shown in Fig 6.7, with hydrogen data in red and deuterium data in blue. The upper panel illustrates full E_r calculations from radial force balance on the x-axis, while the lower panel shows contributions solely from poloidal rotation contributions. The y-axes on either plot are the measured L-H power

thresholds. By comparing the two plots, is observed that the higher edge radial electric field E_r in hydrogen compared to deuterium is found to be correlated to differences in impurity poloidal rotation between isotopes, as well as P_{LH}. Related to this observation, is the L-H transition theory notion that main ion poloidal rotation (zonal flows) can help trigger the L-H transition by formation of a turbulence suppression feedback loop [93, 116, 7]. In light of such data, it is important to note that despite observing systematic impurity poloidal rotation differences between isotopes, no definitive conclusions regarding main ion poloidal rotation can yet be made. However, with the aid of the DIII-D tokamak's excellent diagnostic coverage, main ion poloidal rotation can be inferred. More precisely, there are sufficient measurements to predict main ion poloidal rotation using data acquired from the impurity and main ion charge exchange spectroscopy diagnostics (impCER/miCER). The main ion charge exchange spectroscopy system, similar to impurity counterparts, involves the fitting of visible emission spectra, now of thermal Balmer-α. These spectral fits are used to determine the main ion temperatures and toroidal rotations of the bulk plasma, which when coupled with the previously discussed E_r profiles, can be used to infer the main ion poloidal rotation via radial force balance. The following section will discuss in detail the results of miCER analysis performed by Dr. Shaun Haskey, and extraction of main ion poloidal velocity profiles for both hydrogen and deuterium. It is noteworthy that these analyses are a possible first ever attempt at extracting isotopic main ion poloidal rotation based on experimental main ion measurements. As a result, the analysis goals are to distill the important physics in isotopic poloidal rotation differences, and will be built upon in subsequent studies. Some of the assumptions in the workflows are likely incorrect as a result, but serve as a first attempt in the absence of more refined data analysis techniques.

6.3.1 Main ion radial force balance analysis

As discussed previously in thesis Chapter 3, the main ion charge exchange spectroscopy system at the DIII-D tokamak measures visible light emitted by the plasma main ions at approximately 656 nm [38, 37]. This diagnostic, like impCER, can extract measurements of

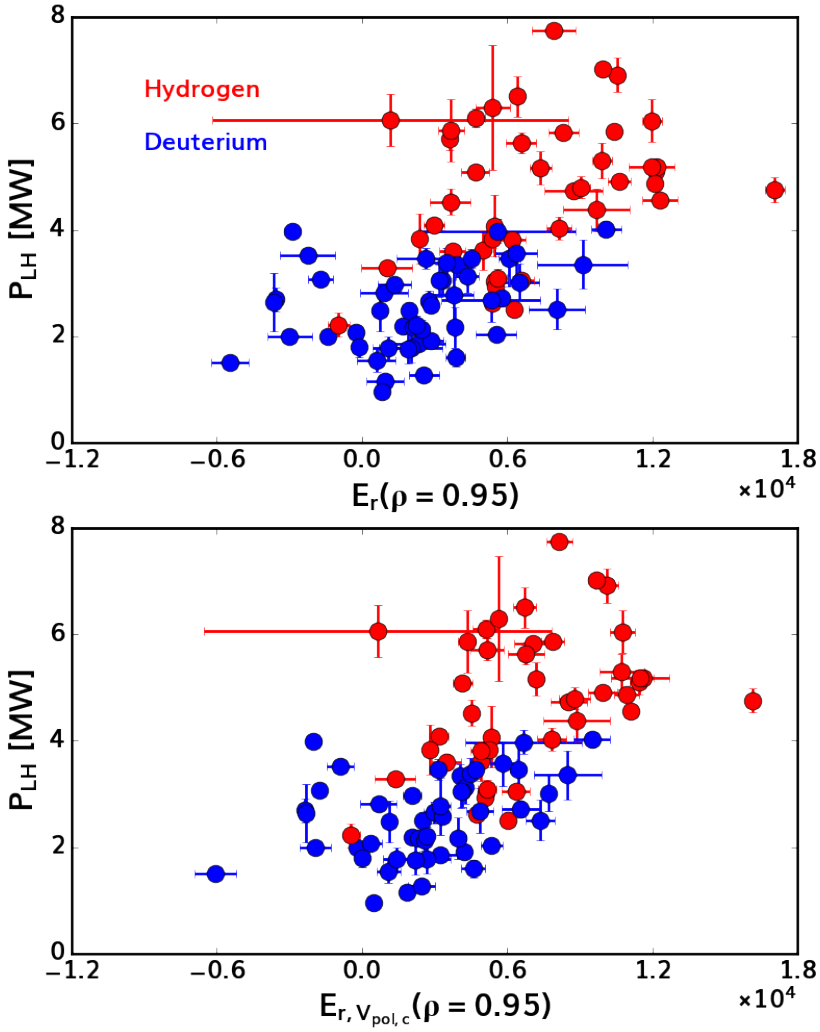

Figure 6.7: TRANSP database of P_{LH} versus L-mode radial electric field E_r at $\rho = 0.95$ just before L-H transition in V/m determined from impurity charge exchange spectroscopy. Upper panel has an x-axis from the full E_r calculation from impCER, and the lower panel has just the contribution from v_{pol} from carbon impurities. The horizontal error bars are determined from the spatial standard deviation of these E_r calculations within $\rho = 0.925 - 0.975$. Red closed circles indicate hydrogen plasmas, while blue data show deuterium counterparts.

main ion temperature (T_i), density (n_i), and velocity (v_i) along a given line-of-sight using the width, area under the curve (integral), and wavelength shift of the spectral line. This diagnostic however, requires a much more complex fitting procedure than impurity charge exchange, and can directly measure only toroidal rotation due to only tangential lines-of-sight. The measured Balmer-α emission by this system is from charge exchange between main ions and several distinct neutral populations, and partly from these distinct neutral populations' emission themselves. The passive emission components are eliminated using time-slice subtraction analysis like that shown in Fig. 3.3. The neutral populations needed for proper modeling include the neutral beam injected particles, fast neutrals, and thermal neutrals. The beam neutrals contain 4 energy components: full H^+, half H_2^+, third H_3^+, and water H_2O^+. These energy components come from the respective ion particles being accelerated to different velocities before neutralization and injection into the plasma. The desired charge exchange emission between these beam injected neutrals and main ions (direct charge exchange signal, DCX) is convolved with emission from beam particles themselves by impact excitation, even after passive subtraction. Charge exchange between these injected beam neutrals and main ions additionally generate a population of thermal neutrals. These thermal neutrals can be impact-excited or undergo charge exchange with surrounding main ions, and form the emission contribution referred to as the halo. Halo emission is localized close to the neutral beam due to finite neutral ionization and spontaneous emission lifetimes. Fast neutrals are born from charge exchange between injected beam neutrals and fast ions. Upon charge exchanging, these neutrals produce a broad Balmer-α spectral feature due to the very high fast particle energies. This part of the spectra, called FIDA, is often used to infer fast ion densities. Unlike the impCER system, miCER observes a residual cold emission component in the Balmer-α spectra even with time-slice subtraction. The origin of this signal is unknown, however it is routinely observed, and increases in amplitude approaching the plasma edge. The DCX and Halo contributions together form the thermal emission spectra, from which the main ion properties can be obtained. Results of main ion analysis for both the reference deuterium and hydrogen plasma's is illustrated in Fig. 6.8 on the left and right respectively. The x-axis represents camera pixel number, a proxy

for wavelength, while the y-axis is pixel count during a single integration time, a proxy for emission intensity ($ph/s/sr/nm/cm^2$). Note how the hydrogen shot analysis requires fitting of both hydrogen and deuterium emission, due to residual deuterium in the given experiment. Analyses based on the fitted spectra indicate a hydrogen purity of approximately 90%. In either experimental spectra, a noticeable residual cold emission contribution with approximately $T_i \approx 0$ eV and $v_{LOS} \approx 0$ km/s must be accounted for in the fitting process to match the experimental spectra. The cold emission contribution is important because it creates degeneracy in the miCER fitting process. Based on previous experimental L-mode main ion temperature and toroidal rotation observations at DIII-D by Grierson [38], one expects the ion temperature measurements between carbon impurity spectroscopy and main ions to be very similar. Deviations between the two are unexpected theoretically due to the very fast thermal equilibration time between the two species (of order microseconds). Therefore, careful interpretation of the miCER results must be taken prior to inferring main ion poloidal velocity.

Deviations between the apparent and true toroidal rotation values in DIII-D L-mode plasmas have been previously observed as linearly correlated to ion temperature measurements [38]. These errors may arise due to both atomic physics distortions, and by not including FIDA emission in the spectral model. In both shots analyzed, FIDA is not included in the fitting process due to its inclusion requiring sophisticated modeling using the code FIDAsim [44]. An ad hoc minor correction of the miCER v_{tor} measurements was used to fix these known biases. The corrections leveraged the expectation that $T_i = T_c$ and any deviations from this trend indicate errors in the miCER fitting process. The apparent miCER toroidal velocities $v_{tor,i}^{uncorr}$ were corrected for both line-of-sight geometry effects, and fittings errors using the following formula:

$$v_{tor,i}^{corr} = v_{tor,i}^{uncorr} \frac{T_i}{T_c} + (v_{tor,impCER}^{corr} - v_{tor,impCER}^{uncorr}) \tag{6.8}$$

In the above equation, T_i and T_c represent the main ion and impurity temperatures respec-

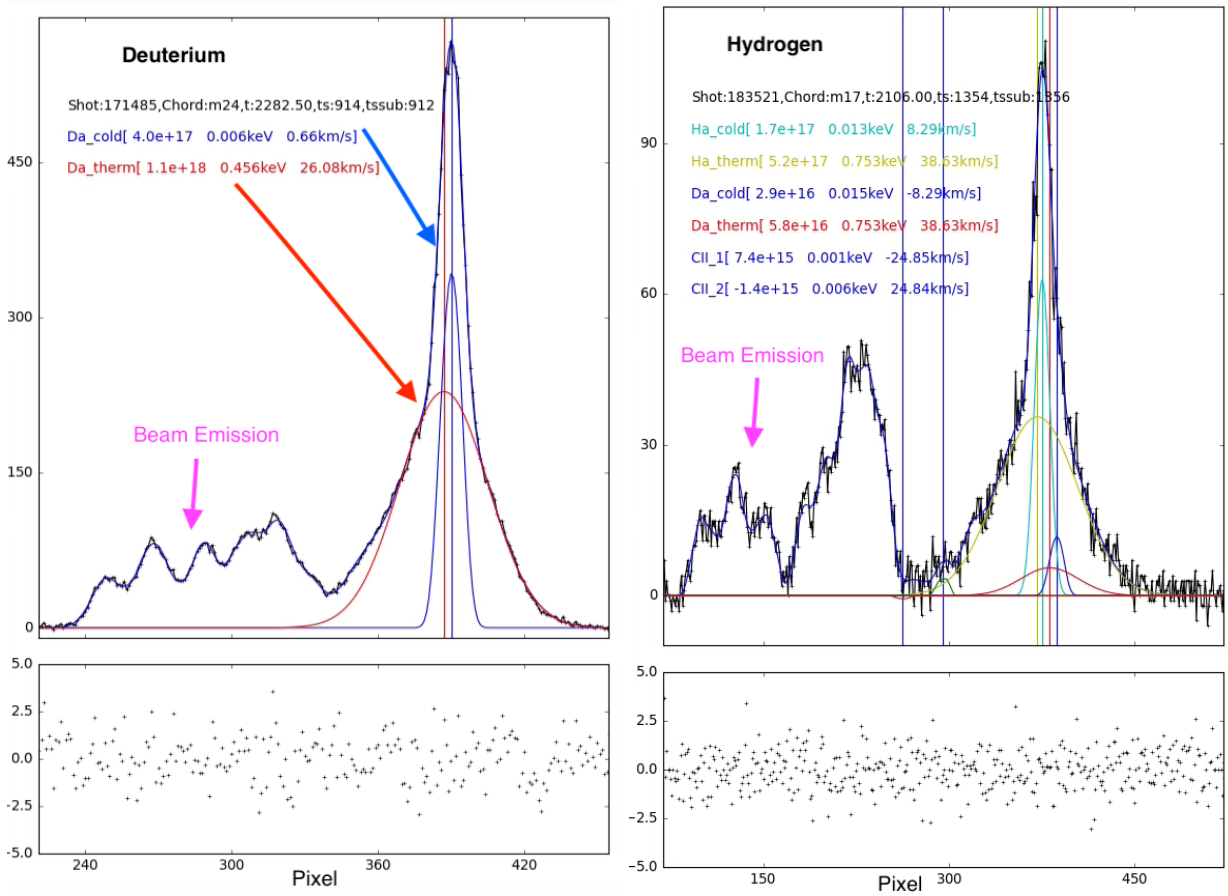

Figure 6.8: Example of deuterium (left) and hydrogen (right) main charge exchange fitted spectra for shots #171485 and #183521. Raw experimental data is shown in black datapoints. The thermal and cold emission contributions to the fitted spectra, along with their inferred temperatures and toroidal rotation velocities, are shown via text. X-axis shows pixel number, a proxy for wavelength and Y-axis shows pixel count during a single integration time, a proxy for brightness. The panels immediately below the spectra show the residuals between the data and fitted model.

tively, while $v^{uncorr}_{tor,impCER}$ and $v^{corr}_{tor,impCER}$ represent the raw and corrected impurity toroidal velocities. The latter two quantities represent the geometrical correction necessary to convert the raw line-of-sight measurements into the toroidal direction, identical between the impCER and miCER systems due to overlapping sight-lines. Such geometrical corrections were 3km/s. The first correction term in equation 6.8 is derived assuming a linear relationship of toroidal velocity deviations with temperature. Following such treatment, inference of main ion poloidal rotation is performed using radial force balance:

$$v_{pol,i} = (E_r - v^{corr}_{tor,i} B_{pol} - \frac{1}{Z_i n_i e} \nabla p_i)/B_{tor} \tag{6.9}$$

Above, the radial electric field E_r is from impurity force balance and the ion pressure gradient is $\nabla p_i = \nabla(n_e - Z_c n_c) T_c$ using the carbon impurity temperature and main ion density calculated from quasi-neutrality. The results from such analyses may be viewed in Fig. 6.9 for deuterium and hydrogen on the right and left columns respectively. Panel 6.9(a) illustrates the radial electric field profiles used in the main ion poloidal rotation inference calculation. Orange solid lines indicate results from impCER force balance, closed circles show DBS measurements, closed triangles illustrate BES measurements, and dashed lines are Langmuir probe measurements. Panel 6.9(b) shows both the main ion and carbon impurity temperatures (T_i and T_c) extracted from charge exchange analysis in orange and blue. Note the miCER temperatures are higher than T_c, consistent with small but important errors in the fitting process. In panel 6.9(c), the uncorrected and corrected carbon impurity toroidal rotation is shown in violet and blue. The differences between the two is approximately 3km/s, representing the geometrical correction in equation 6.8. The uncorrected and corrected main ion toroidal rotation is shown in gray and orange respectively. In Fig. 6.9(d), the impurity ion poloidal rotation is shown in dark blue. The inferred main ion poloidal rotation, using either the uncorrected or corrected main ion toroidal rotation profile, is shown in gray and orange respectively. The toroidal rotation corrections do not change the profile shape, but rather the absolute magnitude. For both hydrogen and deuterium, the corrected main ion poloidal rotation profiles closely resemble the impurity measurements inside ρ=0.96. Outside ρ=0.96,

the main ion poloidal rotations are noticeably larger than impurity counterparts, likely as a result of orbit loss physics. These comparisons suggest DIII-D L-mode isotopic differences in main ion poloidal rotation are similar to those from impurity measurements near the E_r well forming region. The hydrogen poloidal rotation values are noticeably larger in magnitude than deuterium, strongly inconsistent with main ion neoclassical poloidal rotation expectations where $v_{pol,i}^{neo} \approx 0$ [36, 90, 54, 53]. To understand accurately where these isotopic main ion poloidal rotation and E_r differences may originate from, poloidal momentum balance analysis was performed for both hydrogen and deuterium.

6.3.2 Main ion poloidal momentum balance

Based on recent publications by Dr. Keith Burrell and Professor Jim Callen, a rigorous poloidal momentum balance equation for a generalized tokamak geometry was derived [16], with equation (19) reproduced below. Due to the absence of toroidal fluctuation measurements, $\tilde{v}_\phi = 0$ is explicitly assumed:

$$\left[1 - \frac{R^2 B_{tor}^2}{\langle R^2 \rangle \langle B^2 \rangle}\right] \frac{\langle B^2 \rangle}{\langle B_{pol} \rangle^2} \frac{\partial v_{pol}}{\partial t} = -\mu \frac{\langle B^2 \rangle}{\langle B_{pol} \rangle^2} \left(v_{pol} - v_{pol}^{neo}\right) - \frac{B_{pol}}{\langle B_{pol} \rangle} \frac{1}{V'(\psi)} \frac{\partial}{\partial \psi} V'(\psi) \langle \tilde{v}_{pol} (\tilde{v}_r \cdot \nabla_r \psi) \rangle \tag{6.10}$$

In equation 6.10 ψ, R, B_{tor}, B_{pol}, μ, and v_{pol}^{neo}=$-K_1 \partial/\partial r(T_i/ZeB)$ are the poloidal magnetic flux, major radius, toroidal magnetic field, poloidal magnetic field, poloidal flow-damping rate, and neoclassical poloidal ion velocity respectively. K_1 is the commonly used collionality-dependent neoclassical poloidal velocity constant [54, 80]. Additionally, $V'(\psi)$=$dV/d\psi$ where $V(\psi)$ is the volume enclosed in a given flux surface. The magnetic field and major radius quantities in brackets, such as $\langle R^2 \rangle$, $\langle B^2 \rangle$,$\langle B_{pol} \rangle$ represent flux-surface averaged quantities. The expression explicitly links the poloidal rotation at some flux surface location with the flux-surface averaged Reynolds stress. This expression is slightly different from the more

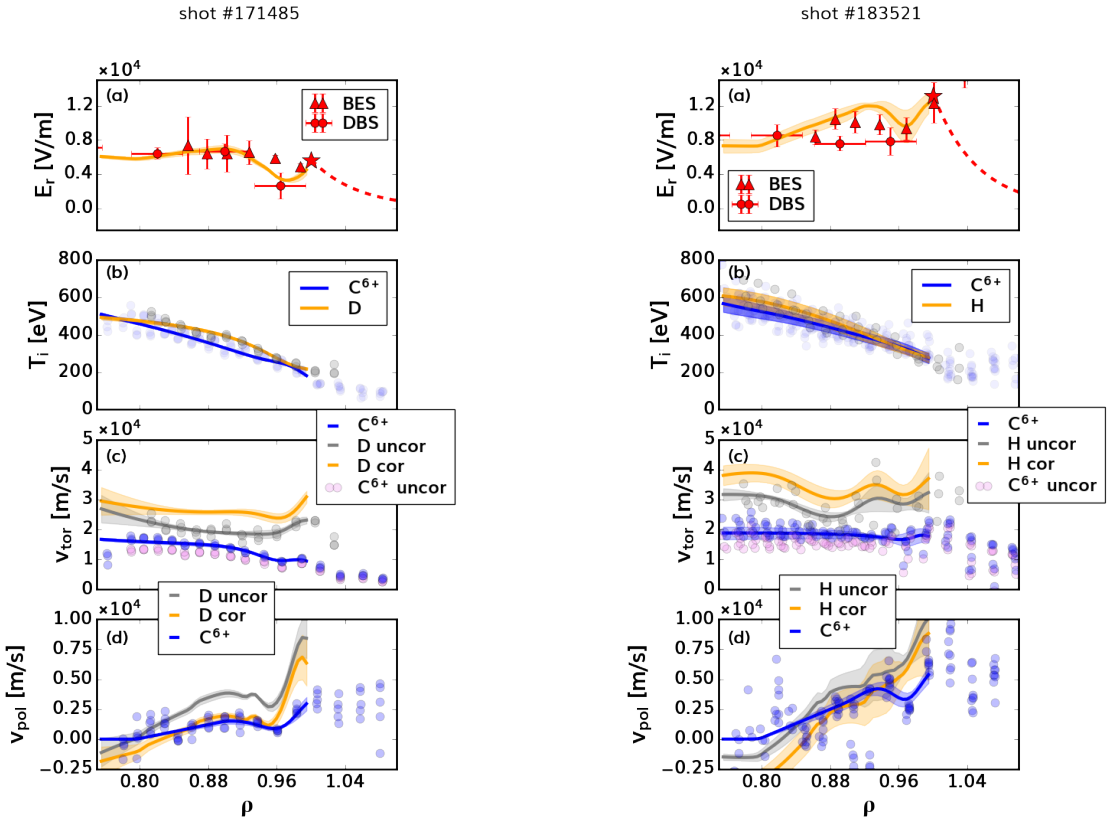

Figure 6.9: Figure illustrating deuterium (left) and hydrogen (right) main ion poloidal inference from force balance vs. radial coordinate ρ. Panel (a) illustrates the radial electric field determined by impurity radial force balance (solid lines), DBS analysis (closed circles), and Langmuir probes (dashed line and closed star). Panel (b) shows ion temperature from the impurity and main ion systems in orange and blue respectively. Panel (c) shows toroidal rotation from impurity (main ion) charge exchange with and without correction in blue and violet (orange and gray), respectively. Panel (d) demonstrates main ion poloidal rotation extracted from radial force balance using the corrected toroidal rotation profiles, with blue data illustrating the impCER measured poloidal rotation. The gray counterpart illustrates the same poloidal rotation prediction using the uncorrected toroidal rotation profiles, also shown in gray on panel (c).

commonly used large aspect ratio poloidal momentum balance equation:

$$(1+2q^2)\frac{\partial v_{pol}}{\partial t} = -\mu\frac{q^2}{\epsilon^2}(v_{pol} - v_{pol}^{neo}) - \frac{\partial}{\partial r}\langle \tilde{v}_{pol}\tilde{v}_r\rangle \tag{6.11}$$

In equation 6.11, q represents the magnetic safety factor, ϵ is the inverse aspect ratio, and $\langle \tilde{v}_{pol}\tilde{v}_r\rangle$ is the turbulent Reynolds stress. Similar to Fig. 2 in [16], a comparison of the coefficients of term 1 (d/dt), term 2 (viscous), and term 3 (Reynolds stress) between the generalized geometry and large aspect ratio formulas was conducted for the DIII-D shots under consideration. The results for such a comparison are shown in Fig. 6.10, evaluated at outboard midplane coordinates. Red curves illustrate the generalized geometry results, while blue show large aspect ratio coefficients. Similar to findings by Burrell and Callen for DIII-D shot 174658, the large aspect ratio coefficients for both the viscous and d/dt terms are larger compared to their generalized geometry counterparts. In particular, at the plasma edge near $\rho = 0.9$ the generalized geometry d/dt and viscous terms are smaller by a factor of 3. The Reynolds stress term is nearly unchanged between the two formulations. Therefore, without a loss of generality, and to enhance formula readability, the Reynolds stress term is cast in its large aspect ratio form for the remainder of this section. Under the assumption of a time independent Reynolds stress, an exact solution to the differential equation 6.10 is calculated. Taking the steady state limit of this differential equation solution, the following main ion poloidal rotation relation from poloidal momentum balance is derived:

$$v_{pol} = v_{pol}^{neo} + \frac{\tau_{pol}}{\left[1 - \frac{R^2 B_{tor}^2}{\langle R^2\rangle\langle B^2\rangle}\right]\frac{\langle B^2\rangle}{\langle B_{pol}\rangle^2}}\frac{\partial\langle \tilde{v}_{pol}\tilde{v}_r\rangle}{\partial r} \tag{6.12}$$

The poloidal rotation damping time τ_{pol} in equation 6.12 is a piece-wise function, dependent on the normalized ion collisionality $\nu_i^* \simeq \frac{4}{3}\sqrt{\pi}\frac{qR}{T_i^2}n_e e^4 Z_{eff}^2\frac{log(\Lambda_i)}{\epsilon^{3/2}}$, where ϵ, and $log(\Lambda_i)$ represent the inverse aspect ratio and Coulomb logarithm respectively.

$$\frac{1}{\tau_{pol}} = \begin{cases} \nu_i^*\nu_b\epsilon^{1/2} & \nu_i^* \leq 1 \\ \nu_b\epsilon^{1/2} & \nu_i^* > 1 \end{cases} \tag{6.13}$$

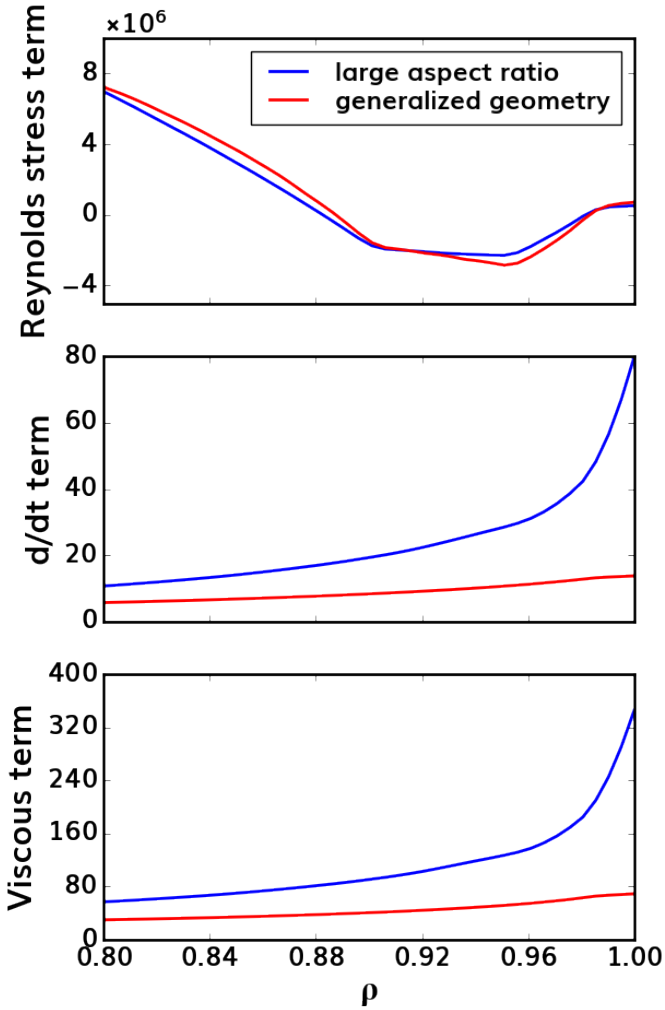

Figure 6.10: A comparison of the poloidal momentum balance equations 6.10 and 6.11 for the generalized geometry and large aspect limits in red and blue respectively. Upper panel shows the coefficients of the Reynolds stress (3rd) term. The middle panel shows a comparison of the d/dt (1st) term. The final panel shows the viscous (2nd) term comparison.

Here, $\nu_b = v_i^{th}/qR$ denotes the ion-transit frequency, where $v_i^{th} = \sqrt{T_i/m_i}$ is the thermal ion speed. The hydrogen and deuterium plasmas studied here are in the banana regime, with $\nu_i^*(\rho = 0.95) < 1$. Using equations 6.12 and 6.13, it is therefore possible to determine the different contributions to main ion poloidal velocity due to neoclassical and turbulent Reynolds stress effects using this reduced model. The neoclassical poloidal rotation can be easily extracted from the existing TRANSP simulations, which automatically calculate neoclassical poloidal rotation velocities using the code NCLASS [49]. The turbulent Reynolds stress contribution to main ion poloidal rotation however requires more detailed calculations. The Reynolds stress can be calculated using Beam Emission Spectroscopy velocimetry analysis [74, 66] which has been previously used to extract experimental measurements of the turbulent Reynolds stress for L-H transition experiments [117]. The basis of such analyses is the generation of a series of 2D turbulence images in the R-Z plane with approximately 1 μs time resolution. Details of the associated BES velocimetry analyses may be found in Appendix D for the reader's reference. It is worth noting that these turbulence images are the result of a combination of electron, main ion, and carbon impurity density fluctuations, as referenced in detail in thesis chapter 5. Additionally, time-delay correlation analysis can be used to extract the turbulent poloidal correlation time and length, and is likewise described in detail in Appendix D. These measurements are useful as they provide two means of calculating the time independent Reynolds stress: explicitly from velocity fluctuations and from $\vec{E} \times \vec{B}$ eddy tilting. The former is a calculation of Reynolds stress with no assumption of its potential physical origin, while the latter assumes the Reynolds stress is generated from $\vec{E} \times \vec{B}$ shear tilting of turbulent eddies. Specifically, one can use the correlation times τ_c, measured $\nabla v_{\vec{E}\times\vec{B}}$, and radial velocity fluctuations $\tilde{v}_r^2$ to estimate the time-independent Reynolds stress induced from $\vec{E} \times \vec{B}$ eddy tilting [30]:

$$\langle \tilde{v}_{pol} \tilde{v}_r \rangle (\theta = 0) = \langle \tilde{v}_r^2 \rangle \nabla (v_{\vec{E}\times\vec{B}}) \tau_c \tag{6.14}$$

Correspondence between the two calculations would suggest the Reynolds stress itself is driven by the E_r profile.

Results from velocimetry analysis for our reference hydrogen and deuterium discharges in L-mode just before L-H transition are shown in Fig. 6.11 in red and blue respectively. Panels (a) and (e) illustrate the radial and poloidal velocity fluctuations vs normalized minor radius ρ. Note how the hydrogen plasma observes both larger radial and poloidal velocity fluctuations, in agreement in with gyro-kinetic predictions in Fig. 4.15. These fluctuation changes are mostly due to the differences in input power between discharges. Panels (b) and (f) show the poloidal correlation times τ_c and lengths $L_{c,pol}$ from time-delay correlation analysis discussed in detail in Appendix D. Similar to velocimetry results, the hydrogen plasma observes a noticeably larger correlation time and length compared to its deuterium counterpart. The radial velocity fluctuations in panel (a), correlation times in panel (b), and previously referenced isotopic E_r profiles provide sufficient information for predicting Reynolds stress from equation 6.14.

Panel (c) illustrates the Reynolds stress calculated from both velocimetry and $\vec{E} \times \vec{B}$ shear eddy tilting using equation 6.14. Results in dark blue and dark red are explicitly from velocity fluctuations for hydrogen and deuterium respectively. For both hydrogen and deuterium, the Reynolds stress near the last closed flux surface and in the scrape off layer appears to approach zero. Inside the pedestal forming region however, the hydrogen discharge's Reynolds stress has a much stronger radial spatial gradient compared to deuterium. This change in spatial gradient comes from changes in the cross-phase between $\tilde{v}_r$ and $\tilde{v}_{pol}$ fluctuations, as may be inferred given the flatness of profiles shown on Fig 6.14(a,e). These isotopic differences are consistent with predictions from equation 6.14, shown in light blue and orange as dashed lines for deuterium and hydrogen respectively. Large deviations between predictions using equation 6.14 and velocimetry results occurs in the vicinity of the separatrix ($\rho > 0.97$). These deviations are likely because of inappropriate application of this reduced model, which is only valid in the closed field line region. Possible conclusions from the agreement of these two quantities inside of $\rho < 0.97$ for either isotope is that the origin of the time-independent Reynolds stress is from $\vec{E} \times \vec{B}$ tilting differences. From these Reynolds stress profiles, sufficient experimental information is available to predict the main

ion poloidal rotation using equation 6.12. Prior to doing so however, a minor modification to the referenced poloidal rotation formula must be made to account for ion-orbit loss effects due to looking so close to the plasma separatrix region. Using a similar ion-orbit torque formulation to that referenced in [116, 51, 86], an additional term is added to the poloidal momentum balance solution:

$$v_{pol} = v_{pol}^{neo} + \frac{\tau_{pol}}{\left[1 - \frac{R^2 B_{tor}^2}{\langle R^2 \rangle \langle B^2 \rangle}\right] \frac{\langle B^2 \rangle}{\langle B_{pol} \rangle^2}} \left(\frac{\partial \langle \tilde{v}_{pol} \tilde{v}_r \rangle}{\partial r} + T_{OL} \right) \tag{6.15}$$

$$T_{OL} = \nu_{ii} v_i^{th} q \epsilon^{-1/2} \frac{\rho_{i,pol}}{r} \frac{exp(-(\nu_i^* + X^4)^{1/2})}{(\nu_i^* + X^4)^{1/2}} exp(-\left(\frac{R - R_{sep}}{\rho_{i,pol}}\right)^2) \tag{6.16}$$

Above $\nu_{ii} = \nu_b \epsilon^{3/2} \nu_i^*$ is the ion-ion collisionality, $\rho_{i,pol} = \frac{m_i v_i^{th}}{e B_{pol}}$ is the poloidal ion gyro-radius, $X = \frac{q E_r}{\epsilon v_i^{th} B_{tor}}$ is the normalized $\vec{E} \times \vec{B}$ rotation speed, R_{sep} is the outboard midplane seperatrix major radius, and r is the plasma minor radius. Equation 6.16 represents the torque induced from ion-orbit loss, taking into account both equilibrium radial electric field orbit squeezing and collisionality effects. Note that this torque does not include X-loss proposed by Chang [25]. Equation 6.15 represents the more complete main ion poloidal momentum balance solution, including neoclassical, turbulent Reynolds stress, and ion orbit-loss effects. Predictions of main ion poloidal rotation for the deuterium and hydrogen reference cases based on equation 6.15 are illustrated on Fig. 6.11 panels (g) and (h) respectively. These solutions are broken into their Reynolds stress and ion orbit-loss contributions, shown as the gray and violet shaded regions. Note how for the hydrogen case, the inner shear layer is correlated with Reynolds stress contributions, while the outer shear layer is from orbit-loss.

These solutions are shown additionally on panel (d) as solid red (H) and blue (D) lines, in comparison to main ion poloidal rotation measurements inferred from radial force balance for hydrogen (orange) and deuterium (light blue) illustrated as shaded regions. Additionally overlayed as closed circles are the carbon poloidal rotation velocities for hydrogen (red) and deuterium (blue). It can be observed that there is reasonable agreement between main ion poloidal rotation predictions from both radial and poloidal force balance considerations.

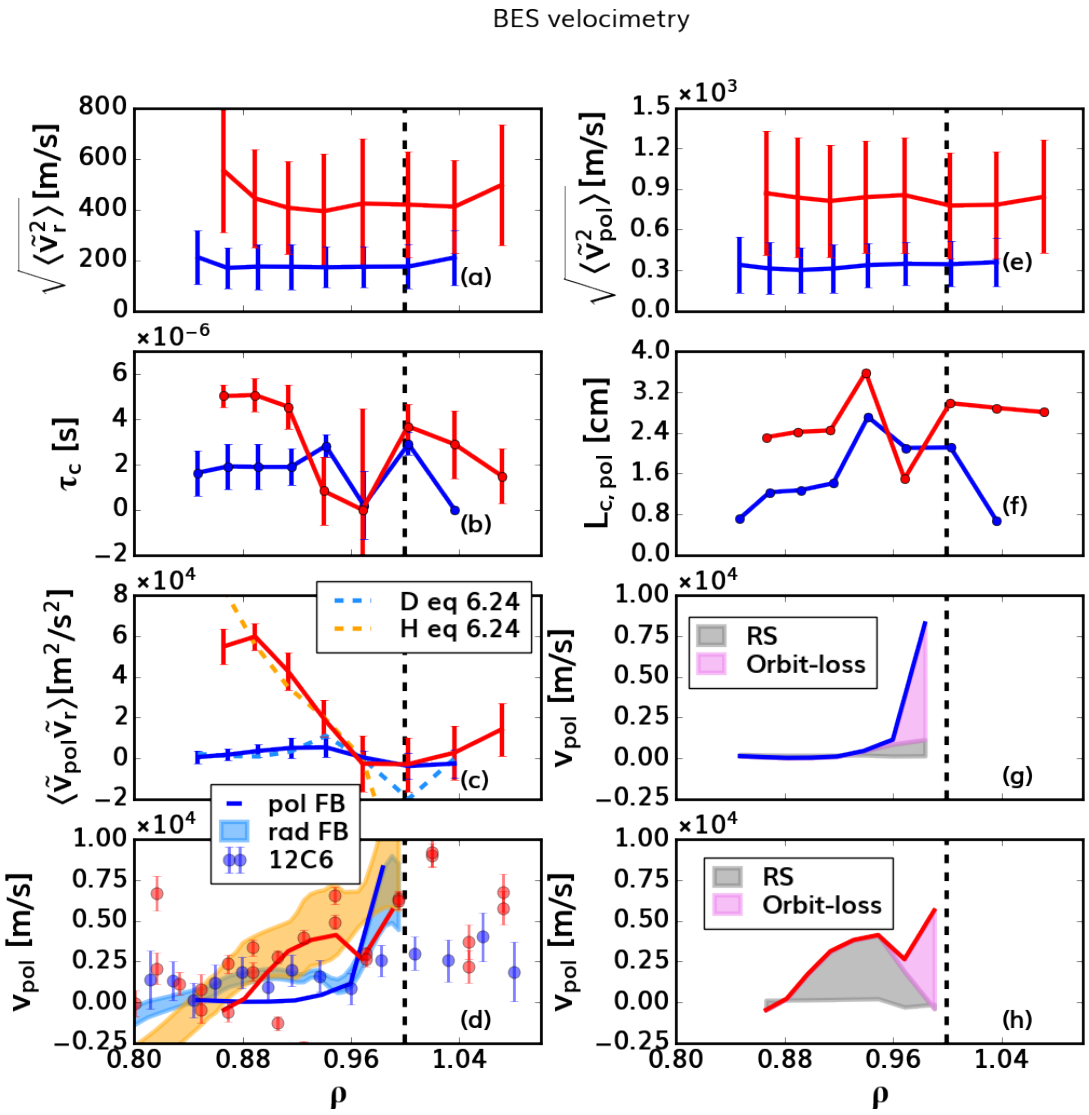

Figure 6.11: Beam emission spectroscopy inferred deuterium (blue) and hydrogen (red) radial velocity fluctuations (a), turbulent correlation times (b), Reynolds stress (c), poloidal rotation velocities (d), poloidal velocity fluctuations (e), and turbulent correlation lengths (f) in L-mode before L-H transition vs. ρ. Panels (g) and (h) illustrate the poloidal rotation contributions from Reynolds stress and orbit-loss for deuterium and hydrogen as the gray and violet shaded regions.

In particular, these calculations appear to suggest the origin of the isotopic poloidal rotation differences referenced previously are mostly the result of differences in Reynolds stress. Furthermore, the differences in Reynolds stress between isotopes appears to be from both differences in the gradient of $v_{\vec{E}\times\vec{B}}$ and local differences in the turbulence properties $\tilde{v}_r^2, \tau_c$. As a result, it appears that there is classical chick-or-the-egg problem, where the ascribed difference in E_r between isotopes in the closed flux region, the change in poloidal rotation velocity, is itself dependent on the value and profile shape of E_r. Such findings suggest the radial electric field and poloidal rotation are likely self-generated in the closed field line region.

One very important potential short-coming of this main ion poloidal rotation analysis is that it has only been performed on 1 discharge pair. As a result, it is still an open question whether these isotopic radial electric field differences are ubiquitous, or a consequence of the specifically chosen discharges. In an attempt to discern between the two possibilities, analysis of other dimensionally matched hydrogen and deuterium discharge pairs was undertaken using impurity charge exchange spectroscopy from the existing database of 80 TRANSP analyzed discharges shown in Fig 6.7. To be more precise, hydrogen and deuterium dimensionally matched discharges 183531 and 171477 at $\langle n_e \rangle = 3 \times 10^{19} m^{-3}$; and 183780 and 171470 at $\langle n_e \rangle = 3.7 \times 10^{19} m^{-3}$ were inspected. Results from the impurity radial force balance analyses may be seen in Fig. 6.12. The times shown are those in L-mode just preceding the 1st L-H transition. The upper/lower left panels indicate the $\langle n_e \rangle = 3, 3.7 \times 10^{19} m^{-3}$ discharge pairs in red and blue for hydrogen and deuterium respectively. The solid lines indicate complete E_r calculations from impurity force balance, while the dashed lines show E_r contributions only from poloidal rotation contributions. In either case, the edge radial electric field in hydrogen is noticeably higher than deuterium counterparts, at approximately 10 kV/m at the separatrix. The deuterium edge E_r is roughly 5 kV/m. Either value is in good agreement with previous measurements from shots 183521 and 171485 with nearly half the line-averaged density. The difference in edge radial electric field inside the closed flux region for these new cases similarly appears to correlate with changes in poloidal velocity between

isotopes, akin to Fig. 6.7. In either case, the hydrogen L-mode radial electric field well is slightly narrower in width and deeper in comparison to deuterium counterparts. Such results suggest a larger $v_{\vec{E}\times\vec{B}}$ shear is necessary in hydrogen plasmas to trigger an L-H transition. These observations are consistent with past observations of higher turbulence decorrelation rates in hydrogen discharges compared to deuterium in L-mode just before transition [117] and gyrokinetic simulation results discussed in Chapter 4 on the mass dependence of $\vec{E}\times\vec{B}$ shear stabilization. These findings imply that the differences in edge E_r between isotopes is closer to a ubiquitous phenomena at DIII-D compared to a shot specific observation. These datasets however do not aid in illuminating how or why the edge radial electric field differs between isotopes. They do however provide an opportunity to understand where the poloidal rotation and L-H power threshold correlations may be coming from.

Analysis of equations 6.14, 6.15, and 6.1 which explain the Reynolds stress, v_{pol}, and E_r observed in experiment can be translated into a very crude L-H transition scaling, even when ignoring all prior L-H theory conjectures. Taking the approximation that $v_{pol} \approx v_{\vec{E}\times\vec{B}}$ in the edge and $v_{pol}^{neo} = 0$, the following simplified expression can be extracted:

$$\left[1 - \frac{R^2 B_{tor}^2}{\langle R^2\rangle\langle B^2\rangle}\right] \frac{\langle B^2\rangle}{\langle B_{pol}\rangle^2} \frac{\partial v_{pol}}{\partial t} = -\mu \frac{\langle B^2\rangle}{\langle B_{pol}\rangle^2} v_{pol} - \langle \tilde{v}_r^2\rangle \frac{\partial \frac{\partial v_{pol}}{\partial r}\tau_c}{\partial r} \tag{6.17}$$

Recall that at the outboard midplane, $\left[1 - \frac{R^2 B_{tor}^2}{\langle R^2\rangle\langle B^2\rangle}\right] > 0$. If v_{pol} is positive, $\frac{\partial v_{pol}}{\partial t} > 0$ is only possible if there is a portion of the rotation profile that is concave down ($\frac{\partial^2 v_{pol}}{\partial r^2} < 0$). Furthermore, this concavity term $\frac{\partial^2 v_{pol}}{\partial r^2}$ must be sufficient strong in comparison to the absolute poloidal rotation v_{pol} for a growing solution to exist. Specifically, the criteria for poloidal rotation to be growing in time is:

$$-\langle \tilde{v}_r^2\rangle \tau_c \frac{\partial^2 v_{pol}}{\partial r^2} > \mu \frac{\langle B^2\rangle}{\langle B_{pol}\rangle^2} v_{pol} + \langle \tilde{v}_r^2\rangle \frac{\partial v_{pol}}{\partial r}\frac{\partial \tau_c}{\partial r} \tag{6.18}$$

Therefore, if the L-H transition trigger criteria is that v_{pol} must be allowed to grow in time,

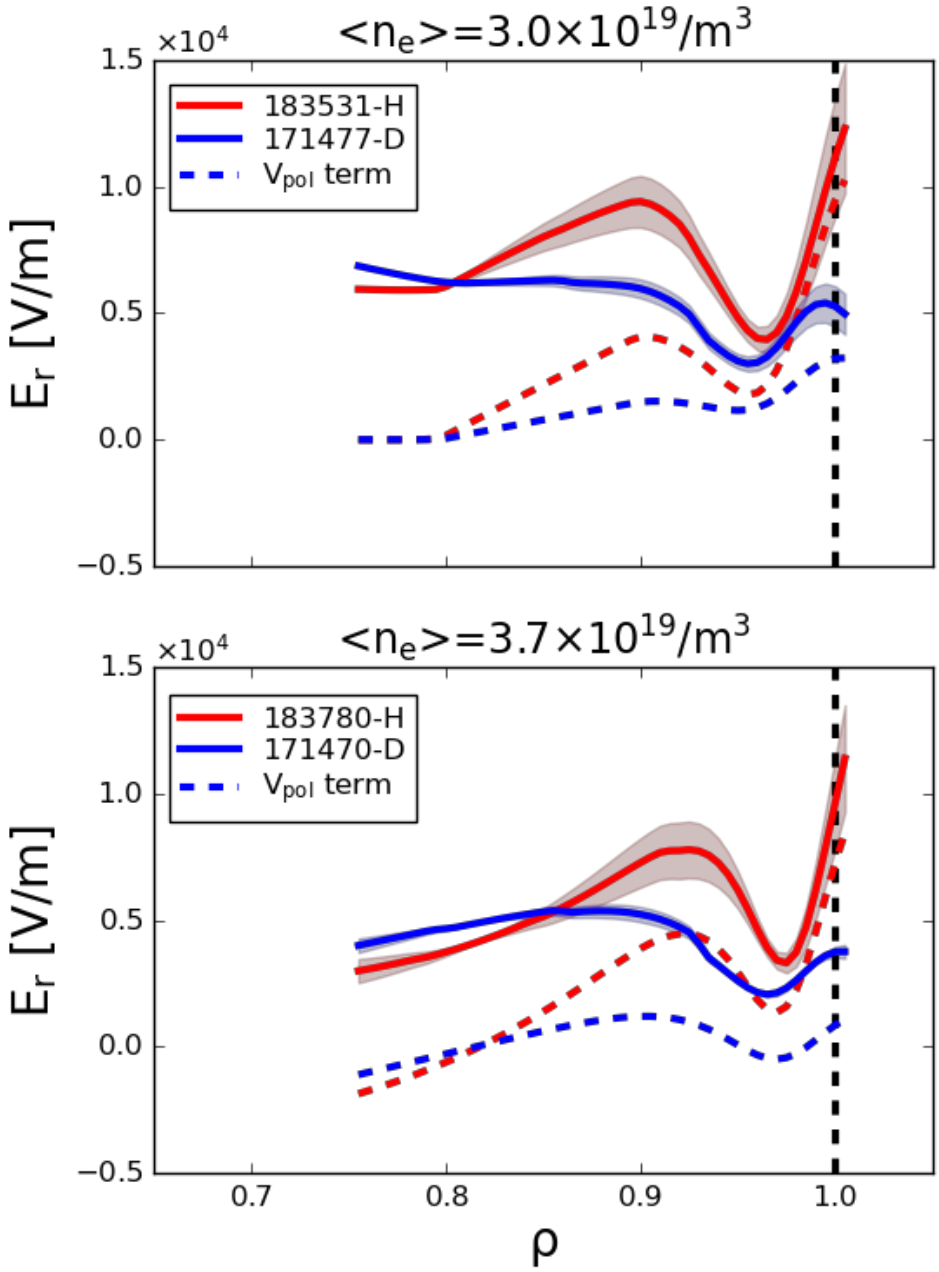

Figure 6.12: Radial electric field profiles of hydrogen (red) and deuterium (blue) ITER similar DIII-D plasmas at higher densities compared to previously analyzed experiments. Solid lines indicate full E_r predictions, while dashed lines show only contributions from the poloidal velocity force balance component.

this criteria implies that the absolute value of the edge poloidal rotation velocity helps control this threshold level. This trend is consistent with the linear correlation between P_{LH} and v_{pol} seen via a large DIII-D database shown in Fig. 6.7. This idea is additionally consistent with the observation that E_r has a well-like structure which is concave down in the inner shear layer just before transition. Recall that experimentally $\langle \tilde{v}_r^2 \rangle \propto P_{input}$. Therefore, coupled with a reduced transport model, these equations may permit an L-H threshold estimate.

6.4 Summary

During the span of this thesis chapter, experimental analyses were discussed which studied an edge radial electric field E_r isotope effect uncovered between hydrogen and deuterium dimensionally matched plasmas. The differences between hydrogen and deuterium E_r profiles was investigated from two perspectives: in the open field line and closed field line regions. In the open field line region, Langmuir probe data suggested changes in the outer strike point T_e were responsible for the isotope based E_r differences in the scrape off layer. The hydrogen plasma, having a hotter outer strike point, experienced a larger sheath and space potential, leading to a larger E_r compared to deuterium counterparts. With the aid of UEDGE multi-fluid edge-plasma transport modeling, these temperature and electric field differences were correlated with changes in upstream density profile changes, potentially from changes in neutral penetration between isotopes. Further UEDGE simulations discerned that divertor specific isotope effects were unlikely to be responsible for observed scrape off layer E_r differences, with changes inside the closed flux region instead being the dominant contributors. In the closed field line region, radial force balance analysis of both main ions and carbon impurities hinted that differences in poloidal rotation between isotopes may contribute to E_r differences in the closed field line region. Poloidal momentum balance analyses were found to be consistent with these observations, suggesting that isotope based differences in turbulent Reynolds stress are responsible for poloidal rotation changes. The Reynolds stress differences found between hydrogen and deuterium are consistent with $\vec{E} \times \vec{B}$ eddy tilting predictions. Consequently, the observed Reynolds stress differences between

isotopes are found to be directly related to the equilibrium E_r profile, suggesting the poloidal rotation and E_r are self-generated quantities. These closed field line analyses therefore fall short of discovering the precise origin of the closed field line E_r isotope effects due to this circular dependence on E_r, however point to differences in poloidal rotation and Reynolds stress as important contributing phenomena.

Much can potentially be learned from the observations made in the detailed profile analysis. In particular, the expressions which appear to accurately predict the plasma's Reynolds stress (equation 6.14), v_{pol} (equation 6.15), and E_r (equation 6.1) can likely be coupled together into a series of non-linear equations which feedback on one-another. Additional observations suggesting a nearly time-independent separartrix E_r and v_{pol} for either isotopic configuration permit the usage of simple boundary conditions in modeling. Detailed numerical analysis of these equations with such considerations in mind, which is beyond the intended scope of this section and thesis document, may be sufficient to estimate a rudimentary power threshold if bifurcating behavior is observed. These initial experimental analyses and observations lay the groundwork for such advanced numerical modeling, and possible L-H threshold predictions.

CHAPTER 7

Test of isotope observations with new hydrogen data

In this thesis chapter, following heat flux isotope effect findings discussed in detail in chapter 4, a special DIII-D PhD experiment in hydrogen was conducted to investigate whether differences in Z_{eff} between isotopes may be responsible for the observed L-H transition power threshold isotope effect. The material presented in this chapter, similar to previous, have been submitted to the Nuclear Fusion scientific journal for publication. The chapter sections below discuss the experimental hypothesis tested, the design criteria for the experiments executed, plasma observations prior to L-H transition, and at L-H transition. The experiments conducted, which successfully injected more carbon than naturally sputtered in hydrogen plasmas to match deuterium counterparts using the Impurity Powder Dropper system, successfully observed Ion Temperature Gradient (ITG) turbulence suppression in L-mode prior to L-H transition. Confirmation of ITG stabilization is verified by TGLF simulations of dimensionally matched hydrogen discharges with and without active carbon injection. At the L-H transition however, the power threshold was not observed to change significantly in magnitude with carbon seeding. As a result, the observed heat transport isotope effects originating from natural differences in carbon content between hydrogen and deuterium plasmas observed previously are found to be decoupled from the L-H power threshold, and not the controlling isotopic behavior. Unchanged as a result of the impurity seeding is the edge radial electric field isotopic effect, poloidal rotation, and turbulent Reynolds stress of the hydrogen plasmas. These observations hint that the isotopic differences in E_r discussed in detail in chapter 6 are more fundamental phenomena, potentially closely connected with the actual isotopic behavior responsible for the P_{LH} isotope effect.

7.1 Hypothesis

Based on the previously described flux-matched CGYRO simulations and turbulence predictions, a hydrogen L-H transition experiment was conducted to test if impurity seeding might reduce the L-H power threshold in hydrogen. The experiments, similar to previously described discharges, were undertaken in the ITER-similar-shape, with ITER relevant edge safety factor ($q_{95} = 3.6$), nearly balanced beam torque, at low density ($n_e < 3.0 \times 10^{19}/m^3$), and in the favorable ion ∇B drift direction. Impurity seeding was performed using the DIII-D Impurity Powder Dropper system [70, 29], which gravitationally drops powder from above the tokamak at the toroidal angle $\phi_{IPD} = 195°$ with a controllable mass flow rate, described in detail in thesis chapter 3. For the experiments undertaken here, carbon powder was injected at a rate between 1-10 mg/s to dope hydrogen plasma to an impurity content comparable to standard deuterium counterparts.

The hypothesis of the experiment, based off previously described nonlinear CGYRO predictions and turbulence observations, was that increased main ion dilution in hydrogen plasmas would stabilize micro-turbulence, allowing for steeper kinetic profiles. In particular, Ion Temperature Gradient (ITG) turbulence was hypothesized as being strongly stabilized, leading to both a steeper ion temperature gradient (a/L_{T_i}) and reduced v_{pol} due to a lower turbulent Reynolds stress. These changes, by radial force balance, would allow for a deeper radial electric field (E_r) well in the plasma edge under carbon seeded conditions. This larger $\vec{E} \times \vec{B}$ shear would then help trigger an L-H transition with less power than normally necessary for hydrogen plasmas. The key observations sought in this experiment to test this hypothesis were as follows:

- Is there Ion Temperature Gradient turbulence stabilization with carbon seeding?

  Test by observing density and power matched hydrogen plasmas for changes in T_i

- Is there a difference in the radial electric field with carbon seeding?

  Test to discern E_r changes at matched density and power.

- Is there a difference in the turbulent Reynolds stress with and without carbon seeding?

  Test by analysis of 2D Beam Emission Spectroscopy velocimetry data.

7.2 Experimental Set-up and Results

The special hydrogen experiments conducted included 2 power ramps per discharge using a combination of (hydrogen) neutral beam and electron cyclotron auxiliary heating. Discharge conditions were chosen to be as ITER similar as possible, with the plasmas being restricted to the ITER similar shape, $q_{95} \approx 3.6$, the low density branch $\langle n_e \rangle = 1 - 3 \times 10^{19} m^{-3}$, and using balanced hydrogen neutral beam injection. Results from the experiments conducted may be seen in Fig. 7.1. In red is a standard hydrogen plasma without active carbon seeding, and in orange is a density matched hydrogen discharge with carbon injected using the IPD system. Panel (a) shows the line-averaged density in units of cm^{-3} vs. time (seconds). Panel (b) illustrates the neutral beam (P_{NB}, solid) and electron cyclotron (P_{EC}, dashed) heating applied in MW. Panel (c) shows the single impurity Z_{eff} measured from $n_{C^{6+}}$ ion and n_e electron densities. Panel (d) contains the applied plasma current in MA, and toroidal field in Tesla. Panel (e) indicates the edge Balmer-α recycling light in units of ph/s/sr/cm^2. Panel (f) shows the outer core impurity ion temperature T_i in units of eV. From panels (a) and (e) one observes a sudden rise in line-averaged density and drop in Balmer-α recycling at 2340 and 2210 ms, and 4120 and 4220 ms for the 1st and 2nd power ramps in shots 196403 and 196462 respectively. These times indicate the 1st and 2nd L-H transitions for these shots. The 1st power ramp is dominantly neutral beam heated, while the 2nd power ramp is a nearly 50/50 mixture of neutral beam and EC heating. Note how the carbon doped plasma in orange observes a slightly delayed L-H transition in the 1st power ramp, and vice versa in the 2nd power ramp. The discharge Z_{eff} values illustrated on panel (c) are observed to be substantially higher in the carbon doped orange discharge compared to the standard case in red, as expected due to carbon seeding from the IPD system. Additionally, the anticipated ion temperature changes with and without carbon seeding from the hypothesis outlined

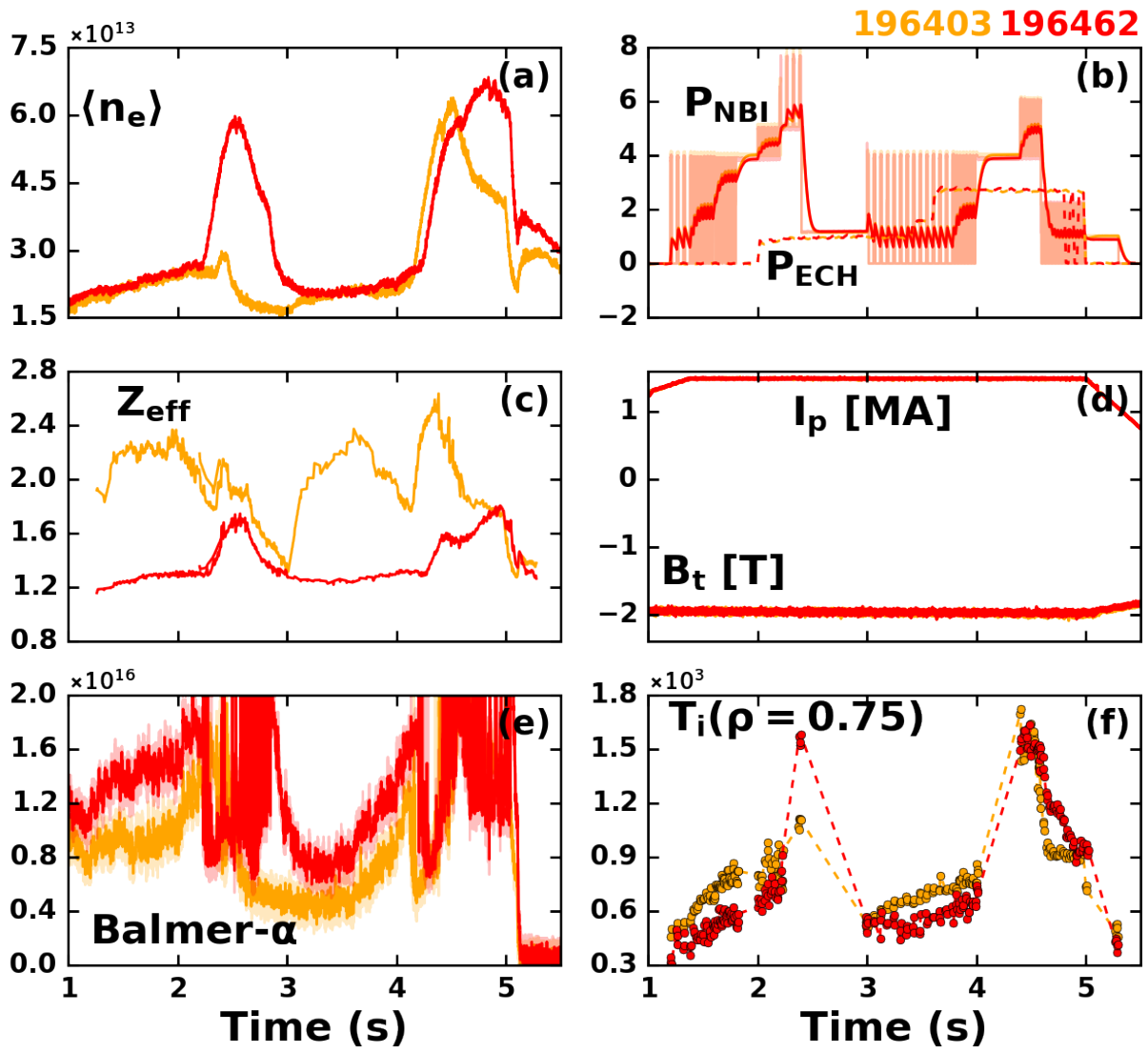

Figure 7.1: Results from DIII-D hydrogen experiments seeding more carbon than naturally sputtered to a density matched standard hydrogen discharge. Standard hydrogen shot traces are shown in red, and the carbon seeded hydrogen plasma traces are in orange.

above were observed, with shot 196403 having routinely higher L-mode ion temperatures compared to the standard hydrogen reference. These preliminary results hint that ITG turbulence stabilization is indeed produced by carbon doping, but leads to no substantial change in the L-H transition power threshold.

These special hydrogen experiments, counter to our hypothesis and expectations, did not illustrate a lower P_{LH} with increasing Z_{eff}. Figure 7.2 demonstrates the results of the experiment, showing normal hydrogen and deuterium transitions in red and blue respectively. In orange are the hydrogen experiments with more than the naturally occurring carbon impurity content, added using the impurity powder dropper system. Note that P_{LH} does not appear to change as Z_{eff} is increased, indicating that it neither helps or hinders with the transition. Similar experiments in hydrogen with Neon gas seeding (not shown) yielded similar results to carbon after accounting for changes in radiative losses. Such observations motivated a more detailed inspection of the standard reference and carbon doped hydrogen discharges illustrated in Fig. 7.1.

7.2.1 L-mode before L-H transition

Detailed profile analysis of shots 196403 and 196462 in L-mode prior to L-H transition was undertaken to identify where the aforementioned hypothesis may have been incorrect. Comparing the two plasmas at identical timing and input powers in L-mode well before the L-H transition, one observes the impact of impurity injection on the plasma profiles clearly. Figure 7.3 illustrates the kinetic profiles in L-mode for the IPD and non-IPD plasma discharges in orange and red respectively. Panels (a), (b), (c), (d), (e), (f), (g), and (h) illustrate the discharge's electron densities, fully stripped carbon impurity densities, ion temperature, electron temperature, impurity poloidal rotation, turbulent Reynolds stress, impurity toroidal rotation, and radial electric field profiles respectively. The solid contours show fitted profiles, with raw experimental data shown as closed circles. The radial electric field profiles shown are those extracted from impurity charge exchange radial force balance as solid contours, and from Doppler BackScattering analysis as closed circles. While the total electron den-

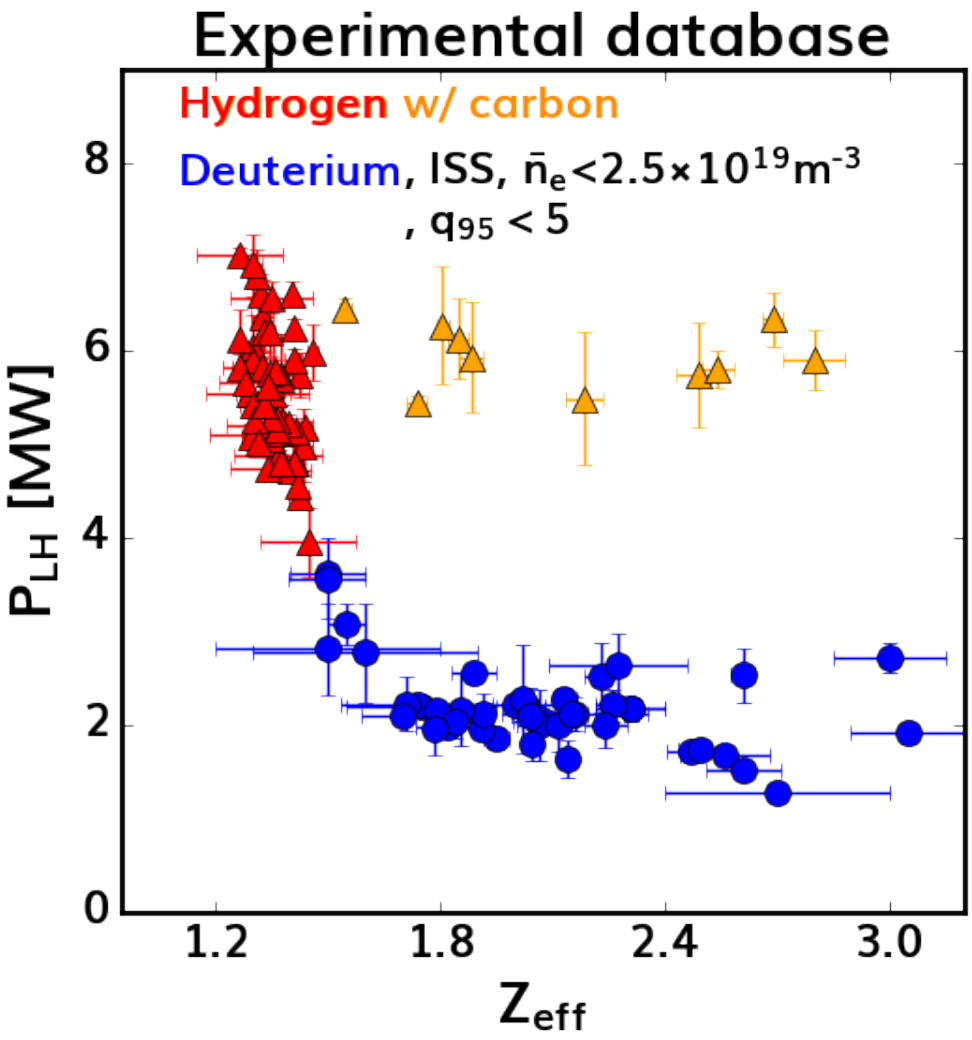

Figure 7.2: P_{LH} vs. L-mode Z_{eff} from $n_{C^{6+}}$ (impCER) and n_e (TS) respectively. Red triangles (blue circles) indicate hydrogen (deuterium) transitions. Orange triangles indicate special hydrogen discharges with active carbon injection from the impurity powder dropper (IPD) system. All discharges shown are in ITER-similar shape, the low density P_{LH} branch, and $q_{95} < 5$.

sity is nearly matched, the carbon content is between 5-7 times higher in the IPD plasma ($Z_{eff} = 1.2 \rightarrow 2.0$). Concurrently, under identical heating conditions, the ion temperature is increased from 1.3 to 2.0 keV on-axis, with gradient steepening going all the way to the plasma edge. Similarly, an increased T_e on-axis is observed, although less dramatic in nature. Gyro-fluid analysis using the code TGLF confirms the observed increase in ion temperature is consistent with increased main ion dilution stabilizing ITG turbulence by up-shifting the ITG critical gradient. Fig. 7.4 demonstrates this behavior by illustrating a 1D scan of normalized ion temperature gradient around the experimental conditions shown in Fig. 7.3. Red and orange closed circles show TGLF saturation rule 2 predictions of ion heat flux for shots 196462 and 196403 respectively, while vertical dashed lines indicate experimental ion temperature gradients. Note particularly that TGLF predicts that there is indeed a shift in the ITG critical ion temperature gradient analogous to results in Fig. 4.9. The experimental gradients are additionally found to be nearly at the critical gradient threshold for either plasma. These TGLF simulations confirm the hypothesis expectation that ITG turbulence was stabilized by carbon doping.

An unanticipated additional change resulting from this impurity injection was a substantial drop in impurity toroidal rotation between the carbon injected plasma (orange) and standard reference (red), likely due to an increase in the plasma's moment of inertia and an additional toroidal momentum sink due to stronger charge exchange losses. Furthermore, measurements of E_r by both impurity force balance and Doppler back-scattering, counter to expectations, did not illustrate signs of a deeper well in the ITG stabilized plasma. In particular, it appears that E_r is nearly unchanged between either case. Similarly, the impurity v_{pol} was unchanged with the turbulence stabilization clearly observable. BES velocimetry analysis, similar to that performed in Fig. 6.11, indicated minimal changes in the turbulent Reynolds stress, counter to hypothesis expectations. Therefore, the lack of increased $\vec{E} \times \vec{B}$ shear with increasing ion temperature gradient was likely the point of failure in the prior hypothesis, with the potential culprit being the unchanging edge v_{pol} and turbulent Reynolds stress. These L-mode results motivated additional analysis just prior to L-H transition.

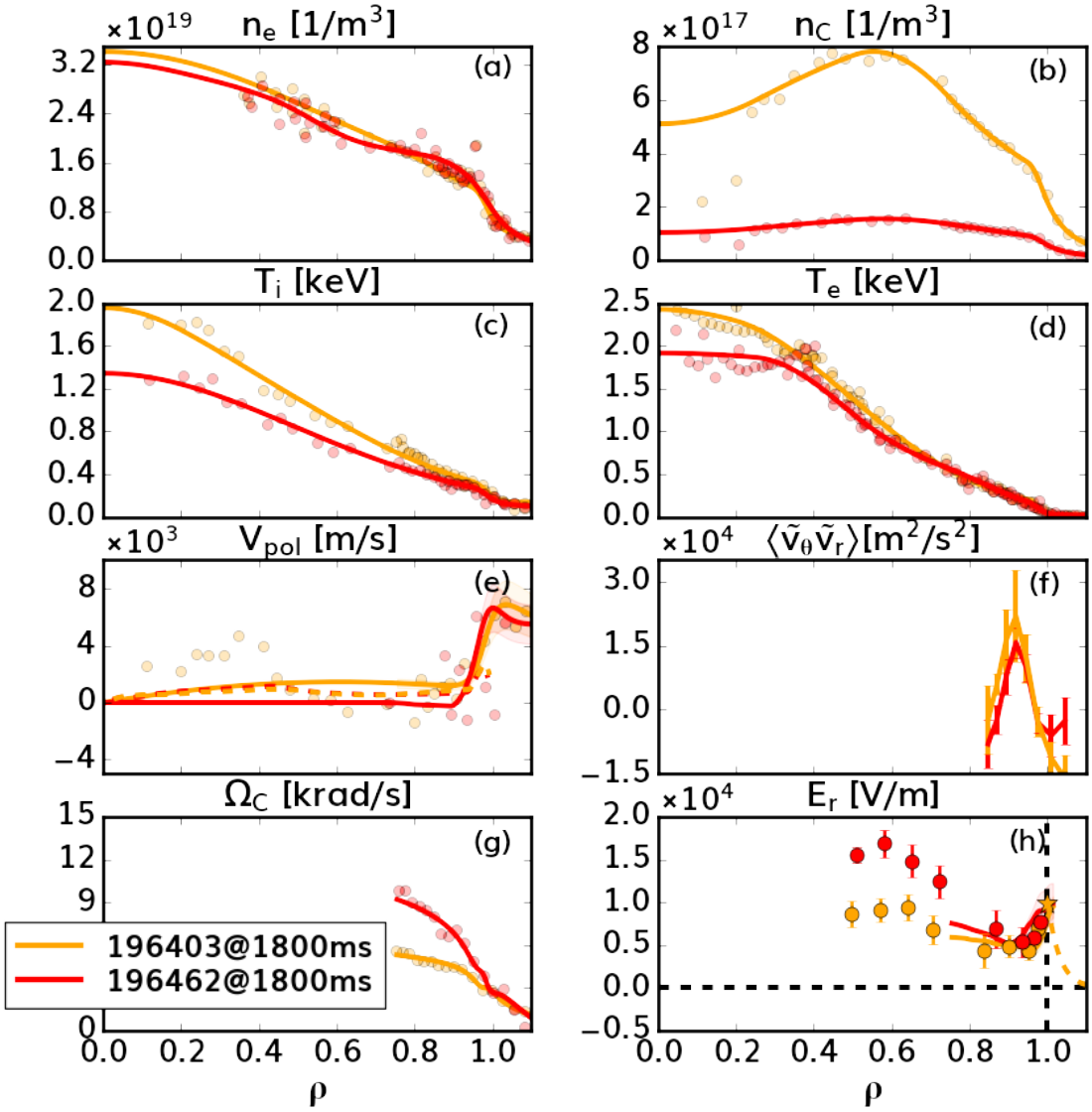

Figure 7.3: Kinetic profiles from a density and power matched set of hydrogen experiments in L-mode. Red illustrates a standard hydrogen discharge, and orange demonstrates hydrogen with active carbon injection. Noteworthy, a steepened ion temperature T_i profile and flattened toroidal rotation profile Ω_C are observed with active carbon injection.

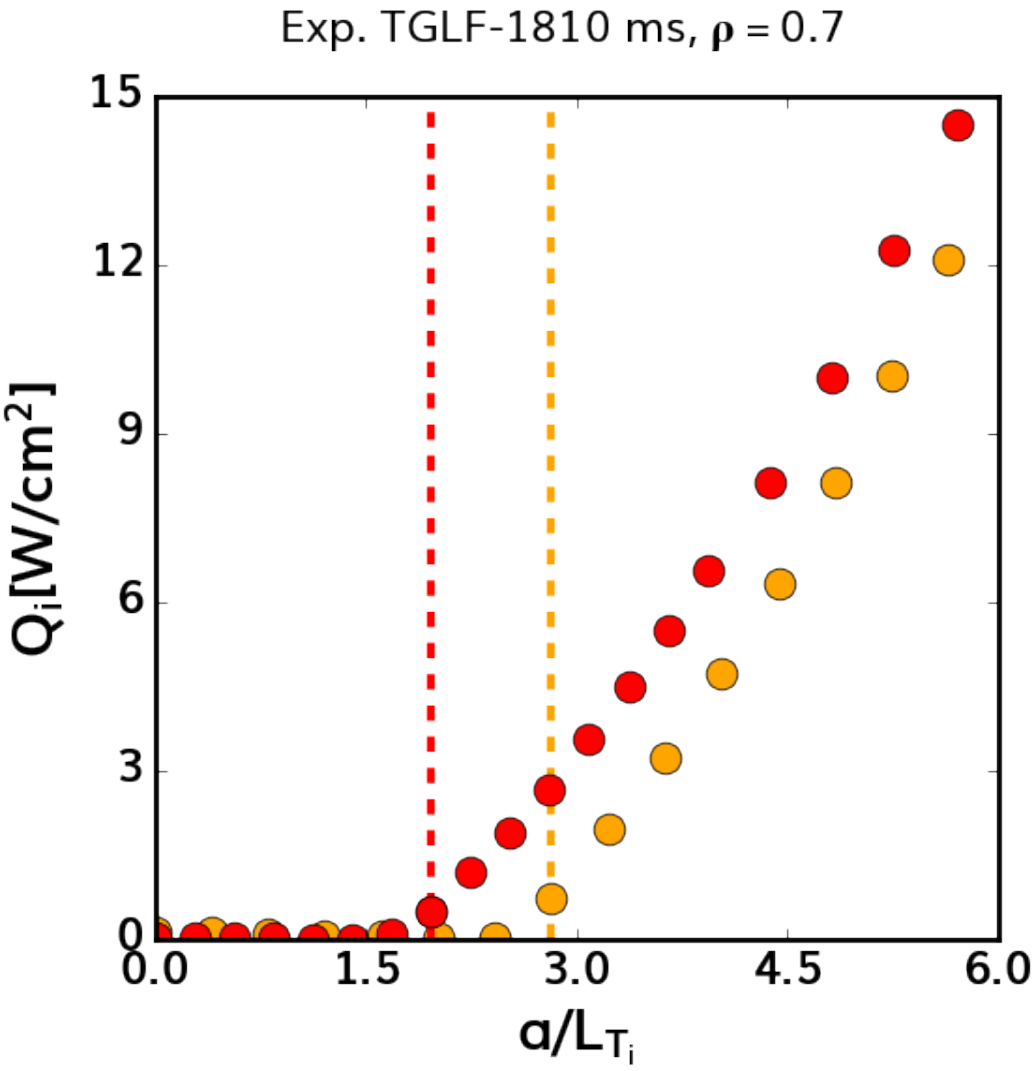

Figure 7.4: TGLF 1D ion temperature gradient scans around experimental results from the profiles fitted in Fig. 7.3. Red closed circles show the standard reference hydrogen discharge 196462, and orange counterparts show the carbon doped discharge 196403. Vertical dashed lines indicate experiment normalized ion temperature gradients extracted shown profiles.

7.2.2 At L-H transition

Dissimilar to earlier times during the L-mode phase well before the L-H transition, the kinetic profiles of the standard and carbon doped plasmas are extremely similar to one another. These profile similarities may be viewed on Fig. 7.5, with identical plotting organization to Fig. 7.3 shown previously. Note how the electron density, ion temperature, and electron temperature kinetic profiles are essentially overlapping, indifferent to the carbon seeding. Additionally, the poloidal rotation, turbulent Reynolds stress, and radial electric fields are very similar for either plasma prior to transition. Similar to in L-mode well before L-H transition, the impurity toroidal rotation is substantially lower in the carbon doped plasma compared to the standard hydrogen case, likely as a result of changes in the plasma's moment of inertia and larger charge exchange momentum losses. These observations suggest that the L-H power threshold is, at the very least, unlikely to be linked with a critical toroidal rotation profile. Further conclusions are difficult to discern given the striking profile similarities just prior to the L-H transition time, which is speculated to be the result of moving from a critical gradient to "stiff" transport regime.

7.3 Summary

In this thesis chapter, a special hydrogen L-H power threshold experiment was described which utilized the Impurity Powder Dropper system to dope plasmas with more carbon than naturally sputtered. The hypothesis of the experiment, based on experimental analyses from thesis chapters 4, 5, and 6 was that carbon doping would stabilize Ion Temperature Gradient driven turbulence. Such stabilization was thought to enable easier H-mode access by allowing steeper ion temperature gradients and reduced turbulent Reynolds stress, which in turn would allow for larger $\vec{E} \times \vec{B}$ rotation shear. This hypothesis however was proven to be incorrect, with hydrogen experiments with carbon doping illustrating no change in the L-H power threshold. As a result, the observed heat transport isotope effects originating from natural differences in carbon content between hydrogen and deuterium plasmas recorded previously

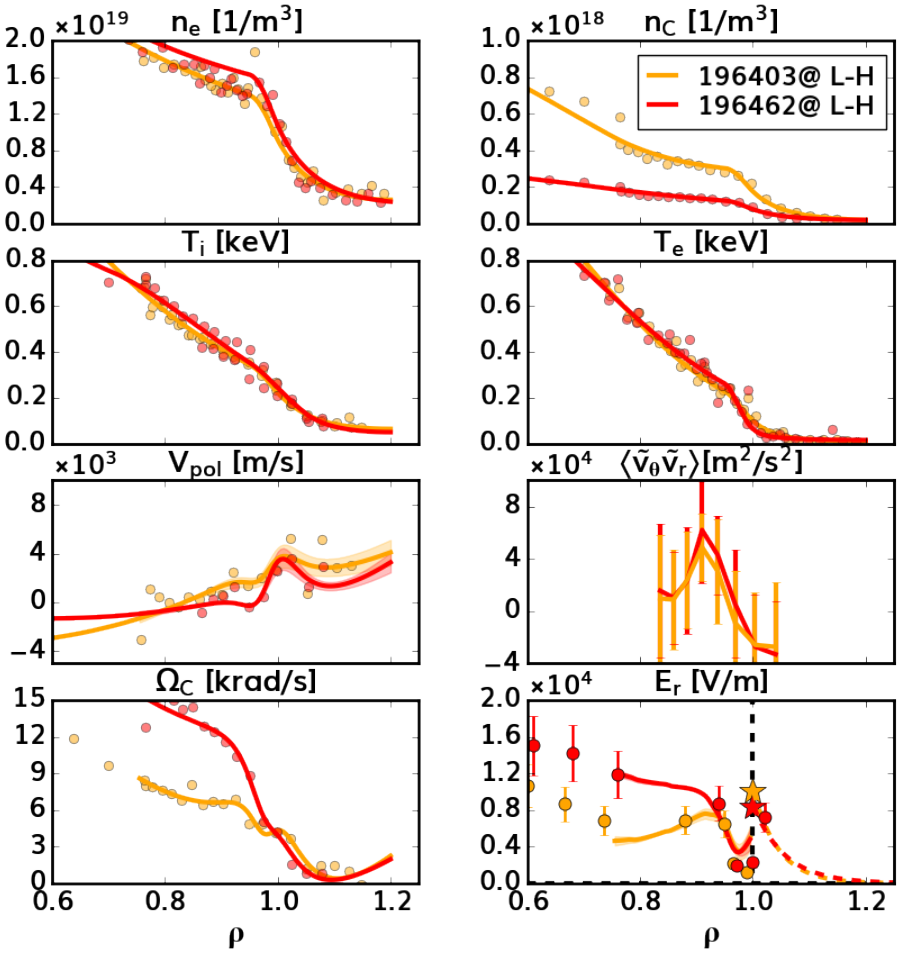

Figure 7.5: Kinetic profiles from a density and power matched set of hydrogen experiments in L-mode. Red illustrates a standard hydrogen discharge, and orange demonstrates hydrogen with active carbon injection. Noteworthy, a steepened ion temperature T_i profile and flattened toroidal rotation profile Ω_C are observed with active carbon injection.

appear decoupled from the L-H power threshold, and not the controlling isotopic behavior. Prior to L-H transition, ITG stabilization is observed, however no substantial changes in the edge radial electric field or turbulent Reynolds stress are identified. At L-H transition, the carbon seeding appears to be inconsequential, with nearly all profiles matching just before the transition time. These analyses and observations suggest the Reynolds stress and radial electric field are not easily changed by ITG turbulence stabilization, and in particular hint that isotopic differences in the edge E_r profile may be closely connected with the P_{LH} isotope dependence.

CHAPTER 8

Conclusions

8.1 Summary and Discussion

The analyses in this thesis have contributed to a more complete understanding of the isotope effects at play within tokamak plasmas. These isotope effects may be divided into two potential sub-categories, heat transport related and radial electric field related isotope effects. Among the heat transport related isotope effects, discussed in detail in thesis chapter 4, the most important is identified as resulting from differences in carbon concentrations in hydrogen and deuterium plasmas. These differences in carbon dilution, which are the result of mass dependent sputtering of graphite tile material, are found to dramatically alter ion temperature gradient turbulence behavior. Specifically, by using the gyrofluid and gyrokinetic codes TGLF and CGYRO, the isotopic impurity behavior is observed to downshift the ion temperature critical gradient for hydrogen compared to deuterium as a consequence of main ion dilution. This heat transport isotope effect was found to be consistent with experimental database trends with respect to plasma effective ion charge Z_{eff}, where increasing Z_{eff} is found to be correlated with a lower L-H power threshold. This correlation, specifically tied to low collisionality plasmas in the banana regime, is experimentally found to reverse as collisionality is increased to the Pfirsch-Schluter regime. Secondary isotope effects in the plasma edge (ρ=0.9) and shear layer (ρ=0.95) were additionally identified which contribute to increased hydrogen heat flux compared to deuterium. These effects, uncovered using the code CGYRO, were found to be associated with an isotopic electron non-adiabaticity effect originally discovered by Dr. Emily Belli [4, 5] and mass dependent $\vec{E} \times \vec{B}$ shear stabilization originally found by Garcia [32] at ρ=0.9 & 0.95 respectively.

These heat transport effects, when considered in totality, allowed for matching of simulated and measured electron and ion heat fluxes at multiple radial locations, ranging from the core to the far edge for both hydrogen and deuterium. These simulations, as a result provided unprecedented information on the turbulence properties of these plasmas. Extraction of raw temperature, density, and velocity fluctuations predicted from these flux-matched nonlinear CGYRO simulations discovered that the origin of the heat flux differences between isotopes was a result of changes in radial velocity fluctuation amplitudes, with density and temperature fluctuations found to be remarkably similar between hydrogen and deuterium. These raw fluctuation spectra, using the computational framework established by White and Holland [113, 47], were used to compute synthetic measurements for comparison to DIII-D's suite of turbulence diagnostics, discussed in detail in chapter 5. Synthetic measurements from both the Beam Emission Spectroscopy and Correlation Electron Cyclotron Emission diagnostics, after accounting for isotope dependencies from beam impact excitation rates and $\vec{E} \times \vec{B}$ rotation, are found to be in good agreement with existing experimental measurements. These comparisons, in addition to velocimetry analysis detailed in chapter 6 which uncovered higher radial velocity fluctuations $\tilde{v}_r$ in hydrogen plasmas compared to deuterium, further validated gyrokinetic simulation predictions from the code CGYRO. These activities have served as a possible first of a kind benchmark of edge gyrokinetic modeling, a tool necessary for enabling accurate predictions of future fusion device performance.

These heat transport isotope effects however, were not the only isotope effects unearthed over the course of this thesis. As alluded to in synthetic diagnostic modeling, sizable differences in the edge $\vec{E} \times \vec{B}$ rotation between hydrogen and deuterium were uncovered within DIII-D plasmas. These edge radial electric field differences between isotopes were further confirmed using 4 independent E_r diagnostic systems at DIII-D: impurity charge exchange spectroscopy, Doppler BackScattering, Beam Emission Spectroscopy, and Langmuir probes. All 4 diagnostics were found to observe an edge radial electric field isotope effect where $E_r(H) \approx 2E_r(D)$. The differing measurement methods of these systems permitted investigation of the E_r isotopic behavior from two perspectives: in the open and closed field line

regions. Analysis of the open field line region, leveraging Langmuir probe measurements at the outer strike point, found the higher E_r in hydrogen is the result of a larger sheath potential and strike point temperature T_e. Using the UEDGE fluid modeling code, these temperature and electric field differences in the scrape off layer were found to be correlated to a small but important shift in the upstream density profile between isotopes. Specifically, density changes inside the separatrix, possibly the result of isotopic neutral penetration, are found to be necessary for explaining the observed differences in E_r and T_e. In the closed field line region however, radial force balance analysis using the charge exchange spectroscopy diagnostic implicated differences in the (impurity/main ion) poloidal rotation between isotopes as potentially explaining edge E_r differences, counter to naive neoclassical expectations. These v_{pol} differences between isotopes, by poloidal momentum balance modeling, were attributed to differences in turbulent Reynolds stress between isotopes with hydrogen plasmas observing a much more pronounced Reynolds stress spatial gradient. These Reynolds stress differences were found to consistent with residual stress induced from $\vec{E} \times \vec{B}$ eddy tilting. As a result, in the closed field line region, the edge radial electric field and poloidal rotation appear to be self-generated in nature, and associated with differences in Reynolds stress between isotopes.

Based on the documented heat transport and radial electric field isotope effects, a special hydrogen L-H power threshold experiment was undertaken to test the hypothesis if P_{LH} can be reduced by active carbon injection using the Impurity Powder Dropper system. The experiment, contrary to our hypothesis, did not observe a change in the power threshold with added carbon impurities. More detailed investigation into the discharges uncovered that, while ITG based turbulence was indeed stabilized by carbon seeding, this turbulence change had no consequence on the edge radial electric field, associated shearing rate, and Reynolds stress. These data help confirm the existence of the heat transport isotope effects seen previously, however demonstrate that the L-H power threshold isotope effect is not controlled by this specific isotopic heat transport phenomena. This observation is consistent with the thought that poloidal rotation, and not pressure gradients, are the important E_r force balance

contribution needed for triggering the L-H transition. These data additionally hint that the persistent differences in edge radial electric field between hydrogen and deuterium plasmas are more fundamentally linked to the L-H power threshold.

8.2 Future Directions

8.2.1 Numerical L-H transition simulations

Based on these experimental findings, advanced numerical simulations of the L-H transition can possibly be undertaken to distinguish the impact of the isotopic $E_r(\rho = 1)$ boundary condition on power threshold requirements. Specifically, implementation of a self consistent poloidal rotation, time independent Reynolds stress, and E_r calculation based on equations 6.15, 6.1, and 6.14 coupled to a transport model such as TGLF with existing experimental data could be used to determine transition criteria. Such simulations, if proven consistent with experimental observations, may lay the groundwork for accurate isotopic predictions of the L-H power threshold in future devices such as ITER, SPARC, and ARC.

8.2.2 Correlation lengths, times, and Reynolds stress

The correlation lengths and times, as well as the local Reynolds stress, can potentially be determined from the flux-matched hydrogen and deuterium CGYRO simulations shown in thesis chapters 4 and 5. These calculations can possibly be done using the raw CGYRO fluctuation spectra in spectral space (k_x, k_y), or in real space (R,Z) as a result of the synthetic diagnostic signal processing identical to that described in chapter 6. These synthetic measurements may be useful as they can be compared to experiment, providing further validation of gyrokinetic predictions against tokamak data.

8.2.3 Coupled TGYRO and UEDGE simulations

The TGYRO gyrofluid simulations, similar to those shown in thesis chapter 4 (which are used to predict the heat transport coefficients all the way to the plasma edge), can potentially be coupled to the code UEDGE. UEDGE, which requires transport coefficients to run, may then be able to predict the boundary and scrape off layer conditions based on physically meaningful transport coefficients. Such coupled simulations, if proven accurate enough to replicate existing experimental data, may provide a rough method for determining the interplay between the edge turbulence and scrape off layer physics. Such predictions may help give insight into expected divertor heat load conditions in eventual tokamak reactors, and materials requirements necessary to survive such harsh environments.

8.2.4 Global CGYRO simulations

The edge local flux-tube nonlinear CGYRO simulations, like those shown in thesis chapter 4, can potentially be extended into global simulations using simulation architecture similar to those used by Dr. Jeff Candy in reference [21]. These simulations may help capture physics missed by local approximations, and may aid in illuminating the global impact of the $\vec{E} \times \vec{B}$ shear profile on the stabilization of drift-wave turbulence. Such simulations may be instructive for validating the accuracy of the presently shown local simulations, and discerning to what extent global simulations may be necessary to capture the turbulence suppression mechanism intricately linked with the L-H transition.

APPENDIX A

DIII-D L-H transition database

In this thesis appendix, details on the large L-H transition database formed as part of this experimental thesis are provided. Additional documentation on the sub-set of database shots analyzed using TRANSP, as well as their associated TRANSP runIDs, will be provided for the reader.

A.1 Database Information

The large DIII-D L-H transition database formed as part of this thesis, was undertaken with the explicit goal of identifying key physics parameters which elucidate the origin of the L-H transition isotope effect. As a result, many plasma state parameters were recorded during the database formation process. All quantities were determined in the L-mode phase just before L-H transition using an approximate 30 ms time window. The L-H transition times for all discharges were determined manually by consideration of four parameters: edge Balmer-α light, line-averaged density $\langle n \rangle$, normalized plasma pressure β_N, and normalized energy confinement time H_{98}. Specifically the L-H transition time was taken as when a sudden drop in edge Balmer-α recycling light, immediately followed by a rise in line-averaged density $\langle n \rangle$, normalized plasma pressure β_N, and normalized energy confinement time H_{98} occurs. In total, the database consists of 692 L-H transitions in plasmas consisting of deuterium, hydrogen, and helium main ions. Table A.1 summarizes in detail the parameters at L-H transition that were recorded, in addition to their ranges within the database respectively.

From this large set of DIII-D L-H transitions, approximately 80 transitions were selected for detailed analysis using the OMFIT modules OMFITprofiles and TRANSP. These

Table A.1: L-H transition database parameters recorded and extracted from existing MDSplus DIII-D data

Quantity	MDSplus Pointname	Description	Range
shot #			
species		D, H, He	
t_{LH}		L-H transition time	0.3-5.8 s
P_{NB}	PINJ	Neutral beam power	0-8.3 MW
T_{NB}	TINJ	Neutral beam torque	-2-5.7 N-m
P_{OH}	POH	Ohmic heating power	0-1.8 MW
P_{ECH}	PECH	Electron Cyclotron heating power	0-4.3 MW
$P_{rad,core}$	Prad_core	Core radiation loss power	0-1.1 MW
$P_{rad,tot}$	Prad_tot	Total radiation loss power	0-4.5 MW
$\frac{dW_{dia}}{dt}$	Wdia	Diamagnetic stored energy loss power	-0.5-3.5 MW
$\langle n \rangle$	DENSITY	Line-averaged density	0.7-6.4$\times 10^{19} m^{-3}$
B_{tor}	BT	Toroidal magnetic field	-2.2-2.0 T
I_p	IP	Plasma current	0.4-1.6 MA
q_{95}	q95	Edge magnetic safety factor	3-15
R_0	RMAXIS	Magnetic axis major radius	1.67-1.78 m
$R_{mid,out}$	RMIDOUT	Outboard midplane separatrix major radius	2.0-2.31 m
κ	KAPPA	Plasma elongation	1.5-1.95
δ_u	TRITOP	Upper triangularity	0.05-0.8
δ_l	TRIBOT	Lower triangularity	0.1-0.9
V_{loop}	VLOOP	Loop voltage	0-1.9 V
τ_E	TAUE	Global energy confinement time	20-400 ms
H_{98}	H_THH98Y2	Normalized energy confinement factor	0.17-0.9
I_{I-coil}	IU30	I-coil currents	0-5.3 kA
I_{C-coil}	C319	C-coil currents	0-5.5 kA
Z_{eff}	ZEFFT8	$Z_{eff}(\rho = 0.75)$ from C^{6+} impurities	1.1-3.5
T_i	CERATIT8	Ion temperature, $T_i(\rho = 0.75)$ from C^{6+}	150-750 eV
Ω_C	CERAROTT8	Toroidal rotation, $\Omega_C(\rho = 0.75)$ from C^{6+}	-30-60 krad/s
P_{LH}		$P_{NB} + P_{ECH} + P_{OH} - P_{rad,core} - \frac{dW_{dia}}{dt}$	0.75-8 MW

analyses, which fitted profiles across each respective L-H transition, form a much more comprehensive dataset with detailed temporal and spatial information of plasma quantities such as $n_e(\rho)$, $Z_{eff}(\rho)$, $T_i(\rho)$, and $E_r(\rho)$ from impurity radial force balance. The TRANSP runsIDs and approximate L-H transition times of these analyses are provided in tables A.2, A.3, and A.4 below.

Table A.2: TRANSP L-H transition sub-database part 1.

Shot #	Species	TRANSP runID	t_{LH} [s]
171486	D	171486K46	1.58
183521	H	183521K55	1.85
171480	D	171480K10	2.124
183765	H	183765K03	2.06
171494	D	171494K13	2.042
183563	H	183563K07	3.54
161223	D	161223K01	1.75
161217	D	161217K03	1.8
182443	D	182443K03	3.575
156905	D	156905K04	0.83
156908	D	156908K04	0.81
158348	H	158348K06	4.54
158347	H	158347K01	2.19
183550	H	183550K02	1.12
183541	H	183541K04	1.145
183970	H	183970K01	1.19
161225	D	161225K09	5.43
161224	D	161224K06	1.83
161232	D	161232K07	1.915
161226	D	161226K04	3.21
161228	D	161228K06	2.99
158335	H	158335K04	1.59
158353	H	158353K04	4.89
158337	H	158337K06	1.87
158344	H	158344K07	2.02
158295	H	158295K09	1.57
183977	H	183977K01	3.18
183982	H	183982K02	1.38
183971	H	183971K01	1.17
183494	H	183494K01	3.535
183503	H	183503K01	1.88
184040	H	184040K01	1.67
161229	D	161229K03	5.1
161218	D	161218K01	1.85
158358	H	158358K01	4.93
158334	H	158334K02	1.14

Table A.3: TRANSP L-H transition sub-database part 2.

Shot #	Species	TRANSP runID	t_{LH} [s]
158291	H	158291K03	3.25
183515	H	183515K01	2.16
183516	H	183516K01	2.05
183526	H	183526K02	1.88
171491	D	171491K01	3.68
171492	D	171492K01	1.82
171493	D	171493K01	1.67
155193	D	155193K01	1.25
155199	D	155199K01	1.24
184006	H	184006K01	3.62
158348	H	158348K07	1.78
156903	D	156903K01	0.89
155205	D	155205K01	1.16
161231	D	161231K07	1.88
155189	D	155189K01	1.4
156896	D	156896K01	0.82
183915	H	183915K01	2.27
158333	H	158333K01	4.4
171510	D	171510K03	1.22
139993	D	139993K01	1.07
139996	D	139996K01	1.02
186162	D	186162K01	1.8
161239	D	161239K01	2.53
141991	D	141991K01	2.91
186150	D	186150K02	2.85
171470	D	171470K02	2.88
171475	D	171475K02	1.6
158357	H	158357K01	1.91
158352	H	158352K01	2.9
183531	H	183531K02	3.39
184036	H	184036K03	1.81
183782	H	183782K01	2.87
183777	H	183777K01	2.9

Table A.4: TRANSP L-H transition sub-database part 3.

Shot #	Species	TRANSP runID	t_{LH} [s]
171471	D	171471K01	4.83
161215	D	161215K02	1.83
169007	D	169007K01	0.75
192090	D	192090K03	3.3
192090	D	192090K11	1.91
192089	D	192089K05	1.675
192089	D	192089K04	3.3
192408	D	192408K01	1.4
183773	H	183773K01	2.03
192410	D	192410K01	1.42
192413	D	192413K01	1.5
192411	D	192411K04	1.34
183776	H	183776K01	3.98
192088	D	192088K01	1.72
192080	D	192080K02	3.7
192414	D	192414K01	1.62
183998	H	183998K01	4.86
156898	D	156898K01	0.83
183993	H	183993K02	3.14
183984	H	183984K01	1.07

APPENDIX B

DIII-D PhD Experiment Design

In this appendix, a brief description of the DIII-D PhD run time experimental planning procedure is given. This includes discussion on the neutral beam programming considerations used, as well as the principle scan (Z_{eff}) methodology.

B.1 Beam Programming Programming

For the data acquired during this thesis, simultaneous BES + CER measurements while satisfying the constraints $T_{inj} \approx 0$ N-m and $P_{inj} < 2$ MW were highly desired, particularly for deuterium experiments with low P_{LH}. Using the DIII-D Beams OMFIT module, often used to predict the NBI power and torque, a narrow range of voltage and perveance settings was uncovered which fit within these experimental constraints. Fig. B.1 illustrates such a DIII-D Beams prediction based on shot 191000. The closed circles show the measured injected powers (left) and torques (right) for shot 191000 at the experimental beam voltages. The solid/dashed lines indicate predictions of the leftward/rightward neutral beam's power and torque, scanning voltage around their experimental values. Note how lowering the beam voltages tends to decrease both the beam power and beam injected torque. The range of attainable beam voltages is approximately between 40-81 kV. To enable low power and balanced beam injection, both the CER 33LT and BES 15LT beams were operated close to their lowest possible power and torque settings, balanced against a single 21RT beam. The 21RT beam was chosen because it was predicted to inject the most torque per unit power into the tokamak as illustrated in Fig. B.1 as the dashed red curves. The 33LT CER and 15LT BES beams were chosen because they permit high accuracy edge diagnostic measurements.

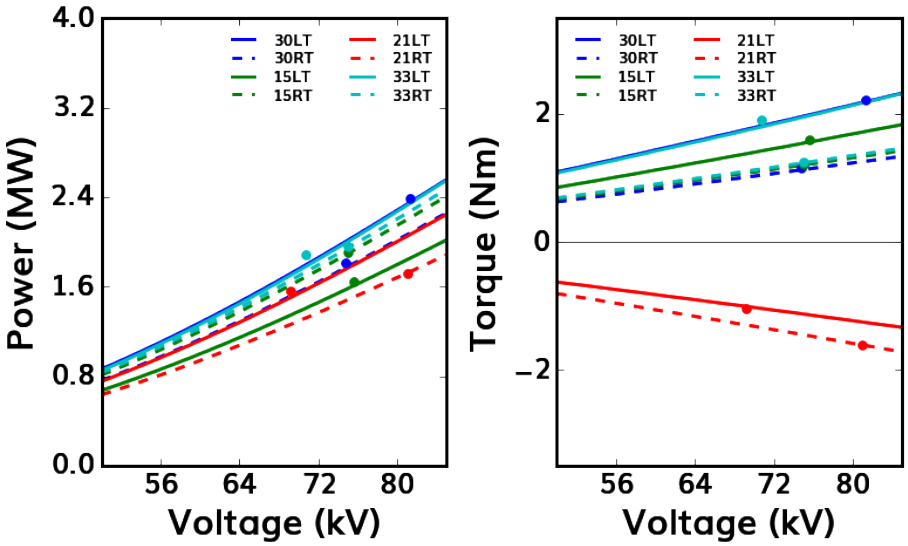

Figure B.1: DIII-D Beams OMFIT module predictions for shot 191000 used in preparation for the deuterium L-H transition experimental design. Closed circles illustrate the experiment's injected powers, torques, and voltages. Solid/dashed curves show the LT/RT beam sources predicted output powers (left) and torque (right) when scanning the beam voltage.

The neutral beam settings which satisfied the constraints $T_{inj} \approx 0$ N-m and $P_{inj} < 2$ MW using the 21RT, 15LT, and 33LT sources were voltages of {80, 50, 45} kV and perveances of {2.65, 2.4, 2.5} respectively. The predicted DIII-D beam injected powers were {1.77, 0.66, 0.67} MW, while the predicted torques were {-1.67, 0.84, 0.83} N-m. These deuterium beam settings were determined with the help of Dr. Shaun Haskey and Dr. Joe Rauch, a DIII-D neutral beam programmer and neutral beam operator respectively. Their input confirmed the beam settings above were within the currently achievable beam settings safety margins. Note that the instantaneous total injected power is nearly 3 MW, noticeably higher than the expected L-H power threshold of 2 MW for deuterium plasmas. To avoid potentially over-powering the experiments immediately into H-mode, as well as to enable accurate determination of the L-H power threshold and time-slice subtraction CER analysis, a power ramp using duty cycled neutral beams was designed. In this power ramp, the 21RT, 15LT, and 33LT neutral beam sources had their duty cycle increased from 25% to 100% in power steps of rough 200 ms (on the order of the an energy confinement time). As a result, the time-average injected power in each steps are 25% to 100% of the total

injected power of 3 MW. In the final step of the power ramp, when the plasmas are expected to be in H-mode, very brief 15 ms neutral beam blips from the 30LT source at nearly full voltage (80 kV) were added to enable a double check of impCER carbon impurity density measurements from the derated 330LT beams. The impCER density measurements from low voltage beams, which are reliant on accurate neutral beam penetration calculations, are prone to systematic uncertainties from inaccurate beam density calculations and benefit from such absolute density checks. Immediately following the final step of the initial power ramp, the original 3 beam sources were turned off, while the 21LT and 30RT neutral beams were fired at 67 and 69 kV with perveances of {2.8, 2.5} for {1.4, 1.5} MW and {-1.0, 1.0} N-m of injected power and torque respectively at 25% duty cycle. This was to maintain a reasonably high core plasma temperature to avoid excessive voltage-seconds losses and flux consumption during the intermediate L-mode phase. Approximately 1 second after the end of the first power ramp, a secondary power ramp using a mixture of electron cyclotron and neutral beam heating was started. Based on available gyrotron constraints (only Luke and Leia), 1.2 MW of ECH was injected at $\rho = 0.4$, as well as 33LT, 15LT, 21RT injection from 25% to 50% duty cycle. The neutral beam timing was programmed using the DIII-D neutral beam timing program TIMCON, with the designed beam program outputs shown in detail in Fig B.2. The TIMCON timing files generated as part of experimental planning are stored on the DIII-D iris cluster at `/fusion/d3d/d3share/timcon/setup_files/callahank/PowerRampBalBeam_bad_ECH.tcnb` for the reader's potential reference. These updated neutral beam programming elements helped recreate deuterium shots 171485-6 with BES measurements.

B.2 Experimental Goals

The goals of the PhD thesis experiments undertaken were to successfully create the deuterium experiment with the above neutral beam constraints for simultaneous CER and BES measurements, and attempt to modify the plasma impurity content Z_{eff} in both deuterium and hydrogen discharges to record its impact on P_{LH}. The levers for raising and lowering

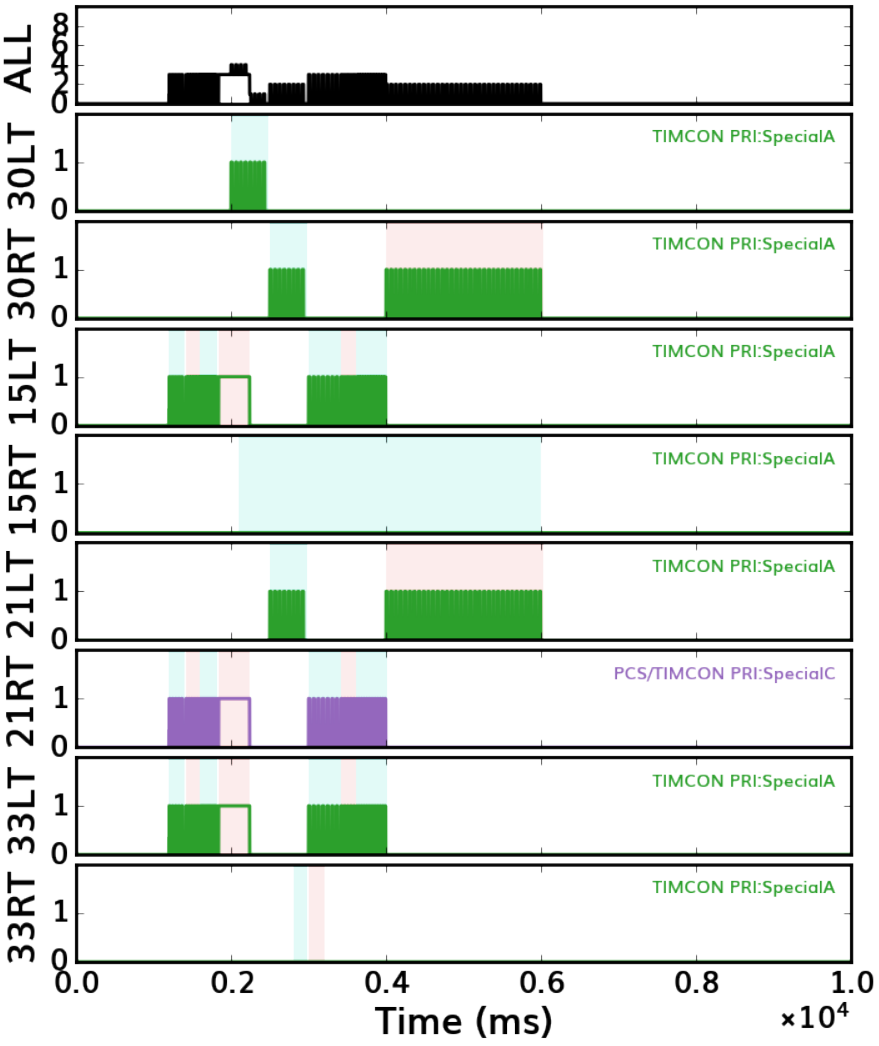

Figure B.2: TIMCON neutral beam programming used for shot 192089. Note how the 15LT, 21RT, and 33LT beam sources have identical timing. The light blue/red background shading indicate the different beam timing phases (power steps) where the duty cycles were changed.

Z_{eff} in the intended deuterium experiments were using the DIII-D impurity powder dropper system [70, 29] and known interdependence between injected torque and impurity content. In hydrogen discharges, only active impurity injection using the DIII-D impurity powder dropper system was necessary, with the goal of matching carbon concentrations from regular deuterium plasmas. The impurity powder dropper system, which gravitational drops powder from the top of the tokamak near the toroidal angle $\phi_{IPD} = 195°$, was used to controllably raise the plasma carbon content. For the given experiments, the IPD system was configured to drop carbon powder into the tokamak at a mass flow rate within the range 1-10 mg/s. Additionally, lowering the carbon content in deuterium plasmas was accomplished by learning from the historical DIII-D L-H transition database in Appendix A. Specifically, it was discovered that there is an interdependence between injected torque and plasma impurity content Z_{eff}, particularly where increased torque appears to result in cleaner plasmas (less carbon). The origin of this interdependence is suspected to be from higher torque plasmas having a larger carbon out-flux due to stronger centrifugal forces or the injection of counter-beams creating larger carbon sputtering by enhanced prompt beam losses. Whatever the cause, this dependency was used as a method for making deuterium plasmas with carbon contents closer to hydrogen counterparts. A figure illustrating the observed torque and carbon impurity content dependence seen in the existing DIII-D data is shown in left panel of Fig. B.3. Red closed circles illustrate hydrogen data, while blue circles show deuterium data. The light blue closed triangle represents the reference deuterium discharge that is the recreation target, DIII-D shots 171485/6. Additional neutral beam timing programs were developed where the torque constraint $T_{inj} \approx 0$ N-m was relaxed to permit lowering Z_{eff}. The changes made to the beam programming included removing the 210° and 30RT beams, and relaxing the stringent settings imposed on the 150LT, 33LT, and 30LT beams for torque cancellation. The TIMCON timing files for this portion of the experiment are stored on the DIII-D iris cluster at `/fusion/d3d/d3share/timcon/setup_files/callahank/PowerRampHighTorque_okay_ECH_short.tcnb`. The beam timing program used in experiment is shown on the right-hand panel of Fig. B.3 for the reader's reference.

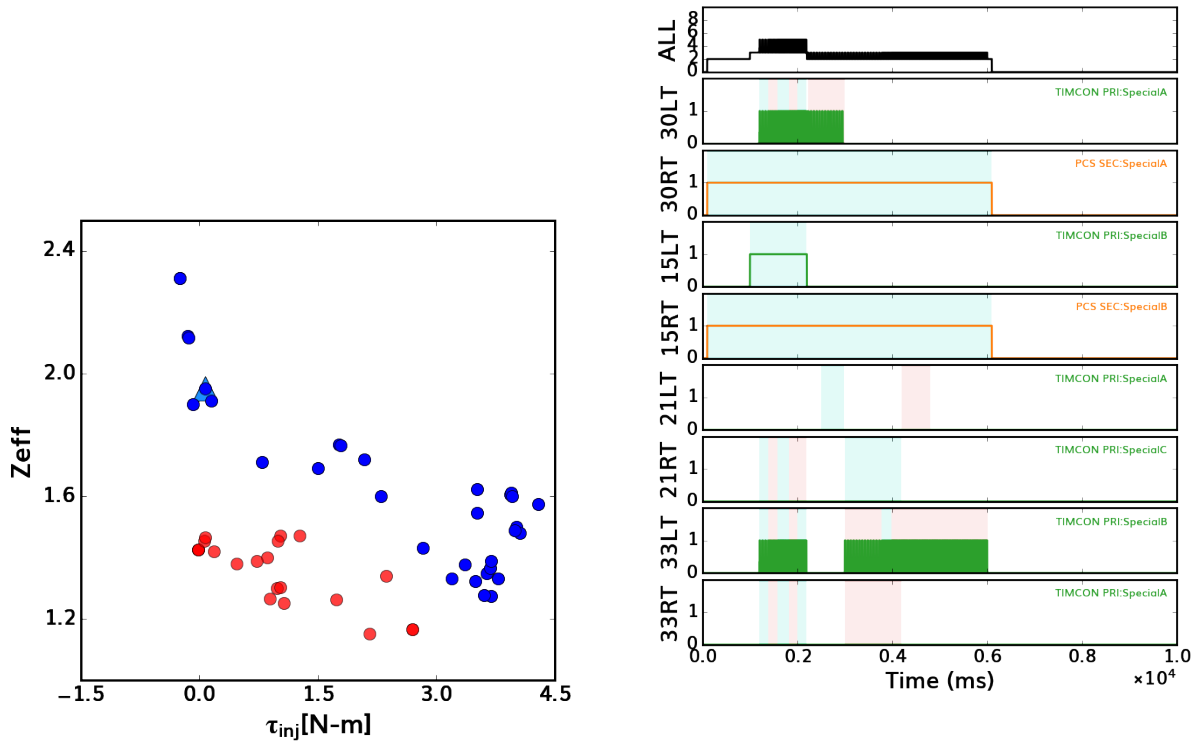

Figure B.3: Left panel: Plasma impurity content Z_{eff} as measured by impCER carbon density and Thomson Scattering electron density vs. time-averaged injected neutral beam torque. Red/blue closed circles illustrate hydrogen/deuterium historical data at L-H transition. The light blue triangle indicates the target reference discharge 171485 for recreation. Right panel: TIMCON neutral beam programming used for shot 192411, where injected torque constraints were relaxed to enable lower carbon impurity content. Note how the 30RT and 15RT traces are shown in orange, on standby, ready to replace their LT counterpart if a technical beam malfunction should occur. The light blue/red background shading indicate the different beam timing phases (power steps) where the duty cycles were changed.

A cartoon summary of the planned DIII-D experimental shot architecture is shown in Fig. B.4, specifically for the low torque deuterium discharge planning process. The top panel illustrates the duty cycle of the different neutral beam sources versus time. The solid orange curve illustrates the 21RT, 33LT, and 15LT beam timings; the solid green curve like-wise shows the 30RT and 21LT beam timing; and the solid gray line is the 30LT beam duty cycle. The middle panel shows the expected injected input power as predicted from DIII-D Beams OMFIT calculations, including changes from the beam duty cycle. The solid blue curve shows the neutral beam power, while the violet and black curves demonstrate the electron cyclotron and total auxiliary input powers respectively. The dashed gray lines illustrate the historical auxiliary power required for L-H transition for a purely NBI heated plasma (171485/6) and pure ECH plasma (191028) for transition. The bottom panel shows the total (time-averaged) NB injected torque, similarly from the DIII-D Beams OMFIT module calculations. The second power ramp with electron cyclotron heating has both gyrotrons (Luke and Leia) turn on simultaneously as opposed to individually as a result of a hardware limitation where both gyrotrons were tied to the same high voltage power supply, thus not independent.

It is with these neutral beam and electron cyclotron heating programming considerations in mind that DIII-D PhD run time was successfully used to study how changes in Z_{eff} alter the L-H power threshold in both hydrogen and deuterium.

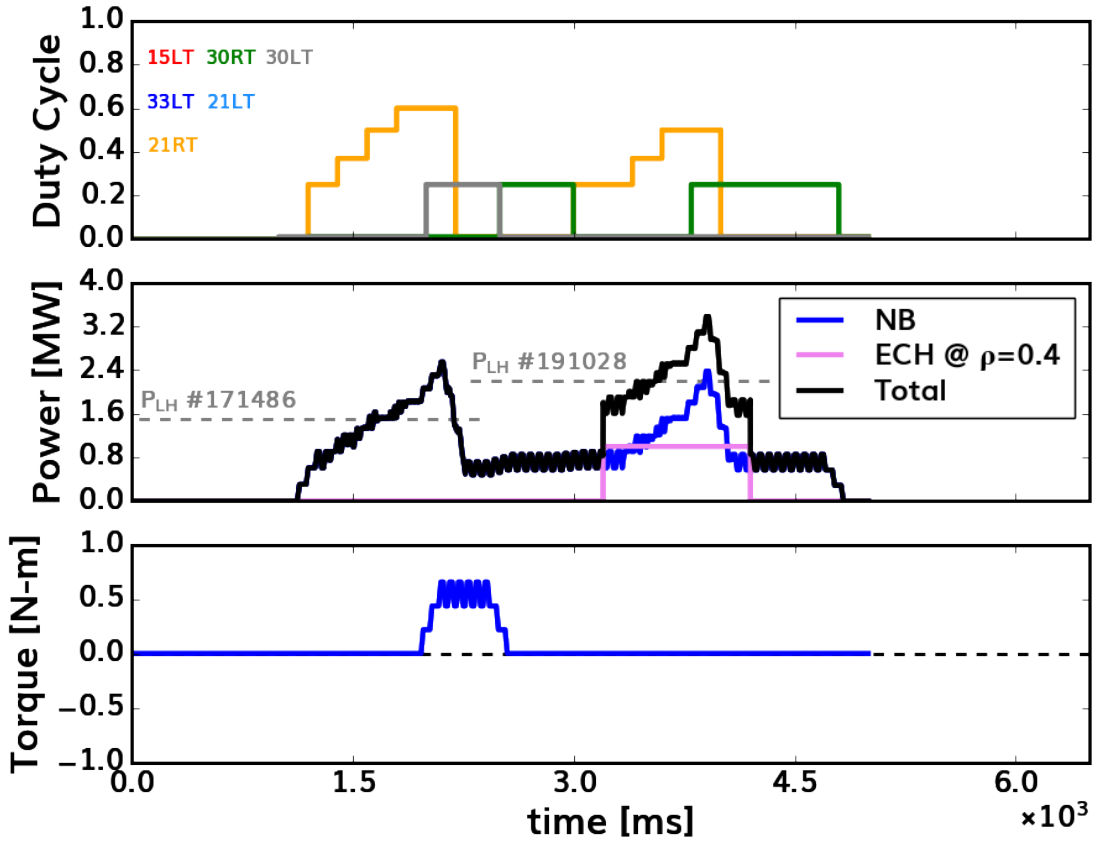

Figure B.4: Cartoon of the neutral beam programming design used for the deuterium L-H transition experiment conducted. The upper panel indicates the different beams duty cycle versus time in ms. The orange curve shows the duty cycle for the 21RT, 33LT, and 15LT. Likewise the green curve illustrates the 21LT and 30RT beam duty cycles, while gray shows 30LT. The middle panel indicates the neutral beam, electron cyclotron, and total injected auxiliary power in blue, violet, and black respectively. The gray dashed lines indicate historical L-H power threshold auxiliary powers. The lower panel shows the neutral beam injected torque, as calculated from DIII-D Beams OMFIT calculations.

APPENDIX C

Gyrofluid and Gyrokinetic simulation details

In this appendix, additional details regarding the gyrofluid and gyrokinetic simulation results shown in thesis chapter 4 are provided for the reader's edification.

C.1 TGYRO Saturation Rule comparisons

As part of the TGYRO analysis workflow, whose key results are shown in thesis Fig. 4.8, TGYRO simulations were performed for all available saturation rules for both hydrogen and deuterium shots 183521 and 171486. The simulations which utilized saturation rule 0 and 1 are shown below for completion. Identical to the previously referenced plots for sat 2, the red and blue solid lines indicate the experimental electron temperature, ion temperature, electron heat flux, ion heat flux, and normalized temperature length scale profiles vs normalized minor radius coordinate ρ. The experimental heat fluxes shown were determined from TRANSP power balance analysis. The dashed lines illustrate the flux matched TGYRO solutions, where the ion and electron temperature profiles and gradient length scales were adjusted to find a flux matching solution between TGLF reduced model predictions and power balance expectations. The star symbols indicate the radial grid points used in the TGYRO simulations. All simulations shown are electromagnetic (ϕ, $A_{\parallel}$, $A_{\perp}$), however no substantive profile prediction differences are noticed when compared to simpler electrostatic counterparts. This is consistent with the expectation that low β plasmas usually have electrostatic ITG/TEM dominant turbulence.

Fig. C.1 summarizes TGYRO simulation results using saturation rule 0. Note how both the predicted ion and electron temperature profiles following flux-matching are noticeably

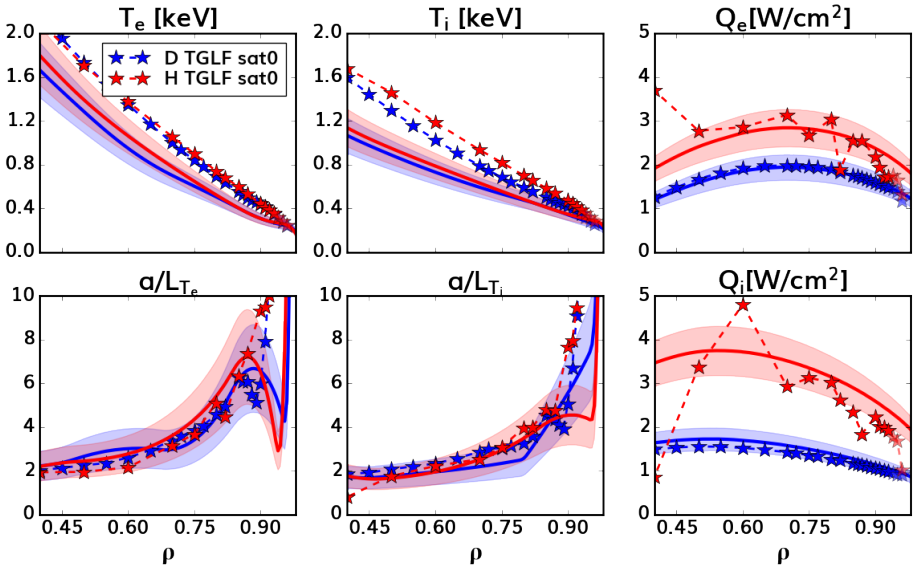

Figure C.1: L-mode temperature profiles and normalized gradients approximately 10 ms before L-H transition for hydrogen (red) and deuterium (blue) plasmas at DIII-D vs normalized radius ρ in solid lines. Heat flux profiles are from TRANSP power balance analysis, with the time-averaged variation in heat flux as error bands, also shown as solid lines. Red and blue (H,D) dashed lines and closed star symbols indicate TGLF flux matching solutions to T_i and T_e using sat. rule 0.

higher than those from experiment. The potential origin of these deviations, by inspection of the normalized temperature length scales, is an over-prediction of the gradients in the edge where $\rho > 0.85$. Based on these deviations, the predictions from TGYRO using sat 0 were determined to be poorly matched to experiment.

Fig. C.2 likewise summarizes TGYRO simulation results from applying saturation rule 1. These predictions, as may be expected by using a much more modernized and physics informed saturation rule, are in closer agreement with experiment compared to saturation rule 0 results. In particular, deuterium ion and electron temperature profile predictions appear to be in excellent agreement with experiment. Hydrogen simulations however appear to contain a large over-prediction in ion temperature. Inspection of these simulations suggests that changes in the edge normalized ion temperature gradient length scales with $\rho > 0.85$ are likely the cause. These observations are considered to much closer approximations of

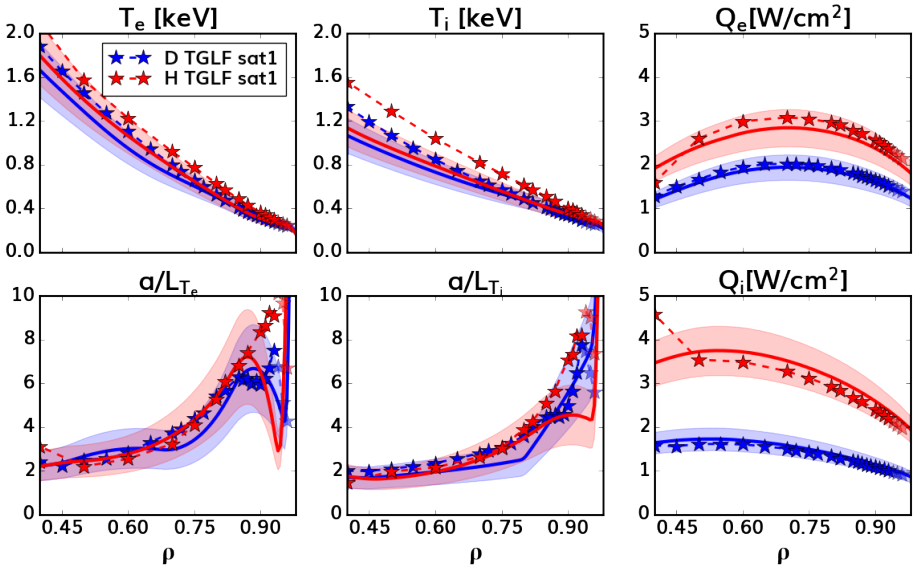

Figure C.2: L-mode temperature profiles and normalized gradients approximately 10 ms before L-H transition for hydrogen (red) and deuterium (blue) plasmas at DIII-D vs normalized radius ρ in solid lines. Heat flux profiles are from TRANSP power balance analysis, with the time-averaged variation in heat flux as error bands, also shown as solid lines. Red and blue (H,D) dashed lines and closed star symbols indicate TGLF flux matching solutions to T_i and T_e using sat. rule 1.

experiment compared to saturation rule 0 results.

Fig. C.3 illustrates results from TGYRO simulations using saturation rule 2, with some additional figure components not shown in the main thesis text figure. The dash blue and red lines again indicate the TGYRO predicted temperature profiles by attempting to flux match TGLF sat 2 predictions to experimental power balance results. These sat 2 simulations, for both hydrogen and deuterium this time, observe ion and electron temperature profiles in close correspondence to experimental measurements. As a result, they are considered to be a better reduced physics model compared to sat 0 or sat 1, as one might naively expect as the newest saturation rule model. In order to help determine the physics effect which creates the heat flux differences between hydrogen and deuterium despite remarkably similar profiles, the deuterium TGYRO solutions were controllably modified. Specifically, the shown profiles were fed the carbon content from the hydrogen (red) simulations while maintaining quasi-

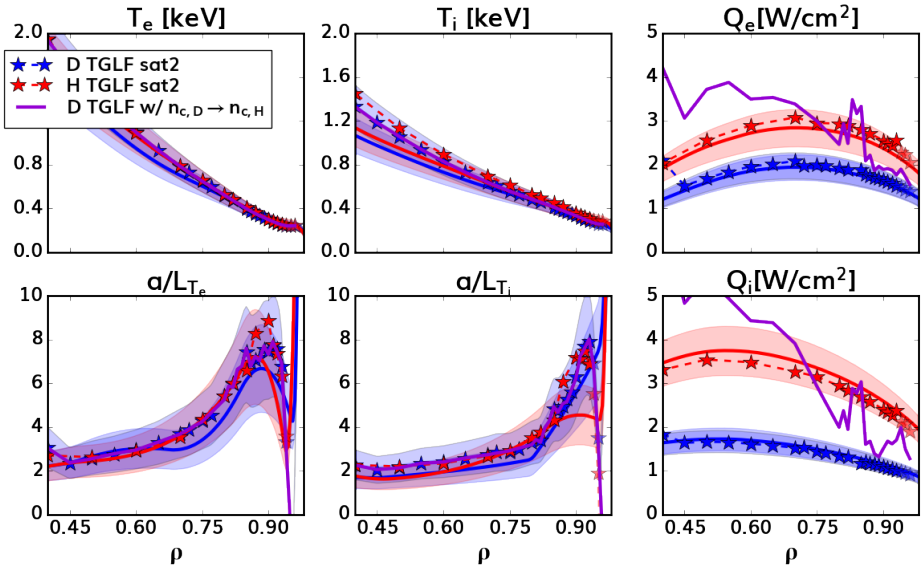

Figure C.3: L-mode temperature profiles and normalized gradients approximately 10 ms before L-H transition for hydrogen (red) and deuterium (blue) plasmas at DIII-D vs normalized radius ρ in solid lines. Heat flux profiles are from TRANSP power balance analysis, with the time-averaged variation in heat flux as error bands, also shown as solid lines. Red and blue (H,D) dashed lines and closed star symbols indicate TGLF flux matching solutions to T_i and T_e using sat. rule 2. The violet solid line is a TGYRO simulation with the D profile solutions and hydrogen carbon density profile.

neutrality. With this single change imposed, TGYRO was run for a single iteration to predict the resulting (not flux matched) turbulent heat fluxes, shown as the solid violet line. These special deuterium simulations indicated that this simple swapping of carbon density profiles dramatically increases both the predicted ion and electron heat fluxes. It is due to these initial swapped simulation results that 1D scans were performed to identify the physics origin of how the carbon density profile is influencing turbulence properties.

C.2 Gyrokinetic simulation details

The flux-matched gyrokinetic results presented in thesis chapter 4, which were meant as a direct follow up to gyrofluid simulation results above, were conducted with certain settings under the guidance of Dr. Emily Belli, Dr. Chris Holland, Dr. Arash Ashourvan, and

Dr. Tom Neiser. It is the goal of this section to describe the variables of these simulations for future reference. All simulations were local flux-tube runs with partially electromagnetic fields (ϕ and $A_{\|}$) with 3 plasma species (electrons, main ions, and carbon impurities) and non-adiabatic electron physics included. The simulations were ion-scale, with $k_y = k_\theta \rho_s < 1.1$, with normalization such that $\rho_s = \rho_{s,D}$ (and $c_s = c_{s,D}$) for all cases. The associated tables are color coded to indicate the quantitative differences between hydrogen and deuterium simulation inputs.

Table C.1: Input parameters for deuterium flux-matched nonlinear CGYRO simulations at $\rho = 0.7$

Quantity	Value
n_y	16
n_x	210
Box Size	12
Δk_y	0.067
a/L_{n_e}	1.377
a/L_{T_e}	3.698
a/L_{n_D}	1.092
a/L_{T_D}	2.765
a/L_{n_C}	2.665
n_D/n_e	0.819
n_C/n_e	0.03014
Z_{eff}	1.904
T_D/T_e	0.8447
$\nu_{ei}[a/c_s]$	0.1484
a/c_s [μs]	3.096
$\gamma_e[a/c_s]$	2.48×10^{-2}
β_e	3.857×10^{-4}
$\rho^* = \rho_{s,\text{unit}}/a$	1.981×10^{-3}
q	-1.789
$\hat{s} = rd(\ln q)/dr$	1.713
κ (elongation)	1.459
δ (triangularity)	0.16184
ζ (squareness)	-0.01475

Table C.2: Input parameters for hydrogen flux-matched nonlinear CGYRO simulations at $\rho = 0.7$

Quantity	Value
n_y	16
n_x	210
Box Size	12
Δk_y	0.067
a/L_{n_e}	1.377
a/L_{T_e}	3.698
a/L_{n_H}	1.336
a/L_{T_H}	2.765
a/L_{n_C}	1.843
n_H/n_e	0.919
n_C/n_e	0.0135
Z_{eff}	1.405
T_D/T_e	0.8447
$\nu_{ei}[a/c_s]$	0.1484
a/c_s [μs]	3.096
$\gamma_e[a/c_s]$	2.48×10^{-2}
β_e	3.857×10^{-4}
$\rho^* = \rho_{s,\text{unit}}/a$	1.981×10^{-3}
q	-1.789
$\hat{s} = rd(\ln q)/dr$	1.713
κ (elongation)	1.459
δ (triangularity)	0.16184
ζ (squareness)	-0.01475

Table C.3: Input parameters for deuterium flux-matched nonlinear CGYRO simulations at $\rho = 0.9$

Quantity	Value
n_y	16
n_x	210
Box Size	28
Δk_y	0.067
a/L_{n_e}	4.426
a/L_{T_e}	6.574
a/L_{n_D}	4.583
a/L_{T_D}	5.558
a/L_{n_C}	3.685
n_D/n_e	0.8247
n_C/n_e	0.02921
Z_{eff}	1.876
T_D/T_e	1.106
$\nu_{ei}[a/c_s]$	0.507
a/c_s [μs]	4.9211
$\gamma_e[a/c_s]$	9.86×10^{-2}
β_e	6.802×10^{-5}
$\rho^* = \rho_{s,\text{unit}}/a$	1.002×10^{-3}
q	-3.029
$\hat{s} = rd(\ln q)/dr$	3.925
κ (elongation)	1.58068
δ (triangularity)	0.27219
ζ (squareness)	-0.03904

Table C.4: Input parameters for hydrogen flux-matched nonlinear CGYRO simulations at $\rho = 0.9$

Quantity	Value
n_y	16
n_x	210
Box Size	28
Δk_y	0.067
a/L_{n_e}	4.426
a/L_{T_e}	6.574
a/L_{n_H}	4.470
a/L_{T_H}	5.558
a/L_{n_C}	3.917
n_H/n_e	0.9204
n_C/n_e	0.01326
Z_{eff}	1.398
T_D/T_e	1.106
$\nu_{ei}[a/c_s]$	0.507
a/c_s [μs]	4.9211
$\gamma_e[a/c_s]$	9.86×10^{-2}
β_e	6.802×10^{-5}
$\rho^* = \rho_{s,\text{unit}}/a$	1.002×10^{-3}
q	-3.029
$\hat{s} = rd(\ln q)/dr$	3.925
κ (elongation)	1.58068
δ (triangularity)	0.27219
ζ (squareness)	-0.03904

Table C.5: Input parameters for deuterium flux-matched nonlinear CGYRO simulations at $\rho = 0.95$

Quantity	Value
n_y	16
n_x	210
Box Size	40
Δk_y	0.067
a/L_{n_e}	8.592
a/L_{T_e}	11.97
a/L_{n_D}	7.502
a/L_{T_D}	11.90
a/L_{n_C}	14.35
n_D/n_e	0.8405
n_C/n_e	0.02658
Z_{eff}	1.797
T_D/T_e	1.080
$\nu_{ei}[a/c_s]$	0.616
a/c_s [μs]	5.5437
$\gamma_e[a/c_s]$	4.808×10^{-1}
β_e	3.425×10^{-5}
$\rho^* = \rho_{s,\text{unit}}/a$	7.969×10^{-4}
q	-3.6408
$\hat{s} = rd(\ln q)/dr$	5.63176
κ (elongation)	1.63473
δ (triangularity)	0.31610
ζ (squareness)	-0.05148

Table C.6: Input parameters for hydrogen flux-matched nonlinear CGYRO simulations at $\rho = 0.95$

Quantity	Value
n_y	16
n_x	210
Box Size	40
Δk_y	0.067
a/L_{n_e}	8.592
a/L_{T_e}	11.97
a/L_{n_H}	8.564
a/L_{T_H}	11.90
a/L_{n_C}	8.915
n_H/n_e	0.9193
n_C/n_e	0.01345
Z_{eff}	1.404
T_D/T_e	1.080
$\nu_{ei}[a/c_s]$	0.616
a/c_s [μs]	5.5437
$\gamma_e[a/c_s]$	1.603×10^{-1}
β_e	3.425×10^{-5}
$\rho^* = \rho_{s,\text{unit}}/a$	7.969×10^{-4}
q	-3.6408
$\hat{s} = rd(\ln q)/dr$	5.63176
κ (elongation)	1.63473
δ (triangularity)	0.31610
ζ (squareness)	-0.05148

APPENDIX D

Radial electric field analysis details

In this appendix, the finer details of the radial electric field analyses results shown in thesis chapter 6 will be shown. This includes an initial brief description of the radial profile fitting analyses performed using the OMFITprofile workflow, followed by using the resulting profiles to determine E_r from the following diagnostics: impurity charge exchange spectroscopy, Doppler BackScattering, Beam Emission Spectroscopy, and Langmuir probes arrays. The shots shown are those analyzed in detail in chapters 4, 5, and 6, low density ITER similar shaped DIII-D L-mode plasmas at conditions similar to that expected in ITER's Augmented 1st plasma stage.

D.1 Profile fitting analysis

Profile fitting analysis was performed using the OMFIT framework [67], and in particular the OMFITprofiles fitting module [60]. This interactive module employs a workflow which allows for the extraction of experimental profile data from DIII-D's MDSplus database, time slicing of raw experimental data, profile fitting using a list of potential fitting functions, and calculation of derived quantities. Some examples of commonly used fitting functions include radial basis functions, splines, inverse length scales, and MTANH functions. Most fitting analyses used the radial basis function or inverse length scales fitting methods to determine radial profiles. This analysis workflow was executed for the deuterium and hydrogen reference shots 171485 and 183521 during the 1st power ramps (NBI only) to extract how the plasma profiles evolve as $P_{loss} = P_{input} - P_{rad,core} - \partial W_{dia}/\partial t \rightarrow P_{LH}$. Fig. D.1 illustrates the deuterium (left) and hydrogen (right) plasma profile changes from well into L-mode in

purple, to at the L-H transition time in yellow. The electron temperature measurements (T_e) illustrated as closed circles, are extracted from both Thomson scattering [72] and Electron Cyclotron Emission [3] data. Similarly, electron density (n_e) is determined from a combination of Thomson scattering data and profile reflectometry. The fully stripped carbon impurity density (n_C), ion temperature (T_i), toroidal rotation (Ω_C), and poloidal rotation (v_{pol}) are determined using data from the impurity charge exchange spectroscopy system (impCER) [27]. Note in both hydrogen and deuterium the carbon toroidal rotation inside $\rho = 0.9$, where $\rho = \sqrt{\psi_N}$ is the square root of the normalied toroidal flux, increases approaching the L-H transition time (purple $\rightarrow$ aqua $\rightarrow$ green $\rightarrow$ yellow). Simultaneously, the ion temperature profiles are observed to increase approaching the transition time, while poloidal rotation appears to be relatively static. In particular, the magnitude of edge impurity poloidal rotation appears to be consistently larger in hydrogen (6 km/s) compared to its deuterium counterpart (3 km/s). Such observations are striking as they point to possible differences in the time evolution of the radial electric field E_r as power is added between different isotopes.

D.2 Radial electric field profiles

To investigate these potentially different time evolving radial electric field profiles in greater detail, and potential differences between isotopes, it is prudent to use all available diagnostic data at our disposal. At the DIII-D tokamak, there exist 4 independent diagnostics which are capable of determining the (edge) E_r profile: impCER, Doppler BackScattering, Beam Emission Spectroscopy, and Langmuir probes. It is the goal of the following sections to detail the analyses used to determine E_r using each of these diagnostic systems. Such an approach has the benefit of allowing for the identification and compensation of potential systematic errors prone to each analysis method, and enable high confidence in the determined E_r profile.

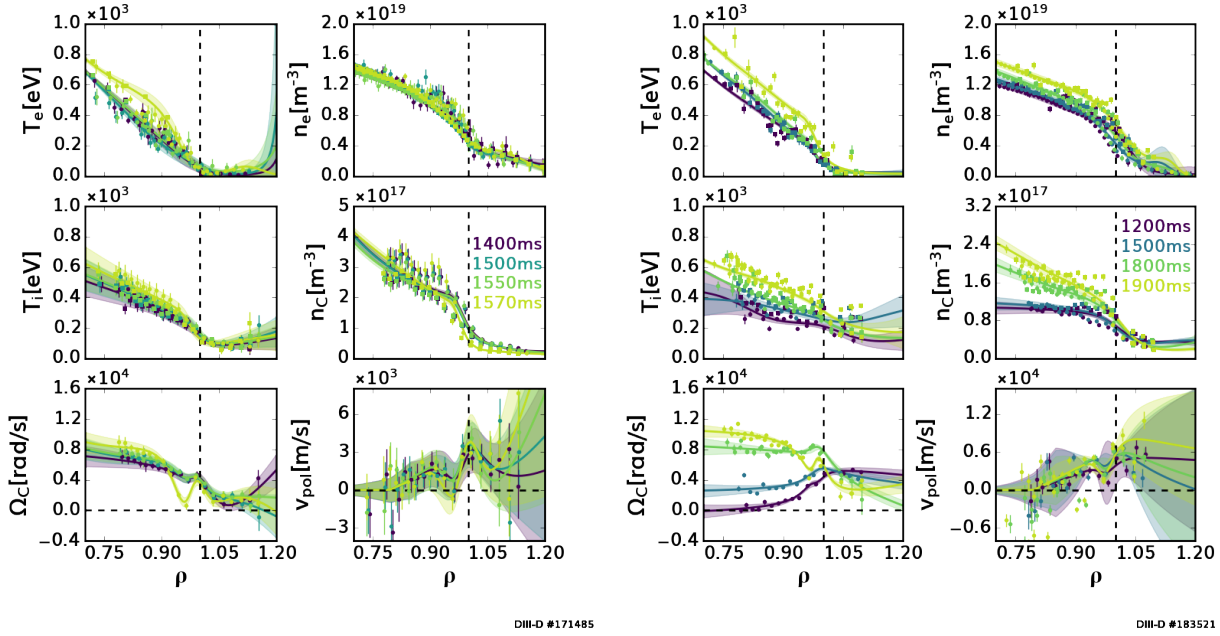

Figure D.1: Radial profiles for the reference deuterium (left) and hydrogen (right) plasmas fitted using OMFITprofiles. The closed circles indicate raw experimental data, while the solid lines show radial profile fits. Color coding indicates times in L-mode approaching the L-H transition time.

D.2.1 Impurity Charge Exchange Recombination Spectroscopy

The longest standing, and therefore by culture, most trusted system in determining the radial electric field profile at the DIII-D tokamak is the impurity charge exchange recombination spectroscopy system (impCER) [27]. This system however, is not without its shortcomings, and is subject to both systematic and random errors. As described in Ch. 3, the impCER system is based upon observing visible light emitted by impurity atoms (usually fully stripped carbon) as they charge-exchange with injected neutral beam particles to gain an electron in an excited state. To be more precise, spectral emission at 529 nm is very usually observed, with carbon being the monitored impurity due to its strong presence in the tokamak due to erosion of the graphite main chamber and divertor tiles. With the modulation of neutral beam sources, measurement of light emission from active charge exchange (between carbon atoms and neutral beam particles) and passive emission (between carbon atoms and naturally occurring edge neutrals) can be disentangled to precisely determine the carbon's local density (n_C), temperature (T_i), and velocity along a given line-of-sight (v_{LOS}). This analysis, which subtracts away passive emission, dubbed CERFIT analysis, was performed on shots 171485 and 183521 to enable very accurate impurity profile measurements, accounting for systematic errors often resulting from passive emission contamination. The data and profiles illustrated in Fig. D.1 show results from such CERFIT analyses. These profile fits can be directly used to determine the radial electric field profile using the impurity radial force balance formula:

$$E_r = \frac{1}{Z_C n_C e}\nabla p_C + v_{tor,C} B_{pol} - v_{pol,C} B_{tor} \tag{D.1}$$

In the above equation, $\nabla P_C = \nabla(T_i n_c)$ is the impurity pressure gradient, $v_{tor,C} = R\Omega_C$ is the toroidal rotation velocity, B_{pol} is the poloidal magnetic field, and B_{tor} is the toroidal magnetic field. Note that the impCER system, like most profile diagnostics at the DIII-D tokamak, measure quantities at the outboard mid-plane. As a result, the radial gradients and magnetic field strengths, which are not flux functions, are evaluated specifically with respect to the outboard mid-plane coordinates. The different contributions to the radial

electric field, based on equation D.1, can divided up into 3 distinct terms: $E_{r,\nabla P_C}$, $E_{r,V_{tor,C}}$, and $E_{r,V_{pol,C}}$ respectively. This deconstruction of the radial electric field into its constituent parts can be useful for discerning where the difference in E_r between isotopes is possibly originating from. Such an analysis was performed on shots 171485 and 183521, using the same time slices as in Fig. D.1.

Fig. D.2 illustrates the deuterium reference discharge's radial electric field evolution approaching the L-H transition time inferred from impurity force balance. Additionally it shows the contributions from each of the 3 force balance terms mentioned previously, also as they change in time. Note how, similar to the previous profile observations, the toroidal rotation contribution $E_{r,V_{tor,C}}$ appears to increase in magnitude inside $\rho = 0.9$ as time evolves forward and power is added. The poloidal rotation contribution $E_{r,V_{pol,C}}$ for this deuterium reference appears to be nearly static prior to the L-H transition time at 1570ms. The total radial electric field demonstrates both of these qualities, an increasing magnitude inside $\rho = 0.9$ and nearly fixed value at the separatrix at $\rho = 1.0$ of approximately 5-6 kV/m approaching the L-H transition time. Quite interestingly, the time just before transition (in green) demonstrates a radial electric field well in the edge that is slightly asymmetric, with the inner shear layer ($\rho \approx 0.9$) demonstrating a higher maximum field strength compared to that at the boundary by nearly 2kV/m. This observation is noteworthy as it is similarly observed in the hydrogen reference case just before transition.

The hydrogen reference discharge's radial electric field profile, and constituent parts from radial force balance considerations, are shown in Fig. D.3. Similar to profile evolution trends observed in Fig. D.1, the toroidal rotation contribution to E_r is observed to noticeably grow inside $\rho = 0.9$. This is very likely the result of both added power and changes in the injected neutral beam torque. Additionally the diamagnetic contribution to the electric field $E_{r,\nabla P_C}$ is observed to become more negative as time approaches the L-H transition time ($\approx$1900ms). Similar to the deuterium reference, the poloidal rotation contribution $E_{r,V_{pol,C}}$ appears nearly static in time, especially at the separatrix. These trends are observable in the total radial electric field profile, where one observes a steady increase in magnitude inside $\rho = 0.9$

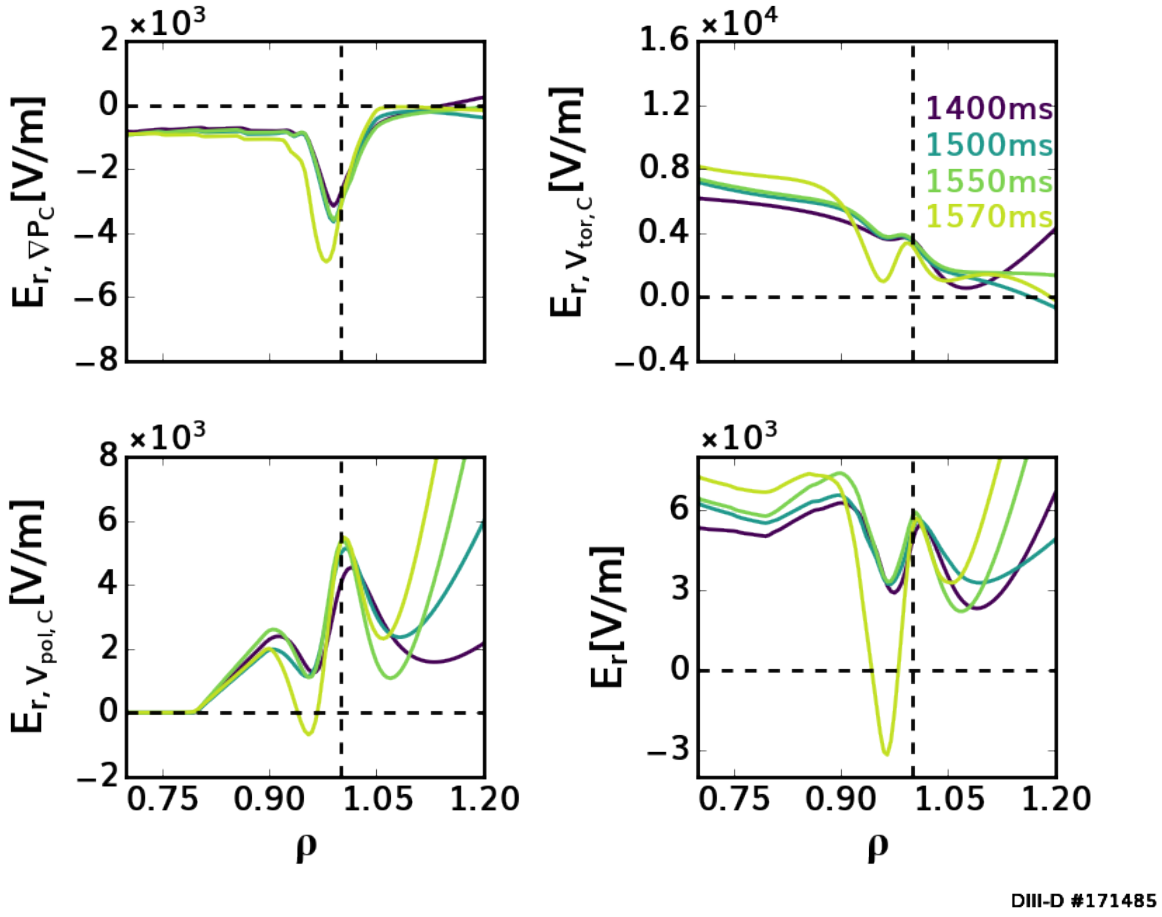

Figure D.2: Radial electric field measurements extracted from impCER radial force balance analysis for the reference deuterium plasma. Color coding indicated different times approaching the L-H transition. Upper left/rigtht panels: Diamagnetic and toroidal rotation contributions to the radial electric field. Lower left panel: poloidal rotation contribution to E_r. Lower right panel: Total radial electric field profile inferred from force balance.

approaching the L-H transition time, a deepening of the radial electric field well seemingly from the changing diamagnetic contribution between $0.9 < \rho < 0.97$, and nearly static in time boundary condition at the separatrix with $E_r = 10 - 12kV/m$. Additionally, very similar to the deuterium reference discharge just before the L-H transition time (1800ms here in green) the peak inner shear electric field is slightly larger than at the separatrix by approximately 2 kV/m. These similarities point to specific radial electric field well conditions possibly necessary for helping instigating the L-H transition in low rotation plasmas. Key among these observations, potentially could be the interplay between the edge ($\rho = 0.9$) and separatrix E_r, and how differences in boundary conditions between isotopes can either facilitate or prevent an E_r well from forming, and as a consequence limit H-mode access. Noteworthy here, one observes the following separatrix radial electric field trend: $E_r(H) \approx 2E_r(D)$. To uncover if this trend may be nonphysical, and the result of imperfections in the impCER diagnostic or radial force balance considerations, additional independent diagnostics will be analyzed.

D.2.2 Doppler BackScattering

The Doppler BackScattering diagnostic (DBS) at the DIII-D tokamak is one which injects beams of microwaves into the plasma from the outboard mid-plane. These injected microwaves are refracted as they enter the scrape off layer and closed flux surface regions, and eventually hit a critical cut-off flux surface to which they become tangent to. At this "turning point", part of the injected microwave can be back-scattered off of local electron density fluctuations in the plasma. These back-scattered waves then travel back along the initial injection trajectory, having picked up a Doppler shift in frequency due to the background plasma's motion. This Doppler shift, which is the result of both the plasma bulk motion and turbulence phase velocity, can be used to infer the plasma's $v_{\vec{E}\times\vec{B}}$ rotation and E_r profile. DBS analysis for shots 183521 and 171485 was undertaken using the DBS60 subsystem, which is comprised of 8 channels injecting microwaves from 55-75 GHz into the plasma. The system was set up to inject microwaves in the X-mode polarization, at a small but finite poloidal

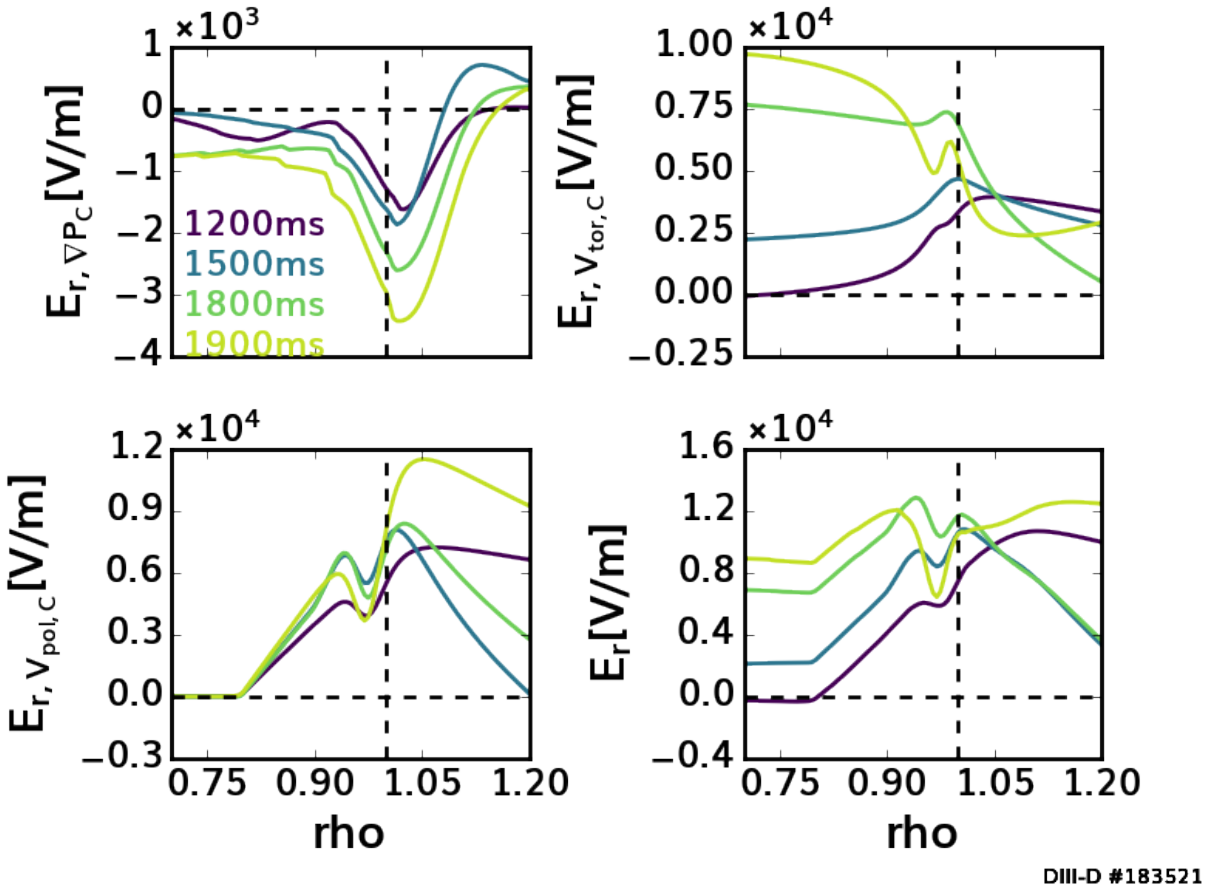

Figure D.3: Radial electric field measurements extracted from impCER radial force balance analysis for the reference hydrogen plasma. Color coding indicated different times approaching the L-H transition. Upper left/rigtht panels: Diamagnetic and toroidal rotation contributions to the radial electric field. Lower left panel: poloidal rotation contribution to E_r. Lower right panel: Total radial electric field profile inferred from force balance.

injection angle ($\approx 6-8°$). The beam trajectories, which cannot be measured directly, are calculated using the beam tracing code GENRAY [88] to extract the beams' back-scattering locations and scattering wave-number $k_\perp$. From all the above, one can estimate $v_{\vec{E}\times\vec{B}}$ from the following expression:

$$v_{Doppler} = \omega_{Doppler}/k_\perp = v_{E\times B} + \tilde{v}_{ph} \tag{D.2}$$

Above $\omega_{Doppler}$ and $k_\perp$ are the measured Doppler shift frequency and perpendicular scattering wave-number of the back-scattered beam respectively. The quantity $\tilde{v}_{ph}$ is the turbulence phase velocity. An example of the injected ray trajectories for the hydrogen reference shot 183521 at 1800ms are illustrated in Fig. D.4 in the left-most panel. Note how the higher injection frequency channels propagate further into the plasma before cutting-off. This cut-off surface is a function of both the magnetic field strength and electron density of the plasma. To be more precise, it is the right hand cut-off frequency: $f_{rh} = 1/2(f_{c,e} + \sqrt{f_{c,e}^2 + 4f_{p,e}^2})$. Recall how the electron cyclotron frequency is $f_{c,e} \propto eB/m_e$ and electron plasma frequency is $f_{p,e}^2 \propto n_e$. Instructive for the reader, on the right-most panel a table of GENRAY outputs is provided. Of particular importance here are the spatial locations of cut-off in ρ and the scattering wave-numbers. The DBS Doppler shift calculation for each channel is performed using a Gaussian or Gaussian-like (Lorentz, Voigt, etc.) fit to the fourier transform of the raw experimental data. An example of such a fitting procedure is shown in Fig. D.5. The solid lines illustrate experimental data from the DBS diagnostic, while the dashed lines illustrate the best fits of the experimental data using a Gaussian (or Gaussian-like) function. Note how the observed Doppler shift frequency becomes smaller as the channels look closer to the edge of the plasma (d3 at $\rho = 0.77$ vs. d6 at $\rho = 0.45$). This trend is partly due to the plasma's change in $\vec{E}\times\vec{B}$ velocity with radius, and the changing $k_\perp$ probed by each channel. This is important because as the channels get closer to the plasma edge, they measure smaller $f_{Doppler}$ values. In the region near $f_{Doppler} \approx 0$, the measured peak can often become degenerate with a commonly observed zero frequency peak. As a result, channels closer to the edge require special inspection and can be prone to large systematic errors due to peak degeneracy.

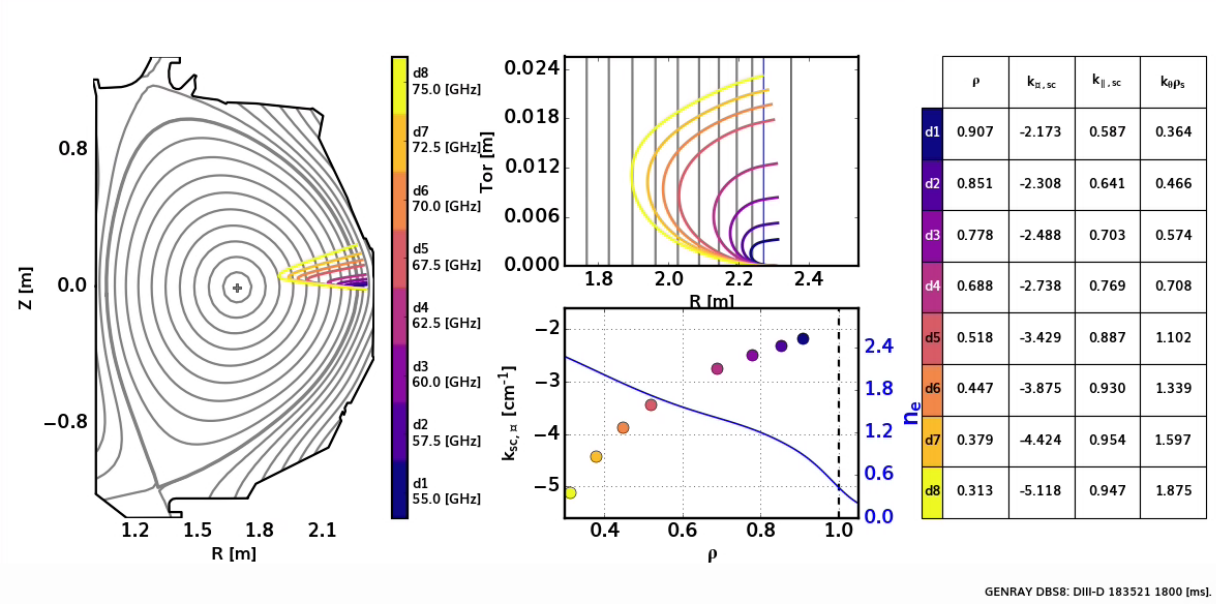

	ρ	$k_{\Xi,sc}$	$k_{\parallel,sc}$	$k_\theta \rho_s$
d1	0.907	-2.173	0.587	0.364
d2	0.851	-2.308	0.641	0.466
d3	0.778	-2.488	0.703	0.574
d4	0.688	-2.738	0.769	0.708
d5	0.518	-3.429	0.887	1.102
d6	0.447	-3.875	0.930	1.339
d7	0.379	-4.424	0.954	1.597
d8	0.313	-5.118	0.947	1.875

Figure D.4: GENRAY results for hydrogen discharge 183521 at 1800 ms. Left panel illustrates the equilibrium reconstruction in black, along with the injected DBS rays color coded by injection frequency. Upper middle panel illustrates ray trajectories in the top-down tokamak view in the toroidal and radial directions, Lower middle panel shown the electron density profile used by GENRAY to calculate the cut-off frequency in blue, and closed circles shown the scattering perpendicular wavel-number. Right panel illsurates a table of GENRAY outputs.

By analogy, this peak degeneracy is very similar to the passive emission contamination in impCER analysis, however no active DBS subtraction of this peak is currently possible. This near zero Doppler shift peak can contaminate DBS measurements, inferring smaller velocities than may actually be present in the plasma. The center of the non-zero frequency peak is taken to be the measured Doppler frequency $f_{Doppler} = \omega_{Doppler}/(2\pi)$. Note that the DBS diagnostic unfortunately cannot directly measure the turbulence phase velocity $\tilde{v}_{ph}$, representing an additional systematic error. Thankfully this quantity is normally found to be nearly constant with ρ, or negligibly small in magnitude. Conversion of the DBS rotation measurements to E_r profiles was done assuming outboard mid-plane coordinates, and in particular using the relation: $E_r(\rho) = v_{\vec{E}\times\vec{B}}\ B_{tor,mid}(\rho)$

Under the circumstances/DBS settings for both the hydrogen and deuterium experiments, the turbulent phase velocity of $\tilde{v}_{ph} \times B_{tor} \approx 3kV/m$ was found to be necessary to bring con-

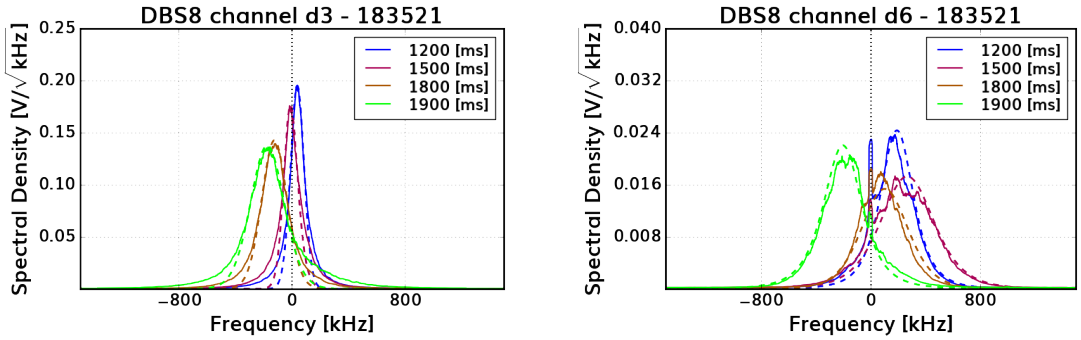

Figure D.5: The spectral density of two DBS channels for shot 183521 in solid lines, alongside best fits using a Gaussian fitting function. Color coding indicates fits at different instances in time, shown in the figure legend.

sistency between radial force balance and DBS measurements. This observation is in conflict with past comparisons between DBS and impCER diagnostics of the radial electric field E_r at the DIII-D tokamak [73]. It is currently unknown what may differ between these currently shown experiments and those compared previously. A comparison of both the reference deuterium and hydrogen discharges between the DBS and impCER predictions is illustrated in Fig. D.6. The DBS predictions of E_r, compensated for $\tilde{v}_{ph} \times B \approx 3kV/m$, are shown as closed circles connected with dashed lines. The previously illustrated impCER predictions are shown as the solid lines. The colors, similar to before, indicate time approaching the L-H transition time. Noteworthy among this diagnostics comparison, both systems predict a large increase in the radial electric field inside $\rho = 0.9$ in the hydrogen reference plasma as time evolves forward. Additionally, the approximate depth of the DBS radial electric field well in L-mode appears to be consistent with that observed by force balance considerations. Such comparisons therefore give greater confidence in the E_r profiles observed, and in particular the differences seen between the two isotope experiments. Additional comparisons however are necessary to justify the choice of trusting radial force balance calculations as sufficiently accurate to correct DBS data. As a result, the following section will detail the third E_r diagnostic available at DIII-D: Beam Emission Spectroscopy.

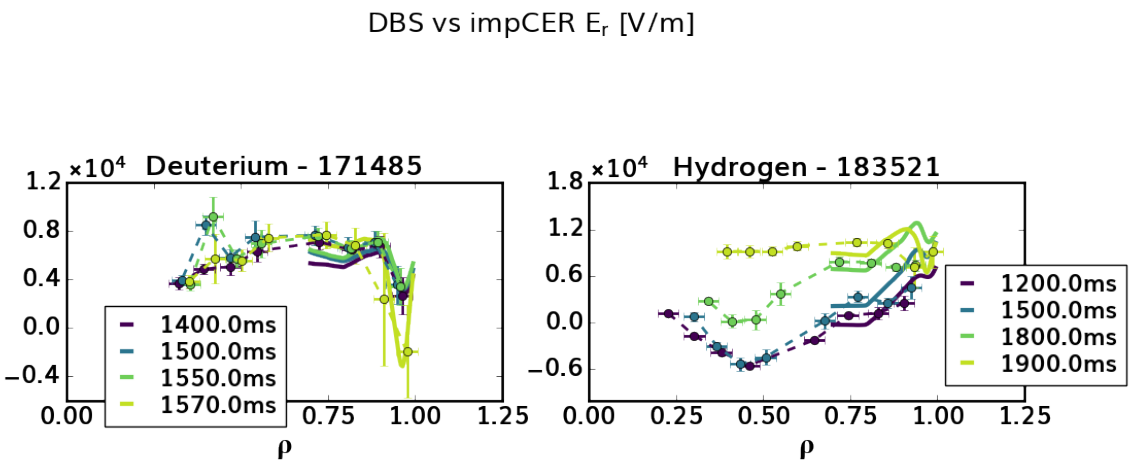

Figure D.6: Comparison of the time dependent deuterium (left) and hydrogen (right) radial electric field measurements from DBS and impCER. DBS results are shown as dashed lines with closed circles, and impCER results are indicated by solid lines. Line colors indicate time approach the L-H transition.

D.2.3 Beam Emission Spectroscopy

The Beam Emission Spectroscopy diagnostic system, or BES in short, measures light intensity fluctuations from Doppler shifted Balmer-α emission near 656 nm. As the name implies, BES measures Balmer-α light specifically emitted by neutral beam particles (from the 150° beam-line at DIII-D) in the n=3 atomic state. These neutrals' emission are distinguishable from thermal Balmer-α because of their larger Doppler shift from the neutral beams' high injection energies (40-81 kV), and are primarily the result of atomic impact excitation of neutral beam particles by the background plasma. As a result, the BES intensity signal and corresponding fluctuations are (to zeroth order) related to the local electron, main ion, and impurity density. A more complete description of this process is given in the synthetic diagnostic chapter of this thesis. Pertinent here, the BES diagnostic at DIII-D contains a highly configurable 64 channel array which can be used to study turbulence properties in great detail. For the reference deuterium and hydrogen experiments under consideration here, the BES diagnostic was configured into a 8x8 grid in the (R,Z) plane at the plasma edge to study

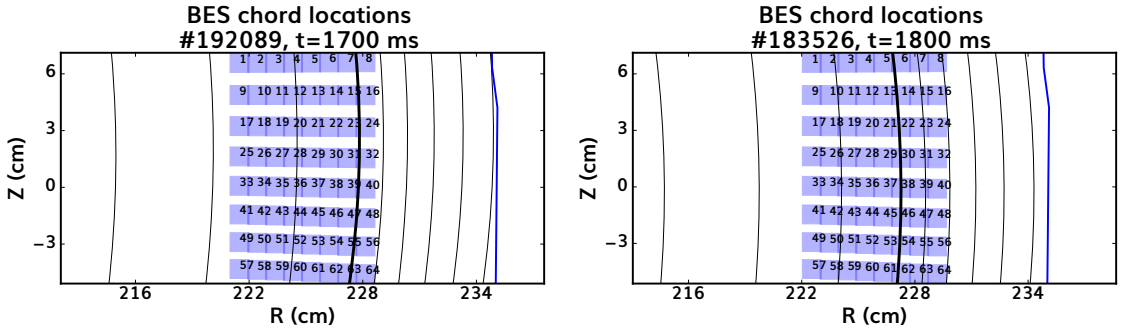

Figure D.7: Deuterium (left) and hydrogen (right) reference discharge's Beam Emission Spectroscopy channel layout. Both experiments had BES aimed at the midplane edge with a 8x8 grid on R-Z plane.

edge turbulence phenomena. Fig. D.7 illustrates the experimental BES channel layout for the hydrogen (183526) and deuterium (192089) reference experiments on the left and right respectively. From these 64 channels, two rows of channels near the outboard mid-plane (33-40,41-48) were analyzed to extract $v_{\vec{E}\times\vec{B}}$ rotation and radial electric field measurements. Specifically, vertical rotation measurements were extracted from these channels using the cross phase between two vertically displaced channels. The linear slope of the two vertically adjacent channels' cross-phase vs. frequency was used to determine the turbulent eddy time delay τ_C. This time delay, along with the vertical separation between the channels Δz, was used to compute the plasma's rotation speed:

$$v_z = \Delta Z/\tau_C = v_{E\times B} + \tilde{v}_{ph} \tag{D.3}$$

Similar to DBS measurements, BES rotation measurements can be contaminated by velocity contributions from the plasmas' turbulent phase velocity $\tilde{v}_{ph}$. This phase velocity however, is not a priori identical to that observed by DBS. In particular, the turbulent phase velocity is known to be a function of poloidal wave-number k_θ. The DBS and BES turbulence diagnostics, which are sensitive to turbulence structures of differing k_θ, likely observe completely different turbulence phase velocities as a result. This value, similar to DBS, is often found to be negligibly small or a near constant offset. Nevertheless, care must be taken in correct-

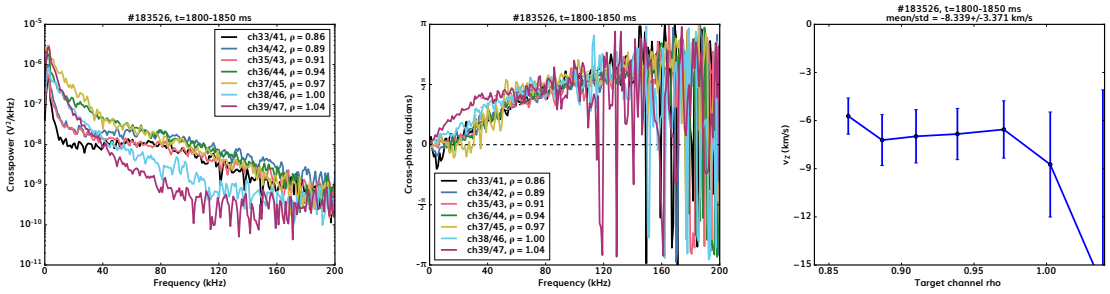

Figure D.8: Hydrogen reference plasma's BES measured cross-power vs. frequency (left), cross-phase vs frequency (middle), and vertical velocity vs. ρ (right) for a row of channels close to the tokamak midplane. Solid lines in the cross-phase vs. frequency plot indicate experimental data, while dashed lines show linear slope fits used to extract v_z.

ing for such systematic uncertainties. Fig. D.8 illustrates the hydrogen reference plasma's BES analysis results. On the left-most column, the cross-power of each channel pair vs. frequency are illustrated as solid lines. In the center column, the channel pairs' cross-phase vs. frequency are similarly plotted as solid lines. The fitted linear slope of cross-phase vs. frequency for each pair are over plotted as dashed lines. Note how the cross-power is largest around 0 kHz, and strongly decreasing with frequency. Simultaneously, the lowest frequency cross-phase contributions appear to be near zero until approximately 40 kHz. At frequencies above 120kHz, the cross-power is nearly at the noise level of the diagnostic signal, and the cross-phase begins to contain frequent phase-skips vs. frequency. Based on these observations, the cross-phase linear slope fits were explicitly limited to the frequency range above where non-zero cross-phase ($f > 40$ kHz) is found and below where phase skipping begins to appear ($f < 120$ kHz). These linear slope best fits, along with equation D.3 are used to calculate the BES predicted vertical (poloidal) velocity shown in the right-most column vs. radial coordinate ρ. Identical to the previously described hydrogen analysis, Fig. D.9 illustrates similar plots for the deuterium reference discharge BES analysis. Akin to before, the linear fits of cross-phase vs. frequency were bounded to be above the frequency range where cross-phase is close to zero, and below where phase skips start to occur. Note how on the right-most column of the deuterium reference discharge BES analysis summary, the vertical velocity has an apparent jump discontinuity around $\rho = 0.92$ which is likely nonphysical in

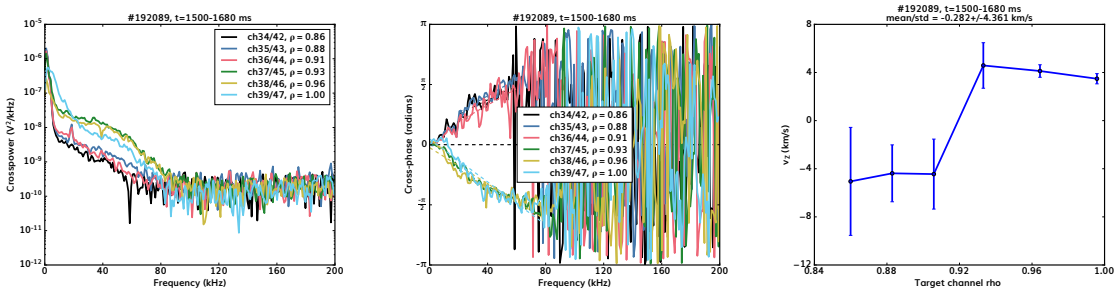

Figure D.9: Deuterium reference plasma's BES measured cross-power vs. frequency (left), cross-phase vs frequency (middle), and vertical velocity vs. ρ (right) for a row of channels close to the tokamak midplane. Solid lines in the cross-phase vs. frequency plot indicate experimental data, while dashed lines show linear slope fits used to extract v_z.

nature based on impCER and DBS diagnostic predictions. Compensation for this potential analysis error was performed by using the negative absolute value of the predicted v_Z for this particular discharge, as opposed to the raw BES analysis predictions.

Identical to DBS measurements, v_Z from BES analyses is converted to radial electric field measurements assuming outboard mid-plane coordinates: $E_r(\rho) = v_{\vec{E}\times\vec{B}}\ B_{tor,mid}(\rho)$. A comparison of the BES predicted radial electric field to impCER force balance measurements for both hydrogen (red) and deuterium (blue) reference plasma's just before L-H transition is shown on the left-most column of Fig. D.10. Note-worthily, no explicit correction for turbulent phase $\tilde{v}_{ph}$ was found to be necessary for achieving good correspondence between the two diagnostics. In particular, both the magnitude and shape of the edge radial electric field profile appears to be remarkably consistent between the impCER and BES measurement systems for either isotope. Such observations seem to suggest $\tilde{v}_{ph} \approx 0$ for the experimental DIII-D cases under considerations, in good coincidence with historical BES/impCER comparisons [65]. It is important to note, that despite its relatively high level of accuracy in determining the E_r profile, the BES diagnostic requires substantial time averaging to be useful. This time resolution trade-off, in the context of comparison between DBS and impCER, makes discerning fast timescale E_r changes challenging. This same time resolution issue is something shared by the 4th and final (edge) E_r profile diagnostic currently available at DIII-D: the fixed Langmuir probe array.

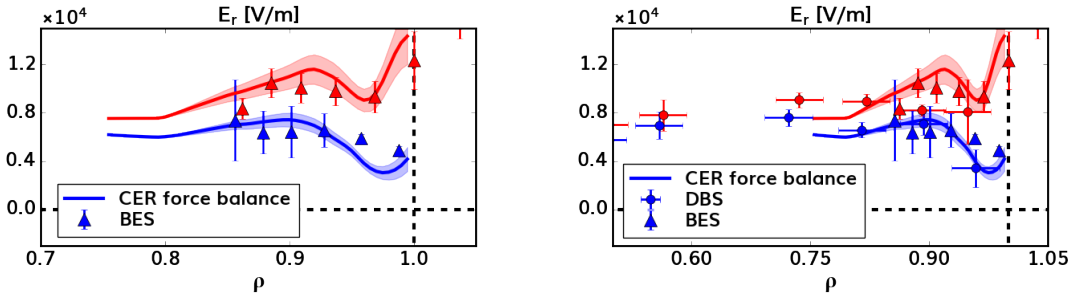

Figure D.10: Radial electric field profiles inferred from Beam Emission Spectroscopy analyses (close triangles), compared to previous calculations from impCER shown as solid lines and DBS in closed circles. Red data indicated hydrogen, and blue illustrates deuterium.

D.2.3.1 Velocimetry

The BES diagnostic can additionally be used to extract velocity fluctuation measurements from a series of 2D turbulence images. The images produced from velocimetry analyses for the hydrogen and deuterium plasmas under consideration (183526,192089) are shown in Fig. D.11 as examples. Note how the turbulent structures, shown as the over-densities in red and under-densities in blue, appear to move with respect to time in the figures. It is this motion, or more precisely the radial and vertical velocities of these structures, which is used to extract the radial and vertical velocity fluctuations. These velocity fluctuation data are then smoothed with respect to some averaging time τ, and directly used to compute the radial and poloidal velocity fluctuations $\langle\tilde{v}_r^2\rangle$,$\langle\tilde{v}_{pol}^2\rangle$, and the Reynolds stress $\langle\tilde{v}_{pol}\tilde{v}_r\rangle$. Recall the explicit assumption when solving the main ion poloidal momentum balance equation 6.10 to produce equation 6.12 was that the Reynolds stress was time independent. Choosing the proper time smoothing necessary to enforce time-independence, while not being so big as to average away all fluctuations to zero, is therefore necessary. To help find this appropriate smoothing time window for extracting the time-independent part of the Reynolds stress from

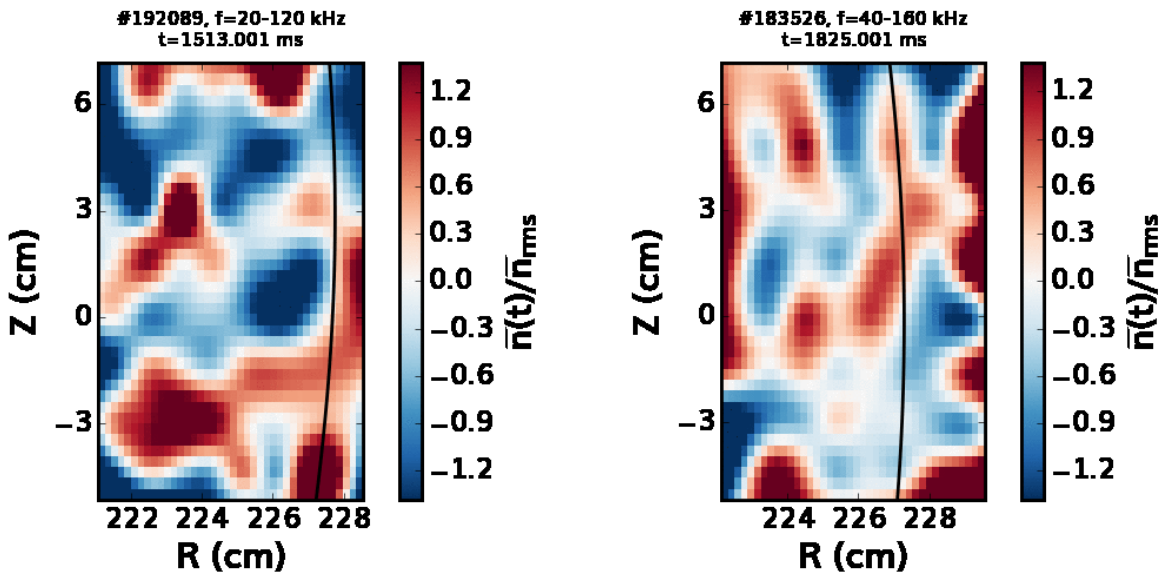

Figure D.11: Turbulence images produced from BES data for reference deuterium (left) and hydrogen (right) discharges preceding the L-H transition time. Red contours show over-densities, and blue contours under-densities. Y-axis is the vertical axis in tokamak midplane coordinates, and the x-axis is in major radius units.

velocimetry analyses, BES time-delay correlation analysis results were leveraged.

The time-scale of interest must be with respect to the same frame of reference as velocimetry analysis (in the lab frame). To meet this experimental constraint, the smoothing time of the Reynolds stress measurements was extracted from the BES time-delay auto-correlation function, also in the lab frame. The time-delay auto-correlation function is computed by determining the correlation between a given signal with itself displaced in time by some value Δt. Results of these experimental calculations for the reference deuterium and hydrogen cases are illustrated in the upper panel of Fig. D.12 in blue and red respectively. Note how the signals appear to exhibit characteristics of both an exponential decay function and oscillating cosine/sine function. Based on this functional form, a best fit to the experimental data was undertaken using the following fitting expression:

$$\langle C(t)\ C(t+\Delta t)\rangle = a\ exp(\frac{-|\Delta t|}{b})\ cos(c|\Delta t| + d) \tag{D.4}$$

The approximate best fit to auto-correlation experimental data in the region $|\Delta t| > 30\ \mu s$

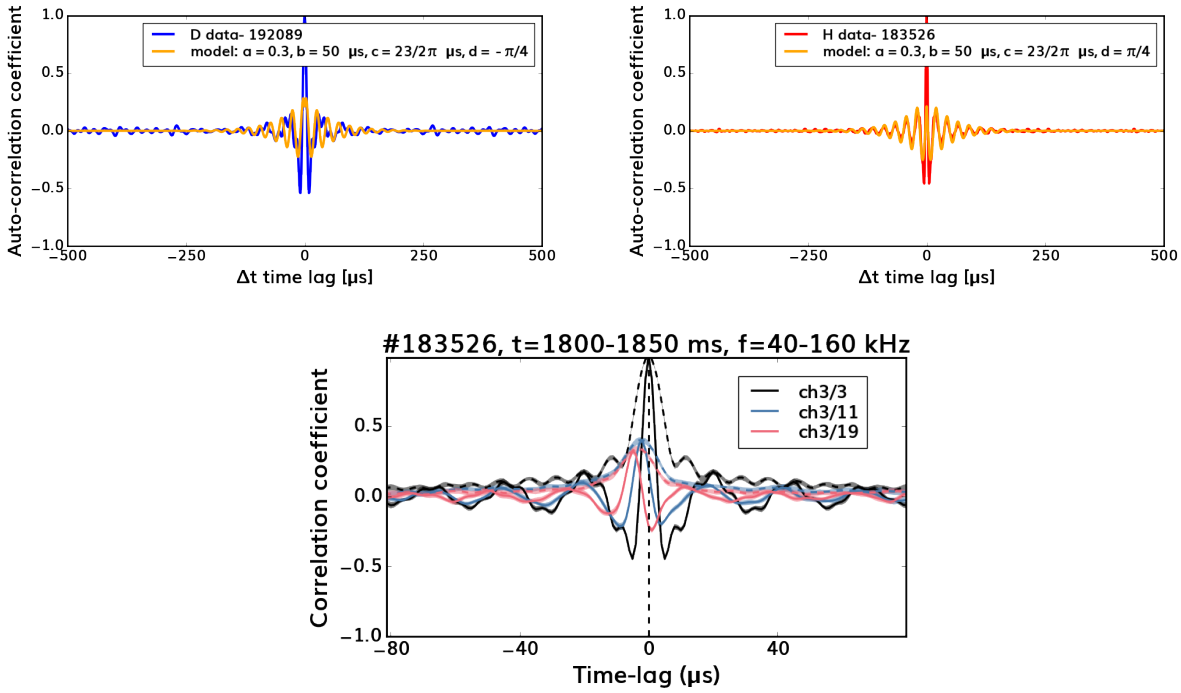

Figure D.12: Upper panel: Beam emission spectroscopy inferred deuterium/hydrogen time delay auto-correlation on the left and right panels respectively. X-axis is time lag in μs vs. auto-correlation on the y-axis. Blue/red indicates experimental BES data, and orange shows a best fit using the equation D.4. Lower panel: Correlation vs. time lag between several vertically displaced channel pairs (solid lines), along with Hilbert transforms (dashed lines).

is plotted in orange for Fig. D.12. Most important for the analysis above is the exponential decay time (b) of the measurement. For either the hydrogen or deuterium experimental cases, the e-folding time was 50 μs. The auto-correlation magnitude and oscillation frequency between hydrogen and deuterium were similar (a=0.3, c= $23/2\pi$ μs), while the phase shift differed by approximately $\pi/2$ between isotopes. There remains appreciable correlation in the experimental deuterium and hydrogen signals inside one e-folding time. As a result, the smoothing time for BES Reynold stress calculations was chosen to be $\tau = 2b = 100$ μs, or the $1/e^2$ folding time where correlations approach the experimental noise level. With this initial velocity smoothing time window in hand, time-independent Reynolds stress calculations can be made. Note that this smoothing time is not the turbulent correlation time, but more akin to an instrumental response function.

D.2.3.2 Correlation Analysis

The poloidal turbulent correlation time however can be extracted from time-delay correlation analysis. This quantity is extracted from the Hilbert transform of the previously shown correlation coefficient profiles in Fig. D.12, but from vertically separated channel pairs. An example of several channels' correlation coefficient profiles vs. time-lag as solid lines, and their respective Hilbert transforms in dashed lines, are shown in the lower panel of Fig. D.12 for reference. The maximum correlation coefficient of these Hilbert transforms and time-lag of maximal Hilbert correlation for many vertically (poloidally) displaced channels are used to determine the turbulent correlation time. The latter time-lag quantity is known as the delay time. These correlation amplitudes, organized versus absolute delay time, are exponentially fit with the constraint of 1 at $\Delta t = 0$ to extract an exponential decay rate τ_c. This exponential decay rate is the turbulence correlation time τ_c. Fig D.13 shows analysis results for the reference deuterium (left) and hydrogen (right) discharges along a single vertical column for the reader's review. Black points illustrate the time delay from the maximum experimental correlation coefficient, and blue data show time delays from the maximum correlation coefficient Hilbert tranform (envelope functions). Note how the turbulence cor-

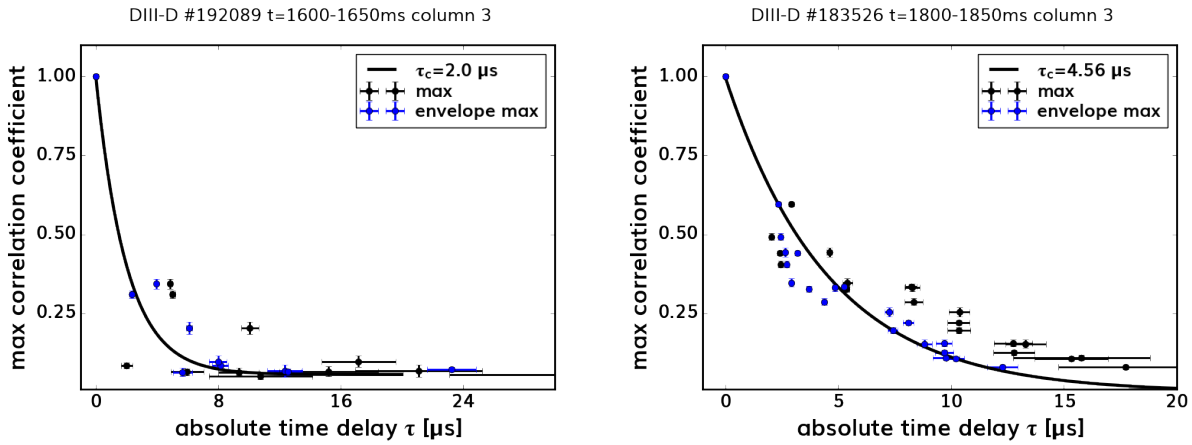

Figure D.13: Deuterium (left) and hydrogen (right) reference discharge's correlation analyses for column 3. Blue data indicate delay times from Hilbert transform results, and black data indicated time delays from raw correlation functions. Black solid lines show best fits to the envelope (Hilbert) data using a constrained exponential decay function.

relation time is larger in hydrogen compared to deuterium, with both substantially smaller than the Reynolds stress smoothing time $\tau = 100\ \mu s$. This same exponential fitting procedure is used to extract the turbulent correlation length L_c by replacing the delay time on the x-axis of Fig D.13 with the absolute vertical channel separation ΔZ.

D.2.4 Langmuir probe analysis

The extraction of a scrape off layer radial electric field from Langmuir probe measurements is determined starting from open field line momentum conservation. Specifically parallel force balance assuming a singly ionized species can be represented as follows [97, 26, 99]:

$$E_{\|} = \frac{j_{\|}}{\sigma_{\|}} - \frac{1}{en_e}\nabla_{\|}P_e - \frac{0.71}{e}\nabla_{\|}T_e \tag{D.5}$$

Above the first, second, and third terms are forces induced from friction, a pressure gradient, and thermo-electric gradient respectively. The quantity 0.71 is a numerical coefficient valid explicitly assuming singly ionized ions [14]. The quantity $j_{\|} = en(v_i - v_e)$ is the current den-

sity parallel to the field lines with some ion and electron speeds v_i and v_e. $\sigma_{\parallel} = e^2 n/(m_e \nu_{ei})$ is the electrical conductivity due to electron-ion collisions with frequency ν_{ei}. Equation D.5 may be integrated in space from the outer divertor target plate to the outboard midplane to derive an expression for the outboard midplane space potential. Under the assumptions of no parallel current $j_{\parallel} = 0$ and exponentially decaying scrape off layer profiles (which are assumed in the modeling process), the following expression for midplane space potential is extracted [71].

$$\phi_{s,omp} = \phi_{fl} + \phi_{sheath} + \phi_{\Delta T_e} \tag{D.6}$$

$$\phi_{sheath} = \frac{\log_e(\frac{2m_i}{m_e \pi}) T_{e,osp}}{2} \tag{D.7}$$

$$\phi_{\Delta T_e} = 0.71 + \frac{\log_e(2)}{\log_e(T_{e,omp}/T_{e,osp})}(T_{e,omp} - T_{e,osp}) \tag{D.8}$$

Above $\phi_{s,omp}$ represents the outboard mid-plane space potential, and ϕ_{fl} the outer strike point floating potential respectively. The sheath potential ϕ_{sheath} represents the potential which accelerates ions as they impinge on the divertor tiles. This same potential also prevents/screens electrons from approaching the wall, unless they have sufficient initial energy to overcome this potential difference. The thermo-electric potential $\phi_{\Delta T_e}$ represents the force pushing electrons from the hotter outboard mid-plane to the cooler outer strike point.

From the lower single null (LSN) divertors of the DIII-D L-H isotope experiments referenced previously, Langmuir probes were set up to acquire data at both the inner and outer strike points to determine scrape off layer properties. The experimental set up of the probe arrays is illustrated in Fig. D.14. The equilibrium reconstruction shown is from EFIT01 (magnetic probes only equilibrium reconstruction), which is believed to be the most accurate reconstruction for scrape off layer (SOL) analysis owing to the locations of the magnetic probes being on or inside the DIII-D limiter/vacuum vessel structures. The solid black contour on the plot represents the plasma separatrix (aka last closed flux surface). The locations where this contour intersects the machine wall, near the L-9 and F10 Langmuir probes re-

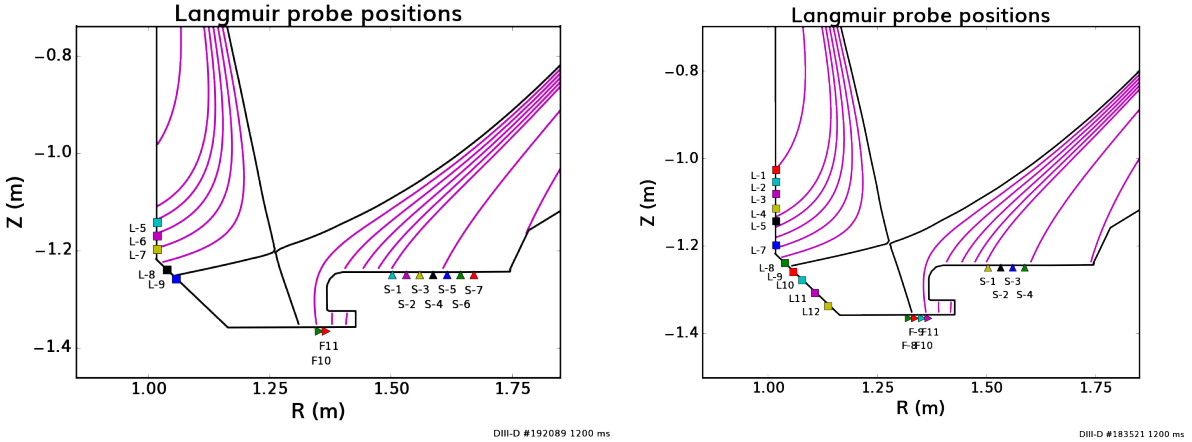

Figure D.14: Fixed Langmuir probe array set up for shot 192089 (deuterium; left) and 183521 (hydrogen; right).

spectively, are typically referred to as the inner and outer targets or inner and outer strike points (ISP/OSP). The violet lines outside this black contour represent open magnetic field line flux surfaces. Langmuir probe channels that were available for this shot are illustrated on the high field side as closed squares, with low field side counterparts represented as closed triangles. Commonly used nomenclature at DIII-D involving the lower divertor structure typically splits the low field side Langmuir probe measurements into two distinct regions: the floor and shelf. The floor is the lowest part of the divertor structure, most easily identified as where the Langmuir probe channel symbols are illustrated as sideways triangles. The shelf, as the name suggests, is the raised portion of the low field side divertor structure, where the Langmuir probe array symbols are triangles which are faced right-side up. The small horizontal protrusion closest to the F11 Langmuir probe is the inlet for a pump, which extracts particles from the plasma to help maintain density control. These shots had a very gentle strike point sweep, where the inner and outer strike points are swept slowly in space using DIII-D 's plasma control system (PCS). These sweeps are valuable from the perspective of Langmuir probe analyses because it exposes the fixed probes to different open field lines, enabling a much more detailed and accurate reconstruction of the plasma properties in the scrape off layer. The fixed probe arrays were able to acquire data of the plasma's electron density n_e, electron temperature T_e, floating potential ϕ_{fl}, and electron particle flux

Γ_e along both inner and outer strike points. From these measurements, analysis was undertaken to extract the plasma's space potential at the outboard mid-plane. The temperature $T_{e,omp}$ in equation D.8 represents the electron temperature at the outboard mid-plane. This quantity, due to uncertainty in the precise accuracy of flux mapping, is usually extracted from power balance considerations as opposed to from radial profile measurements [59, 98]. The calculation of this quantity was performed using the parallel electron heat flux equation:

$$q_{tot,e} = \left(\frac{1}{q_{e,fl}} + \frac{1}{q_{e,spitzer}}\right)^{-1} \tag{D.9}$$

The quantities $q_{tot,e}$, $q_{e,fl}$, and $q_{e,spitzer}$ represent the total parallel electron heat flux incident on the outer target, the flux-limited electron heat flux, and Spitzer conductivity limited heat flux respectively. The total electron heat flux at the outer target can be extracted from TRANSP power balance results using the following relation:

$$q_{e,tot} = \frac{1}{4}\frac{P_{SOL}}{A_{target}} \tag{D.10}$$

$$A_{target} = 2\pi R \frac{B_{pol}}{B_{tot}} \lambda_q \tag{D.11}$$

$$\tag{D.12}$$

Above P_{SOL} represents the total heat flux determined from TRANSP power balance calculations at $\rho = 1.0$ [43, 39]. For our deuterium and hydrogen plasmas respectively this is approximately 2 MW and 3.3 MW. The division by 4 is meant to account for 1/2 of the total heat flux loss crossing the separatrix going to either the electron or ion channels, and 1/2 of these losses going to either the inner or outer strike points. The target area A_{target} is determined by the OSP major radius R, ratio of poloidal to total magnetic field strength B_{pol}/B_{tot}, and the heat flux width λ_q. The outer strike point heat flux width can be extracted

experimentally from the Langmuir probe measurements using the relation:

$$Q_{e,LP}(R_{target}) = \Gamma_e T_e = Q_{e,0}\ exp(-R_{target}/\lambda_q) \tag{D.13}$$

The exponential fit, which will be shown later, for the cases considered produced λ_q of 2.0 mm and 1.9 mm for hydrogen and deuterium respectively. Using these data, the experimental total electron heat flux was calculated. This total heat flux from experiment is then compared to predictions from parallel electron power balance, represented as the right-hand side of equation D.9. The expression used to calculate the flux-limited electron heat flux is:

$$q_{e,fl} = \alpha_e n_e \sqrt{T_e/m_e} T_e \tag{D.14}$$

$$\alpha_e = 0.3 \tag{D.15}$$

Likewise the Spitzer conductivity heat flux contribution expression used was:

$$q_{e,spitzer} = \frac{2\kappa_e (T_e)^{7/2}}{7 l_\parallel} \tag{D.16}$$

$$\kappa_e = \frac{2.16 \times 25,000}{\Lambda_e (1 + 0.27 Z_{eff})} \tag{D.17}$$

Above Λ_e represents the electron Coulomb logarithm and Z_{eff} is the plasma impurity content. The parallel connection length $l_\parallel$ was estimated as 20 m from existing DIII-D literature. Note how both contributions of the expression above depend strongly on the assumed electron temperature. Therefore, it is possible to extract the outboard mid-plane T_e using the estimated total electron heat flux. In particular, the larger than linear dependence of both terms makes slight changes in electron temperature cause drastic changes in predicted total heat flux, allowing for temperature estimates which are relatively insensitive to errors in power accounting and λ_q estimation. Results of this calculation are shown for the experimental deuterium and hydrogen conditions in Fig. D.15 as the left and right panels, respectively. The closed black circles represent solutions to the right hand side of equation D.9, and the

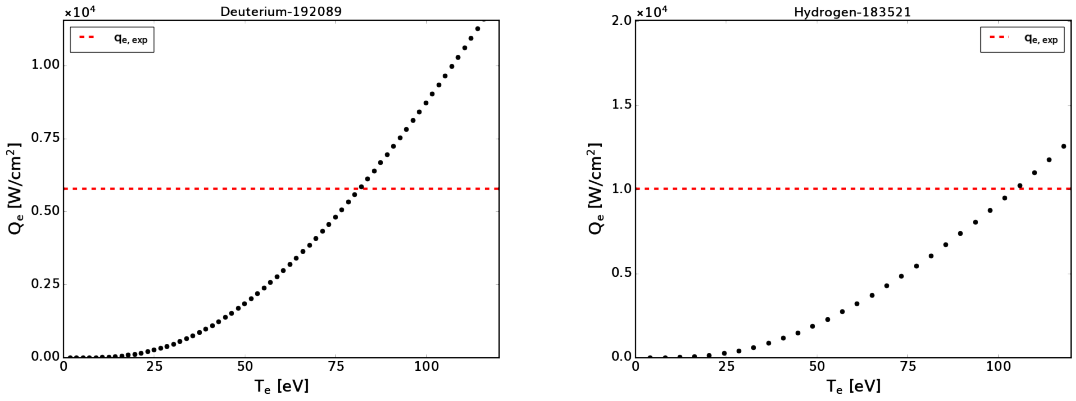

Figure D.15: Parallel electron power balance calculations to determine outboard midplane electron temperature in deuterium (left) and hydrogen (right). Black contours represent LHS solutions to equation D.9 for varying values of T_e, while red contours shows RHS solutions using experimental TRANSP power balance and heat flux width results. The intersection point between the two curves represents the predicted electron temperature from parallel power balance considerations.

red horizontal lines show left hand side solutions from the power balance calculations based on experimental TRANSP and λ_q measurements. The intersection point between the two curves indicates the outboard mid-plane electron temperature. For the deuterium and hydrogen cases under consideration, the analysis predicts $T_{e,omp} = 80, 105eV$. These values appear within the uncertainty of Thomson Scattering data, and are both slightly larger than the peak outer target temperatures (30,60 eV) as one might naively expect.

From these OMP temperature estimates, equation D.8 was used to calculate the expected space potential and radial electric field. More precisely, the calculated space potential was mapped to outboard mid-plane radial coordinates using the EFIT01 equilibrium reconstruction, and fit with an exponential function of the form:

$$\phi_{s,OMP}(R_{mid}) = \phi_{s,0}\ exp(-R_{mid}/\lambda_R) + c \tag{D.18}$$

From these exponential profile fits, the spatial gradient was taken to calculate the scrape off layer radial electric field profile via $E_r = -\nabla\phi_s(R_{mid})$. Figure D.16 illustrates the outboard mid-plane space potential estimates from Langmuir probe data as closed circles,

and exponential fits as solid lines on the left-most panel. Immediately to the right are the inferred scrape off layer radial electric field E_r profiles extracted from these fits. Note how the maximum field at the separatrix is roughly 2 times larger in hydrogen (red) compared to deuterium (blue), with 13.2 vs. 5.6 kV/m. These data are found to be in good consistency with the radial electric field measurements from the other 3 independent diagnostics used to measure E_r: impCER, DBS, and BES. The lowest panel of Fig. D.16 illustrates such a comparison by showing all 4 available E_r profile predictions for hydrogen and deuterium just before L-H transition. The Langmuir probe results are illustrated here as the dashed lines. The value of E_r predicted by these analyses at the separatrix, represented as the closed stars, closely matches predictions from both BES and impCER analyses. This is noteworthy as it demonstrates that no isotope dependent turbulent phase velocities for DBS or BES, or errors in poloidal rotation calculations are likely attributable to the different separatrix E_r seen between isotopes. Therefore, it is most likely that these differences are indeed physical, and not simply due to diagnostic or analysis errors.

The Langmuir probe data in its entirety for both the hydrogen and deuterium plasma cases are shown in Fig. 6.2, on both the inner and outer strike point regions. The raw Langmuir probe measurements for n_e, ϕ_{fl}, and T_e are shown for the inner and outer strike points on Fig. 6.2(a-b,e-f,g-h) respectively. The previously referenced outer strike point electron heat flux fits used to extract the heat flux width λ_q are shown in Fig. 6.2(d) as blue (D) and red (H) solid lines. Similarly, the outer strike point space potential fits used to extract scrape off layer radial electric field profiles are shown in Fig. 6.2(j). The labels in Fig. 6.2(j) indicate the inferred separatrix radial electric field. It is noteworthy that the origin of the difference in space potential and radial electric field between isotopes, is the result of a larger outer strike point electron temperature T_e in hydrogen compared to deuterium. More precisely, this change is the consequence of the higher temperature in hydrogen plasmas outer strike point increasing the sheath potential contribution to the mid-plane space potential. In addition to these higher outer strike point temperatures, the Langmuir probes observed a high and low field side density asymmetry in either isotope. The asymmetry in either case

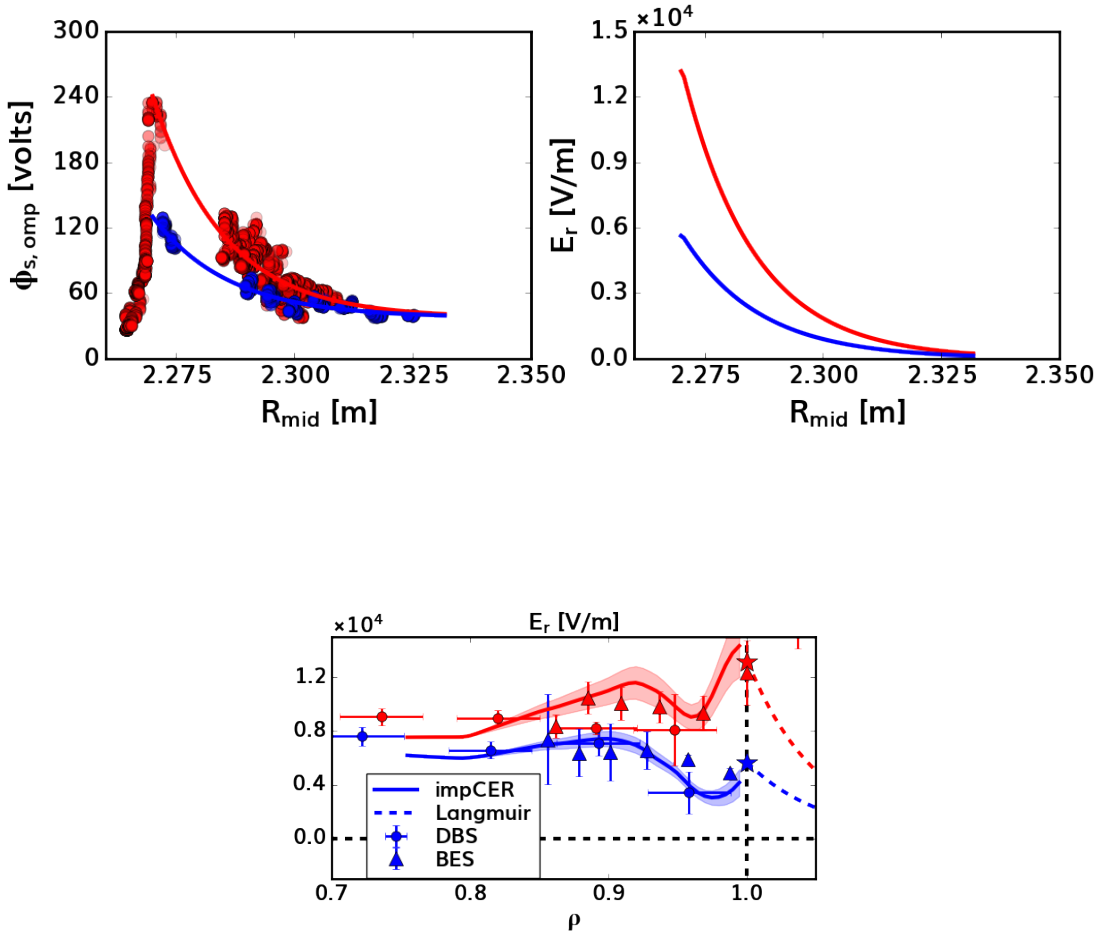

Figure D.16: Upper panels: Exponential fits to the outboard mid-plane space potential (left) and radial electric field (right) vs. outboard major radius R. Red and blue closed circles illustrate Langmuir probe predictions based on solutions based on equation D.8. Solid lines indicate fits to experimental space potential data and predicted SOL radial electric fields. Lower panel: Langmuir probe inferred SOL E_r shown as a dashed line, with the value at the separatrix illustrated as a closed star. Comparison to previously shown E_r measurements for hydrogen and deuterium from impCER, DBS, and BES are shown as solid lines, closed circles, and closed triangles.

shows a noticeably higher electron density at the inner strike point location as compared to the outer. These observations are consistent with findings in other previously studied DIII-D plasmas also in favorable ∇B drift configuration. This asymmetry appears to be roughly 2 times larger on the deuterium high field side compared to hydrogen, potentially allowing a detached inner strike point in deuterium due to larger absolute density (where detachment is defined as when $T_e < 5eV$). Upon closer inspection of the low field side electron densities between isotopes, Langmuir probe data appears to suggest a possible inward shift of hydrogen data compared to deuterium. These Langmuir probe observations potential implicate slight changes in density profiles (in-out asymmetries and outboard radial shifts) between isotopes as important for understanding the observed differences in radial electric fields.

REFERENCES

[1] The ADAS Project 2023 OPEN-ADAS (available at: https:// open.adas.ac.uk/).

[2] M. E. Austin, R. F. Ellis, and T. C. Luce. Determination of wall reflectivity for ECE frequencies in DIII-D. Technical Report GA-A22581; CONF-970405-2, General Atomics, San Diego, CA (United States), May 1997.

[3] M. E. Austin and J. Lohr. Electron cyclotron emission radiometer upgrade on the DIII-D tokamak. *Review of Scientific Instruments*, 74(3):1457–1459, Mar. 2003.

[4] E. A. Belli, J. Candy, and R. E. Waltz. Reversal of turbulent gyroBohm isotope scaling due to nonadiabatic electron drive. *Physics of Plasmas*, 26(8):082305, Aug. 2019.

[5] E. A. Belli, J. Candy, and R. E. Waltz. Reversal of Simple Hydrogenic Isotope Scaling Laws in Tokamak Edge Turbulence. *Physical Review Letters*, 125(1):015001, June 2020.

[6] M. Bessenrodt-Weberpals et al. The isotope effect in ASDEX. *Nuclear Fusion*, 33(8):1205, Aug. 1993.

[7] H. Biglari, P. H. Diamond, and P. W. Terry. Influence of sheared poloidal rotation on edge turbulence. *Physics of Fluids B: Plasma Physics*, 2(1):1–4, Jan. 1990.

[8] B. Bigot. Progress toward ITER's First Plasma. *Nuclear Fusion*, 59(11):112001, Nov. 2019.

[9] A. Blom and C. Jupén. Parametrization of the Zeeman effect for hydrogen-like spectra in high-temperature plasmas. *Plasma Physics and Controlled Fusion*, 44(7):1229–1241, July 2002.

[10] M. Bornatici, R. Cano, O. De Barbieri, and F. Engelmann. Electron cyclotron emission and absorption in fusion plasmas. *Nuclear Fusion*, 23(9):1153–1257, Sept. 1983.

[11] C. Bourdelle et al. L to H mode transition: parametric dependencies of the temperature threshold. *Nuclear Fusion*, 55(7):073015, July 2015.

[12] C. Bourdelle, C. Maggi, L. Chôné, P. Beyer, J. Citrin, N. Fedorczak, X. Garbet, A. Loarte, F. Millitello, M. Romanelli, Y. Sarazin, and JET EFDA Contributors. L to H mode transition: on the role of Z_{eff}. *Nuclear Fusion*, 54(2):022001, Feb. 2014.

[13] B. Braams. *Computational studies in tokamak equilibrium and transport*. PhD thesis, June 1986. Available from INIS: http://inis.iaea.org/search/search.aspx?orig_q=RN:18038616 INIS Reference Number: 18038616.

[14] S. Braginskii and M. Leontovich. *Reviews of plasma physics*. Consultants Bureau New York, 1965.

[15] K. H. Burrell. Tests of causality: Experimental evidence that sheared E×B flow alters turbulence and transport in tokamaks. *Physics of Plasmas*, 6(12):4418–4435, Dec. 1999.

[16] K. H. Burrell and J. D. Callen. Turbulence-driven flow dynamics in general axisymmetric toroidal geometry. *Physics of Plasmas*, 28(6):062502, June 2021.

[17] K. H. Burrell, T. N. Carlstrom, E. J. Doyle, D. Finkenthal, P. Gohil, R. J. Groebner, D. L. Hillis, J. Kim, H. Matsumoto, R. A. Moyer, T. H. Osborne, C. L. Rettig, W. A. Peebles, T. L. Rhodes, H. StJohn, R. D. Stambaugh, M. R. Wade, and J. G. Watkins. Physics of the L-mode to H-mode transition in tokamaks. *Plasma Physics and Controlled Fusion*, 34(13):1859, Dec. 1992.

[18] K. Callahan, C. Chrystal, B. Grierson, S. Haskey, W. Heidbrink, and J. Herfindal. Integrated Z_{eff} analysis on the DIII-D Tokamak. *Journal of Instrumentation*, 14(10):C10002–C10002, Oct. 2019.

[19] K. J. Callahan, L. Schmitz, T. A. Carter, E. A. Belli, C. Chrystal, S. R. Haskey, B. A. Grierson, K. E. Thome, S. P. Smith, G. R. McKee, G. M. Staebler, C. Holland, A. Ashourvan, and Z. Yan. On the origin of the DIII-D L-H power threshold isotope effect. *Nuclear Fusion*, 63(12):126009, Sept. 2023. Publisher: IOP Publishing.

[20] J. Candy, E. A. Belli, and R. V. Bravenec. A high-accuracy Eulerian gyrokinetic solver for collisional plasmas. *Journal of Computational Physics*, 324:73–93, Nov. 2016.

[21] J. Candy, E. A. Belli, and G. Staebler. Spectral treatment of gyrokinetic profile curvature. *Plasma Physics and Controlled Fusion*, 62(4):042001, Feb. 2020. Publisher: IOP Publishing.

[22] J. M. Canik, R. Maingi, V. A. Soukhanovskii, R. E. Bell, H. W. Kugel, B. P. LeBlanc, and T. H. Osborne. Measurements and 2-D modeling of recycling and edge transport in discharges with lithium-coated PFCs in NSTX. *Journal of Nuclear Materials*, 415(1, Supplement):S409–S412, Aug. 2011.

[23] T. Carlstrom, K. Burrell, R. Groebner, A. Leonard, T. Osborne, and D. Thomas. Comparison of L-H transition measurements with physics models. *Nuclear Fusion*, 39(11Y):1941–1947, Nov. 1999.

[24] R. A. Chaban, S. Mordijck, A. M. Rosenthal, A. Bortolon, J. W. Hughes, M. Knolker, F. M. Laggner, T. H. Osborne, L. Schmitz, K. E. Thome, and T. M. Wilks. The role of isotope mass on neutral fueling and density pedestal structure in the DIII-D tokamak. *Nuclear Fusion*, 64(4):046008, Feb. 2024. Publisher: IOP Publishing.

[25] C. S. Chang, S. Kue, and H. Weitzner. X-transport: A baseline nonambipolar transport in a diverted tokamak plasma edge. *Physics of Plasmas*, 9(9):3884–3892, Sept. 2002.

[26] A. V. Chankin, D. P. Coster, G. Corrigan, S. K. Erents, W. Fundamenski, A. Kallenbach, K. Lackner, J. Neuhauser, R. Pitts, t. A. U. Team, and J.-E. Contributors. Fluid code simulations of radial electric field in the scrape-off layer of JET. *Plasma Physics and Controlled Fusion*, 51(6):065022, May 2009.

[27] C. Chrystal, K. H. Burrell, B. A. Grierson, S. R. Haskey, R. J. Groebner, D. H. Kaplan, and A. Briesemeister. Improved edge charge exchange recombination spectroscopy in DIII-D. *Review of Scientific Instruments*, 87(11):11E512, Nov. 2016.

[28] H. Dudding, F. Casson, D. Dickinson, B. Patel, C. Roach, E. Belli, and G. Staebler. A new quasilinear saturation rule for tokamak turbulence with application to the isotope scaling of transport. *Nuclear Fusion*, 62(9):096005, Sept. 2022.

[29] F. Effenberg, A. Bortolon, H. Frerichs, B. Grierson, J. Lore, T. Abrams, T. Evans, Y. Feng, R. Lunsford, R. Maingi, A. Nagy, R. Nazikian, D. Orlov, J. Ren, D. Rudakov, W. Wampler, and H. Wang. 3D modeling of boron transport in DIII-D L-mode wall conditioning experiments. *Nuclear Materials and Energy*, 26:100900, Mar. 2021.

[30] N. Fedorczak, P. H. Diamond, G. Tynan, and P. Manz. Shear-induced Reynolds stress at the edge of L-mode tokamak plasmas. *Nuclear Fusion*, 52(10):103013, Sept. 2012. Publisher: IOP Publishing and International Atomic Energy Agency.

[31] R. J. Fonck, P. A. Duperrex, and S. F. Paul. Plasma fluctuation measurements in tokamaks using beam-plasma interactions. *Review of Scientific Instruments*, 61(11):3487–3495, Nov. 1990.

[32] J. Garcia, T. Görler, F. Jenko, and G. Giruzzi. Gyrokinetic nonlinear isotope effects in tokamak plasmas. *Nuclear Fusion*, 57(1):014007, Dec. 2016. Publisher: IOP Publishing.

[33] P. Gohil, T. Evans, M. Fenstermacher, J. Ferron, T. Osborne, J. Park, O. Schmitz, J. Scoville, and E. Unterberg. L–H transition studies on DIII-D to determine H-mode access for operational scenarios in ITER. *Nuclear Fusion*, 51(10):103020, Oct. 2011.

[34] P. Gohil, T. Jernigan, T. Osborne, J. Scoville, and E. Strait. The torque dependence of the H-mode power threshold in hydrogen, deuterium and helium plasmas in DIII-D. *Nuclear Fusion*, 50(6):064011, June 2010.

[35] P. Gohil, T. Jernigan, J. Scoville, and E. Strait. The H-mode power threshold in hydrogen plasmas in DIII-D. *Nuclear Fusion*, 49(11):115004, Nov. 2009.

[36] B. Grierson, K. Burrell, W. Solomon, R. Budny, and J. Candy. Collisionality scaling of main-ion toroidal and poloidal rotation in low torque DIII-D plasmas. *Nuclear Fusion*, 53(6):063010, June 2013.

[37] B. A. Grierson, K. H. Burrell, C. Chrystal, R. J. Groebner, S. R. Haskey, and D. H. Kaplan. High resolution main-ion charge exchange spectroscopy in the DIII-D H-mode pedestal. *Review of Scientific Instruments*, 87(11):11E545, Nov. 2016.

[38] B. A. Grierson, K. H. Burrell, W. W. Heidbrink, M. J. Lanctot, N. A. Pablant, and W. M. Solomon. Measurements of the deuterium ion toroidal rotation in the DIII-D tokamak and comparison to neoclassical theory. *Physics of Plasmas*, 19(5):056107, May 2012.

[39] B. A. Grierson, X. Yuan, M. Gorelenkova, S. Kaye, N. C. Logan, O. Meneghini, S. R. Haskey, J. Buchanan, M. Fitzgerald, S. P. Smith, L. Cui, R. V. Budny, and F. M. Poli. Orchestrating TRANSP Simulations for Interpretative and Predictive Tokamak Modeling with OMFIT. *Fusion Science and Technology*, 74(1-2):101–115, Aug. 2018.

[40] R. J. Groebner, K. H. Burrell, and R. P. Seraydarian. Role of edge electric field and poloidal rotation in the L-H transition. *Physical Review Letters*, 64(25):3015–3018, June 1990. Publisher: American Physical Society.

[41] A. A. Haasz and J. W. Davis. Hydrogen Isotopic Effects on the Erosion of Carbon. *Fusion Science and Technology*, 50(1):58–67, July 2006.

[42] S. R. Haskey, B. A. Grierson, C. Chrystal, A. Ashourvan, K. H. Burrell, R. J. Groebner, E. A. Belli, L. Stagner, D. J. Battaglia, T. Stoltzfus-Dueck, and A. Bortolon. Main ion and impurity edge profile evolution across the L- to H-mode transition on DIII-D. *Plasma Physics and Controlled Fusion*, 60(10):105001, Oct. 2018.

[43] R. J. Hawryluk. AN EMPIRICAL APPROACH TO TOKAMAK TRANSPORT. In B. Coppi, G. G. Leotta, D. Pfirsch, R. Pozzoli, and E. Sindoni, editors, *Physics of Plasmas Close to Thermonuclear Conditions*, pages 19–46. Pergamon, Jan. 1981.

[44] W. W. Heidbrink, D. Liu, Y. Luo, E. Ruskov, and B. Geiger. A Code that Simulates Fast-Ion D \$ and Neutral Particle Measurements. *Communications in Computational Physics*, 10(3):716–741, Sept. 2011.

[45] J. C. Hillesheim et al. L-H transition studies in hydrogen and mixed ion species plasmas in JET. In *Proceedings of the 44th EPS Conference on Plasma Physics*, volume 41F, pages 1158–1161. European Physical Society, 2017.

[46] F. L. Hinton and R. D. Hazeltine. Theory of plasma transport in toroidal confinement systems. *Reviews of Modern Physics*, 48(2):239–308, Apr. 1976.

[47] C. Holland, A. E. White, G. R. McKee, M. W. Shafer, J. Candy, R. E. Waltz, L. Schmitz, and G. R. Tynan. Implementation and application of two synthetic diagnostics for validating simulations of core tokamak turbulence. *Physics of Plasmas*, 16(5):052301, May 2009.

[48] W. Horton. Drift waves and transport. *Reviews of Modern Physics*, 71(3):735–778, Apr. 1999. Publisher: American Physical Society.

[49] W. A. Houlberg, K. C. Shaing, S. P. Hirshman, and M. C. Zarnstorff. Bootstrap current and neoclassical transport in tokamaks of arbitrary collisionality and aspect ratio. *Physics of Plasmas*, 4(9):3230–3242, Sept. 1997.

[50] N. T. Howard, P. Rodriguez-Fernandez, C. Holland, T. Odstrcil, B. Grierson, F. Sciortino, G. McKee, Z. Yan, G. Wang, T. L. Rhodes, A. E. White, J. Candy, and C. Chrystal. Simultaneous reproduction of experimental profiles, fluxes, transport coefficients, and turbulence characteristics via nonlinear gyrokinetic profile predictions in a DIII-D ITER similar shape plasma. *Physics of Plasmas*, 31(3):032501, Mar. 2024.

[51] S.-I. Itoh and K. Itoh. Model of L to H-Mode Transition in Tokamak. *Physical Review Letters*, 60(22):2276–2279, May 1988. Publisher: American Physical Society.

[52] G. L. Jackson et al. Effects of impurity seeding in DIII-D radiating mantle discharges. *Nuclear Fusion*, 42(1):28, Jan. 2002.

[53] J. Kim, K. H. Burrell, P. Gohil, R. J. Groebner, Y.-B. Kim, H. E. St. John, R. P. Seraydarian, and M. R. Wade. Rotation characteristics of main ions and impurity ions in H-mode tokamak plasma. *Physical Review Letters*, 72(14):2199–2202, Apr. 1994. Publisher: American Physical Society.

[54] Y. B. Kim, P. H. Diamond, and R. J. Groebner. Neoclassical poloidal and toroidal rotation in tokamaks. *Physics of Fluids B: Plasma Physics*, 3(8):2050–2060, Aug. 1991.

[55] J. E. Kinsey, G. M. Staebler, and R. E. Waltz. The first transport code simulations using the trapped gyro-Landau-fluid modela). *Physics of Plasmas*, 15(5):055908, Mar. 2008.

[56] L. Lao, J. Ferron, R. Groebner, W. Howl, H. St. John, E. Strait, and T. Taylor. Equilibrium analysis of current profiles in tokamaks. *Nuclear Fusion*, 30(6):1035–1049, June 1990.

[57] L. L. Lao, H. S. John, R. D. Stambaugh, A. G. Kellman, and W. Pfeiffer. Reconstruction of current profile parameters and plasma shapes in tokamaks. *Nuclear Fusion*, 25(11):1611, Nov. 1985.

[58] E. A. Lazarus, J. D. Bell, C. E. Bush, A. Carnevali, J. L. Dunlap, P. H. Edmonds, L. C. Emerson, O. C. Eldridge, W. L. Gardner, H. C. Howe, D. P. Hutchinson, R. R. Kindsfather, R. C. Isler, R. A. Langley, C. H. Ma, P. K. Mioduszewski, M. Murakami, L. E. Murray, G. H. Neilson, V. K. Paré, S. D. Scott, D. J. Sigmar, J. E. Simpkins, K. A. Stewart, C. E. Thomas, R. M. Wieland, J. B. Wilgen, A. L. Wintenberg, W. R. Wing, and A. J. Wootton. Confinement improvement in beam heated ISX-B discharges with low-z impurity injection. *Journal of Nuclear Materials*, 121:61–68, May 1984.

[59] A. W. Leonard, A. G. McLean, M. A. Makowski, and P. C. Stangeby. Compatibility of separatrix density scaling for divertor detachment with H-mode pedestal operation in DIII-D. *Nuclear Fusion*, 57(8):086033, July 2017. Publisher: IOP Publishing.

[60] N. C. Logan, B. A. Grierson, S. R. Haskey, S. P. Smith, O. Meneghini, and D. Eldon. OMFIT Tokamak Profile Data Fitting and Physics Analysis. *Fusion Science and Technology*, 74(1-2):125–134, Aug. 2018.

[61] J. L. Luxon. A design retrospective of the DIII-D tokamak. *Nuclear Fusion*, 42(5):614, May 2002.

[62] C. F. Maggi et al. Isotope effects on L-H threshold and confinement in tokamak plasmas. *Plasma Physics and Controlled Fusion*, 60(1):014045, Jan. 2018.

[63] Y. R. Martin and T. Takizuka. Power requirement for accessing the H-mode in ITER. *Journal of Physics: Conference Series*, 123:012033, July 2008.

[64] G. McKee, K. Burrell, R. Fonck, G. Jackson, M. Murakami, G. Staebler, D. Thomas, and P. West. Impurity-Induced Suppression of Core Turbulence and Transport in the DIII-D Tokamak. *Physical Review Letters*, 84(9):1922–1925, Feb. 2000.

[65] G. R. McKEE, R. J. Fonck, D. K. Gupta, D. J. Schlossberg, M. W. Shafer, R. L. Boivin, and W. Solomon. Plasma Turbulence Imaging via Beam Emission Spectroscopy in the Core of the DIII-D Tokamak. *Plasma and Fusion Research*, 2:S1025–S1025, 2007.

[66] G. R. McKee, R. J. Fonck, D. K. Gupta, D. J. Schlossberg, M. W. Shafer, C. Holland, and G. Tynan. Turbulence velocimetry of density fluctuation imaging data. *Review of Scientific Instruments*, 75(10):3490–3492, Oct. 2004.

[67] O. Meneghini et al. Integrated modeling applications for tokamak experiments with OMFIT. *Nuclear Fusion*, 55(8):083008, Aug. 2015.

[68] A. M. Messiaen et al. High confinement and high density with stationary plasma energy and strong edge radiation cooling in the upgraded Torus Experiment for Technology Oriented Research (TEXTOR-94). *Physics of Plasmas*, 4(5):1690–1698, May 1997.

[69] S. Migliuolo. Ion temperature gradient driven impurity modes. *Nuclear Fusion*, 32(8):1331, Aug. 1992.

[70] A. Nagy, A. Bortolon, D. M. Mauzey, E. Wolfe, E. P. Gilson, R. Lunsford, R. Maingi, D. K. Mansfield, R. Nazikian, and A. L. Roquemore. A multi-species powder dropper for magnetic fusion applications. *Review of Scientific Instruments*, 89(10):10K121, Oct. 2018.

[71] U. Plank, D. Brida, G. D. Conway, T. Happel, A. E. Hubbard, T. Pütterich, C. Angioni, M. Cavedon, R. Dux, T. Eich, R. Fischer, P. Hennequin, and ASDEX Upgrade Team. Experimental study of the edge radial electric field in different drift configurations and its role in the access to H-mode at ASDEX Upgrade. *Physics of Plasmas*, 30(4):042513, Apr. 2023.

[72] D. M. Ponce-Marquez, B. D. Bray, T. M. Deterly, C. Liu, and D. Eldon. Thomson scattering diagnostic upgrade on DIII-D. *Review of Scientific Instruments*, 81(10):10D525, Oct. 2010.

[73] Q. Pratt, T. Rhodes, C. Chrystal, and T. Carter. Comparison of Doppler backscattering and charge exchange measurements of E × B plasma rotation in the DIII-D tokamak under varying torque conditions. *Plasma Physics and Controlled Fusion*, 64(9):095017, Aug. 2022. Publisher: IOP Publishing.

[74] G. M. Quénot, J. Pakleza, and T. A. Kowalewski. Particle image velocimetry with optical flow. *Experiments in Fluids*, 25(3):177–189, Aug. 1998.

[75] T. D. Rempel, R. F. Gandy, and A. J. Wootton. Density fluctuation effects on electron cyclotron emission correlation measurements in optically gray plasmas. *Review of Scientific Instruments*, 65(6):2044–2048, June 1994.

[76] C. P. Ritz, H. Lin, T. L. Rhodes, and A. J. Wootton. Evidence for confinement improvement by velocity-shear suppression of edge turbulence. *Physical Review Letters*, 65(20):2543–2546, Nov. 1990.

[77] A. Rosenthal, J. Hughes, F. Laggner, T. Odstrčil, A. Bortolon, T. Wilks, and F. Sciortino. Inference of main ion particle transport coefficients with experimentally constrained neutral ionization during edge localized mode recovery on DIII-D. *Nuclear Fusion*, 63(4):042002, Apr. 2023.

[78] F. Ryter, M. Cavedon, T. Happel, R. M. McDermott, E. Viezzer, G. D. Conway, R. Fischer, B. Kurzan, T. Pütterich, G. Tardini, M. Willensdorfer, and the ASDEX Upgrade Team. L-H transition physics in hydrogen and deuterium: key role of the edge radial electric field and ion heat flux. *Plasma Physics and Controlled Fusion*, 58(1):014007, Jan. 2016.

[79] F. Ryter et al. Survey of the H-mode power threshold and transition physics studies in ASDEX Upgrade. *Nuclear Fusion*, 53(11):113003, Nov. 2013.

[80] L. Schmitz. The role of turbulence–flow interactions in L- to H-mode transition dynamics: recent progress. *Nuclear Fusion*, 57(2):025003, Jan. 2017. Publisher: IOP Publishing.

[81] L. Schmitz et al. Reducing the L-H transition power threshold in ITER-similar-shape DIII-D hydrogen plasmas. *Nuclear Fusion*, 62(12):126050, Nov. 2022.

[82] L. Schmitz, L. Zeng, T. L. Rhodes, J. C. Hillesheim, E. J. Doyle, R. J. Groebner, W. A. Peebles, K. H. Burrell, and G. Wang. Role of Zonal Flow Predator-Prey Oscillations in Triggering the Transition to H-Mode Confinement. *Physical Review Letters*, 108(15):155002, Apr. 2012.

[83] M. Schneider et al. Modelling one-third field operation in the ITER pre-fusion power operation phase. *Nuclear Fusion*, 59(12):126014, Dec. 2019.

[84] P. A. Schneider, P. Hennequin, N. Bonanomi, M. Dunne, G. D. Conway, and U. Plank. Overview of the isotope effects in the ASDEX Upgrade tokamak. *Plasma Physics and Controlled Fusion*, 63(6):064006, June 2021.

[85] S. D. Scott et al. Isotopic scaling of confinement in deuterium–tritium plasmas. *Physics of Plasmas*, 2(6):2299–2307, June 1995.

[86] K. C. Shaing and E. C. Crume. Bifurcation theory of poloidal rotation in tokamaks: A model for L-H transition. *Physical Review Letters*, 63(21):2369–2372, Nov. 1989. Publisher: American Physical Society.

[87] L. M. Shao et al. On the role of the hydrogen concentration in the L-H transition power threshold in EAST. *Nuclear Fusion*, 61(1):016010, Nov. 2020.

[88] A. P. Smirnov, P. O. Box, and D. Mar. The GENRAY Ray Tracing Code.

[89] J. Snipes et al. H mode power threshold database for ITER. *Nuclear Fusion*, 36(9):1217–1264, Sept. 1996.

[90] W. M. Solomon, K. H. Burrell, R. Andre, L. R. Baylor, R. Budny, P. Gohil, R. J. Groebner, C. T. Holcomb, W. A. Houlberg, and M. R. Wade. Experimental test of the neoclassical theory of impurity poloidal rotation in tokamaksa). *Physics of Plasmas*, 13(5):056116, May 2006.

[91] G. Staebler, E. A. Belli, J. Candy, J. Kinsey, H. Dudding, and B. Patel. Verification of a quasi-linear model for gyrokinetic turbulent transport. *Nuclear Fusion*, 61(11):116007, Nov. 2021.

[92] G. M. Staebler, J. Candy, N. T. Howard, and C. Holland. The role of zonal flows in the saturation of multi-scale gyrokinetic turbulence. *Physics of Plasmas*, 23(6):062518, June 2016.

[93] G. M. Staebler and R. J. Groebner. Limit cycle oscillations and L/H transitions from two dimensional mean field momentum transport equations. *Nuclear Fusion*, 55(7):073008, June 2015. Publisher: IOP Publishing.

[94] G. M. Staebler, J. E. Kinsey, and R. E. Waltz. Gyro-Landau fluid equations for trapped and passing particles. *Physics of Plasmas*, 12(10):102508, Oct. 2005.

[95] G. M. Staebler, J. E. Kinsey, and R. E. Waltz. A theory-based transport model with comprehensive physics. *Physics of Plasmas*, 14(5):055909, May 2007.

[96] G. M. Staebler, R. E. Waltz, J. Candy, and J. E. Kinsey. New Paradigm for Suppression of Gyrokinetic Turbulence by Velocity Shear. *Physical Review Letters*, 110(5):055003, Jan. 2013.

[97] P. C. Stangeby. *The plasma boundary of magnetic fusion devices*. Plasma physics series. Institute of Physics Pub, Bristol ; Philadelphia, 2000.

[98] P. C. Stangeby, J. M. Canik, J. D. Elder, C. J. Lasnier, A. W. Leonard, D. Eldon, M. A. Makowski, T. H. Osborne, and B. A. Grierson. Identifying the location of the OMP separatrix in DIII-D using power accounting. *Nuclear Fusion*, 55(9):093014, Aug. 2015. Publisher: IOP Publishing.

[99] P. C. Stangeby and A. V. Chankin. Simple models for the radial and poloidal E × B drifts in the scrape-off layer of a divertor tokamak: Effects on in/out asymmetries. *Nuclear Fusion*, 36(7):839, July 1996.

[100] E. J. Strait. Stability of high beta tokamak plasmas*. *Physics of Plasmas*, 1(5):1415–1431, May 1994.

[101] E. J. Strait. Magnetic diagnostic system of the DIII-D tokamak. *Review of Scientific Instruments*, 77(2):023502, Feb. 2006.

[102] C. Sung, W. A. Peebles, C. Wannberg, T. L. Rhodes, X. Nguyen, R. Lantsov, and L. Bardóczi. A frequency tunable, eight-channel correlation ECE system for electron temperature turbulence measurements on the DIII-D tokamak. *Review of Scientific Instruments*, 87(11):11E123, Aug. 2016.

[103] K. Tanaka et al. Isotope effects on transport in LHD. *Plasma Physics and Controlled Fusion*, 63(9):094001, Sept. 2021.

[104] F. Troyon and R. Gruber. A semi-empirical scaling law for the -limit in tokamaks. *Physics Letters A*, 110(1):29–34, July 1985.

[105] H. Urano et al. Hydrogen isotope effects on ITG scale length, pedestal and confinement in JT-60 H-mode plasmas. *Nuclear Fusion*, 53(8):083003, July 2013.

[106] F. Wagner. A quarter-century of H-mode studies. *Plasma Physics and Controlled Fusion*, 49(12B):B1, Nov. 2007.

[107] F. Wagner, R. Bartiromo, G. Becker, H. Bosch, A. Eberhagen, G. Fussmann, O. Gehre, J. Gernhardt, G. Gierke, E. Clock, O. Gruber, G. Haas, G. Janeschitz, F. Karger, M. Keilhacker, A. Kislyakov, O. Klüber, M. Kornherr, P. Kotzé, K. Lackner, M. Lenoci, G. Lisitano, A. Mahdavi, H.-M. Mayer, K. McCormick, D. Meisel, V. Mertens, E. Müller, H. Murmann, H. Niedermeyer, W. Poschenrieder, H. Rapp, F. Ryter, J. Roth, F. Schneider, G. Siller, P. Smeulders, F. Söldner, E. Speth, K. Steinmetz, K.-H. Steuer, and O. Vollmer. Experimental evidence for neoclassical ion transport effects in the H-transition of ASDEX. *Nuclear Fusion*, 25(10):1490–1495, Oct. 1985.

[108] F. Wagner, G. Becker, K. Behringer, D. Campbell, A. Eberhagen, W. Engelhardt, G. Fussmann, O. Gehre, J. Gernhardt, G. V. Gierke, G. Haas, M. Huang, F. Karger, M. Keilhacker, O. Klüber, M. Kornherr, K. Lackner, G. Lisitano, G. G. Lister, H. M. Mayer, D. Meisel, E. R. Müller, H. Murmann, H. Niedermeyer, W. Poschenrieder, H. Rapp, H. Röhr, F. Schneider, G. Siller, E. Speth, A. Stäbler, K. H. Steuer, G. Venus, O. Vollmer, and Z. Yü. Regime of Improved Confinement and High Beta in Neutral-Beam-Heated Divertor Discharges of the ASDEX Tokamak. *Physical Review Letters*, 49(19):1408–1412, Nov. 1982.

[109] F. Wagner, G. Fussmann, T. Grave, M. Keilhacker, M. Kornherr, K. Lackner, K. McCormick, E. R. Müller, A. Stäbler, G. Becker, K. Bernhardi, U. Ditte, A. Eberhagen,

O. Gehre, J. Gernhardt, G. v. Gierke, E. Glock, O. Gruber, G. Haas, M. Hesse, G. Janeschitz, F. Karger, S. Kissel, O. Klüber, G. Lisitano, H. M. Mayer, D. Meisel, V. Mertens, H. Murmann, W. Poschenrieder, H. Rapp, H. Röhr, F. Ryter, F. Schneider, G. Siller, P. Smeulders, F. Söldner, E. Speth, K. H. Steuer, Z. Szymanski, and O. Vollmer. Development of an Edge Transport Barrier at the H-Mode Transition of ASDEX. *Physical Review Letters*, 53(15):1453–1456, Oct. 1984. Publisher: American Physical Society.

[110] R. E. Waltz, G. M. Staebler, W. Dorland, G. W. Hammett, M. Kotschenreuther, and J. A. Konings. A gyro-Landau-fluid transport model. *Physics of Plasmas*, 4(7):2482–2496, July 1997.

[111] G. Wang, T. L. Rhodes, and W. A. Peebles. New, improved analysis of correlation ECE data to accurately determine turbulent electron temperature spectra and magnitudes (invited). *Review of Scientific Instruments*, 92(4):043523, Apr. 2021.

[112] J. Weiland, A. B. Jarmén, and H. Nordman. Diffusive particle and heat pinch effects in toroidal plasmas. *Nuclear Fusion*, 29(10):1810, Oct. 1989.

[113] A. E. White, L. Schmitz, G. R. McKee, C. Holland, W. A. Peebles, T. A. Carter, M. W. Shafer, M. E. Austin, K. H. Burrell, J. Candy, J. C. DeBoo, E. J. Doyle, M. A. Makowski, R. Prater, T. L. Rhodes, G. M. Staebler, G. R. Tynan, R. E. Waltz, and G. Wang. Measurements of core electron temperature and density fluctuations in DIII-D and comparison to nonlinear gyrokinetic simulations. *Physics of Plasmas*, 15(5):056116, May 2008.

[114] A. E. White, L. Schmitz, W. A. Peebles, T. A. Carter, T. L. Rhodes, E. J. Doyle, P. A. Gourdain, J. C. Hillesheim, G. Wang, C. Holland, G. R. Tynan, M. E. Austin, G. R. McKee, M. W. Shafer, K. H. Burrell, J. Candy, J. C. DeBoo, R. Prater, G. M. Staebler, R. E. Waltz, and M. A. Makowski. A correlation electron cyclotron emission diagnostic and the importance of multifield fluctuation measurements for testing nonlinear gyrokinetic turbulence simulations. *Review of Scientific Instruments*, 79(10):103505, Oct. 2008.

[115] D. G. Whyte, M. R. Wade, D. F. Finkenthal, K. H. Burrell, P. Monier-Garbet, B. W. Rice, D. P. Schissel, W. P. West, and R. D. Wood. Measurement and verification of zeff radial profiles using charge exchange recombination spectroscopy on DIII-D. *Nuclear Fusion*, 38(3):387, Mar. 1998.

[116] X. Wu, G. Xu, B. Wan, J. Juul Rasmussen, V. Naulin, and A. Henry Nielsen. One-dimensional modelling of limit-cycle oscillation and H-mode power scaling. *Nuclear Fusion*, 55(5):053029, May 2015.

[117] Z. Yan, P. Gohil, G. McKee, D. Eldon, B. Grierson, T. Rhodes, and C. Petty. Turbulence and sheared flow structures behind the isotopic dependence of the L-H power threshold on DIII-D. *Nuclear Fusion*, 57(12):126015, Dec. 2017.

[118] Z. Yan, G. McKee, R. Fonck, P. Gohil, R. Groebner, and T. Osborne. Observation of the L H Confinement Bifurcation Triggered by a Turbulence-Driven Shear Flow in a Tokamak Plasma. *Physical Review Letters*, 112(12):125002, Mar. 2014.